Investigations on Single and Multilayer TiO_2 based Thin Films for use as Transparent Conducting Electrode

Submitted in
fulfillment of the requirements for the degree of

Doctor of Philosophy

by

Satyavir Singh
(ID No. 2013RPH9533)

Under the Supervision of

Prof. Kanupriya Sachdev

DEPARTMENT OF PHYSICS

MALAVIYA NATIONAL INSTITUTE OF TECHNOLOGY JAIPUR

January 2019

This work is dedicated to my beloved parents,

wife Tina and son Anirudh

And above all,

To the Almighty God!

DECLARATION

I, **Satyavir Singh**, declare that this thesis titled, "***Investigations on Single and Multilayer TiO_2 based Thin Films for use as Transparent Conducting Electrode***" and the work presented in it are my own. I confirm that:

- This work was done wholly or mainly while in candidature for a research degree at this university.
- Where any part of this thesis has previously been submitted for a degree or any other qualification at this university or any other institution, this has been clearly stated.
- Where I have consulted the published work of others, this is always clearly attributed.
- Where I have quoted from the work of others, the source is always given. With the exception of such quotations, this thesis is entirely my own work.
- I have acknowledged all main sources of help.
- Where the thesis is based on work done by myself, jointly with others, I have made clear exactly what was done by others and what I have contributed myself.

Date: Satyavir Singh

(ID No. 2013RPH9533)

CERTIFICATE

This is to certify that the thesis entitled "***Investigations on Single and Multilayer TiO_2 based Thin Films for use as Transparent Conducting Electrode***" being submitted by **Mr. Satyavir Singh (ID No: 2013RPH9533)** is a bonafide research work carried out under my supervision and guidance in fulfillment of the requirement for the award of the degree of **Doctor of Philosophy** in the Department of Physics, Malaviya National Institute of Technology, Jaipur, India. The matter embodied in this thesis is original and has not been submitted to any other University or Institute for the award of any other degree.

Place: Jaipur
Date:

Dr. Kanupriya Sachdev
Professor
Department of Physics
MNIT Jaipur

ACKNOWLEDGEMENTS

First of all, I am grateful to The Almighty God for establishing me to complete this work. It is a pleasant aspect for me to express my deep and sincere gratitude to the people due to whom it has been possible for me to accomplish my Ph.D. thesis. It is very simple to list them all but very difficult to express the thanks for their innumerable support.

First of all, I would like to express my sincere gratitude to my thesis supervisor Dr. K. Sachdev, Professor, Department of Physics and Head, Materials Research Centre, for bringing me to this amazing field and providing endless support to my research. My Ph. D. period under her supervision has been an extraordinary period of my life. I have found her very good teacher as well as very good guardian. She has always given me time to discuss scientific things in spite of her busy schedule. I am really very fortunate to have Dr. K. Sachdev as my supervisor in my life. I am extremely thankful to her and I will always be indebted to her for her great and invaluable support.

I am greatly indebted to Dr. K. Asokan, IUAC, New Delhi, who provided me an opportunity to join his group, and gave access to the laboratory/research facilities. His unfailing support and continuous encouragement throughout the research work and during writing thesis made this work accomplishable.

It is a very pleasant opportunity for me to express my sincere thanks to Head of Department of Physics, MNIT Jaipur for providing the administrative support and necessary facilities in the Department for accomplishment of my research work. I also thank the faculty members of the Department and DREC members with whom I had an opportunity to discuss academics at various stages of my work. In addition, I acknowledge the support provided by non-teaching staff members of Department of Physics, MNIT Jaipur.

I convey my sincere thanks to Materials Research Centre (MRC) administration, scientific and technical staff for their help at various stages of my work. I am extremely thankful to MRC for making available the equipment's and facilities without which I would not have completed my research work.

I am indebted to Dr. D. Kanjilal, Director, Inter University Accelerator Centre (IUAC), New Delhi, for giving me the opportunity of doing the research work at the centre.

I am thankful to Dr. Vikas Shrama, MNIT Jaipur and post doctoral fellow at IIT Delhi for the stimulating discussions and constant encouragement.

I acknowledge the support provided by my colleagues Mr. Dinesh Saini, Mr. Sachin Surve, Ms. Neeru Sharma, Mr. Himanshu Sharma, Mr. Mahendra Rathore, Mr. Arun Vinod, Ms. Smita Howlader, Ms. Suniksha Gupta, other lab mates, project students and all seniors for moral support and discussion.

The acknowledgement would remain incomplete without mentioning my wife Tina and my family members for their faith, kind support, love, patience and constant encouragement. Their endless love, guidance, teaching, training and invaluable support at each and every moment showed me the way to proceed in life.

January, 2019
Satyavir Singh

ABSTRACT

In the present study, Nb doped TiO_2 (NTO) single layer thin films and Oxide/Metal/Oxides multilayer structure such as TiO_2/Ag/TiO_2 and NTO/Ag/NTO have been explored for their use as transparent conducting electrodes in optoelectronic devices. Transparent resistive switching random access memory (ReRAM) devices have been fabricated using Al_2O_3 layer and multilayer transparent conducting electrodes. The multilayer structures have been deposited using rf/dc sputtering on glass substrates at room temperature. The thickness of the top and bottom oxide layers has been varied to obtain the optimum thickness of the sandwich structure in terms of maximum figure of merit. The optimized thickness was found to be TiO_2 (45 nm)/Ag (9 nm)/TiO_2 (45 nm) and NTO (35 nm)/Ag (9 nm)/NTO (35 nm) among all the multilayers.

The pristine specimen of optimized multilayer structures were further implanted with 40 keV N^+ and 100 keV Ar^+ ions to modify their structural, optical and electrical properties. It was observed that implantation leads to enhancement of electrical transport properties and a small simultaneous degradation of optical transmittance and an overall enhancement in the figure of merit after implantation. The crystal structure and thickness of these films have been determined using XRD and RBS respectively. Optical transmittance of the specimens was obtained from UV-Vis Spectrophotometer. Electrical properties were determined by Hall measurements. Transport properties of the specimens were tested for low temperature range (80−340K) and found to be stable in the same range, which suggest their potential use in low temperature environment. Chemical states and stoichiometry of the specimens were analyzed using XPS. The multilayer thin films have shown the electrical resistivity in the order of 10^{-4}−10^{-5} Ω cm and average transmittance in the range of 70%−85%. The obtained results make these multilayer films highly suitable as ITO alternative in various optoelectronic devices.

Transparent ReRAM devices based on Al_2O_3 layer have been fabricated by sputtering on glass substrates at room temperature using TAT and NAN multilayer electrodes. The devices have been characterized by UV-Vis, XPS and I-V measurements. Both devices show good transmittance over the visible region of solar radiation. The chemical state of oxygen in Al_2O_3 was analyzed using XPS. Devices show switching from HRS to LRS and LRS to HRS when subjected to biasing voltage. We believe that

fabrication of transparent ReRAM devices based on Al_2O_3 and such multilayer TCEs will give an impetus to the development of transparent memory devices.

CONTENTS

Chapter 3

Chapter 4

Chapter 5

Chapter 6

Chapter 7

Chapter 8

LIST OF TABLES

LIST OF FIGURES

LIST OF ABBREVIATIONS

TCO:	Transparent Conducting Oxide
TCE:	Transparent Conducting Electrode
TC:	Transparent Conductor
TiO_2:	Titanium Dioxide
Nb:	Niobium
NTO:	Nb doped TiO_2
ITO:	Indium Tin Oxide
XRD:	X-Ray Diffraction
RBS:	Rutherford Backscattering Spectrometry
XPS:	X-ray Photoelectron Spectroscopy
UPS:	Ultraviolet Photoelectron Spectroscopy
FESEM:	Field Emission Scanning Electron Microscopy
EDS:	Energy Dispersive Spectroscopy
AFM:	Atomic Force Microscopy
TEM:	Transmission Electron Microscopy
SAED:	Selective Area Electron Diffraction
UV-Vis:	Ultra Violet- Visible

TAT: $TiO_2/Ag/TiO_2$

NAN: NTO/Ag/NTO

FOM: Figure of Merit

Chapter-1

Introduction

This chapter gives introduction of the Transparent conducting oxides (TCOs) and the criteria for selecting the appropriate TCO for specific devices. Subsequently the materials used for TCOs are discussed with a further explanation of characteristics of multilayer TCO. The industrial applications of the TCOs in various devices are also discussed. The objectives of the thesis are given in the last section.

1.1 Introduction

Transparent conducting oxides (TCOs) comprise a special class of materials that simultaneously exhibit good electrical conductivity and optical transparency in the visible region of light [1,2]. TCOs have attracted great attention due to their unique combination of electrical and optical properties. They are technologically important materials and are used in solar cells, light emitting diodes (LEDs), flat panel displays (FPDs), touch screens, electrochromic windows and transparent heaters [3,4]. Transparent conducting electrodes are key component in various optoelectronic devices and affect the performance of the devices and hence have been largely investigated for new materials with superior properties [5]. Today the role of TCO in active and passive devices has become quite sophisticated and hence enhanced optical, electrical properties and their understandings are significant. The first transparent conductive oxide was prepared by Badeker [6] in 1907 using thermal oxidation of cadmium metal. Post-oxidation of metal films was the earliest technique to prepare the TCO film and tin oxide prepared by same method showed conductivity of 10 S cm^{-1} in 1954 [7]. Indium tin oxide (ITO) films were deposited by Mizuhashi *et al.* in 1979 [8] and conductivity of 2×10^{-4} Ω cm with good transmittance was obtained. ITO has been the most popular material to be used as transparent conductor in various optoelectronic devices but has many limitations such as; scarcity of indium resulting in its high price, requirement of high temperature synthesis for its exceptional properties and its brittle (can crack at low strain of 2–3%) nature. These limitations have propelled the scientific community to search and develop new materials with overcoming these limitations [9,10]. In last 3-4 decades metal doped

oxides [11], graphene [12], thin metallic films [13], carbon nanotubes [14], metallic nanowires [15], metallic grids [16], conducting polymers [17] and oxide/metal/oxide multilayers [18,19] have been investigated for their use as transparent conductors.

Figure 1.1: Transparent conducting oxides for different applications.

Sheet resistance value is an important parameter and the requirement of sheet resistance value of electrode is varied as per the device where it is used; such as for touch screens it should be 400–700 Ω/sq and for thin film solar cells and flat panel displays a value less than 10 Ω/sq is needed [20]. A variety of deposition methods such as sputtering, thermal and e-beam evaporation, sol-gel and pulse laser deposition have been used to prepare TCO thin films. Stoichiometry, microstructure, defects and impurities present in the films are strongly dependent on the deposition methods resulting in change in structural, electrical and optical properties of the TCO thin films with preparation techniques. The semiconductor oxides used for TCO application are large band gap (≥ 3 eV) materials and transmit >80% light and exhibit good conductivity. Pure and perfect stoichiometric semiconductors are poor electrical conductors. The electrical conductivity can be improved by adding some extrinsic defects or impurities or creating oxygen vacancies. These defects and vacancies modify the electronic band structure by adding new electronic states and consequently electrical conductivity changes. Some intrinsic defects already present in semiconductors may act as electron donor centers. Extrinsic dopants may populate the conduction band and provide enough charge carrier density [21]. TCOs thin films are transparent to visible or near infrared region of light due to large band gap and they absorb or reflect ultraviolet (UV) and infrared (IR) radiations. UV radiations are

absorbed by band gap transition and IR radiations are reflected due to plasma resonance absorption or by free electrons.

1.2 Requirements for Transparent Conducting Oxides

High electrical conductivity and high transparency are the essential requirements of transparent conducting oxides when used as front electrode in solar cell so that it passes maximum light to the active layer and provide low resistance in the path of generated charge carriers. To achieve high transmittance (~80%) the material should have wide band gap with $E_g \geq 3eV$, to absorb less incident radiation. The low resistivity of the order of $\sim 10^{-4}$ Ω cm can be obtained by having sufficient charge carriers and good carrier mobility with controlled surface roughness [4]. The conductivity of *n*-type transparent conducting materials is given by $\sigma = \mu ne$; where *n* is electron density, μ is its mobility and *e* is the charge on electron. The high electrical conductivity can be obtained from high carrier density and high mobility. The carrier density can be increased by introducing dopants into the system or embedding a metal layer between two dielectrics layers in a controlled way. Mobility of the carriers can be increased by reducing the grain boundaries, ionized impurities and lattice vibrations. It was reported that crystalline materials are preferred to obtain good conducting TCO thin films [22] but for flexible electronic devices the amorphous transparent conducting electrodes are better choice than crystalline because amorphous structures do not fracture easily and have increased flexibility [23]. Work function matching of TCO material with the next layer is also important and needs to be taken care while choosing both materials [24]. If the work function of both materials matches well, it gives proper band alignment and enhances the efficiency of the device. The properties of TCO are also a function of the substrate temperature at the time of deposition. To ensure the stability of TCO, it is important to deposit the TCO at a temperature higher than its application temperature.

There are some additional TCO requirements for photovoltaic cells and light-emitting diodes. TCO surface roughness, microstructure, adhesion, morphology and interface of two consecutive layer; all these parameters affect the properties of TCO and efficiency of device, so one has to consider all these things while preparing the transparent conductor. The surface roughness of transparent conductor is also equally important to have a better

control of optical properties. Smoother surfaces reflect light and rougher surfaces cause scattering of light and in both situations transmittance decreases. Therefore it is necessary to use an optimized surface roughness. The crystal structure of TCO films viz. fully crystalline, partially crystalline or amorphous, play an important role in TCO properties, because they provide different grain boundaries scatterings. The ability of TCO to resist corrosiveness is related to etching; hence to get high corrosion resistance and chemical stability, the films should be hard to etch. Toxicity of TCO elements should be avoided because they increase the processing cost in prevention from environment.

In thin film solar cells, TC layer works as the front electrode. High work function, thermal stability and low cost are the deciding factors for the TCO material [25]. TC is used as front electrode in flat panel displays (FPDs) and etchability is primary concern for FPDs because easy etchable TC is required for patterning [26]. Low synthesis temperature is also a key factor in FPDs because TC is deposited on thermally sensitive organic dyes. TCO with electrochemical organic gel are used in automobiles and act as dimming rear-view mirrors [27]. For applications in electrochromic windows and mirrors, the TCO should be chemical inert, low cost and highly transparent. The control of radiation or energy exchange between exterior and interior of buildings by smart windows is a main research area in energy saving. Thus, smart windows are used to limit the incoming and outgoing solar radiations from the building [28]; in cold weather high transmittance TCO and in hot weather NIR radiation reflecting TCO is needed. Defrosting windows are used in airplanes and automobile windshields to remove the frozen ice. Low cost and low resistivity are the key requirements of TCs used in defrosting windows [29]. In memory devices, the resistive switching memory (ReRAM) fabricated using TCO/insulator/TCO structure has proven to be a promising candidate due to its simple structure, fast switching and non-volatility. The transparent conducting electrodes have attracted much attention for fabrication of next generation ReRAM memory devices [30]. It is clear from the above discussion that no single TCO would be suitable for the given applications.

1.3 Transparent Conducting Oxide Materials

As given above, TCOs have huge applications, testifying the intensive research and investigations for the last 100 years or more. The TCOs can be classified into two types;

n-type and p-type. Generally, n-type doped transition metal oxides are in used for industrial applications. More than 90% of TCOs are n-type, where majority charge carriers are electrons. It is difficult to prepare p-type TCO due to the intrinsic electronic structure of most of the available metal oxides; therefore, few p-type TCOs have been investigated. Fabrication difficulties of p-type TCO limit its uses as transparent conductor for commercial applications. First p-type TCO of copper aluminum oxide ($CuAlO_{2+x}$) was reported by Kawazoe *et al.* in 1997 [31]. After the fabrication of p-type TCO the development of transparent p–n junction using TCO materials became possible [32]. Most commonly investigated p-type TCOs are $CuAlO_2$, $CuInO_2$, $CuGaO_2$, $CuCrO_2$ and $SrCu_2O_2$ [33]. Indium-Tin-Oxide (ITO) thin films have been widely used as transparent electrodes in various optoelectronic and electro-optic devices such as liquid crystal displays (LCD) [34], flat panel displays [35], solar cell [36], and light emitting diodes [37] due to their attractive combination of electrical conductivity and visible transparency. The ITO is largely used material in LCD devices. ITO is a large band gap degenerate semiconductor and exhibits transmittance of ~90% and resistivity of $\sim 10^{-4}$ Ω cm. The solution processed ITO films deposited on glass substrates, exhibits the good results when annealed at 450˚ C temperature [34].

Metal doped oxide TCOs such as Nb doped TiO_2 (NTO) [38], Al doped ZnO (AZO) [39], Ga doped ZnO (GZO) [40] and fluorine doped SnO_2 (FTO) [41] are largely used as electrodes in various electronic devices. These doped TCOs have shown good electrical conductivity and optical transparency and proven their candidacy against the ITO. Extrinsic doping of metal elements in the host oxide matrix generates an n-type TCO. This may provide one or more free electrons for conduction and creates the defect levels changing the electronic structures of host matrix. Therefore, as a result good conductivity and transparency of TCO can be simultaneously achieved through doping. Indium doped zinc-oxide (IZO) have been used as electrodes in the resistive switching memory (ReRAM) devices fabricated on flexible substrates [42]. The device have shown >80% transmittance, good flexibility with good endurance and retention. Physical vapor deposition techniques are mostly used to fabricate the TCO thin films on glass, quartz and plastic substrates [43]. Some ternary compound semiconductors such as $GaInO_3$,

$MgIn_2O_4$, $ZnSnO_3$ and $Zn_2In_2O_5$ have been investigated as transparent electrodes and shown good results [44].

1.4 Oxide/Metal/Oxide Multilayers as Transparent Conducting Oxides

Since TCO is an important component in optoelectronic devices and affects the performance of the devices, this has encouraged the researchers to find new materials with enhanced properties to meet the present and future energy requirements in terms of quality and large area deposition. The most commonly used TCOs are based on TiO_2, ZnO, SnO_2 and ITO. ITO is a widely used TCO due to its high conductivity and transparency but it is a scarce metal and hence its market value has increased. In addition, advanced and future devices need electrodes with lower resistivity and superior transparency than previously achieved. Among all ITO alternatives, a TCO/metal/TCO multilayer structure meets the all requirements of TCO and decrease the demand of ITO [45]. The electrical and optical characteristics of the sandwiched structure are superior to that of the metal electrode or single layer TCO. The multilayer structures exhibit comparable properties at lower thickness and low temperature and can be deposited onto glass, quartz and inexpensive plastic substrates [46,47]. In the multilayer structure, the middle metal layer is the key element responsible for the transport properties needed such as high carrier density, low resistivity and low sheet resistance. It is observed that the electrical and optical properties of metal layer are strongly dependent on its thickness because transmittance and resistivity both decreases below a critical film thickness [48,49]. The critical thickness depends on the type of metal film, substrates and deposition methods. A less thick film is composed of aggregated islands of metal atoms and becomes a continuous film on increasing the thickness. Island type structures do not conduct properly; reflect more light and reducing the transmittance.

The electrical behavior of multilayer TCO is entirely different from the single layer TCO. Moreover, conduction mechanism of sandwich structures is described by considering the fact that the metal film is embedded between two oxide layers, making an oxide/metal/oxide (OMO) structure [50]. The total electrical resistance of the coplanar configuration measured on the top layer of the multilayer deposited on glass is mainly given by the sandwich metal layer and is given by $1 / R_{total} = 1 / R_{metal} + 2 / R_{oxide}$ and

considering a typical example where $R_{oxide} > 1000\ R_{metal}$, so $R_{total} \approx R_{metal}$. Thus, electrical conductivity of OMO multilayer structure is mainly because of the middle metal layer and is a function of its thickness. A critical thickness of embedded metal film is needed to get continuous path of electrons flow [51]. The multilayer structures exhibit good electrical results at room temperature which suggest the continuous formation of middle metal layer and normally it does not depend on temperature because charge carriers are valence electrons. The mobility of these multilayer films is affected by scattering of the charge carriers from the grain boundaries and from the interface of metal and oxide layers. The transmittance of multilayer films is limited by reflectance losses from metal films and this transmittance is boosted by adding two oxide layers below and above of metal layer. The top and bottom oxide layer act as antireflective coatings. The total transmittance of sandwich structure is improved by adjusting the constructive interference in the beam transmitted from multilayer structure and destructive interference phenomena in the beams reflected from metal and oxides interfaces [19]. To fulfill this condition, the thickness of oxide layers can be varied from 30 nm to 60 nm and maximum transmittance can also be tuned at desired wavelength position and typically at 550 nm [52]. The high transmittance of multilayer structures is due to high refractive index of top and bottom oxide layers [53].

The desirable sheet resistance and transmittance of multilayer TCO are achieved by using different combinations of OMO structures. And the work function also bears an important role in the selection of best OMO structure for a particular application, because matching of work function of TCO and the next layer of device structure is desirable, as contact interface should provide smallest barrier to charge transport [45]. Moreover, annealing and high temperature deposition is not needed to obtain high conductivity and hence these OMO multilayers can be deposited on plastic and glass substrates at room temperature. Apart from high transmittance and high conductivity, of these multilayer electrodes some other characteristics viz. thermal stability and mechanical reliability of device is also needed when deposited on flexible substrates. For manufacturing perspective of flexible devices continuous deposition of electrode on plastic substrates should be unrivaled in terms of processing speed, thermal budget and processing cost. Moreover flexible devices need mechanical stability of transparent electrode against bending and unbending. It has

been reported that mechanical reliability of multilayer film is better (due to higher ductility of middle metal layer) than similar single layer film for flexible devices [54,55]. TCO film crystalline nature, substrate nature and film thickness also affect the mechanical behavior and should also be analyzed to get optimal performance. The OMO multilayer films are durable against the chemical agents present in the atmosphere and humidity, which is important for industrial applications. In OMO multilayer structure the middle metal layer is the main component which is responsible for transparent properties and especially the sheet resistance. Various elements such as Ag, Au, Cu and Al have been investigated for their use as middle metal layer but Ag remains the best choice due to its lowest resistivity (1.6 μΩ cm) among all metals [45]. Various multilayer transparent conducting electrodes of ITO/Ag/ITO [56], TiO_2/Ag/TiO_2 [51], TiO_2/Au/TiO_2 [18], ZnO/Ag/ZnO [57], ZnO/Pt/ZnO [58], SnO_2/Ag/SnO_2 [59] and WO_3/Ag/WO_3 [60] have been fabricated using sputtering and pulse laser deposition techniques on glass, quartz and plastic substrates and investigated. These multilayer films have shown to satisfy the prerequisites and proven their candidacy as a transparent conductor for current and future applications.

1.5 Some Applications of TCOs

The transparent conductors are used in multitude of applications and have an active or passive role. A detailed knowledge of optical and electrical properties of TCO is required to use them in various electronic devices. Transparent conducting electrodes are essential component of optoelectronic devices and widely used in industrial applications. In thin solar cells, the TCO is used as front electrode which passes solar radiations to the main absorber layer and acting as an electrical contact [61]. The multilayer structure has been mostly used in organic light emitting diodes where two or more organic layers are embedded between the top TCO film (as anode) and lower metallic film (as cathode) [62]. TCO have also been used in flat panel displays as front electrodes [26]. This TCO should have good chemical endurance and no etch residue after patterning for flat panel displays application. The ability of TCO to sense the finger in touch screen by direct contact makes them of use in ATM and elevator controls applications [63].

TCO reflect the infrared radiation is used to manufacture energy conserving windows and hence they are largely used in low emissivity windows [64]. Transparent conductors are used in defrosting windows to prevent humidity and moisture in the air from obscuring the view from condensation [65]. The resistive switching memory devices using TCO and an insulator layer have attracted much attention in the area of transparent and flexible electronic devices [66]. Organic photovoltaics are cost effective, renewable and inexpensive source of energy and are a proven replacement of conventional Si-based solar cells. The multilayer TCO films have also been used in organic photovoltaics as transparent conducting electrode [67]. TCO is also an important component of new generation perovskite and heterojunction solar cells [68]. TCOs have also been investigated as electrodes in gas sensing [69] and water splitting [70] applications. Apart from the optoelectronic devices the TCO are used in various devices such as sensors, antenna, MEMS and other energy related devices. The requirement of room temperature deposited TCO is increasing day by day due to emergence of advanced and flexible electronic devices, which needs the deposition of these devices at room temperature on plastic substrates.

1.6 Objectives of the Thesis

The major objective of this work is to develop a cheap & easy way to prepare indium-free transparent single and multilayer conductors for various optoelectronic devices. The proposed research aims at development of transparent conductors having high conductivity and transparency in visible region. To achieve these requirements the sandwich multilayers have been deposited using sputtering at room temperature with varying top and bottom oxide layer thickness and conductivity (of the order of $10^{-4}/10^{-5}$ Ω cm) and transparency (in the range of 70%−85%) obtained for the multilayers having an optimized thickness. These multilayers are further implanted by low energy ions to suitably modify their structural, electrical and optical properties. X-ray photoelectron spectroscopy have been used to study the chemical states of the sample and low temperature Hall measurements were used to investigate the effect of temperature variation (80 K to 340 K) on the transport properties of the specimen. The main objectives of this work are given below:

1. Fabrication of Nb doped single layer transparent conducting electrode using sol-gel and sputtering methods and investigates the doping concentration and post deposition annealing effects on their properties.
2. Fabrication of TiO_2/Ag/TiO_2 and NTO/Ag/NTO multilayer structures at room temperature and optimization of thickness of oxides and Ag layers for maximum figure of merit.
3. To modify structural, optical and electrical properties of the multilayer structures using low energy ion implantation for enhancement of figure of merit.
4. To develop an indium-free single and multilayer transparent conducting electrodes with comparable or higher optical and electrical properties for their application in optoelectronic devices.
5. To develop resistive switching random access memory device based on aluminum oxide using TiO_2/Ag/TiO_2 and NTO/Ag/NTO multilayer transparent conducting electrodes.

Thesis Plan:

Chapter 1 deals with introduction of the transparent conducting oxides (TCOs) and the criteria for selecting the appropriate TCO for specific devices. It includes introduction about the TCO materials, multilayer thin films; Nb doped TiO_2 thin films and applications of the TCOs.

Chapter 2 provides the detailed literature survey in the field of transparent conducting oxide (TCO). The chronological developments and the current status of TCO are presented in this chapter.

Chapter 3 gives the introduction about materials and various characterization methods used in this work. The fabrication, implantation and characterization facilities are discussed in detail.

Chapter 4 reports on the investigations of Nb doped TiO_2 thin films to be used as TCE. This chapter is divided in two sections giving two different synthesis routes.

- Nb doped TiO_2 thin films prepared by sol-gel spin coating method
- Nb doped TiO_2 thin films prepared by sputtering

Chapter 5 describes the fabrication and characterization of TiO_2-Ag-TiO_2 (TAT) multilayer thin films and effect of ion implantation in these films. This chapter is divided into two major sections.

- Nitrogen ion implantation in TAT multilayer structure
- Argon ion implantation in TAT multilayer structure

Chapter-6 reports on impact of ion implantation on properties of NTO-Ag-NTO (NAN) multilayer thin films. This chapter is divided into two major sections.

- Nitrogen ion implantation in NAN multilayer structure
- Argon ion implantation in NAN multilayer structure

Chapter-7 reports on the synthesis and characterization of transparent resistive switching random access memory (ReRAM) device based on Al_2O_3 layer and multilayer transparent electrodes. The TAT and NAN multilayer transparent conducting electrodes with optimized thickness have been used to fabricate the ReRAM devices.

Chapter-8 gives the conclusions obtained from the present investigations and suggests scope for further research work in the TCO area.

Chapter-2

Literature Review

This chapter starts with the introduction of the transparent conducting oxides and further gives historical evolution and advancements made in last few decades. Successive topics of this chapter explain the various fabrication methods of the TCOs, post deposition annealing and implantation effects on the TCOs and their applications. Different synthesis routs for transparent conducting films (single layer and multilayers) are discussed, with emphasis on Nb doped TiO_2 (NTO) thin films as transparent conducting oxides. The effects of thermal treatment on the structural, optical and electrical properties of NTO thin films are also explained. Moreover, ion beam induced modification of metal oxides is a core part of this work and hence thoroughly studied and some previous investigations also have been given. The last section entails the applications of the transparent conduction electrodes in various optoelectronic devices.

2.1 Introduction

Last few years have seen tremendous efforts made in the area of development of transparent conducting oxides (TCOs) searching for new materials and processing methods to improve the performance and to meet the requirements of the newly developed optoelectronic and flexible electronic devices. The journey of TCO was started in 1907 and sequentially developed and still it is progressing with a further scope of improvement. TCOs comprise of materials that are transparent in visible region and electrically conductive having huge applications in the electronic industry. TCOs are crucial components used as transparent conducting electrodes or contacts in solar cells, light emitting diodes, touch screens, electrochromic devices and flat panel displays [71,72].

2.2 History and evolution of Transparent Conducting Oxides

Transparent conducting oxide thin film was first prepared in 1907 by Badeker *et al.* [6]. They synthesized cadmium oxide (CdO) films by thermal oxidation of Cd and obtained a resistivity of ~1.2×10^{-3} Ω cm. The work begun by Badeker was extended by Bauer *et al.*

and TCO films were prepared by post oxidation of metal films of Cd, Tl and Sn in 1937 [73]. The area of transparent conducting oxides gained significance in 1940s when needed for windshield deicing. This led to a regular demand and a huge technological interest in TCOs for industrial purpose [74]. The electrical and optical properties were controlled by changing the oxidation temperature in the range of 350-500 °C and it was observed that higher thickness showed higher resistivity possibly due to incomplete oxidation of thicker layers. The progress made in the area of transparent conductors up to 1955 was reviewed by L. Holland [75]. During 1958−1976 substantial investigations were performed, which were reviewed by Haacke [76] and Vossen [77]. Haacke proposed a unique method to examine the performance of a TCO by taking the optical transmittance and sheet resistance of the specimens together. In 1982 Granqvist [78] reviewed the physical properties and preparation methods of transparent conducting oxide films. In 1983 Chopra *et al.* [1] published a review on transparent conductors discussing the deposition techniques and structural, optical, and electrical properties of transparent conductors (TCs) including their applications. Authors elaborated the conduction mechanism of the TCs in terms of their carrier density and mobility. They explained that defects and doping affect the carrier concentration and the various scattering phenomenon affect the mobility of carriers. The surface stoichiometry and chemical states of the indium-doped zinc oxide (lZO), fluorine-doped tin oxide (FTO) and indium tin oxide (ITO) transparent conductors were analyzed by Major *et al.* [79] in 1986.

In 1997 Yamada *et al.* [80] prepared ZnO based transparent conductors using atomic layer deposition and analyzed the crystal structure of samples by X-ray diffraction technique and electrical properties by Hall measurement system. Gustafsson *et al.* [81] made flexible light emitting diode using transparent conducting electrode as conducting polymer on polyethylene terephthalate (PET) substrates which showed good mechanical properties. They demonstrate that this device can emit a variety of colors giving a new technological potential material for flexible electronic devices. Coutts and Gordon [3,4] reviewed the status and opportunities in transparent conducting oxides research and summarized the deposition methods and post deposition treatments such as annealing and oxidation, which influence the structural, electrical and optical properties of the TCOs films. Stadler and Ellmer [2,5] wrote a comprehensive review on TCOs and explained the

aspects of choosing the latest materials from the existing database system. Ellmer *et al.* summarized the properties and applications of the In_2O_3, SnO_2, ZnO and TiO_2 based TCOs and discussed the possibilities of new materials such as carbon nanotubes, regular metal grids and metal nanowire networks. Transparent conducting oxides are key components of optoelectronic devices and hence have huge industrial applications. The TCO was commercially used in airplane windows in the middle 1940s [82]. In 1955 Ward *et al.* [83] reported that transparent conductors can be used for transparent heating elements applications in automobiles and ships to prevent the formation of mist and ice. ITO and FTO transparent conducting electrodes were used in heterojunction solar cells yielding 6%−8% efficiency [84]. White *et al.* [85] reported the use of ITO as transparent conducting electrode in advanced flat-panel display devices in 1970. The importance of TCO has increased tremendously due to its applications in various energy conversion devices. Researchers are nowadays more interested in non-conventional sources of energy such as light emitting diodes, solar cells and low emissive windows [86] which has boosted the demand of high performance TCOs.

2.3 Various fabrication methods and materials for Transparent Conducting Oxides

Different types of thin film deposition methods have been used to prepare the single and multilayer transparent conducting electrodes viz. Nb doped TiO_2 (NTO), Al doped ZnO (AZO), fluorine doped tin oxide (FTO), indium tin oxide (ITO), ZnO/Ag/ZnO, SnO_2/Ag/SnO_2 and TiO_2/Ag/TiO_2 etc. The structural, optical, electrical and mechanical properties of the TCOs strongly depend on the deposition methods adopted for film preparartion, because the stoichiometry, particle formation, microstructure, nature of impurities and surface roughness; these all are consequences of the synthesis root. The final cost of the transparent conductors depend on the materials used in preparation as well as on the depostions methods also and every technique has its own pros and cons. Most widely used technique employed to deposite the TCO is physical vapour depostion methods which inlude sputtering [87], e-beam evaporation [88] and thermal evaporation [89], with an advantage that these can be used for large area deposition. TCO thin films using metal oxide targets using sputtering technique provides better control on

stoichiometry and in some cases further post depostion heat treatment is not required and highly transparent and conducting films can be prepared. In chemical vapour deposition (CVD) the substrates are exposed to volatile precursors which decomposes on the surface of substrate and to fabricate desired films. In 1990 Maruyama *et al.* [90] prepared indium tin oxide transparent conductive thin films by CVD using indium acetate and tin diacetate as raw materials. Other chemical methods such as spin coating [91], dip coating [92], and spray pyrolysis [93] also have been used to prepare TCO thin films. The main benefits of the chemical synthesis are cost effectiveness and low temperature deposition. On the other hand in chemical synthesis the thickness of films can't be controlled and surface roughness of the films is higher than by physical vapour deposition. High surface roughness of TCE is not desired because it affects the performance of the device by increasing scattering of light and transparency is reduced. Another technique for TCO preparation is pulsed laser deposition (PLD) which has been quite used by researchers. In this method the material from the target is melt and evaporated by high power laser pulses and this ablated material is collected on the substrate. Singh *et al.* [94] prepared the aluminum doped zinc oxide transparent conductive films by pulse laser deposition method and obtain the lowest resistivity of 1.4×10^{-4} Ω cm.

The materials which possess a large band gap (~3 eV), carrier density ~10^{21} cm^{-3}, high mobility (~70 $cm^2V^{-1}s^{-1}$) and resistivity in the range of 10^{-3}–10^{-4} Ω cm are preferred or eligible to be used as transparent conducting oxides [95]. Among the various kinds of materials available for TCOs, TiO_2, ZnO, SnO_2 and In_2O_3 are the popular binary composite materials. Generally undoped metal oxides are poor electrical conductor and their conductivity can be improved by introducing the appropriate dopants such as Nb:TiO_2 (NTO) [38], Al:ZnO (AZO) [39], F:SnO_2 (FTO) [41] and In_2O_3:Sn (ITO) [96]. These materials are wide band gap and exhibit the desired carrier density, mobility and resistivity with good transmittance. ITO the most popular TCO till now has many problems like high temperature deposition, high cost due to scarcity and brittleness. Therefore, many efforts have been made for the development of substitute of ITO. New variety of ternary compounds such as Zn_2SnO_4, $GaInO_3$ and $In_4Sn_3O_{12}$ has been tested as TCO material but applications of these materials are rarely investigated. Metal oxides such as TiO_2, ZnO and SnO_2 are largely used for transparent conductor applications due

to existence of intrinsic defects inside which makes them suitable in terms of high conductivity and transparency [97]. The presence of intrinsic and extrinsic defects viz. interstitial, substitutional lattice site defects and vacancies greatly affects the optical and electrical properties of the TCO and by altering these defects the properties of the materials can be modified [98,99].

2.4 Single and Multilayer Transparent Conducting Oxides

The doping of metals into the metal oxides has been popular for the last 2-3 decades due to their resulting properties of high optical transmittance and electrical conductivity. The advantages of single layer TCO are; they can be easily deposited and do not have any metal and metal oxide interface to study. Kim *et al.* [37] have grown the transparent and conducting indium tin oxide (ITO) films of 200 nm thickness by pulse laser deposition (PLD) on polyethylene terephthalate substrates and studied the gas pressure and substrate temperature effects on the properties. They obtained the optical transparency of ~87% and electrical resistivity of 7×10^{-4} Ω cm at 25 °C and 45 mTorr of oxygen. Kim *et al.* [41] have also deposited fluorine doped tin oxide (F:SnO_2) transparent conductive thin films of ~450 nm thickness by PLD on glass substrates and investigated fluorine doping and substrate temperature effects on the TCO properties. They attained sheet resistance of 12.5 Ω/□ and transmittance of 87% at an optimum target composition of 10 wt.% SnF_2+90 wt.% SnO_2 and optimized deposition conditions of substrate temperature of 300 °C and 7.33 Pa of O_2. Hu *et al.* [100] prepared aluminum doped ZnO (AZO) thin films by magnetron sputtering and investigated the influence of sputtering power on intrinsic defects, crystallinity, electrical and optical properties of AZO. They reported that intrinsic-defects and crystallinity which influences the electrical and optical properties may be controlled by sputtering power. Safeen *et al*. [101] prepared niobium doped TiO_2 (Nb:TiO_2) thin films using sputtering and performed a comparative study of optical and electrical properties with their chemical properties and found resistivity of 1.4×10^{-3} Ω cm with >80% transmittance. The main disadvantage of the single layer doped TCO is that they achieve the required properties at the higher film thickness (~200 nm−500 nm) and due to this large amount of material is needed for film preparation. Post deposition thermal annealing is also required for single layer doped TCOs to get the crystalline

structure and good electrical and optical properties; these drawbacks of the TCOs result in higher cost.

In recent times oxide/metal/oxide (O/M/O) stacked multilayer thin films have emerged as an alternative transparent electrode showing the unique combination of optical and electrical properties which are superior to single layer TCO [45]. The benefits of the multilayer structures are that they can be prepared at low temperatures and with lower thickness (~50 nm−130 nm) than a single layer TCO and no further thermal treatment is required to get good properties. Generally, the top and bottom oxide layers used are TiO_2, SnO_2, ZnO and MgO or their compounds in multilayer structures. A very thin metal layer has to be embedded between two oxide layers (oxide/metal/oxide) which can be Ag, Au, Cu, Al, Pt etc. due to their low resistivities [102]. Among metals, Ag is a good candidate because a very thin layer of Ag (< 20 nm thick) shows low resistance and high transmittance in the visible region of electromagnetic waves [103]. The charge transport phenomenon giving a very low resistivity in O/M/O structures is governed mostly by the sandwiched metal layer [51]. The reflections of visible light are reduced by coating the oxides layers on top and bottom of metal layer which enhances the transmittance of the multilayer structures [50]. In the O/M/O structure, work functions of both oxide and metal layer should be tuned to align the Fermi levels to make charge transportation easier [24]. In recent times the metal embedded trilayer structures of ITO/Ag/ITO [56], TiO_2/Ag/TiO_2 [104], TiO_2/Au/TiO_2 [105], ZnO/Ag/ZnO [106], AZO/Ag/AZO [107], SnO_2/Ag/SnO_2 [59] and FTO/Ag/FTO [108] have been extensively studied and it has been proved that they are high performance TCE and meet the requirements of next generation electronic devices. Zhao *et al.* [104] have deposited the TiO_2/Ag/TiO_2 multilayer structure on glass substrates using sputtering technique. They varied the TiO_2 and Ag layer thickness and analyzed the obtained results. The specimen made of TiO_2 (42 nm)/Ag (10nm)/TiO_2 (42 nm) showed the optimized results with sheet resistance of 4.4 Ω/□ and transmittance of ~89%. Hajj *et al.* [106] have prepared multilayer electrodes of ZnO/Ag/ZnO by ion beam sputtering for flexible device applications. They found the low sheet resistance of 6 Ω/□ with high transmittance of ≥80% for ZnO (35 nm)/Ag (10nm)/ZnO (20 nm) films. Yu *et al.* [59] were prepared the trilayer films of SnO_2/Ag/SnO_2 by magnetron sputtering and studied the influence of SnO_2 and Ag layer thickness variation on the electrical and

optical properties. The trilayer films with 50 nm thick SnO_2 and 5 nm thick Ag exhibited the resistivity of 1.0×10^{-4} Ω cm and an average transmittance of ~94% in the visible region.

2.5 Nb doped TiO_2 as Transparent Conducting Oxides

Modern science and technology requires new functional materials with novel structural, optical, mechanical, electrical and magnetic properties and hence the need for new materials [109]. Doping of metals and incorporation of impurities in TiO_2 has been used to enhance its properties using methods such as chemical mixing, co-sputtering, implantation and chemical vapor deposition. Generally, three main mechanisms are involved regarding modification of TiO_2 which are: band gap narrowing, generation of oxygen vacancies and shifting/creation of the impurity energy levels [110]. Niobium (Nb) is an appropriate dopant largely used in TiO_2 due to its similar atomic radii (Nb: 0.164 nm and Ti: 0.160 nm) and comparable bond lengths of Ti-O and Nb-O, producing less deformation of TiO_2 lattice when incorporated. Nb is a fifth group element and hence it may release one or more free electrons. Nb-doped TiO_2 (NTO) thin films have been very popular in the last two-three decades and are seen as promising transparent conducting electrodes exhibiting very good electrical and optical properties. The anatase NTO films have shown transmittance and resistivity comparable to ITO films. NTO films have high transmittance in visible region, high refractive index and high chemical stability which ITO does not possess. Hence we expect that a new and high performance TCE can be fabricated making use of these properties [111].

Liu *et al.* [112] prepared Nb-doped TiO_2 thin films using sol-gel spin coating method with varying Nb concentration in a range of 0−20 at.%. The prepared thin films were annealed at 550 ˚C for 1 h for (a) three times and (b) multiple times to improve the electrical conductivity. They concluded that multi-round annealing is an effective way to improve conductivity and obtained lowest resistivity of 0.5 Ω at 12 at.% Nb concentration. Hitosugi *et al.* [113] have grown the epitaxial film of anatse $Ti_{0.94}Nb_{0.06}O_2$ which showed a resistivity (ρ) of 2.3×10^{-4} Ω cm with ~95% internal transmittance. Furthermore, they deposited polycrystalline films by sputtering on glass substrates and acquired resistivity of 6.4×10^{-4} Ω cm at room temperature. Furubayashi *et al.* [114] fabricated a TCO of

anatse $Ti_{1-x}Nb_xO_2$ films (x=0.002–0.2) on $SrTiO_3$ substrates by pulse laser deposition technique. The carrier density was varied from 1×10^{19} to 2×10^{21} cm^{-3} and internal transmittance of ~97% for $x\leq0.3$ (film thickness of 40 nm). These films were shown to have optical and transport properties comparable to $In_{2-x}Sn_xO_3$. $Nb_xTi_{1-x}O_2$ in a range of x=0, 0.03, 0.06, 0.12, 0.24 thin films were explored for their use as alternative transparent conductor by Tucker *et al.* [115]. The films were deposited by electron beam evaporation using sol-gel synthesized pellet. Results showed that elevated substrate temperatures provide the lowest resistivity of 1.2×10^{-2} Ω cm for nominal x=0.03 and ~330 °C substrate temperature. Hung *et al.* [116] deposited the niobium-doped titania (TNO) films by co-sputtering of Ti and Nb on glass and silicon substrates with Nb content varied from 0−13 at.%. The prepared films were annealed for 1 h in hydrogen to make them crystalline and conductive. TNO films with 9.7 at.% Nb content showed a larger decrement in the resistivity up to 9.2×10^{-4} Ω cm with carrier density of 6.6×10^{21} cm^{-3} and mobility of 1.0 cm^2 V^{-1} s^{-1}. Maghanga *et al.* [117] prepared TiO_2:Nb thin films by dual target reactive sputtering on glass and aluminum substrates in $Ar+O_2$ plasma. Nb concentration was changed from 0 to 4.9 at.% and films were annealed in vacuum at 450 ˚C. The films deposited on Al_2O_3-coated Al substrates exhibited optically selective reflectance making them useful for solar cell applications.

2.6 Influence of Post Deposition Treatment on Transparent Conductor

The structural, electrical, optical and mechanical properties of the transparent conductors can be modified by changing the synthesis process parameters and thermal heat treatment at different temperatures and in different environments [45]. Tin oxides films have been prepared by Brinzari *et al.* [118] using chemical method. Initially these films were non-stoichiometric and hence the thermal treatment was done to improve their crystallinity, stability, adhesion, surface morphology, transmittance and electrical conductivity. Sheet resistance, mobility, and crystallinity of ultrathin (20 nm) indium tin oxide films were enhanced by post-annealing treatment in an atmosphere [119]. A decrease in sheet resistance of ITO films was observed after 250 ˚C and an optimum value of 336 Ω/□ was obtained at 400 ˚C because at high temperatures effective number of Sn ion dopants has increased. The average transmittance of these films was enhanced to 86.8% due to filling

of oxygen vacancies at high temperature. Warzecha *et al.* [120] prepared and investigated the effects of annealing on the ZnO:Al and tin doped indium oxide (ITO) films. An increase in mobility of ZnO:Al films was achieved by annealing the films at 650 ˚C for 24 hrs. Meanwhile, the resistivity of ITO films was decreased with a partial improvement in mobility after heat treatment. The carrier concentration was maintained > 10^{21} cm^{-3} without any specific trend. These variations in transport properties were attributed to activation of donors and healing of defects in ZnO and ITO films after annealing. Dabney *et al.* [121] have examined the annealing effects on the Nb:TiO_2 thin films prepared using PLD on $LaAlO_3$, $SrTiO_3$ and fused silica substrates. The as prepared films were annealed at 650 ˚C in 1.3×10^{-3} Pa O_2 or in vacuum. The conductivities were enhanced and obtained as 85 S/cm on $LaAlO_3$, 3300 S/cm on $SrTiO_3$ substrates for highest annealing temperature for vacuum annealed films with some reduction in transparency.

TiO_2/Cu/TiO_2 [122] multilayers as transparent composite electrode have been investigated for change in electrical and optical properties with the variation in Cu thickness and annealing temperature. The resistivity of 7.4×10^{-5} Ω cm was obtained for optimized Cu thickness of 11 nm with 86% transmittance. The resistivity of TiO_2/Cu (11 nm)/TiO_2 multilayers reached to 7.4×10^{-5} Ω cm at 150 ˚C annealing temperature with transmittance of 88% in the visible region. Kim *et al.* [123] reported the silver layer stability in SnO_2/Ag/SnO_2 annealed at 100 °C and 200 °C. They found that these films were stable at room temperature and became unstable after annealing due to internal Ag hillocks, void formation in Ag layer and formation of Ag whiskers on SnO_2 surface. Alyamani *et al.* [124] exposed the indium tin oxide (ITO) thin films to gamma γ radiation which was doses by ^{60}Co radioisotope and exposure cycles up to 250 kGy. The optical band gap was found to decrease and extinction coefficient and refractive index increased with the increased radiation dose. The electrical conductivity was improved on gamma irradiation.

2.7 Modification of Metal Oxides by Low Energy Ion Implantation

Ion implantation is a method where electrostatically accelerated beam of desired ions are injected into a material up to required depth. Energy of the injected ions can be varied from few tens of keV to several hundred keV. The ions introduced near to the surface and inside the depth can be measured by the ion mass and energy for a given target material.

Therefore, ion implantation enables us to do precise placement of incident ions into the target material by taking suitable energy and angle of ions. The ions dissipate their kinetic energy via elastic and inelastic collisions with the atoms of the host material and then come to rest. Therefore, as a result huge numbers of defects are created during the passes of ions. Thereby this process provides a way to alter the physical properties of the host material in a precise and controlled way [125,126]. Ion implantation is used to tailor the transport properties of the solids and has led to transistor revolution in electronics. Doping by implantation is a non-equilibrium process for embedding the dopants into materials and there is no segregation, diffusion or precipitation occurring in this process. Low energy ion implantation is unique method for doping purposes because it provides excellent fluence homogeneity for a large area, has small process time and adjustable doping profile [127]. Generally, this technique is very advantageous for changing the specific properties of materials by incorporation of particular ion. Ion implantation of impurities is used to engineer the conduction properties of the solids and has reformed the semiconductor technology [126].

Low energy ion implantation has been widely used to change the structural, optical and electrical properties of the metal oxides such as TiO_2 [128], SnO_2 and ZnO [129]. Different varieties of ions were used to modify the properties of single crystals and single layer metal oxides films but very few reports are available on the multilayer structures. Therefore, there is a large scope to study the ion implantation effects in multilayer films in terms of their surface, structural, electrical, mechanical and optical properties modification. The effect of electron beam irradiation on electrical and optical properties of ITO/Ag/ITO and IZO/Ag/IZO multilayer structures was studied by Hong *et al.* [130]. They found that sheet resistance decreased for both multilayers and transmittance was increased for ITO/Ag/ITO and no change in transmittance was observed for IZO/Ag/IZO. The effect of Xe ion irradiation on ZnO/MWCNT-Ag/ZnO/PET (ZCAZ) stacked multilayers was investigated by Surbhi *et al.* [131]. A large increase in electrical conductivity from 1.14×10^{-7} Ω^{-1} cm^{-1} (pristine) to 7.04×10^{3} Ω^{-1} cm^{-1} was observed and transmittance also increased after Xe ion implantation. The reason of this enhancement in conductivity was attributed to Xe ion induced connectivity between top and Ag-CNT hybrid layers which providing conduction pathways for smooth transfer of electrons.

Stepanov [109] reviewed the modifications produced in TiO_2 by ion implantation and their applications. He reported that the physical and chemical properties of TiO_2 can be successfully modified by implantation for its use the field of optics, magnetic data storage and nano-catalysts. Fromknecht *et al.* [128] have studied the effect of Ar, Sn and W ions implantation in a single crystal TiO_2 with 300 keV energy and fluence was varied from $10^{15}/cm^2$ to $10^{16}/cm^2$. Ion range, lattice location and damage distribution was measured using Rutherford Backscattering and Channeling (RBS-C). A significant increase in conductivity (σ) was observed below displacement per atom values (dpa) of 1. A maximum value of $\sigma = 0.3\ \Omega^{-1}\ cm^{-1}$ for Ar and $\sigma = 30\ \Omega^{-1}\ cm^{-1}$ for Sn and W were observed at dpa≥1. Keshri *et al.* [132] have investigated the influence of 100 keV Ar^+ ion implantation on structural, gas sensing and optical properties of WO_3 films. It was reported that implanted films exhibit good gas sensing response in methane environment and optical properties of the films also improved as the fluence increased from 3×10^{15} to $1\times10^{17}\ cm^{-2}$. Fromknecht *et al.* [133] have implanted the He, Hg and Xe ions into the TiO_2 (rutile) and studied the properties with temperature variation. For every oxidation state the conductivity was enhanced by 12 orders in magnitudes. The damage production and their recovery with temperature were thoroughly studied. The relation between charge states, lattice site occupation and conductivity with large defects production was investigated. Miyakawa *et al.* [134] implanted the H^+ and He^+ ions into oriented WO_3 films. These films were deposited by pulsed laser deposition on sapphire substrates. A significant increase in conductivity (at 300 K) was seen to 3 Scm^{-1} (for He^+ implantation) and to 200 Scm^{-1} (for H^+ implantation) at $1\times10^{17}\ cm^{-2}$ dose. The carrier generation efficiency for H^+ implantation was ~60% and ~10^{-3}% for He^+ implantation. They concluded that large conductivity in highly oriented WO_3 films was due to increase in mobility, which result from reduced grain boundary.

2.8 Applications of Transparent Conducting Electrodes

Transparent conducting oxides thin films have wide variety of industrial applications. The commercial application of TCO was started in 1940s when it was used as transparent heater in aircraft windows [82]. TCO films may also be used in the fabrication of transparent heaters which work as defrosters in aeroplane windshields. The advantage of

these transparent heaters over traditional blowers is that they work uniformly with shorter effective defrosting time over a large area. These applications of TCOs films have proven that they are technologically successful for electronic industry. After the Second World War, the transparent electrodes were used in antistatic windows, selenium rectifier photocells and heated windscreens as front electrodes [135]. The important advancement made by scientists in the area of TCO was when they used SnO_2 in aeroplane cockpit windows as transparent heating layer [136]. In 1960s a thin layer of ZnO was applied in surface acoustic wave application due to its good piezoelectric behavior [137]. In 1960s, a large amount of commercial applications of TCO saw tin or In_2O_3 used in sodium discharge lamps as infrared light filters. The efficiency of this lamp was increased due to decreasing heat losses [138]. With the development of flat-panel display device in 1970 using indium tin oxide (ITO) and showing good results led to it becoming most popular TCO material [139].

Muller *et al.* [140] prepared a thin film solar cell using microcrystalline (lc-Si:H) or amorphous (a-Si:H) silicon absorber or light trapping material, which increases the path length of light and affects the device efficiency. A highly transparent and conducting textured electrode was used as front electrode in silicon p–i–n solar cell which increased the light trapping efficiency. The aluminum doped zinc oxide film was deposited by sputtering and then textured by a wet-chemical etching [141]. The effect of light scattering and optical and electrical properties of ZnO:Al in lc-Si:H and a-Si:H solar cell were reported. The TiO_2/Ag/TiO_2 [104] multilayer electrodes were experimentally and theoretically optimized and then used in P_3HT:PC_{61}BM organic solar cell to enhance the solar input and optical transmittance in the operating wavelength region of the device. This organic solar cell shows higher power conversion efficiency (PCE) efficiency than PCE of solar cell prepared on ITO. Therefore, properties of TiO_2/Ag/TiO_2 electrode can be tailored to specific application and it can be a good choice to replace ITO. Lewis *et al.* [142] evaluated ITO-Ag-ITO (IMI) multilayer structures as transparent conductors for organic light-emitting diode (OLED) application. IMI films deposited on flexible plastic substrate showed lower sheet resistance than ITO with transmittance >80%. OLEDS were prepared using IMI and ITO anodes and it was found that the device with IMI anodes

exhibited enhanced performance with current densities >1 mA/cm^2. This higher performance was a result of lower resistivity of IMI multilayer strictures.

Chen *et al.* [143] have prepared Al doped ZnO (ZAO) films by magnetron sputtering for flat panel display applications. The ZAO films showed resistivity in the range of 10^{-4} Ω cm and transmittance and IR reflectance were comparable to ITO films. It was reported that the resistivity of ZAO films was reduced on adding Al and resistivity variation was ≤1% (temperature range: 50–400°C) in vacuum and ≤5% (temperature range: 50–400°C) in air. Cinnsealach *et al.* [144] developed an electrochromic window using transparent nanostructured TiO_2 films on conducting substrate of F doped tin oxide (FTO). The prepared device showed the efficiency (colouration) of 170 cm^2 C^{-1} at 608 nm, stability for more than 10 000 test cycles and switching time of 1 s, which suggested the industrial potential of the device. Shang *et al.* [145] fabricated a flexible and transparent ITO/HfO_x/ITO resistive switching memory device (RRAM) on PET substrates. This type of memory device is applicable in wearable and portable electronics. The amorphous-nanocrystalline hafnium oxide was used as main switching layer and device exhibited good thermal stability, homogeneous and reproducible resistive switching and transmittance. RRAM has shown good mechanical stability with tensile stress of up to 2.12% due to flexible substrates. It was observed that the electrical and mechanical properties of device depends on the formation of hafnium conductive filaments and is restricted by selection of top and bottom electrodes. The mechanical failure threshold of memory device increased to 3.18% when bottom electrode was replaced with platinum metal.

The literature survey given has covered synthesis and evolution of TCO and its applications. It is also observed that post treatments such as annealing and implantation affect the TCO properties and hence can be used to alter these properties according to requirements. It can be concluded that oxide/metal/oxide multilayer transparent conducting electrodes have huge potential to be used in variety of electronic devices. The last section entails the commercial applications of transparent conductors.

Chapter-3

Materials, Methods and Characterization Techniques

The chapter describes the materials and methods used in the work. Information about the materials is given regarding the parameters such as lattice structures, refractive index, melting points, conductivity and band gap. The low energy ion beam facility used for ion implantation in the multilayers is explained. The methods adopted for preparation of transparent conducting electrodes and techniques for their characterization along with their working principle such as sputtering method, X-ray Diffraction (XRD), Rutherford Backscattering (RBS), X-ray Photoelectron Spectroscopy (XPS), Scanning Electron Microscopy (SEM), Atomic Force Microscopy (AFM), Transmission Electron Microscopy (TEM), UV–Vis Spectroscopy, Hall measurement, Fourier Transform Infrared (FTIR), and Thermogravimetric (TG); used to complete this work are discussed in this chapter.

3.1 Introduction to Transparent Conducting Materials

In 1907, the first TCO was prepared by Badeker [6]. He found that the oxidized cadmium films were transparent with some conductivity. After that a variety of materials have been investigated and adopted in industrial applications. Now days, a wide range of TCO materials such as metal doped oxides, metallic mesh, metallic films, carbon nano tubes, graphene and oxide/metal/oxide multilayers are available. Most of the TCOs are n-type because of their oxygen vacancies formation capability. The TCO materials should exhibit high transmittance in visible region with high conductivity and hence the band gap of these materials should be > 3 eV. The titanium oxide, tin oxide and zinc oxides are favored metal oxides because of their large band gap, presence of native defects, non toxicity and chemical stability. Industry is dominated by indium tin oxide [146] showing transmittance of ~90% with resistivity of $2.\times10^{-4}$ Ω cm; fluorine doped tin oxide [41] displaying transmittance of ~87%, resistivity of 5×10^{-4} Ω cm with band gap of 4.25 eV; aluminum doped zinc oxide [39] exhibiting transmittance of ~80% and resistivity of 2×10^{-4} Ω cm; gallium doped ZnO [40] showing transmittance of ~85% with resistivity of 2.8×10^{-4} Ω cm and niobium doped titanium dioxide [38] displaying absorbance of ~6% at

460 nm with resistivity of 8.4×10^{-4} Ω cm. Ag metal has been extensively used as the embedded middle metal layer in oxide/metal/oxide (O/M/O) multilayer structures. In the O/M/O multilayer structures, high conductivity of Ag thin layer (~10 nm) and high transmittance of TiO_2 in the visible region (400 nm<λ<800 nm) gave us a reason to study the electrical and optical properties of TiO_2/Ag/TiO_2 and NTO/Ag/NTO multilayer structures as transparent conducting electrodes.

3.1.1 Titanium Oxide (TiO_2)

TiO_2 is the most widely studied metal oxide due to its huge industrial applications such as in energy conversion devices, optoelectronic devices, antireflection coatings, anticorrosion films, ceramics, gas sensing, paint, papers, cosmetics, photocatalyst etc., and also in biological applications. Low cost, ability to prepared by many methods and feasibility of tuning its properties are the driving forces to continue research on TiO_2 [147]. Titanium dioxide mainly consists three polymorphs namely, rutile, anatase and brookite as shown in figure 3.1 [148]. Anatase phase of TiO_2 is most commonly used for commercial purposes. Lattice parameters of anatase TiO_2 (tetragonal) are a = b = 3.782 Å, c = 9.502 Å with c/a ratio 2.51 [149,150]. TiO_2 is a large band gap (~3.1 eV) semiconductor material and shows good adhesion on glass/plastic substrates [151,152]. It exhibits strong chemical and mechanical stability and has high dielectric constant [153]. TiO_2 displays transmittance of >90% in visible region due to its high refractive index of ~2.7.

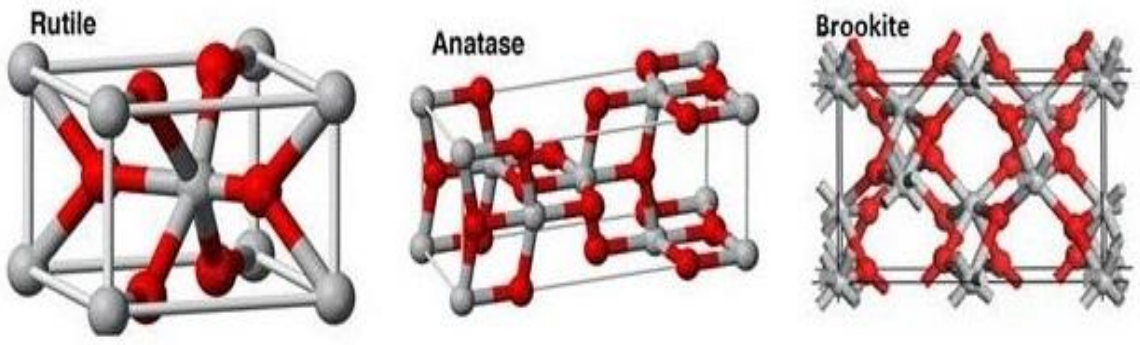

Figure 3.1: Rutile, anatase and brookite lattice structures of titanium dioxide.

3.1.2 Niobium (Nb)

Recently, niobium doped TiO_2 (NTO) films were found to be competitive to aluminum and gallium doped ZnO films and as an alternative to indium tin oxide films for TCO applications [114]. Niobium doping (0−6%) in titania, contribute ~1 electron per Nb atom and provides the high transmittance of ~97%, carrier density of 10^{19} to 2×10^{21} cm^{-3} and resistivity of $2–3\times10^{-4}$ Ω cm. Nb doping creates donor-type centers in TiO_2 lattice and hence electrical conductivity significantly increases [114,154]. In addition to Nb, vanadium (V) and tantalum (Ta) also improve the n-type semiconducting properties of titania, but niobium (Nb) is the most appropriate dopant in TiO_2 due to the similar atomic radii (Nb: 0.164 nm and Ti: 0.160 nm). Also, bond length of Ti-O and Nb-O are comparable causing less deformation of TiO_2 lattice and as Nb is a fifth group element and hence it may release one or more free electrons. In this work, Nb is used as dopant in TiO_2 as donor impurity [155].

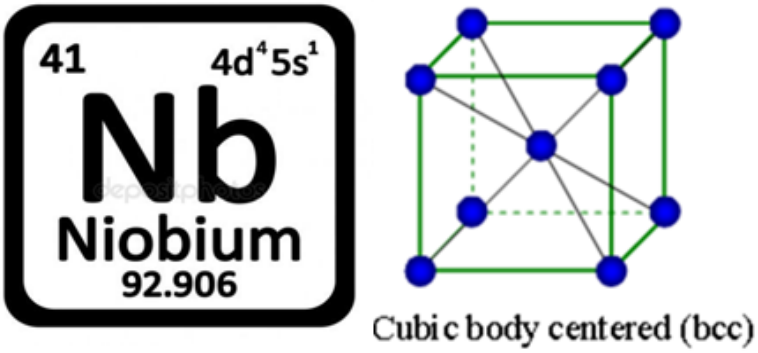

Figure 3.2: Body centered cubic lattice structure of niobium.

3.1.3 Silver (Ag)

Silver (Ag) is most abundantly used material as sandwich layer of oxide/metal/oxide multilayer structure for transparent conducting electrodes applications. Au, Ag, Cu, and Al have been used as the middle metal layer and Ag was selected due to its low resistivity and small absorbance (<5%) in visible range (for thickness ~10 nm) than other materials [156]. Ag has a face-centered cubic lattice with 47 atomic number. It is malleable, ductile, strong, good reflector of light and a good electrical and thermal conductor. Ag shows sufficient resistance to abrasion and corrosion and hence consist adequate ageing resistance. Ag deteriorates with time but maintains its optical and electrical properties. In

addition to this it exhibits a unique combination of optical, thermal and electrical properties [157]. Very thin layer of silver gives high transmittance (>90%) and Ag thin film with ~10 nm thickness display good conductivity and transparency in visible region of light [13]. Furthermore, alloy of Ag decreases the shear resistance and enhances the stability of electrode. The coating of oxide layers on top and bottom side of silver decreases reflectance of light; thereby increasing the transmittance.

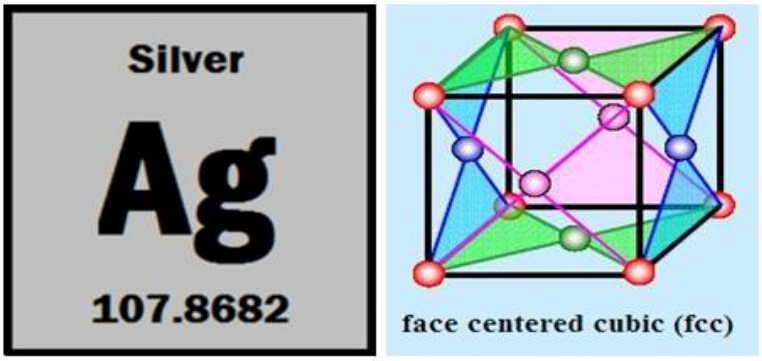

Figure 3.3: Face centered cubic lattice structure of silver.

3.2 TCO Preparation Techniques

3.2.1 Sol-Gel Spin Coating

Sol-gel process is a well known chemical method is used since for various types of thin film preparation [158] and first time silica gel was prepared by sol-gel method in 1845 by M. Ebelman [159]. It is a solution processed deposition method of thin films which involves a sol of metal salts or metal alkoxides working as starting material or precursors with their proper solvents. In addition, some functional additives can be added to solution to stabilize the chemical reaction and that may enhance the homogeneity of sol. The variation of pH value via adding the catalysts (bases and acids) cause the conversion of sol into gel. The catalysts influence the condensation rates and hydrolysis which begins the transformation of sol in to gel and consequently structure of gel (groups or chains) changes. The sol-gel process is a low cost and non-toxic method by which the dopants and extrinsic defects can be easily added to the host matrix and the properties of material can be optimized and altered. Moreover, it is used to deposit homogenous films at low temperature at different type of substrates with good control over material properties [159].

Spin coating method is used to obtain uniform and dense single and multilayer films (thickness of few nanometers to few micrometers) with simple and easy way. Therefore, it is mostly used in industry for many technological applications. In this method the substrate with solution is rotated and due to centrifugal force it spreads over the substrate and the surface tension and viscosity are the deciding factors to achieve smooth films. After deposition the film is heated at some temperature to remove the solvents. Spin coating methods involve the four main steps; spin up, coating, spin down and then heat treatment.

3.2.2 RF-DC Sputtering

Different kind of physical vapor deposition techniques such as sputtering, e-beam and thermal evaporation and pulse laser deposition are available for preparation of films. Uniform, homogeneous and films with good stochiometry can be prepared by sputtering. RF sputtering method is commonly used for oxides and dielectrics deposition and DC sputtering is used for metal deposition [160].

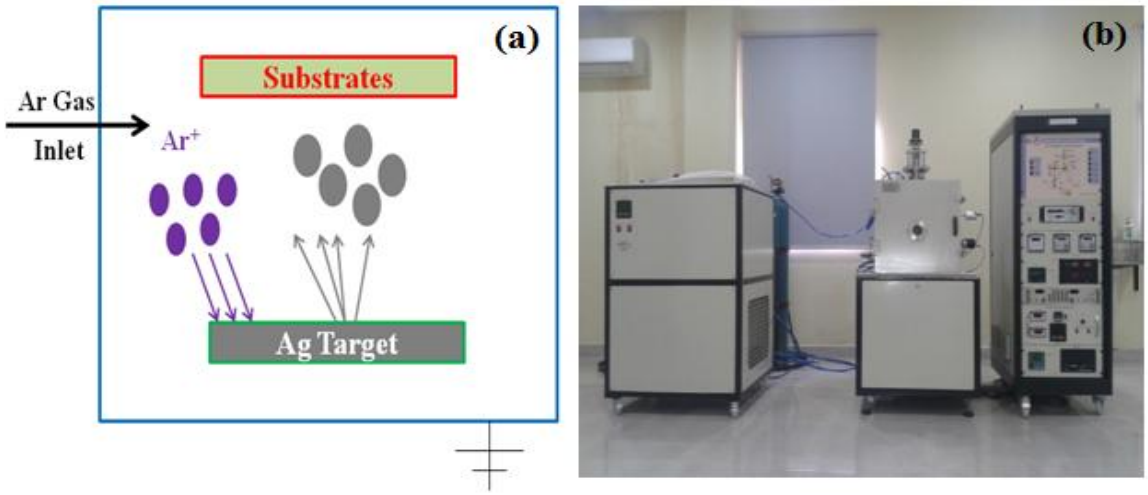

Figure 3.4: (a) Schematic diagram of working of sputtering and (b) RF/DC magnetron sputtering (APT) at MRC, MNIT Jaipur.

In this method, Ar ions are bombarded on the target material and atoms are ejected from the surface of the target and deposited on the substrates. It consists of a vacuum chamber with anode and cathode fixed opposite to each other. The vacuum chamber can be evacuated to desired pressure using vacuum pump. When Ar gas released and a high voltage is applied between anode and cathode it leads to Ar gas getting ionized. These

ions are incident on the target material ejecting atoms from it which are then collected on the substrates providing high quality thin films. The deposition of films is affected by many parameters such as: vacuum level, Ar gas flow, RF/DC source power and the target material used for deposition [161]. Therefore the desired thickness and properties of the films can be obtained by controlling these parameters [162].

3.3 Low Energy Ion Beam Facility

Ion implantation technique was discovered by W. Bradford Shockley *et al.* [163] and it was first used in semiconductors to introduce dopants in a controlled way. Metal based alloys can also be prepared by ion beam techniques and have been studied from 1970s. It is a powerful tool to introduce dopants or impurities into a host material. Irradiation/implantation recrystallizes or generates local amorphous region in the lattice depending on the target material and it has successfully exhibited the applications of this technique for modification of material properties [164]. Accuracy and control over the desired implantation process makes this technique unique and superior to other chemical/physical technique. Besides modification in physical properties of any material, implantation also plays an important role in the preparation of integrated circuits (IC) which requires 10 to 35 implantation steps.

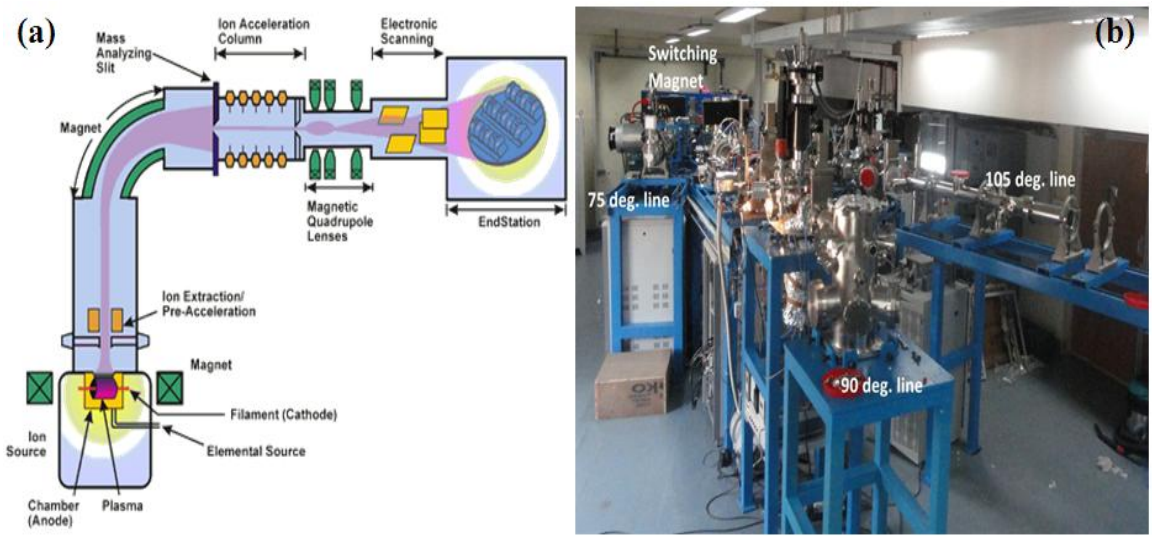

Figure 3.5: (a) Schematic representation of low energy ion beam implanter and (b) low energy ion beam facility (LEIBF) at Inter University Accelerator Centre, New Delhi.

Accurate fluence, purity and exact depth of dopants are advantageous features of the implantation process. The schematic diagram of ion implanter and low energy ion beam facility diagram is shown in figure 3.5. The different types of ion beams can be generated from electron cyclotron resonance (ECR) source and mass of the ions is analyzed by dipole magnet. When low energy ion is introduced in to material it loses its energy through nuclear energy loss and transfers the energy to target lattice thereby generating cascade collision which produces lattice defects and changes the material properties. The generation of defects inside the material depends on the ion species, fluence, mass, energy, implantation angle and hardness and temperature of the host material. The implanted ion collides inelastically with target atoms and loses its all energy and then come to rest and gets implanted.

3.4 Characterization Techniques and Methods

3.4.1 X-ray Diffractometry (XRD)

Crystal structure of the thin films is determined by X-ray Diffraction (XRD). The crystal plane orientation of the material can also be measured using XRD. It is based on Brag's diffraction principle where X-rays are scattered by atoms or planes of crystal lattice. It is a very useful technique to measure the miller indices, inter atomic separation, particle size, stress and lattice constants of the grown thin films.

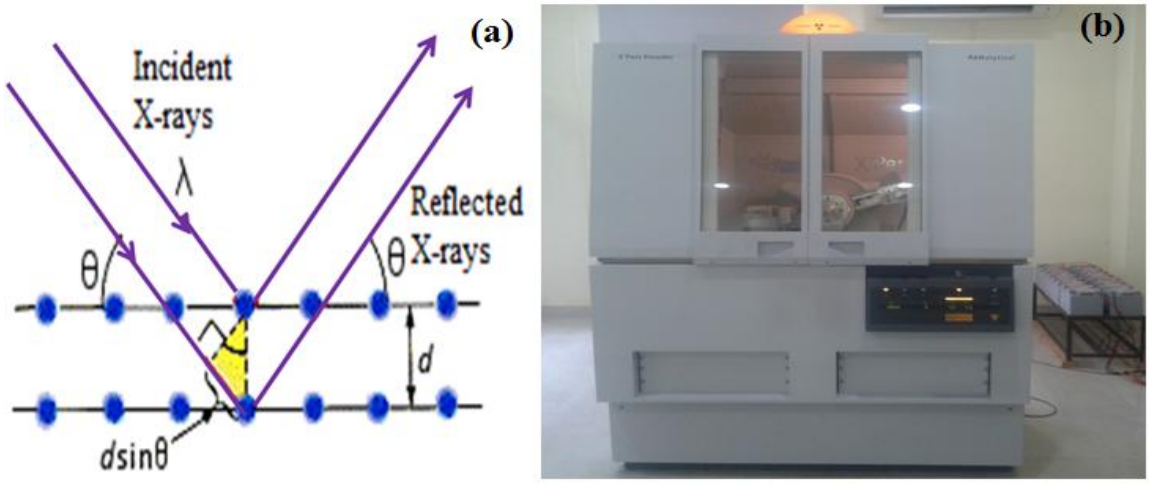

Figure 3.6: (a) Schematic diagram of X-ray diffraction and (b) XRD (X-pert pro Panalytical) machine at MRC, MNIT Jaipur.

XRD machine (PANalytical X'Pert pro) with Cu Kα radiation wavelength of 1.54 Å was used in this work. The prepared thin films were scanned from 20 to 80˚ with 0.02˚ step size for 30 minutes to ensure better quality of signal to noise ratio.

3.4.2 Rutherford Backscattering Spectrometry (RBS)

Rutherford Backscattering Spectrometry (RBS) is an investigation technique widely used in material science to determine the depth distribution of the constituent elements (composition) and thickness of material or thin films [165]. An alpha (α) particles beam (of a few MeV) is sent towards to specimen and the number and energy of ions backscattered in a particular direction with respect to impinging beam are estimated. The energy of the backscattered ions depends on atomic number of host atom. Therefore, the constituent elements of the target material can be identified. Figure 3.7 shows the schematic diagram of RBS and the instrument available at IUAC, New Delhi. The energy of α-particles of this facility was ~2 MeV. The diffusion of one material in to another material in case of multilayer films can also be determined using RBS.

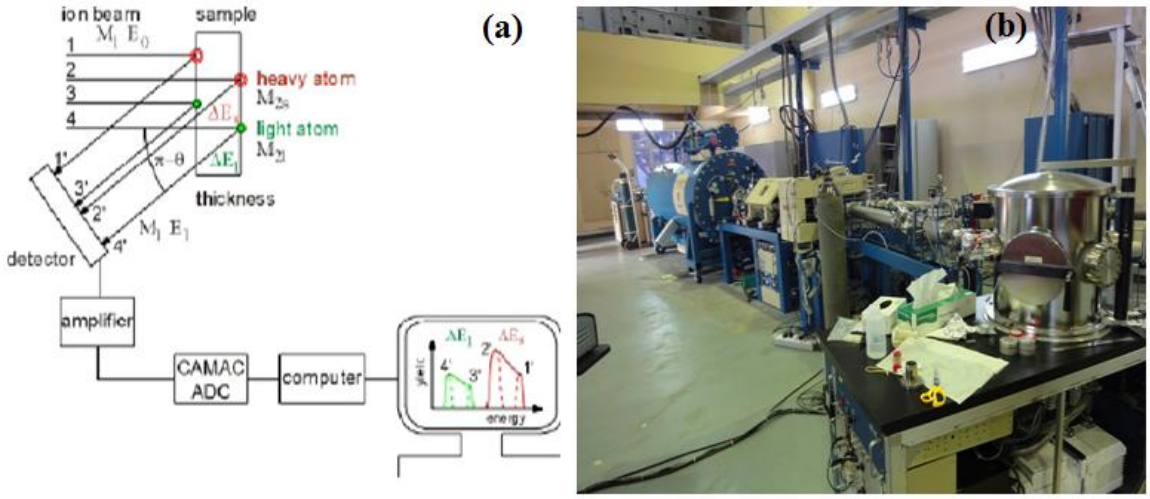

Figure 3.7: (a) Schematic representation of Rutherford Backscattering and (b) RBS system (PARAS) at Inter University Accelerator Centre, New Delhi.

3.4.3 X-ray Photoelectron Spectroscopy (XPS)

X-ray photoelectron spectroscopy (XPS) also known as electron spectroscopy for chemical analysis (ESCA) is a technique which is used to study energy distribution of the emitted electrons from the X-ray irradiated compounds. The number and energy of the

electrons ejected from the specimen surface is determined by analyzer and we obtain a curve between binding energy of photoelectrons and their intensity. Thus, by using this curve the chemical bonding, electronic structure and composition of material can be measured [166]. The energy diagram for XPS and instrument of XPS are given in figure 3.8. XPS is a surface sensitive technique due to low mean free path (inelastic) of emitted electrons thereby it is used to analyze surface properties. The chemical analysis of the multilayer structures can be done through depth profiling mode of XPS, where the top layer is etched with the Ar ion sputtering and signal from lower layer surface can be obtained. The quantitative and chemical analysis of the sample is done through the obtained intensity and binding energy of the photoelectrons and this analysis by XPS is more precise than other techniques.

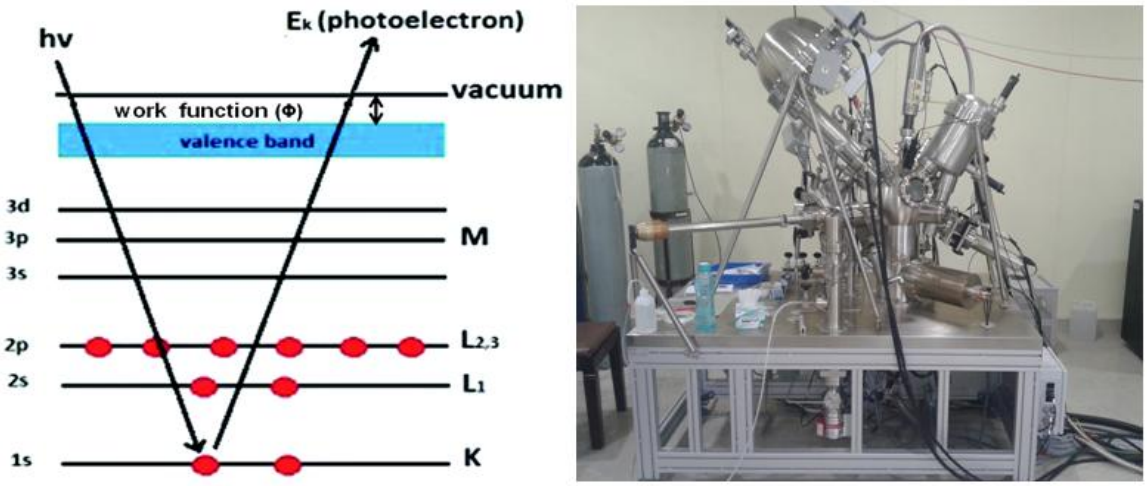

Figure 3.8: (a) X-ray Photoelectron Spectroscopy energy diagram and (b) XPS (Omicron ESCA) instrument at MRC, MNIT Jaipur.

3.4.4 Field Emission Scanning Electron Microscopy (FESEM)

Scanning Electron Microscope (SEM) is mainly used to measure the microstructure and surface morphology of the thin films, bulk, and powder specimens. SEM uses a focused high energy electron beam to produce signals at the surface of the specimen. The interaction of electrons with the specimen reveals the information about microstructure, crystalline structure and texture of the sample [167]. The magnification and resolution of SEM is very high than that of optical microscope because of lower wavelength of the electrons. An energetic electron beam scans the surface of sample and produces signals in

form of back scattered electrons, secondary electrons and characteristic X-rays to generate image of the surface. The surface morphology of prepared thin films was seen at high magnification using Nova NanoFESEM 450, FEI operated at 20 kV under high vacuum. The elemental composition was determined using energy dispersive X-ray spectroscopy (EDS (Bruker, Germany)) detector attached to FESEM. The shematic diagram [168] and instrument of FESEM are given in figure 3.9 (a) and (b). It is useful to have a thin layer of Au or C coating on a non conducting sample to avoid charge accumulation on surface, degrading the quality of the image.

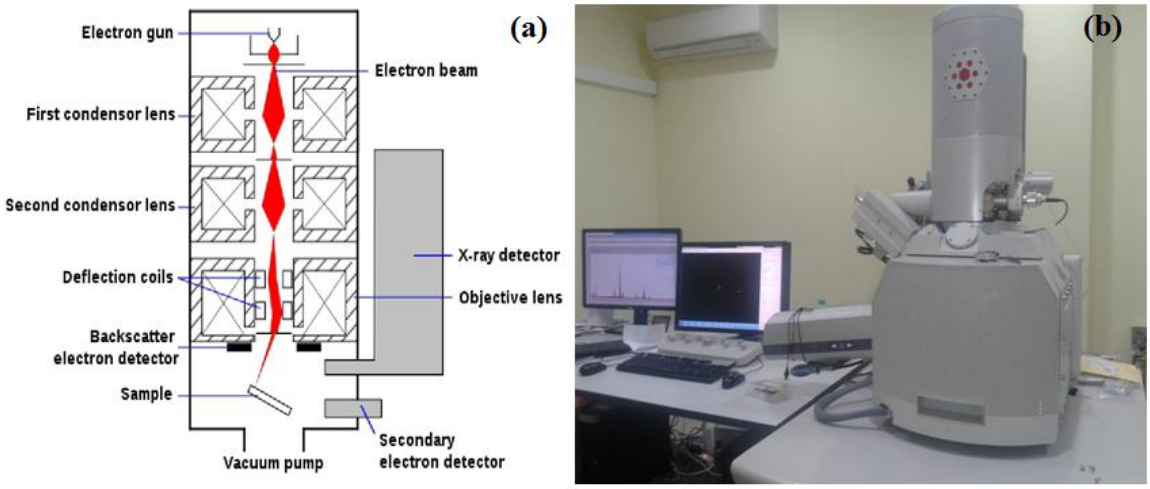

Figure 3.9: (a) Schematic representation of working of scanning electron microscope and (b) FESEM instrument (Nova Nano FE-SEM 450 (FEI)) at MRC, MNIT Jaipur.

3.4.5 Atomic Force Microscopy (AFM)

The atomic force microscope (AFM) is a type of scanning probe microscope (SPM) for imaging the sample surface at nanometer scale. It uses a sharp probe cantilever that scans the surface of sample and gets deflected due to the van der Waal force existing between surface atoms and probe when it is very near to the surface. This deflection is recorded by a photodiode and then monitored by a detector and feedback electronics [169]. A schematic diagram and instrument of AFM are given in figure 3.10. The tip (~10 nm) of cantilever is generally made of silicon or silicon nitride. The AFM mainly works in three main modes, namely contact mode, non-contact mode and tapping mode. In this work, tapping mode of AFM was used for topographical measurements of thin films. In tapping mode the resonant frequency of cantilever is changed by van der Waals forces between

the surface and tip and the topographical image is formed by monitoring these changes. This technique is very useful for investigating the size and distribution of grains, surface roughness and topography of the materials.

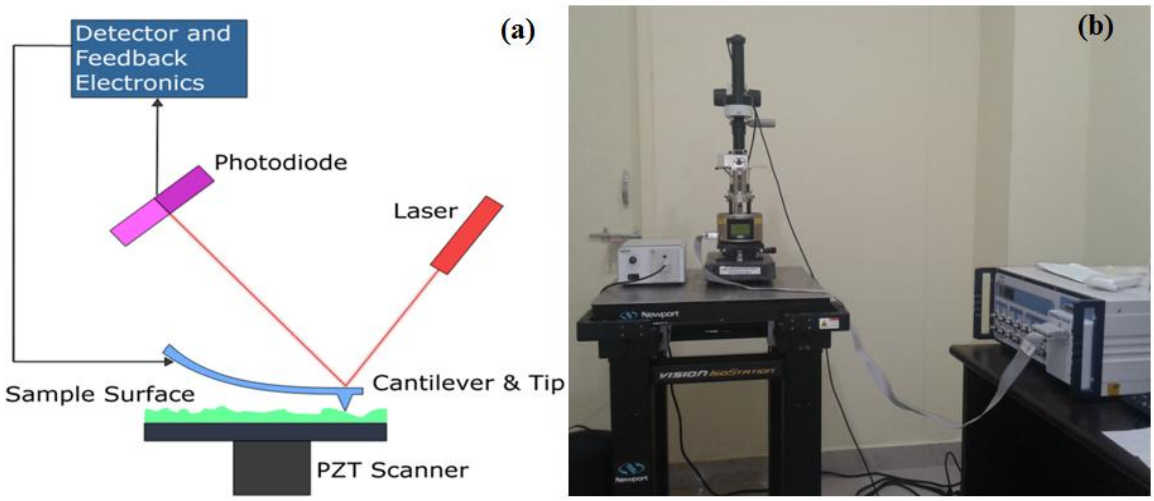

Figure 3.10: (a) Schematic representation of workingof atomic force microscope and (b) Multimode Scanning Probe Microscope (Bruker) at MRC, MNIT Jaipur.

3.4.6 Transmission Electron Microscopy (TEM) with EDS

Transmission electron microscope (TEM) uses electron source as the light source giving very high resolution due to much smaller wavelength of electrons as compared to that of an optical microscope. TEM is a powerful characterization technique and gives important information about the microstructure and crystallinity of a very thin specimen [170]. In TEM, high energy electrons are emitted by an electron gun and then accelerated by the anode (positive attraction) and this electron beam passes through the sample to provide very valuable information. The electron beam is controlled and focused by electromagnetic lenses and it consist an aperture to adjust the contrast of the image. The electron beam with the sample information is allowed to fall on a phosphorescent screen and an image is produced. In the present work, high resolution transmission electron microscopy (HRTEM, FEI: TECNAI G2 with 200 kV electron beam) has been used to investigate the thin film samples. The schematic diagram and instrument of TEM are given in figure 3.11.

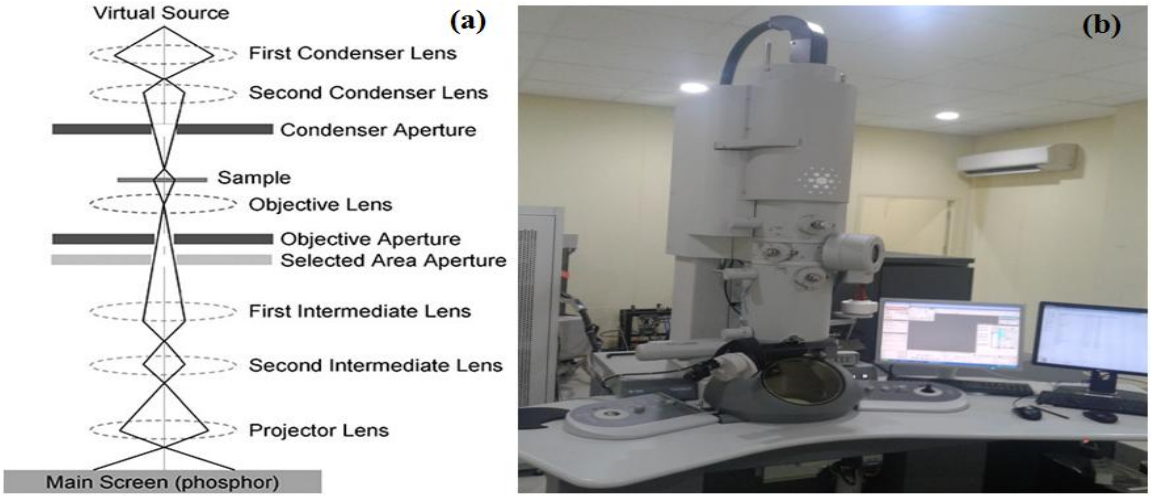

Figure 3.11: (a) Schematic representation of workingof transmission electron microscope and (b) TEM instrument (Tecnai G2 20 (FEI) HR-TEM) at MRC, MNIT Jaipur.

HRTEM generates the sample image through the interference of transmitted and scattered electrons and a nanoscale data of the crystalline material can be extracted. There are two imaging mode in TEM namely bright field mode and dark field imaging. The bright field mode is used to generate contrast imaging. On the other hand in dark field imaging only diffracted beam is used to produce the sample image. Moreover to find the element distribution in the sample, the point or area mapping is used which is accomplished by EDS.

3.4.7 UV–Vis Spectroscopy

UV-VIS-NIR spectroscopy is a very useful technique in material science to investigate the optical properties of materials [171]. In the present work, UV/Vis/NIR Spectrometer (Lambda 750 Perkin Elmer) (figure 3.12) has been used to observe the transmittance, reflectance and absorbance of the thin films. As we know that when light is incident on materials it can be absorbed, transmitted and/or reflected from the material. The optical interaction changes with varying wavelength and gives useful information about the material. The absorbance of light is explained by Beer's and Lambert law which states that absorption is directly proportional to the number of absorbing atoms or molecules. Optical properties such as transmittance and absorbance are very important for TCO materials and band gap can also be determined by Tauc's plot using the absorption peak

in the UV region. In this work, the specimens have been examined for absorbance and transmittance in the visible region (400 nm<λ<800 nm) of light.

Figure 3.12: UV/Vis/NIR Spectrometer (Lambda 750 Perkin Elmer) at MRC, MNIT Jaipur.

3.4.8 Hall Measurement

Hall effect measurement has been an important technique for materials since E. Hall invented the effect in 1879. When a current carrying semiconductor is placed normal to magnetic field a voltage is generated perpendicular to both current and magnetic field. This generated voltage known as Hall voltage. The accumulation of charge carriers on two opposite faces of specimen is deciding the type of semiconductor. Hall effect is used to measure the carrier concentration, carrier mobility, electrical resistivity and type of conductor (n or p type) of materials accurately [172]. Sheet resistance of thin films an important parameter to measure the performance of TCO, can be attained through Hall effect using film thickness and its resistivity. Furthermore, it's simple structure, fast turnaround time and low cost makes it a unique characterization technique in research laboratories and semiconductor industry. Van der Pauw method is mostly used to determine the transport properties of thin films because it gives precise results and can be used for any arbitrary shape for two dimensional specimens. The specimen for measuring electrical properties through Van der Pauw method should be homogeneous and crack free. It uses four point probes fixed on the corners of specimen and passing the current through them and applying perpendicular magnetic field; the resistivity and other

transport properties can be determined. The sample holder and Hall measurement system used to measure the transport properties of the thin film is given in figure 3.13.

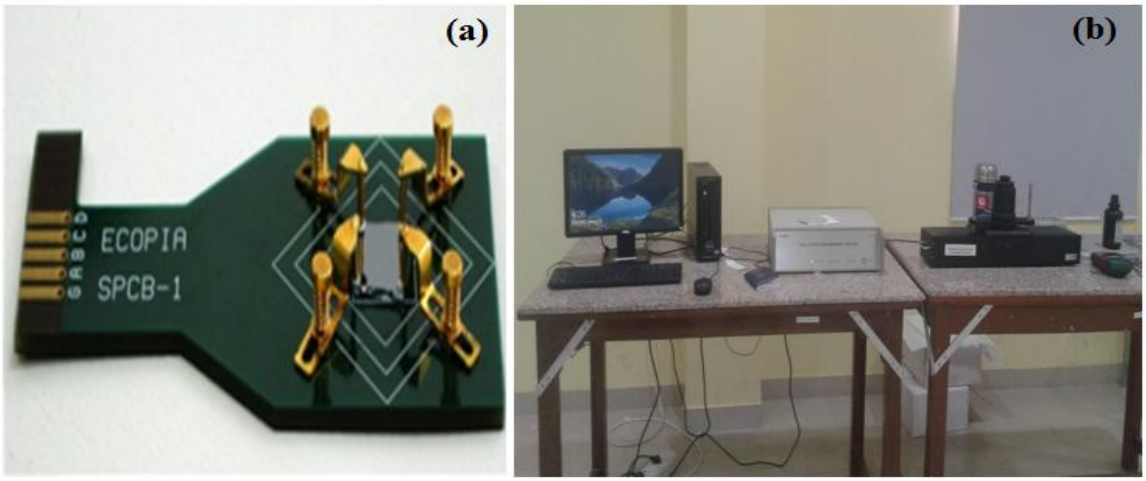

Figure 3.13: (a) Sample holder based on Van der Pauw method and (b) Hall measurement (HMS3000, Ecopia) unit at MRC, MNIT Jaipur.

3.4.9 Fourier Transmission Infrared Spectroscopy (FTIR)

Fourier-transform infrared spectroscopy (FTIR) is used to determine organic or inorganic functional groups in a sample. FTIR is a technique which is used to attain an infrared spectrum of emission or absorption of solid, liquid or a gas. It is a powerful system to recognize the type of chemical bonds in a molecule by generating an infrared emission or absorption spectrum.

Figure 3.14: Fourier Transform Infrared Spectroscopy (FT-IR Spectrum 2 Perkin Elmer) at MRC, MNIT Jaipur.

The particular wavelength absorbed by the specimen is a characteristic of chemical bond present inside the specimen. FTIR instrument used in the current work is given in figure 3.14. The word Fourier-transform infrared spectroscopy arises from the mathematical process of Fourier Transform needed to change the raw data into real spectrum.

3.4.10 Thermogravimetric Analysis (TGA)

Thermogravimetric analysis (TGA) is a thermal analysis technique in which change in mass of the sample under observation is measured with temperature increasing with constant rate. The chemical and physical properties of the material are measured using TGA. It gives information about various physical events such as absorption, desorption, phase transitions and chemical phenomenon viz. thermal decomposition, oxidation, reduction and chemisorptions etc. Therefore TGA is used to study variety of samples like thin films, elastomers, fibers, thermosets and composites. The TGA instrument used for thermal analysis of NTO films is given in figure 3.14.

Figure 3.15: Thermogravimetric Analyzer (STA 6000 Perkin Elmer) at MRC, MNIT Jaipur.

3.4.11 Semiconductor Device Analyzer (SDA)

The IV characterstics of NTO thin films and transparent ReRAM devices were measured using the Semiconductor Device Analyzer (Agilent B1500A) combined with probe station, available at MRC, MNIT Jaipur and is given in figure 3.16. Semiconductor device analyzer is a probe device which consists of many analysis and measurements capabilities

to do current-voltage (IV), capacitance frequency (C-f) and capacitance-voltage (CV) measurements quickly and accurately.

Figure 3.16: Semiconductor Device Analyzer (Agilent B1500A) with probe station at MRC, MNIT Jaipur.

Chapter-4

Investigations on Nb doped TiO_2 Thin Films Prepared by Sol-Gel and Sputtering Method and Post Annealed

4.1 Introduction

The chapter reports investigations of Nb doped TiO_2 (NTO) thin films for their potential application as TCE. Nb doped TiO_2 (NTO) has emerged as a promising TCO material for replacement of ITO. This material possesses a wide band gap (~3.3 eV) [173] and has relatively low electron effective mass ~ m_0 [174]. The chapter is divided in two parts giving two different synthesis routes. First part details the NTO thin films prepared by sol-gel spin coating method and second part reports NTO thin films prepared by sputtering. Deposition techniques have important role in controlling the physical properties of NTO films. The optical and electrical properties of the films strongly depend on morphology, structure and nature of impurities present which are a function of the synthesis route adopted and processing parameters. In this work solution-gelation (Sol-Gel) spin coating method has been adopted as a low cost alternative process to prepare the NTO thin films. This method can be used for large area coating on arbitrary shaped glass substrates and it allows controlling morphological, structure, chemical composition and shape of the specimen by tuning the processing parameters. Sputtering is one of the versatile technique which is commonly used for preparation of NTO thin films. Compared to chemical route, specimens prepared by sputtering have more homogeneity and better control exists over the film composition and thickness.

NTO thin films were prepared using sol-gel spin coating method with varying Nb concentrations. As prepared thin films were annealed at 550 ˚C for 1 h in air to achieve crystallinity, which shows anatase phase. On the other hand, $Ti_{0.97}Nb_{0.03}O_2$ (NTO) thin films were also deposited by rf sputtering and post annealed at 350 ˚C, 450 ˚C and 550 ˚C temperatures. Annealing of NTO films increases the oxygen vacancies in the film which helps in improving ion diffusion in the host matrix enhancing the electrical properties of the films and lowering their resistivity [175]. The objective of this study was to enhance

the electrical conductivity using doping and post annealing of the as prepared NTO thin films. The NTO thin films exhibited electrical resistivity of ~10^{-2} Ω cm and optical transmittance of ≥80% with low surface roughness after post annealing for sputter deposited NTO thin films.

4.2 Experimental details

NTO films were prepared by sol–gel spin coating method. The sources of titanium and niobium were tetrabutyl titanate (TBT) and niobium (V) chloride respectively. Acetyl acetone (AcAc) was added as a chelating agent with acetic acid and ethanol as catalyst and solvent respectively. TBT was dissolved in ethanol in a flask (flask A), and stirred for 1 h at room temperature. Niobium chloride with acetic acid and AcAc were dissolved in ethanol in a flask (flask B), which was also stirred for 2 h at room temperature. The niobium chloride solution was added into TBT solution and the final solution was stirred for 2 h at room temperature. The obtained final light yellow solution used for coating was aged for 20 h at room temperature. The concentration of Nb for doping was varied and taken as 0, 0.3, 0.5, 0.8, 1, 1.5, and 2 at. %. The glass substrates were cleaned using standard cleaning method. These slides were stored in ethanol to keep them clean and fresh. The films (~400 nm thick) were spin coated using aged sol with a fixed spin speed of 3000 rpm for 1 min. The deposited films were dried in air at 120 ˚C for 15 min and then annealed at 550 ˚C for 1 h in air.

Anatase TiO_2 powder (99.99% purity, from Alfa Aesar) and niobium powder (> 99% purity, from Himedialabs) were used to prepare the target (2 inch dia. & 3 mm thickness) for the sputtering process. The NTO powder ($Ti_{0.97}Nb_{0.03}O_2$) was mixed by planetary ball mill for 10 hrs. The milled powder was pressed into disc to make a pellet, and then sintered at 1100 ˚C for 10 h in the presence of oxygen to achieve high density target. This target was used to deposit Nb doped TiO_2 (NTO) ~400 nm thin films by rf magnetron sputtering at room temperature on glass and silicon substrates. For deposition, sputtering chamber was initially evacuated down to 6×10^{-6} mbar. The magnetron discharge was made by a gas mixture of Ar and O_2; gas ratio of 15 sccm Ar and 2.5 sccm O_2 was maintained during the process. A constant working pressure of 7×10^{-3} mbar was maintained during deposition. The deposition was done at 120 W rf power for 6 hours at a

rate of 0.2 Å/sec. The silicon substrates were cleaned by the standard RCA process for deposition. Quartz and glass substrates were cleaned by ultrasonication with ethanol, acetone and TCE (trichloroethylene) each for 20 minutes with the cleaning process repeated three times.

X-Ray Diffractometer (Panalytical X-Pert Pro) was used to determine the crystal structure of NTO films. The Multimode Scanning Probe Microscope (Bruker) and Nova Nano FE-SEM 450 (FEI) were used to measure the topography and morphology of the NTO films. LAMBDA 750 (Perkin Elmer) UV-Vis-NIR Spectrophotometer was used to find the optical transmittance and absorbance. The resistivity and sheet resistance of specimens were measured using four probe method Chemical states were analyzed by X-ray photoelectron spectroscopy (XPS, Omicron ESCA). HRTEM images and SAED pattern were obtianed from T20 ST FEI – Technai G^2 transmission electron microscope (TEM) operating at 200 keV. Carrier concentration, carrier mobility and resistivity of the specimens were measured by HMS3000, Ecopia using a magnetic field of 0.57 T. Fourier Transform Infrared (FTIR) data was acquired using FT-IR Spectrum 2 (Perkin Elmer) and thermogravimetric (TG) behavior was studied using STA 6000 (Perkin Elmer).

4.3 Nb doped TiO_2 Thin Films by Sol-Gel Spin Coating Method

The sol-gel method is a promising method for producing homogeneous and large area thin films at low cost. This method can also be used in fabrication of nano particles, sheets and fibers at room temperature. The schematic diagram of NTO film preparation using sol-gel spin coating is given in figure 4.1.

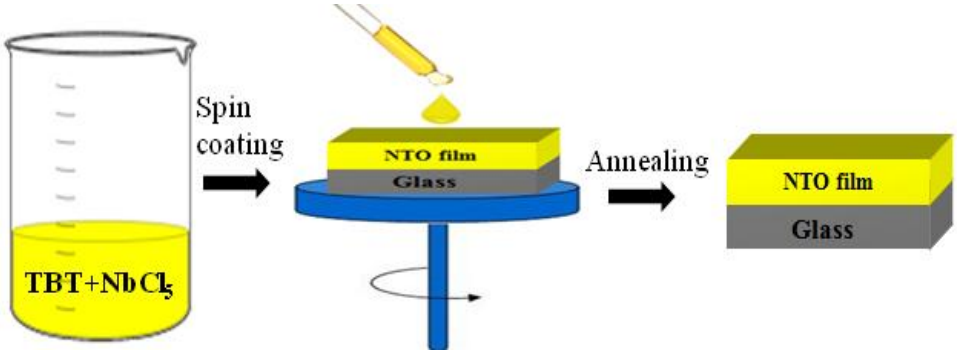

Figure 4.1: Schematic diagram of NTO film preparation using sol-gel spin coating.

4.4 Results and discussion

4.4.1 Structural properties

Figure 4.2 (a) shows the X-ray diffraction (XRD) pattern of the Nb doped TiO_2 (NTO) thin films with Nb composition in the range of 0−2 at. % . As-deposited pure TiO_2 and NTO films were amorphous due to room temperature preparation of films. Annealing of thin films at 550˚C led to increase in crystallinity. Annealed NTO films show a sharp peak at 2θ position of ~25.5˚, which can be assigned to the (101) anatase Nb:TiO_2 reflection plane. The weak peaks at ~37.7˚ and 48.1˚ in the annealed samples are due to the (004) and (200) anatase reflection plane. Figure 4.2 (b) shows a shift in the position of the (101) peak to lower angular side with increase in Nb content. Similar results were seen by Su *et al.* [176] and the shift has been attributed to Nb atoms replacing Ti atoms in the crystal on doping.

Crystallite size has been calculated by using Debye–Scherrer formula (Eq. 4.1). Inter-planar spacing (d-spacing) between atoms was obtained using Bragg's Law (Eq. 4.2).

$$D = \frac{0.94\lambda}{\beta cos\theta} \tag{4.1}$$

$$2d \sin\theta = n\lambda \tag{4.2}$$

where D is the diameter of the particle, θ is the diffraction angle, λ is the wavelength of X-rays, d is inter-planar spacing and β is the full-width at half maximum of the XRD peak. The calculated crystallite size of deposited NTO thin films in the anatase (101) direction is given in table 4.1. It was observed that the crystallite size reduces with increasing Nb concentration. The substitution of Ti by Nb atoms in TiO_2 lattice produces some strain (as Nb atom is larger) which may hamper growth of TiO_2. The same characteristics were reported by Uyanga *et al.* [177].

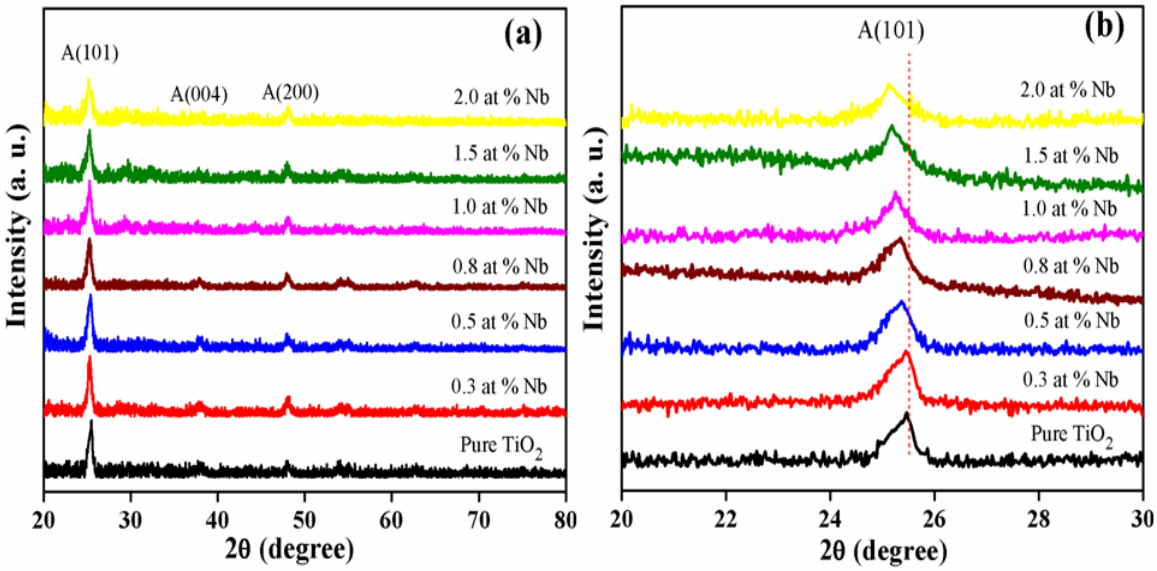

Figure 4.2: (a) XRD patterns of the pure TiO_2 and NTO films post-annealed at 550 ˚C, (b) magnified pattern in the range of 20˚ to 30˚.

Lattice strain and lattice constants have been calculated using Eq. 4.3 and Eq. 4.4.

$$\text{Lattice Strain} = \frac{\beta}{4\tan\theta} \tag{4.3}$$

$$\frac{1}{d^2} = \frac{h^2+k^2}{a^2} + \frac{l^2}{c^2} \tag{4.4}$$

Inter-planar spacing, crystallite size, lattice strain and lattice constants for pure TiO_2 and NTO films have been calculated and are given in table 4.1.

Table 4.1: Crystallite size, lattice strain and lattice constants of pure TiO_2 and NTO films with different Nb concentration.

S. No.	Nb concentration (at %)	Angle (θ) (degree)	d spacing (Å) (±0.05)	Crystallite size (nm)	Lattice Strain ($\times10^{-2}$)	Lattice constants	
						a (Å)	c (Å)
1	0	12.75	3.48	15.2	1.00	3.77	9.17
2	0.3	12.72	3.49	15	1.09	3.78	9.19
3	0.5	12.69	3.50	14.9	1.10	3.78	9.25
4	0.8	12.67	3.51	14.7	1.13	3.79	9.29
5	1.0	12.62	3.52	14.2	1.16	3.79	9.52
6	1.5	12.58	3.53	13.4	1.21	3.79	9.67
7	2.0	12.55	3.54	12.6	1.47	3.81	9.79

4.4.2 Raman spectroscopy

Raman spectra of pure and Nb doped TiO_2 thin films between 100 and 800 cm^{-1} are shown in figure 4.3. Obtained Raman modes of TiO_2 are in good agreement with the XRD results. No impurity phase was observed. Four main peaks of anatase TiO_2 appear at 146 cm^{-1}, 396 cm^{-1}, 518 cm^{-1} and 639 cm^{-1}; these peaks are assigned to E_g (ν6), B_{1g}, A_{1g} and E_g (ν1) vibration modes of TiO_2 [178]. Trizio *et al.* [179] reported that separate Nb phase may possibly appear if the Nb concentration increases beyond a certain limit (> 10 mol %). No such feature has been observed in the range of Nb doping in our case. A slight shift of the B_{1g}, A_{1g} and E_g (ν1) modes to lower wavenumber is observed with increasing Nb content.

The shift in the Raman spectra with increasing Nb content is due to particle size variation as well as due to varying stoichiometry of the system with increasing Nb. The Nb atoms produce some strain in TiO_2 lattice due to the size difference, which may hamper the growth of TiO_2 as a result of which the particle size decreases. Another reason could be variation in oxygen percentage and non stoichiometry of TiO_2 with Nb doping and annealing at 550 ˚C [180,181]. The doping generated defects which include O vacancies, Ti vacancies and O interstitials cause shift in the Raman modes of anatase TiO_2.

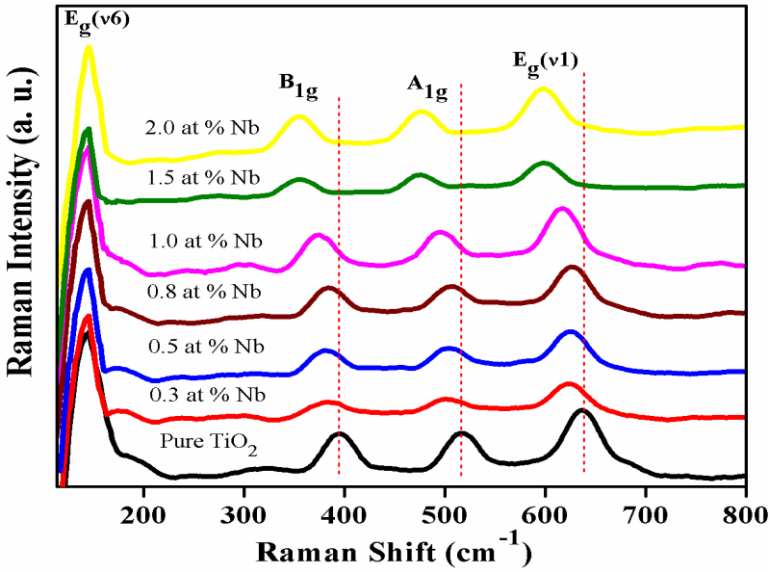

Figure 4.3: Raman spectra of pure TiO_2 and NTO films.

The particle size of NTO films is ~15 nm and small variation is seen (3 nm) on doping, hence less affecting the E_g (v6) mode of Raman spectrum [182]. B_{1g} mode appears because of stretching of Ti−O bond [183], and this observed shift in B_{1g} mode proves that Nb is perfectly doped in TiO_2 lattice [184], which is consistent with XRD results. The varying intensity of Eg (v1) modes positioned at 639 cm^{-1} peak is due to formation of Nb−O bond [179]. Raman modes and Raman peak positions of pure TiO_2 and NTO films with different Nb concentration are tabulated in table 4.2.

Table 4.2: Raman modes and Raman peak positions of pure TiO_2 and NTO films with different Nb concentration.

S. No.	Raman mode	Raman peak position (cm^{-1})						
		Pure TiO_2	0.3 Nb:TiO_2	0.5 Nb:TiO_2	0.8 Nb:TiO_2	1.0 Nb:TiO_2	1.5 Nb:TiO_2	2.0 Nb:TiO_2
1	E_g (v6)	146	145.8	145.6	145.5	145.6	145.4	145.3
2	B_{1g}	396	385	382	380	376	370	365
3	A_{1g}	518	512	508	506	504	495	485
4	E_g (v1)	639	630	627	625	619	607	603

4.4.3 Fourier Transmission Infrared Spectroscopy

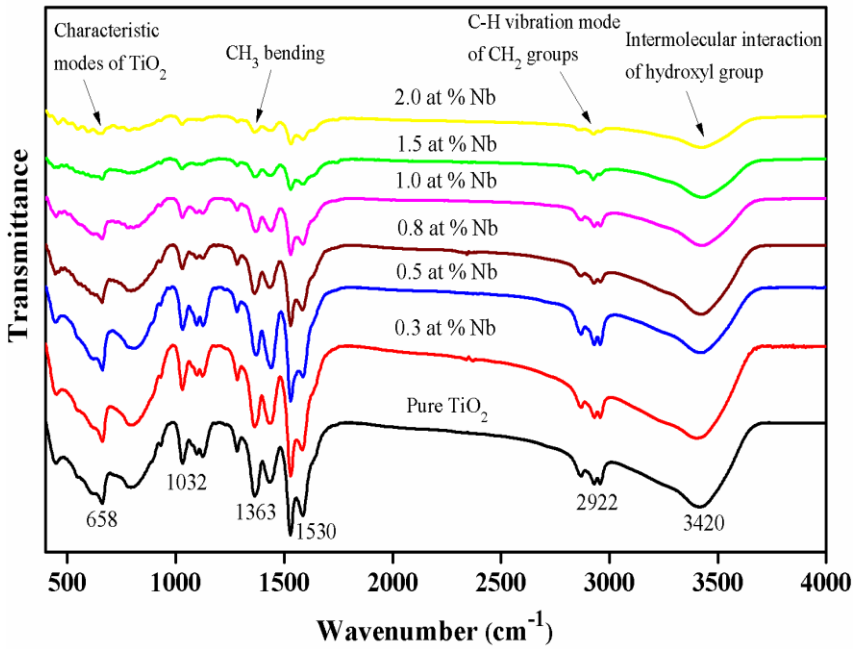

Figure 4.4: FTIR spectra of pure TiO_2 and NTO films.

Figure 4.4 shows the FTIR spectra of pure TiO_2 and NTO films for 400 to 4000 cm^{-1}. It can be seen from the spectrum that a band in the 600−660 cm^{-1} range is assigned to characteristic modes of TiO_2 [185]. FTIR mode centered at 1363 cm^{-1} is due to CH_3 bending [186]. The mode appearing at 2922 cm^{-1} indicates C-H vibration mode of CH_2 groups, which is designated as antisymmetric mode [187]. The broad range band centered at 3360−3600 cm^{-1} indicates the existence of hydroxyl groups, which is possibly due to readsorption of water from the environment [188].

4.4.4 Transmission Electron Microscope Analysis

The microstructure of pure TiO_2 and NTO (2 at%) films was further analyzed by TEM. TEM results alongwith selected area electron diffraction (SAED) pattern provide better understanding about the crystalline nature of TiO_2. Figure 4.5 (a) and (c) exhibit TEM images of pure TiO_2 and NTO (2 at%) films.

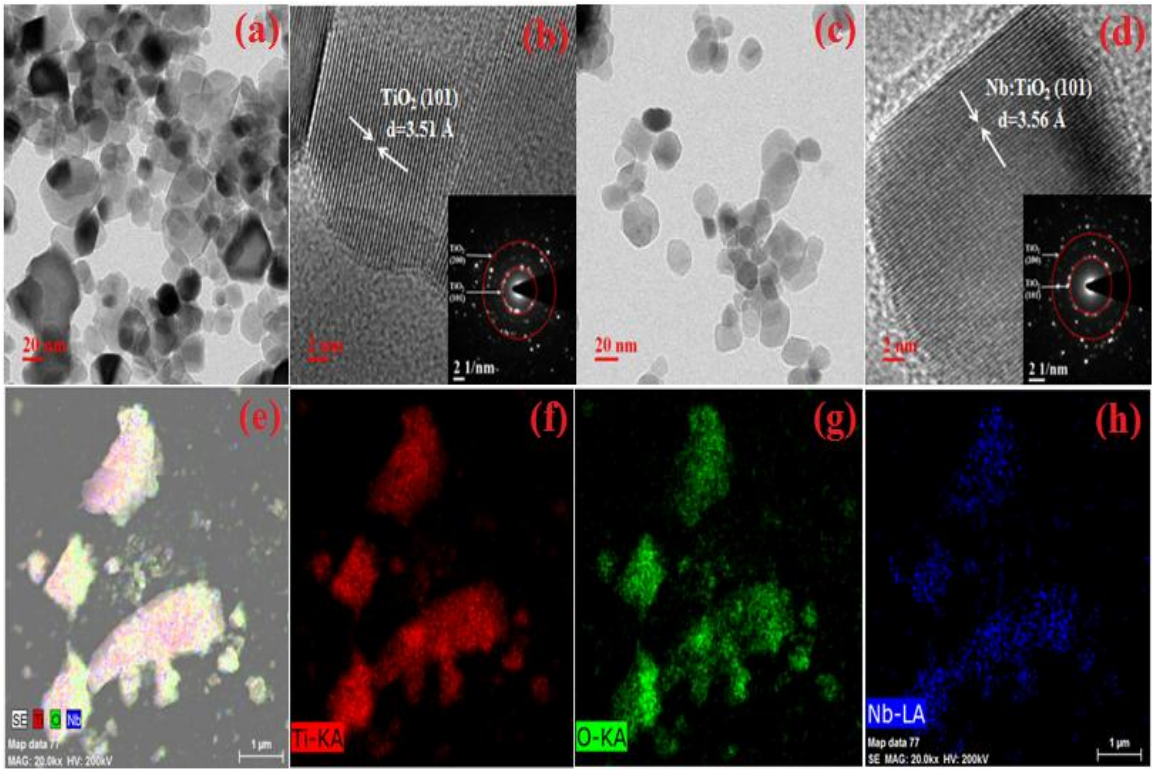

Figure 4.5: TEM images of pure TiO_2 and NTO (2 at% Nb) thin films (a) pure TiO_2 TEM image, (b) HRTEM image of pure TiO_2 with SAED pattern, (c) NTO TEM image, (d) HRTEM image of NTO with SAED pattern and (e-h) Elemental mapping of NTO film for Ti, O and Nb.

Figure 4.5 (b) and (d) shows the high resolution micrographs obtained from TEM and further investigated by digital micrograph to measure the interplaner distance. The d-spacing for pure TiO_2 and NTO samples was 3.51±0.05 Å and 3.56±0.05 Å respectively, which is nearly equal to the d-spacing values obtained from XRD results. The inset of figure 4.5 (b) and (d) shows the SAED pattern, which confirm the existence of anatase TiO_2 (101) and (200) diffraction planes. Figure 4.5 (e-h) shows the elemental mapping establishing the presence of Ti, O and Nb in the NTO film [189].

4.4.5 Surface characterization

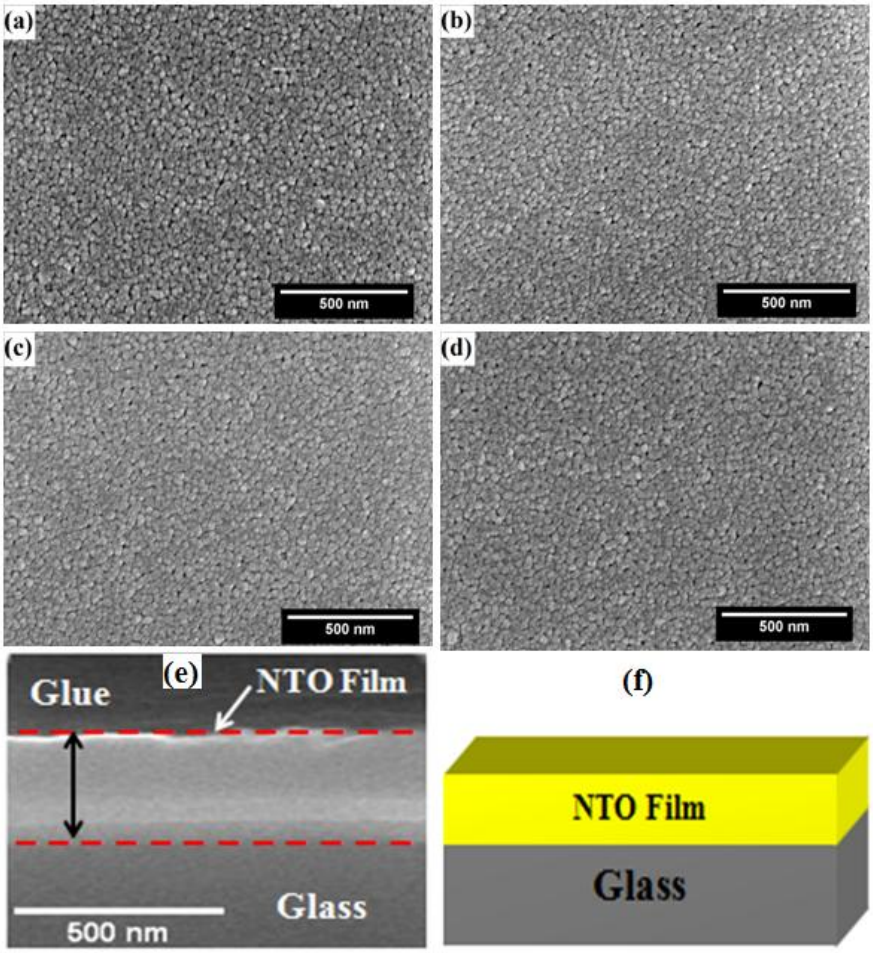

Figure 4.6: SEM images (a) pure TiO_2, (b) 0.5 at.% Nb:TiO_2, (c) 1 at.% Nb:TiO_2, (d) 2 at.% Nb:TiO_2, (e) cross-sectional FE-SEM image of NTO film and (f) schematic diagram of NTO film.

The surface morphology of NTO thin films was studied by FESEM for various Nb concentrations. Figure 4.6 shows the SEM images of TiO_2 thin films with 0, 0.5, 1.5 and 2 at% Nb at 100k× magnification. SEM micrographs show homogeneous and uniform surface morphology of NTO films. It is seen from SEM micrographs that films consist of spherical grains and niobium particles are not visible separately, showing complete miscibility of Nb in TiO_2. Similar kind of surface morphology of Nb doped TiO_2 were observed in other reports [190,191]. Figure 4.6 (e) shows the FE-SEM cross sectional image of NTO film, which indicates smooth and uniform deposition of film on glass substrate and gives estimated thickness of the NTO film as about 400 nm. Figure 4.6 (f) shows the schematic diagram of NTO film prepared on glass substrate.

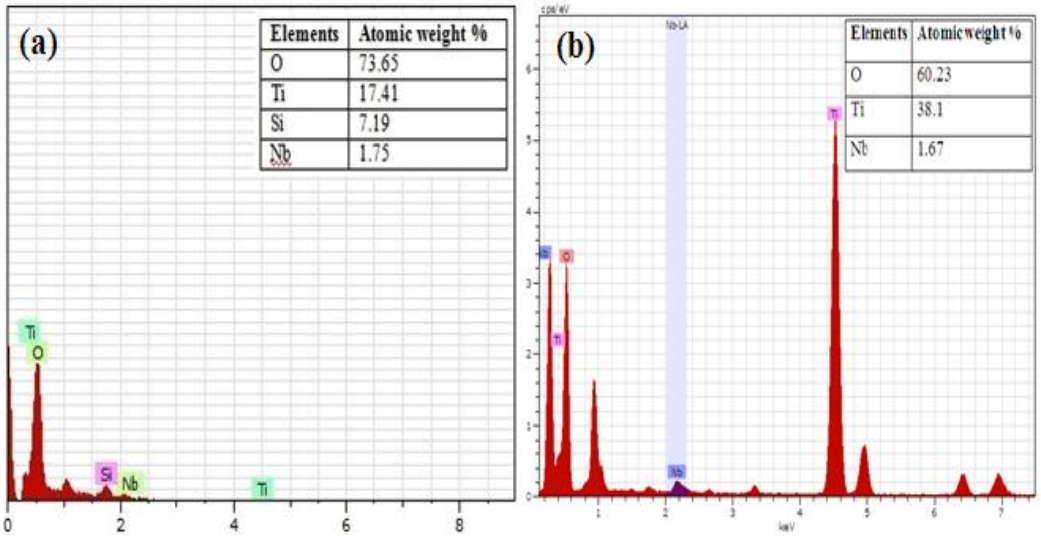

Figure 4.7: (a) SEM EDS (b) TEM EDS spectra of NTO film (2 at.% Nb).

Figure 4.7 (a) shows Energy-Dispersive X-ray (EDS) spectrum of 2 at% NTO film annealed at 550 ˚C for 1 hr obtained from SEM. EDS spectrum confirms the presence of titanium, oxygen and niobium contents in the deposited film. The silicon peak seen in the spectrum appears due to substrate. Obtained results from EDS spectrum of NTO films show existence of 1.75% niobium in the film that is close to the amount of 2% Nb used for NTO film preparation; further assuring presence of no other impurity in the film. Figure 4.7 (b) shows the EDS spectrum of 2 at% NTO film obtained from the TEM.

The topography of NTO films was observed by atomic force microscopy (AFM) with scan area of 1×1 μm^2. Figure 4.8 shows the AFM images for the samples that were

annealed at 550 ˚C. The surfaces of the thin films were very smooth and exhibit low values of root mean square roughness. The undoped film had the highest root mean square (RMS) surface roughness as 0.72 nm and the RMS value decreases with the rising of niobium concentration with a minimum value of 0.28 nm for 2 at% Nb concentration. The decrease in particle size with Nb content may result in reduction of the surface roughness giving smoother films [192]. Software Gwyddion was used to process and analyze the AFM images.

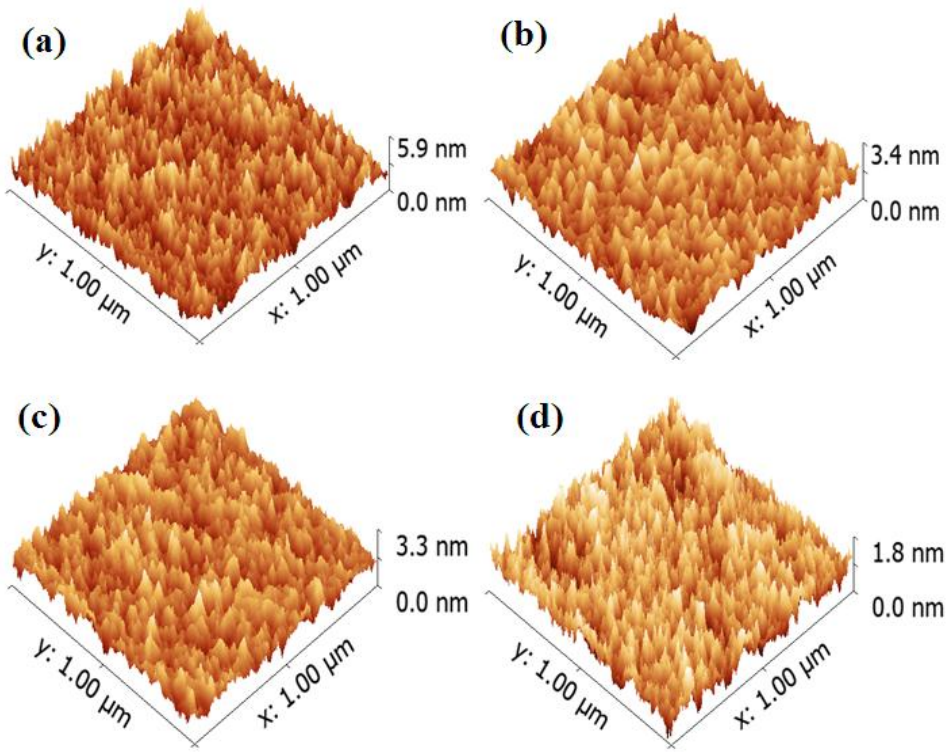

Figure 4.8: 3-D AFM images (a) pure TiO_2 (b) 0.5 at.% Nb:TiO_2 (c) 1 at.% Nb:TiO_2 and (d) 2 at.% Nb:TiO_2.

4.4.6 Thermogravimetric Analysis

Figure 4.9 shows the result of thermogravimetric analysis (TGA) (in the temperature range of 30−850 °C) of pure TiO_2 and NTO samples. It is evident from the graph that all samples show three steps of weight loss. The first loss observed at ~100 °C occurs because of expulsion of adsorbed water [193]. The second weight loss between 150 and 300 °C is due to removal of organics present in the sample. The third weight loss (in the range of 380 to 420 °C) occurs because of expulsion of hydroxyls which exist inside the sol-gel prepared films [194]. TGA results exhibit that the organic impurities are

eliminated approximately below the annealing temperature making the sample thermally stable thereafter.

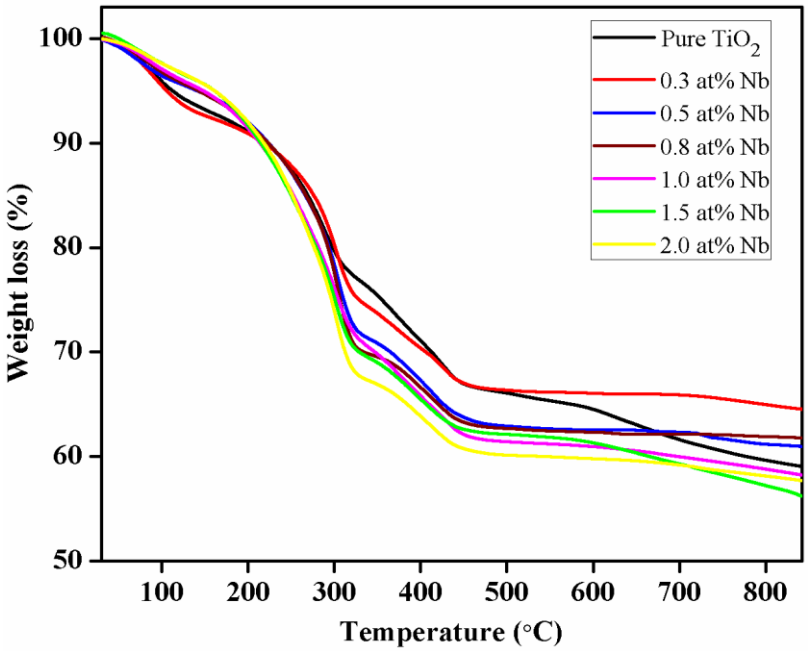

Figure 4.9: TGA (30−850 °C) spectra of pure and Nb doped TiO_2 thin films.

4.4.7 Optical analysis

The UV-Vis optical transmittance spectra for $Nb_xTi_{1-x}O_2$ (x=0, 0.003, 0.005, 0.008, 0.01, 0.015, 0.02) films annealed at 550 ˚C are shown in figure 4.10. The average transmittance for pure TiO_2 film was ~85% in the visible region (400 nm<λ<800 nm). Pure TiO_2 film shows higher transmittance than Nb doped TiO_2 thin films. The average transmittance decreases from 85% to 70% with increase of Nb concentration from 0 at% to 2 at%. Moreover the average transmittance of these sol-gel spin coated films is lower than that of the NTO film prepared by sputtering or PLD technique [22,195]. This may be because of oxygen deficiencies produced during annealing in the films and low crystalline quality of the sol-gel deposited films as compared to that produced by sputtering or PLD. Tauc plot [196] between $(\alpha h\nu)^{1/2}$ and photon energy (hν) has been plotted and is used to find the band gap of NTO films. The band gap was obtained as 3.5 eV for pristine TiO_2 film from the intersection of fitted line with abscissa and decreased to 3.43 eV and 3.22 eV for 1.0 at% Nb and 2.0 at% Nb doped TiO_2 films respectively. Decrease in transmittance of the NTO films with increasing metal doping is primarily due to creation of the scattering

centres by Nb atoms [197]. The decreasing surface roughness with Nb content may lead to increase in reflection, resulting in degradation of transmittance properties.

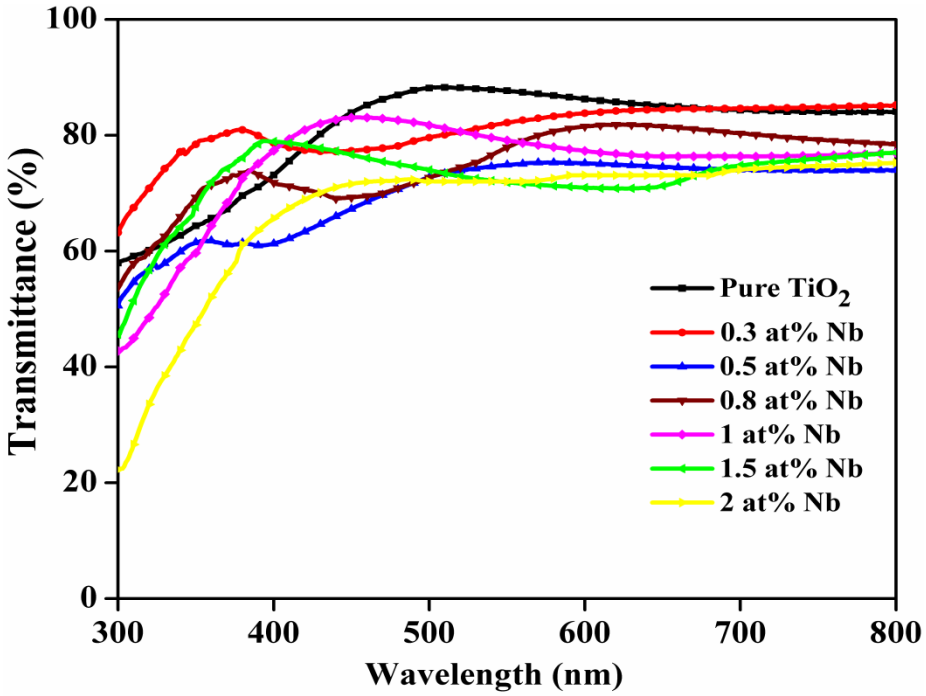

Figure 4.10: Optical transmittance spectra of pure TiO_2 and NTO films.

4.4.8 Electrical analysis

Figure 4.11 shows room temperature electrical properties of the NTO thin films annealed at 550 ˚C. The resistivity of thin films was measured by the Vander Pauw method [198] using semiconductor device analyzer (Agilent B1500A) applied to 10×10 mm^2 samples. A plot of resistivity at room temperature versus Nb concentration shows decrease in resistivity with increasing Nb content. Nb doping led to a decrease in resistivity from 171.2 Ω cm for 0.2 at% to 3.6 Ω cm for 2 at% Nb. The minimum resistivity value of ~3.6 Ω cm, is comparable to the results reported by Liu *et al.* [112] for sol-gel method and lower than the reported by Zhao *et al.* [199] for films prepared by same method. Annealing of films reduces resistivity which might be because of the oxygen vacancies introduced during annealing and helpful for Nb ions to contribute electrons to the conduction band of the TiO_2 thin films. Obtained optical transmittance, band gap, resistivity and sheet resistance of pure TiO_2 and NTO films are given in table 3.

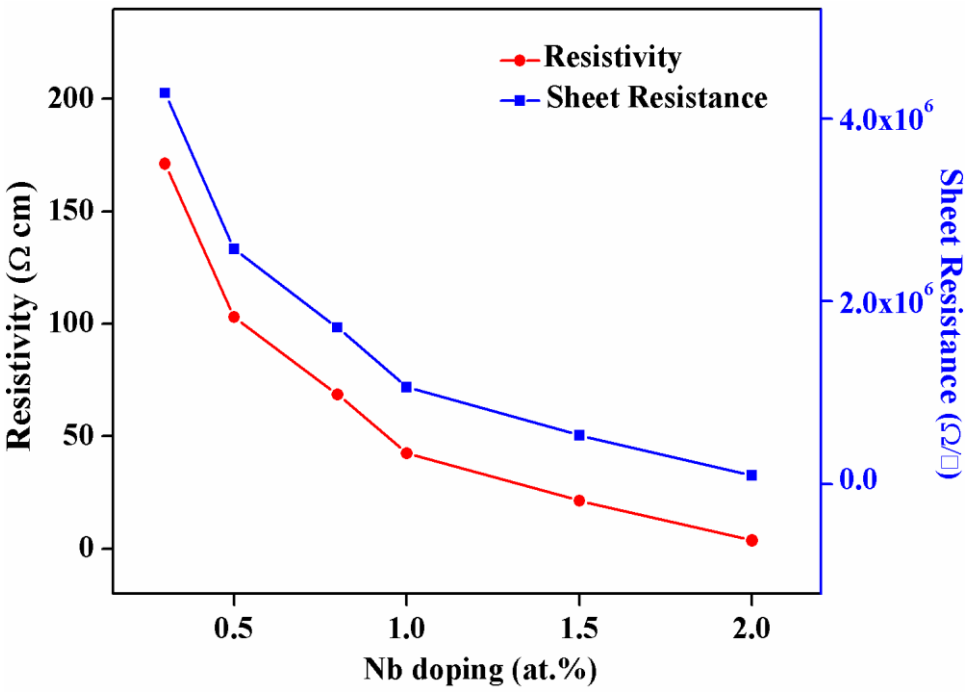

Figure 4.11: Electrical resistivity and sheet resistance of NTO thin films annealed at 550℃.

Table 4.3: Optical transmittance, Band gap, Resistivity and Sheet resistance of pure TiO_2 and NTO films with different Nb concentration.

S. No.	Nb concentration (at %)	Transmittance (%)	Band gap (eV)	Resistivity (Ω cm)	Sheet resistance (MΩ/□)
1	0	85	3.5	–	–
2	0.3	82	3.49	171.17	8.56
3	0.5	75	3.47	102.93	5.16
4	0.8	78	3.45	68.59	3.43
5	1.0	77	3.43	42.46	2.12
6	1.5	74	3.36	21.38	1.07
7	2.0	72	3.22	3.65	0.18

4.4.9 X-ray Photoelectron Spectroscopy

The chemical composition of the pristine and doped TiO_2 films was determined using XPS. The typical survey spectra of TiO_2 and NTO (2 at.% Nb) films are shown in figure 4.12 (a). The survey spectrum contains the dominant signals of Ti 2p and O 1s and weak signals of C 1s and niobium (Nb 3d and 3p). The core level spectra of Ti 2p for pristine and doped films are shown in figure 4.12 (b). The spectra exhibit binding energy as 458.84 and 464.42 eV for Ti $2p_{3/2}$ and Ti $2p_{1/2}$ respectively. The binding energy difference of Ti $2p_{1/2}$ and Ti $2p_{3/2}$ peaks is 5.6 eV, which is consistent with energy

splitting reported for Ti 2p [200,201]. For NTO these peaks are shifted to 458.94 eV and 464.5 eV positions, which is because of substitution by Nb^{5+} in TiO_2 lattice and the existence of Nb-O-Ti bond formation [177]. The intensity of Ti $2p_{3/2}$ peak in doped film decreased slightly and doping causes a low energy shoulder on Ti $2p_{3/2}$ peak, which can be interpreted as due to Ti^{3+} peak at 457 eV [202]. Defects were created due to Nb doping in form of oxygen vacancies as confirmed by presence of Ti^{3+} state in XPS spectra. The existence of Ti^{3+} state causes band gap reduction validated by Tauc plot, which results decrement in electrical resistivity.

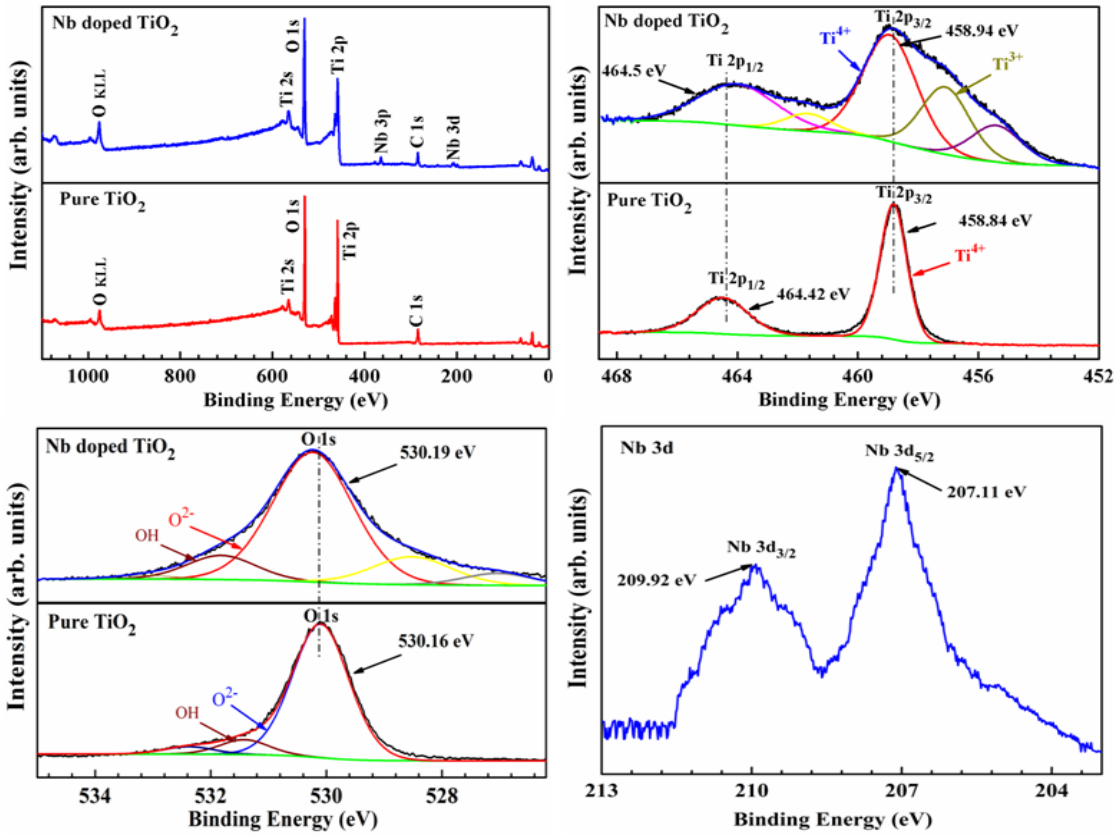

Figure 4.12: XPS spectra of pure TiO_2 and NTO (2 at.% Nb) films (a) survey scan, (b) Ti 2p (c) O 1s and (d) Nb 3d.

The core level spectra of O 1s for both films are shown in figure 4.12 (c). The high intensity peak at 530.16 eV is characteristic of metallic oxide, which is in good agreement with binding energy of O 1s for TiO_2 [203]. Another peak at 531.4 eV may be assigned to oxidized hydrocarbon [204] and peak positioned at 532.6 eV is assigned to hydroxyl group (Ti-OH) present on the TiO_2 film surface. The OH group belongs to hydroxyl

group formed during sol-gel preparation of films [177]. Figure 4.12 (d) shows the core level spectra of Nb 3d for the doped film. The binding energies of 207.11 eV and 209.92 eV are assigned to $3d_{5/2}$ and $3d_{3/2}$ of Nb^{5+}, respectively, which contain a spin-orbit splitting of 2.8eV. The result indicates that the oxidation state of Nb in NTO film is mainly 5+ [176]. The Nb concentration (~1.8 at %) in doped film determined through XPS is nearly equal to our experimental value and is also in agreement with the EDS result.

4.5 Nb doped TiO_2 Thin Films by Sputtering

$Ti_{0.97}Nb_{0.03}O_2$ (NTO) thin films were also deposited by rf sputtering and post annealed at 350 ˚C, 450 ˚C and 550 ˚C in air to investigate the behavior of films annealed at different temperatures. The structural, electrical and optical properties were then examined as function of the annealing temperature. NTO films deposited by sputtering method possess equivalent optical and electrical properties to those of ITO along with special properties such as high refractive index and high chemical stability [111]. In addition, Ti, a major component of these films is much more abundant in nature.

4.6 Results and discussion

4.6.1 Structural Properties

Figure 4.13 shows the X-ray diffraction pattern (XRD) of the Nb doped TiO_2 thin films deposited on glass substrate for different post deposition annealing temperatures. In the XRD pattern, the as deposited film is amorphous because of room temperature deposition. A sharp peak appeared at the 2θ position of ~25.5 when film was annealed at 350 ˚C; this peak can be assigned to (1 0 1) anatase Nb:TiO_2 reflection plane. The other peak marked at the 2θ position of ~56.1 corresponds to (2 1 1) anatase Nb:TiO_2 reflection plane. No Nb_2O_5 phase was observed in XRD pattern, and matches with results reported by other groups [113,116]. From figure 4.13 one can observe that the Nb doped TiO_2 anatase phase appears through post annealing the films in the temperature range 350 − 550 ˚C. Temperature higher than 550 ˚C would deform the glass substrate and may cause diffusion of NTO film in the glass substrate. Our study confirms that post annealing of NTO thin films is a simple method to generate crystallization of anatase phase.

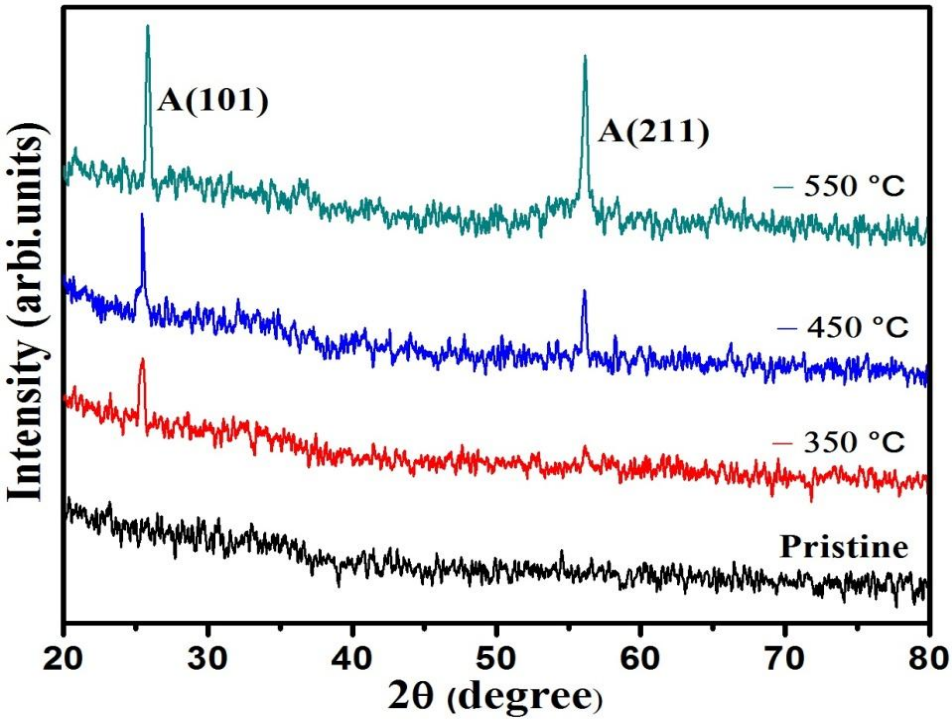

Figure 4.13: XRD pattern of the $Ti_{0.97}Nb_{0.03}O_2$ (NTO) thin films, annealed at various temperatures.

4.6.2 Raman spectroscopy

Raman spectroscopy analysis of the Nb doped TiO_2 samples sputter deposited and then annealed at 350 ˚C, 450 ˚C and 550 ˚C is shown in figure 4.14. All samples show the characteristic modes of anatase TiO_2, consistent with the XRD results shown in figure 4.13; no impurity phase was observed. Peaks centered at 146 cm^{-1} and 396 cm^{-1} are associated with E_g (υ6) and B_{1g} vibration modes respectively [176]. Peak centered at 522 cm^{-1} corresponds to silicon substrate and no niobium bands are observed, suggesting no phase separation of niobium or formation of NbO_x in the samples [177]. The E_g mode positioned at 146 cm^{-1} mainly emerges due to extension vibration of the anatase structure of TiO_2. The peak position and shape of the E_g mode is attributed to the strain, phonon confinement and anharmonic effect of lattice potential and this is affected by the annealing treatment [205,206].

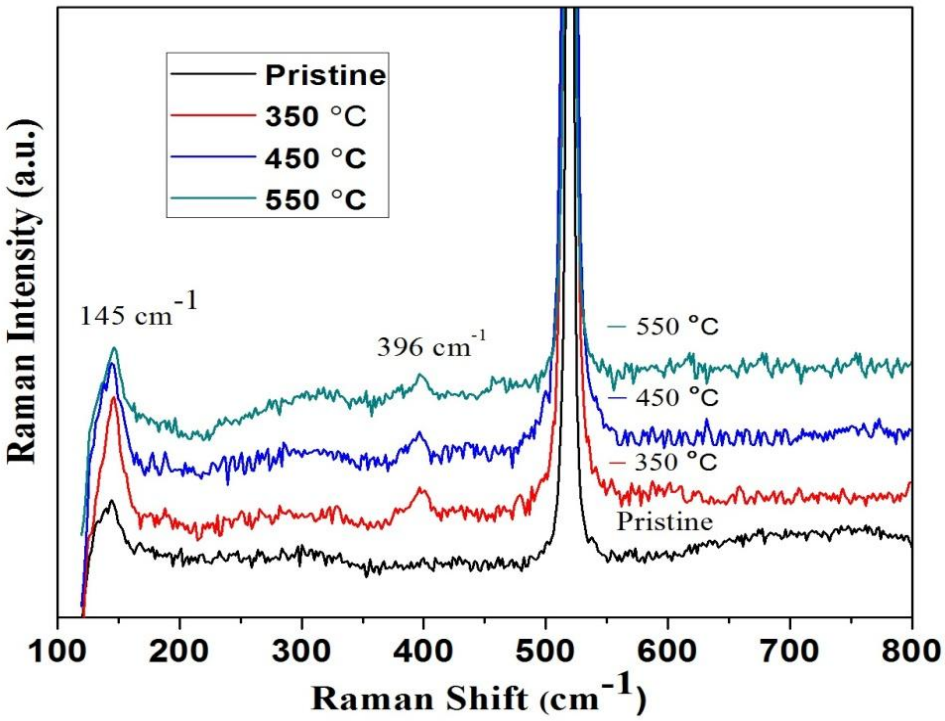

Figure 4.14: Raman spectra of the $Ti_{0.97}Nb_{0.03}O_2$ (NTO) thin films, annealed at various temperatures.

4.6.3 Surface characterization

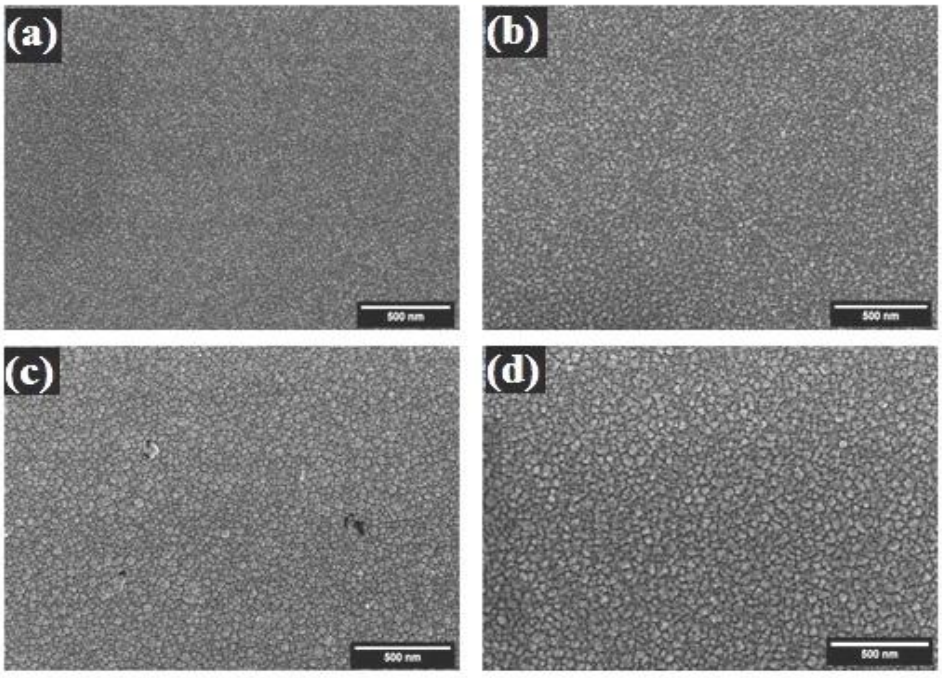

Figure 4.15: SEM images of NTO film of 400 nm thick on glass substrate (a) Pristine (b) 350 ˚C (c) 450 ˚C and (d) 550 ˚C.

The surface morphology of Nb doped TiO_2 thin films characterized by the Nova Nano FE-SEM 450 (FEI) are shown in figure 4.15. The microstructures were observed at 100k× magnification for various NTO films. Figure 4.15 shows that the morphology of the samples is uniform and homogeneous, with no other impurity observed. The films possess a dense and granular structure of ~40 nm average size in diameter. Similar type of microstructures was reported in previous report [191].

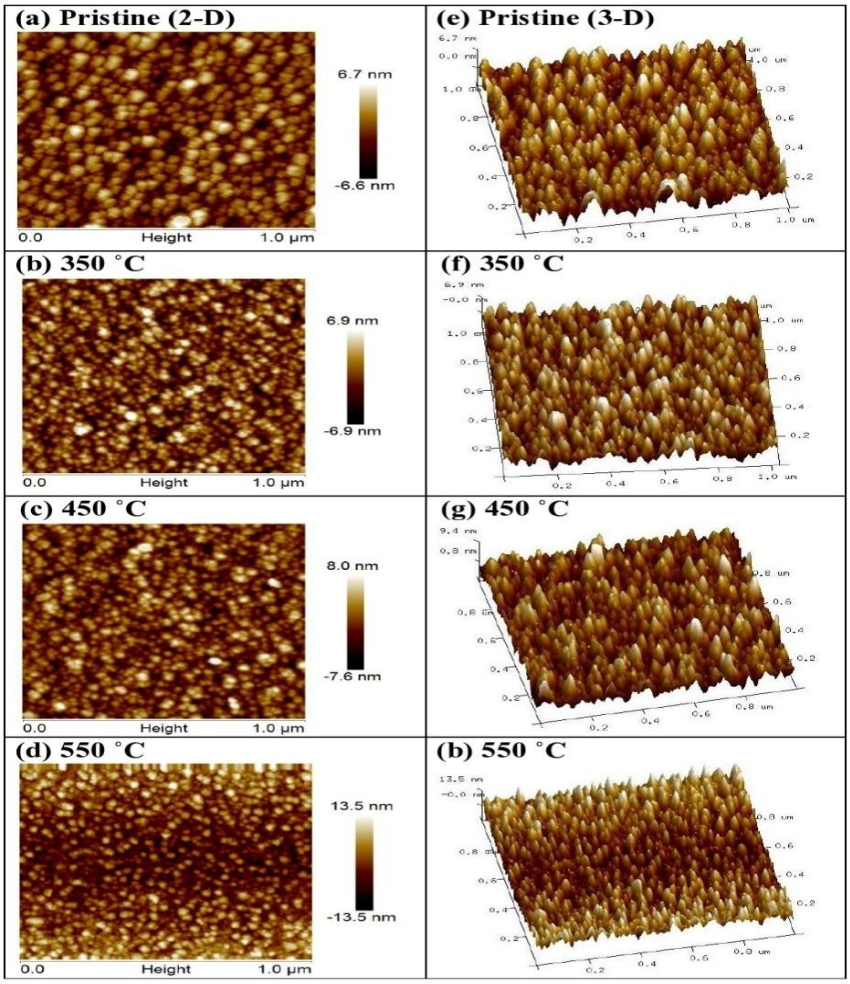

Figure 4.16: AFM surface topography of NTO films annealed at various temperatures (a) 2-D images (b) 3-D images.

Figure 4.16 shows the surface topography of the Nb doped TiO_2 thin films characterized by atomic force microscopy done by Multimode Scanning Probe Microscope (Bruker), using a surface scan area of 1×1 μm^2. The AFM images depict a relatively smooth surface of pristine sample than the annealed samples. These images

show crack free and dense surface composed of grains with repeatable pattern. The root mean square (RMS) value for the pristine sample was measured to be 1.97 nm, and surface roughness increased with annealing from 2.37 nm to 4.46 nm in the temperature range 350 ˚C − 550 ˚C, shown in table 4.4. Such small values of roughness show that the as prepared and annealed films grown on glass were very smooth and good for TCO application. Enhancement in the surface roughness with annealing could be because of increase of grain size after annealing. Similar topography for Nb doped TiO_2 thin films have been reported by many research groups [207,208].

Table 4.4: Surface roughness (nm) of NTO thin films for various annealing temperatures.

Annealing temperature	RT	350 ˚C	450 ˚C	550 ˚C
Roughness (nm)	1.97	2.37	2.51	4.46

The film thickness was measured by making a step on the film and then processed by the NanoScope Analysis software. The step on the image is shown in figure 4.17 (a). Calculated thickness of the film comes approximately 400 nm from figure 4.17 (b).

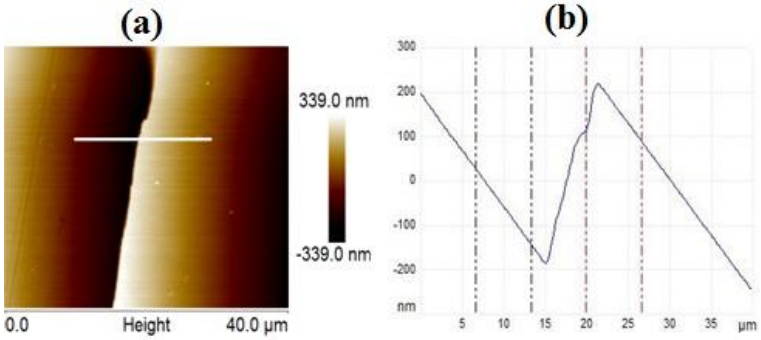

Figure 4.17: (a) Step size on the NTO film and (b) thickness calculation by AFM.

4.6.4 Optical analysis

Figure 4.18 shows optical transmittance of $Ti_{1-x}Nb_xO_2$ (x = 0.03) thin films grown on glass substrates. In the visible region (λ = 350 – 800 nm) the optical transmittance of the NTO films was typically 70 – 75% and similar type of transmittance curve has been observed in previous reports [116,195]. The transmittance graph shows slight oscillatory behavior due to interference between the light reflected from the surface of

the film and the interface [199,209]. From figure 4.18 one can see that pristine film exhibits 75% transparency, which decreases as annealing temperature increases. Increase in root mean square roughness of the surface could be the reason for this. Films with higher surface roughness cause more scattering of light thus degrade the transparency of the films.

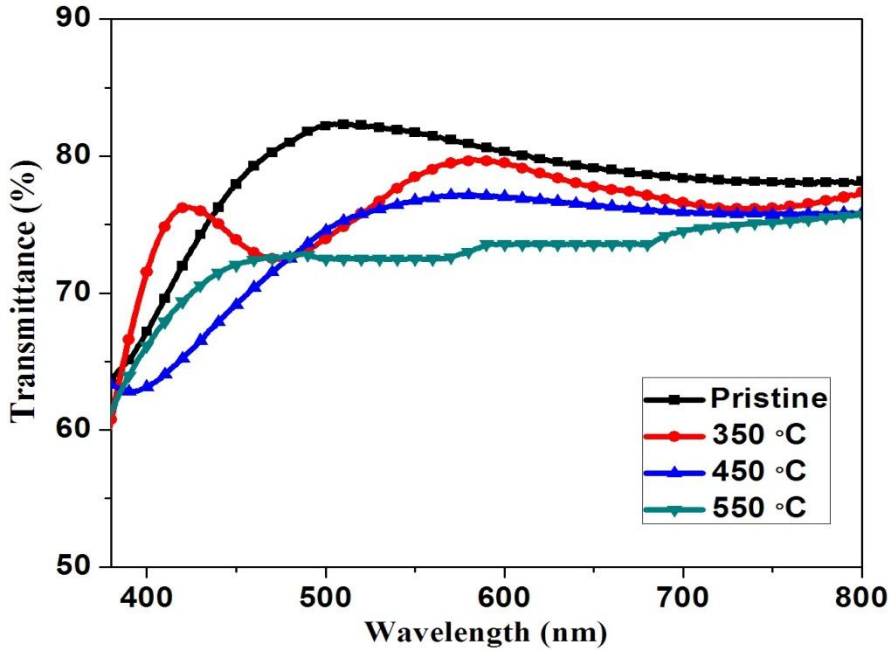

Figure 4.18: Optical transmittance spectra of NTO thin films annealed at various temperatures.

4.6.5 Electrical analysis

The electrical properties of the NTO thin films were measured by Hall effect measurement. Figure 4.19 shows the resistivity, carrier concentration and Hall mobility of the samples as a function of the annealing temperature. A graph of resistivity versus annealing temperature is shown in figure 4.19 (a). The films show resistivity at room temperature as 9.8 Ω.cm and minimum resistivity was obtained ~3.2×10^{-2} Ω cm at 450 ˚C. This behavior is consistent with results reported by Wang *et al.* [22]. The carrier concentration and mobility versus annealing temperature are shown in figure 4.19 (b) and (c). The mobility increases with the annealing temperature and has maximum value at 450 ˚C. This shows 450 ˚C is the optimum temperature for post annealing to prepare more conductive NTO thin films. In highly

doped films electron scattering may be the possible reason for higher resistivity and lesser mobility at high temperatures.

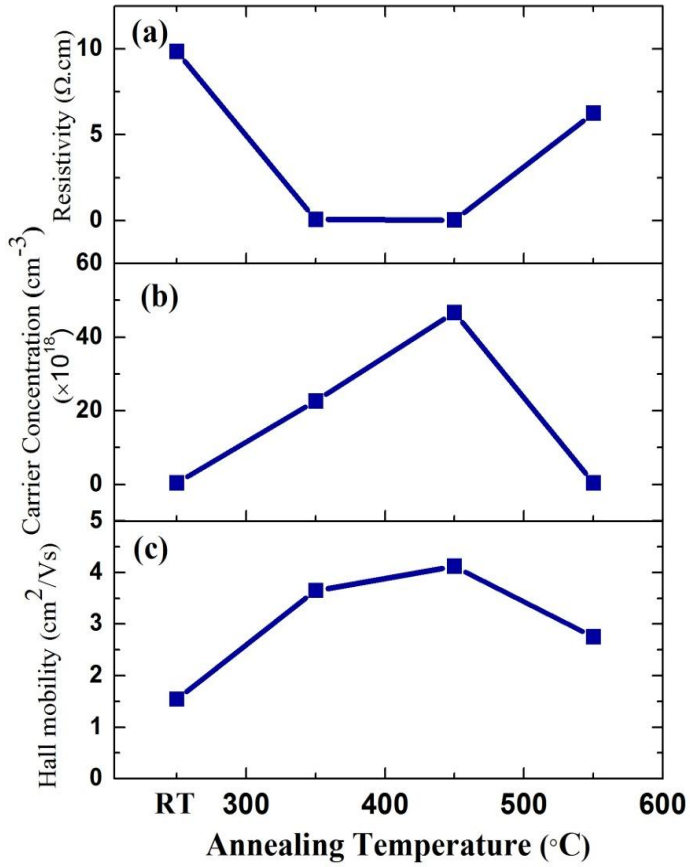

Figure 4.19: (a) Resistivity, (b) carrier concentration and (c) Hall mobility of NTO films as function of annealing temperature.

4.7 Conclusion

NTO thin films were fabricated on glass substrates with varying Nb content (0−2 at. %) using sol-gel spin coating method. Annealing of as deposited amorphous films at 550 ˚C in air led to good crystallinity and increase in electrical conduction. The average particle size calculated using Scherrer formula came out to be 15 nm. The resistivity decreased with increase in Nb and minimum resistivity of 3.56 Ω cm was observed at 2 at. % Nb. The films exhibited good transparency; 70-85% in the visible range. The films were smooth having very small value of roughness and became smoother with greater Nb content. XPS analysis showed appearance of Ti^{3+} peak at 457 eV in doped films, leading to band gap narrowing and decrement in electrical

resistivity. HRTEM investigations confirmed the high crystallinity of TiO_2 and elemental mapping exhibit presence of Nb in NTO films. It can be concluded that such low cost sol-gel deposited NTO thin films have a good scope to be used for TCO applications.

$Ti_{0.97}Nb_{0.03}O_2$ thin films prepared by rf sputtering were investigated for effect of post deposition annealing on the electrical and optical properties of the films. The films deposited on glass substrates were annealed in the temperature range 350 – 550 ˚C. Annealing led to decrease in resistivity by two orders. The pristine film had a high resistivity of 9.8 Ω.cm decreasing to 3.2×10^{-2} Ω cm on annealing at 450 ˚C. However the resistivity of the samples increased on annealing at 550 ˚C. Hence it can be concluded that 450 ˚C is the optimum annealing temperature for these films to enhance their conductivity. Deposited NTO films possess good transparency with an average transparency of 75% in the visible region. The optical properties are slightly degraded on annealing, as the transmittance decreases to ~70%. The maximum surface roughness of the films below 5 nm makes them highly suitable for TCO applications.

Chapter-5

Fabrication and Characterization of TiO_2-Ag-TiO_2 Multilayer Thin Films and Their Ion Implantation Effects

5.1 Introduction

This chapter reports the fabrication and characterization of highly conductive and transparent TiO_2/Ag/TiO_2 (referred hereafter as TAT) multilayer films fabricated by sputtering on glass substrates at room temperature. To start with, the thickness of bottom and top TiO_2 layers was varied from 25 to 65 nm to obtain optimized thickness values of the three layers (45 nm/9nm/45 nm) for maximum figure of merit. At 9 nm thickness the embedded Ag layer became continuous as reflected from good electrical conduction. These optimized multilayer films were implanted with the N^+ and Ar^+ ions to investigate ion implantation effects on film properties. In ion implantation process, one can implant specific ions in host material at the desired depth by selecting suitable energy. The range of ions depends on the ion species, mass and energy and the target material composition. Depending upon these parameters, the mechanism of modification of the physical and chemical properties of solids differs. Generally, the interest of implantation is to engineer the structural, optical and electrical properties of the materials by choosing proper ions [126]. Out of the various techniques used for modifying the basic properties of the materials; ion implantation has been found to effective and useful for defect production and impurity doping in materials to tune their properties for desired application [126,210]. Ion implantation or irradiation method influences the lattice structure of metal oxides and also affects the optical properties and electronic structures.

5.2 Experimental details

TiO_2 powder (Alfa-Aesar, 99.99% purity) was used for target preparation. This powder was pressed into 2-inch pellet and then sintered at 1100 ˚C for 10 hrs to get better structural stability for film deposition. Commercial Ag target (99.99% purity) was used for Ag film deposition. Glass substrates of $1\times1cm^2$ were cleaned using standard cleaning

processes. Before deposition, TiO_2 and Ag targets were pre-sputtered for 15 minutes to remove contaminants. RF source for oxide layers and DC source for metal layer deposition were used in TAT structure preparation using sputtering method at 100 W and 16 W with 15 sccm Ar flow, respectively. The TiO_2/Ag/TiO_2 structure was sequentially prepared at room temperature on glass substrates without any vacuum break. The base pressure of the chamber was ~5×10^{-6} mbar and working pressure during TiO_2 deposition was ~6×10^{-3} mbar and ~1.6×10^{-2} mbar for Ag layer. The TiO_2/Ag/TiO_2 multilayer structures were consecutively deposited on cleaned glass substrates. The top and bottom TiO_2 layer thickness were varied from 25 nm to 65 nm to obtain the optimum thickness for maximum figure of merit. The thickness of Ag layer was kept constant at ~9 nm. The optimized as-deposited TAT films were implanted with 40 keV N^+ and 100 keV Ar^+ ions with varying fluences at room temperature using the low energy ion beam facility at the Inter-University Accelerator Centre (IUAC), New Delhi, India.

The crystal structure of the TAT multilayer films was investigated by using an X-Ray Diffractometer (Panalytical X-Pert Pro) with CuKα radiation. Rutherford Backscattering Spectrometry (RBS) was performed using 1.7 MV tandem accelerator facility with 2 MeV He^+ ions at scattering angle of 165^o at IUAC, New Delhi for thickness and compositional studies. The morphology and topography of the films were imaged from Nova Nano FE-SEM 450 (FEI) and atomic force microscopy done by Multimode Scanning Probe Microscope (Bruker). Optical transmittance and absorbance were measured using LAMBDA 750 (Perkin Elmer) UV-Vis-NIR Spectrophotometer. Carrier concentration, carrier mobility and resistivity of TAT multilayer films were measured by HMS3000, Ecopia using a magnetic field of 0.57 T. Sheet resistance was evaluated using the four-point-probe technique. Composition, valence and chemical states of TAT films were analyzed by the X-ray photoelectron spectroscopy (XPS, Omicron ESCA). For XPS measurement monochromatic Al K_α (1486.7 eV) source with a mean radius of 124 mm was used and monochromatic X-ray resolution as confirmed by FWHM was 0.6 eV. The vacuum pressure of the chamber was ~ 4×10^{-10} mbar.

5.3 Optimization of TiO_2 thickness

The TAT films were deposited by sputtering method on glass substrates. The thickness of top and bottom TiO_2 films was varied from 25 to 65 nm and then an optimized thickness was obtained for maximum figure of merit. The thickness of middle metal layer was kept constant at ~9 nm forming a continuous film. Figure 5.1 (a) shows the XRD pattern of TAT multilayer films with varying TiO_2 thickness. Peaks observed at 38.18˚, 44.28˚, 64.62˚ and 77.51˚ are assigned to Ag (111) (200), (220) and (311) diffraction planes (JCPDS No. 04-0783). Figure 5.1 (b) exhibits the optical transmittance of TAT multilayer films for different TiO_2 thickness in the visible region (350 nm<λ<800 nm). The transmittance values for TiO_2 thickness of 25, 35, 45, 55 and 65 nm were obtained as 75%, 78%, 80%, 76% and 74%, respectively. The highest transmittance of ~80% was obtained for the 45 nm thick TiO_2. For thinner TiO_2 layer the transmittance is low because of the strong light reflection caused by Ag layer and the thicker TiO_2 layer absorbs more light intensity, leading to a decrease in the transmittance of TAT multilayer films. Hence, TAT multilayer films with (~45 nm/~9 nm/~45 nm) show the desirable optical results.

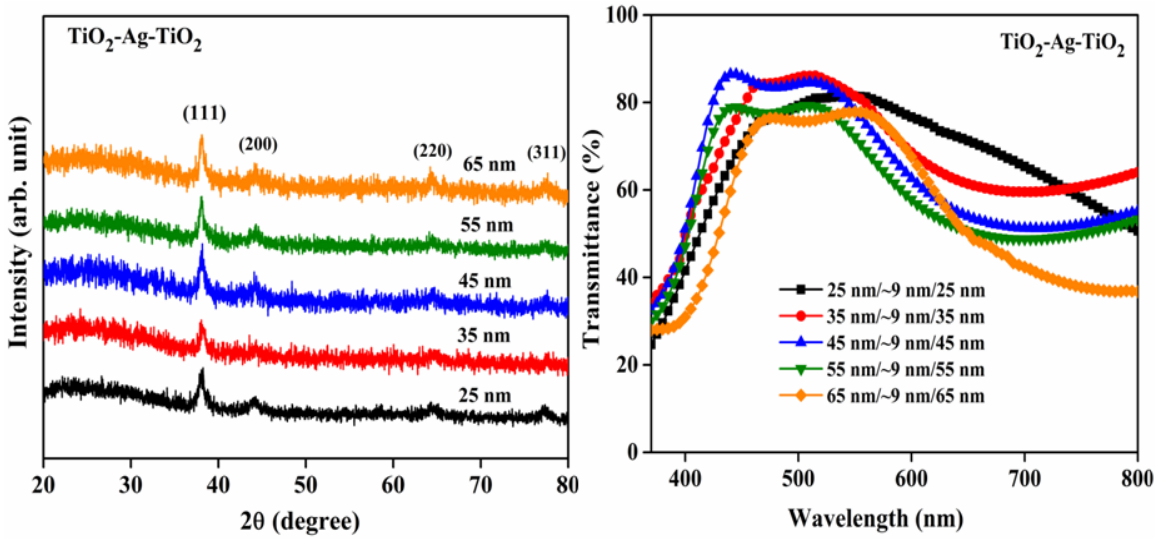

Figure 5.1: (a) XRD pattern and (b) Transmittance spectra of TAT multilayer films with different TiO_2 thickness.

Figure 5.2 (a) exhibits the electrical resistivity, carrier mobility and carrier concentration of TAT multilayer films for different TiO_2 thickness. Resistivity of 25 nm thick TiO_2 was obtained as 1.76×10^{-4} Ω cm, which becomes 3.85×10^{-4} Ω cm with increasing TiO_2 layer

thickness. Figure 5.2 (b) shows the sheet resistance and Haacke figure of merit of TAT films as a function of TiO_2 layer thickness. The sheet resistance increased from 17.6 Ω/□ to 38.6 Ω/□ with increasing TiO_2 thickness. Ideally, both electrical conductivity and optical transmittance should be as high as possible for a TCE. The figure of merit is used as a tool to evaluate the performance of TCE. Haacke figure of merit (FOM) of the specimen [76] has been calculated using the following formula.

$$\Psi_{TC} = \frac{T_{av}{}^{10}}{R_s} \tag{5.1}$$

FOM for 25 nm thick TiO_2 layer was obtained as 4.1×10^{-3} Ω^{-1}, which is increased to 5.2×10^{-3} Ω^{-1} for 45 nm thick TiO_2, and reduced to 1.1×10^{-3} Ω^{-1} 65 nm thickness. The multilayer structure of TiO_2/Ag/TiO_2 (45 nm/9 nm/45 nm) gives the maximum figure of merit and hence was used for further modification.

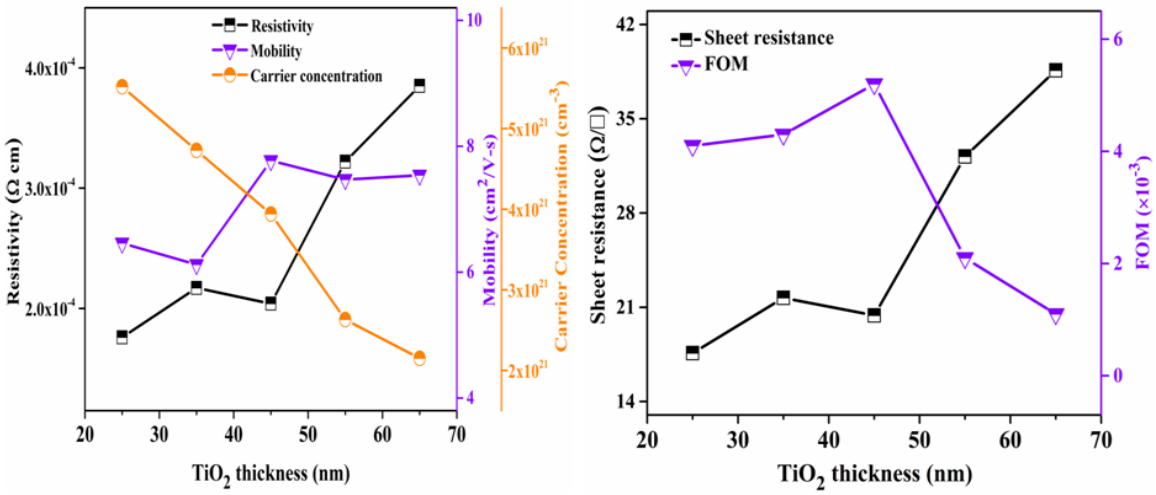

Figure 5.2: (a) Resistivity, mobility and carrier concentration and (b) Sheet resistance and Haacke figure of TAT multilayer films with different TiO_2 thickness.

5.4 N^+ (40 keV) Ion Implantation in TiO_2/Ag/TiO_2 Multilayer Thin Films

The optimized pristine TAT (45 nm/9 nm/45 nm) films were implanted with 40 keV N^+ ions for different fluences (1×10^{14}, 5×10^{14}, 1×10^{15}, 5×10^{15} and 1×10^{16} ions/cm^2). The objective of this study was to investigate the effect of N^+ implantation on the optical and electrical properties of TAT multilayer films. Ion doping is a unique method to restore the vacant oxygen sites in a TiO_2 lattice, and N-ion was taken as a particular choice [211]. It was reported that ion-doped in TiO_2 causes band bending due to an alteration in electron

concentration via charge transfer between a dopant and conduction band or valence band [212]. In N-doped TiO_2, new energy states are introduced above the valence band of the TiO_2, by increasing the electron density [213]. According to Asahi *et al.* [211] doping of N into TiO_2 contributes to band gap narrowing to provide visible-light response. The nuclear energy loss (S_n) and electronic energy loss (S_e) values for 40 keV N^+ ions were obtained as 20.13 and 13.3 eV/Å respectively; as calculated by the SRIM-2010 software. These values show that entire passage of these ions in the film is dominated by nuclear energy loss. The stopping range of N^+ ions was 60 nm, which is less than the film thickness (100 nm) thus implanting the ions in the film. Figure 5.3 shows the schematic process of nitrogen ion implantation in the TAT multilayer films.

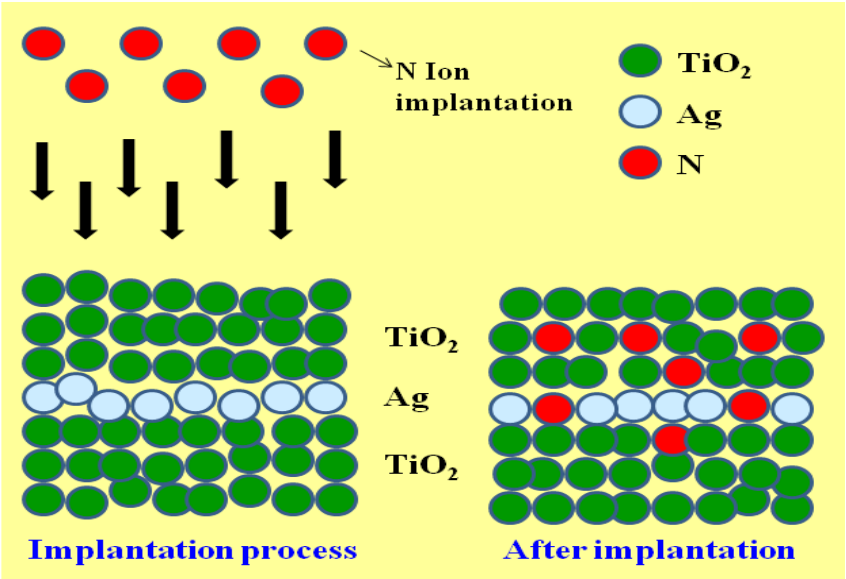

Figure 5.3: Schematic showing the fabrication of nitrogen ion implanted TAT multilayer film.

5.5 Results and discussion

5.5.1 Structural Properties

The X-ray diffraction (XRD) pattern of the pristine and implanted $TiO_2/Ag/TiO_2$ multilayer films for different fluence is shown in figure 5.4. The absence of any peak for TiO_2 shows its amorphous behavior which is expected because the deposition was done at room temperature. Peaks at $2\theta = 38.15^\circ$, 44.3°, 64.6° and 77.5°, are assigned to the (111), (200), (220) and (311) planes of Ag (JCPDS No. 04-0783) respectively. On implantation, the intensity of the Ag (111) peak slightly increased with the ion fluences. The slight

improvement in crystallinity of Ag is caused by annealing of TAT films during implantation process. Ion implantation produces the stress in the TAT multilayer system and consequently crystallite size changes. FWHM, crystallite size, residual stress and lattice constant have been calculated for pristine and N^+ ion implanted films and are shown in table 5.1.

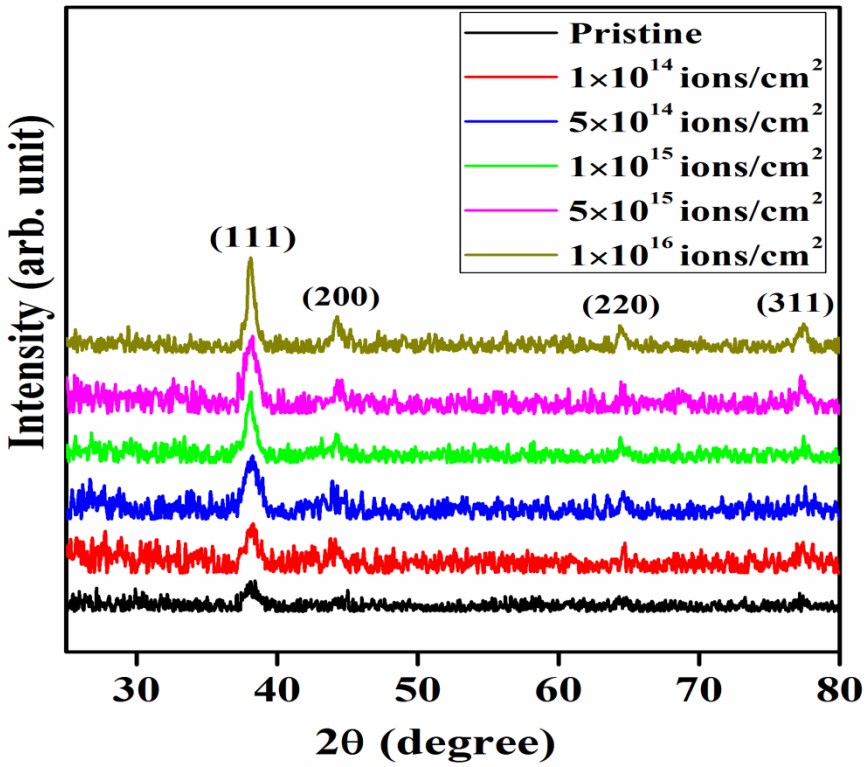

Figure 5.4: XRD pattern of pristine and N^+ ion implanted films of TAT.

Table 5.1: FWHM, crystallite size, stress and lattice constants of pristine and N^+ ion implanted TAT films.

S. No.	Fluence (ion cm^{-2})	FWHM	Crystallite size (nm)	Residual Stress	Lattice constant c (Å)
1	0	0.6605	13.3	-0.401	4.093
2	1×10^{14}	0.5144	16.9	-0.627	4.097
3	5×10^{14}	0.6318	13.9	-0.741	4.099
4	1×10^{15}	0.5401	16.3	-0.171	4.089
5	5×10^{15}	0.6116	14.4	-0.285	4.091
6	1×10^{16}	0.5188	16.8	-0.228	4.090

5.5.2 Rutherford Backscattering Spectrometry

The RBS measurement was carried out to determine the thickness and stoichiometry of TAT multilayer films. Figure 5.5 shows the RBS spectrum along with the SIMNRA-fitted

profile of TiO_2/Ag/TiO_2 multilayer structure. This spectra show the elemental peaks corresponding to Ti, O and Ag ions. The thickness of the each layer was measured using fitted curve and obtained as TiO_2 (45±5 nm)/Ag (9±1 nm)/TiO_2 (45±5 nm). RBS results clearly show the formation of TiO_2 with pure Ag layer as middle layer and are consistent with the XPS data discussed in next section.

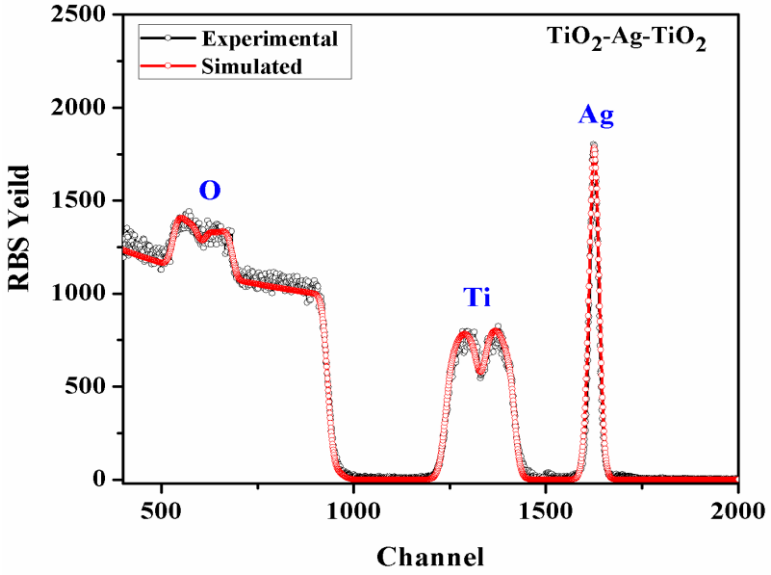

Figure 5.5: RBS spectrum of TAT multilayer structure with fitted profile.

5.5.3 X-ray Photoelectron Spectroscopy

Figure 5.6 shows the XPS spectra of TiO_2/Ag/TiO_2 pristine and N^+ ion implanted (fluence of 1×10^{16} ions/cm^2) films (N−TAT). Typical survey scans of TAT pristine and N−TAT films are shown in Figure 5.6 (a). Survey scans of pristine film and N^+ ion implanted films consist of dominant signals from Ti, and O and a weak signal from C, which may be due to ex-situ process of the sample transfer to UHV chamber and a small N signal for N−TAT films. Figure 5.6 (b) shows the Ti 2p core level spectra of top surfaces of the TAT pristine and N−TAT films. The pristine sample exhibits peaks of Ti-$2p_{3/2}$ and Ti-$2p_{1/2}$ at 458.9 and 464.6 eV attributed to Ti^{4+} oxidation state of TiO_2 which is consistent with reported data in literature [203]. The difference between the binding energies of Ti-$2p_{1/2}$ and Ti-$2p_{3/2}$ peak is 5.7 eV, which is also in good agreement with +4 oxidation state of Ti [200,201]. However, peaks due to Ti-$2p_{3/2}$ and Ti-$2p_{1/2}$ core levels of the N−TAT sample appear at 458.3 and 464 eV, respectively indicating change in the binding energy difference after nitrogen implantation. A shift in binding energy of Ti 2p occurs due to

different electronic interaction behavior of Ti with the anions for pure and N-doped TiO_2. N doping induces a significant modification in TiO_2 matrix possibly produced by dopant-induced strain. A shift towards lower side in binding energy of Ti 2p in N-doped TiO_2 is attributed to the improvement in covalent behavior of the bond between Ti and N [214]. These results are in good agreement with previous reports [215,216].

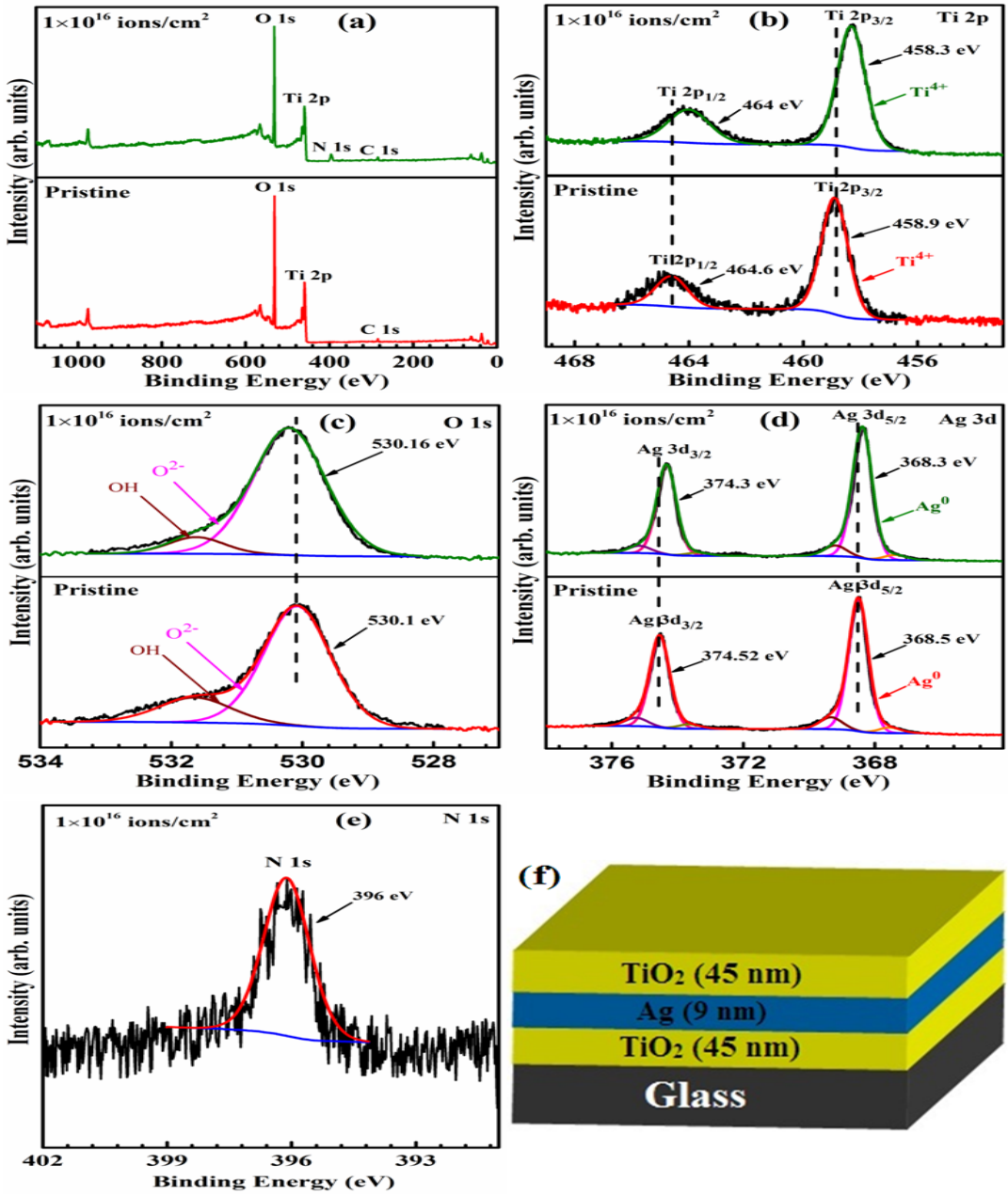

Figure 5.6: XPS spectra of pristine and 1×10^{16} ions/cm^2 implanted films of TAT (a) survey scan, (b) Ti 2p, (c) O 1s, (d) Ag 3d, (e) N 1s and (f) schematic diagram of TAT film.

Figure 5.6 (c) show the high-resolution O 1s core spectra of TAT and N-TAT samples. The O 1s signal of TAT samples appears at 530.1 eV, and on deconvolution, another peak resulted at 531.6 eV which is assigned to OH groups present on the surface. The O 1s spectra of N-TAT sample appear at 530.16 eV, and another peak is at 531.7 eV corresponding to OH species present on the surface of the sample. In both these samples, the O 1s peak appears at the same place indicating the nature of oxygen to be similar. Figure 5.6 (e) shows the N 1s spectra for the TAT films implanted with the fluence of 1×10^{16} ions/cm^2. It can be seen that there is a peak for N at 396 eV. The N 1s peak appearing at 396 eV is attributed to N substituting O sites of TiO_2 lattice [217]. This peak at 396 eV has been identified as the atomic β-N states by Saha *et al.* [218]. In order to determine chemical state of middle Ag layer, the depth profile mode of XPS has been used. The core level spectra of Ag of TAT pristine exhibits two peaks of Ag $3d_{5/2}$ and Ag $3d_{3/2}$ located at 368.5 and 374.52 eV binding energies respectively, indicating presence of metallic Ag^0 in TAT pristine films. Upon introduction of N in TAT sample, new peaks of Ag $3d_{3/2}$ and Ag $3d_{5/2}$ appear with binding energies of 368.3 and 374.3 eV. A shift to lower binding energy in Ag 3d was observed from the position of Ag $3d_{5/2}$ (368.5 eV) and Ag $3d_{3/2}$ (374.52 eV); may be due to the presence of Ag at the interface and interaction with Ti and O ions [219]. Figures 5.6 (a) – (e) indicate incorporation of N in TiO_2 and are suggestive of replacement of O by N ions in the TiO_2 lattice. Substitutional N ions would add electronic states above the valence band edge of TiO_2. The additional electronic states would be responsible for the band gap narrowing, resulting in reduction of electrical resistivity giving a high figure of merit (FOM) for N−TAT sample.

5.5.4 Surface characterization

Figure 5.7 (a) – (f) shows the surface FESEM images of top layer of TiO_2/Ag/TiO_2 multilayer films as a function of ion fluences ranging from 1×10^{14} to 1×10^{16} ions/cm^2. All images were taken at the 100k× magnification. It can observe that the surface morphology of the as-grown TiO_2 film and implanted films is compact and uniform. All images demonstrate a flat surface composed of regular round grain structure with TiO_2 nanoparticles of size 20–40 nm. Similar images of TiO_2 have been reported by other researchers [104]. Figure 5.7 (h) shows the FE-SEM cross sectional image of TAT multilayer structure and each TiO_2 and Ag layer is distinctly visible. The ~10 nm Ag is

embedded between the upper TiO_2 layer (~50 nm) and lower TiO_2 layer (~50 nm). The TiO_2 and Ag layers are seen as smooth and continuous in the deposited films.

Figure 5.8 shows the surface morphology of the TAT multilayer films with varying fluences as observed by the AFM in a scanning area of 1×1 μm^2. Root mean square (rms) roughness of the TAT films as a function of ion fluence is shown in figure 5.9 (a). The rms roughness of the pristine specimen and with ion fluences of 1×10^{14}, 5×10^{14}, 1×10^{15}, 5×10^{15} and 1×10^{16} ions/cm^2 are found to be 1.71, 2.34, 1.94, 1.68, 1.52 and 1.25 nm respectively.

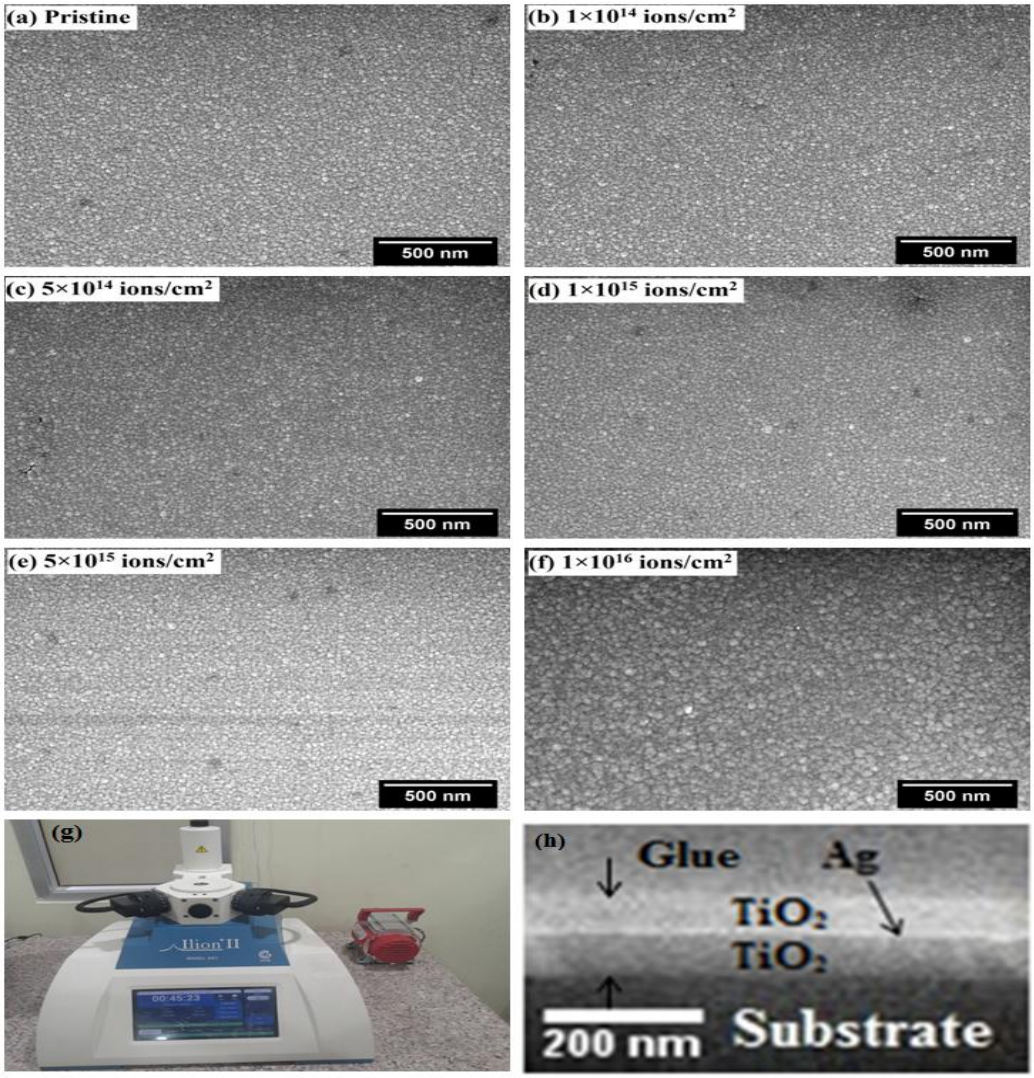

Figure 5.7: (a)–(e) SEM images of the pristine and N^+ ion implanted films of TAT, (g) sample polishing machine, Ilion II and (h) cross-sectional FE-SEM image of TAT multilayer film.

The average roughness of the pristine film is 1.71 nm and increases to 2.34 nm at N^+ ion implantation fluence of 1×10^{14} ions/cm^2. Further increase in ion fluence results in a decrease of average surface roughness to a minimum value of 1.25 nm for highest fluence 1×10^{16} ions/cm^2. Increase in surface roughness for 1×10^{14} fluence implanted sample could be understood in terms of sputtering/etching process during implantation process [220]. High energy N^+ ions used in implantation process etch the surface of the film, deteriorating the surface causing damage to the surface. For further increasing in the N^+ ion fluences, the surface became smoother because the film subjected to higher fluence leads to erosion of existing microstructures on the surface [221]. Figure 5.9 (a) represents the roughness variation with fluence and figure 5.9 (b) and (c) shows the depth histogram of TAT pristine and highest implanted films.

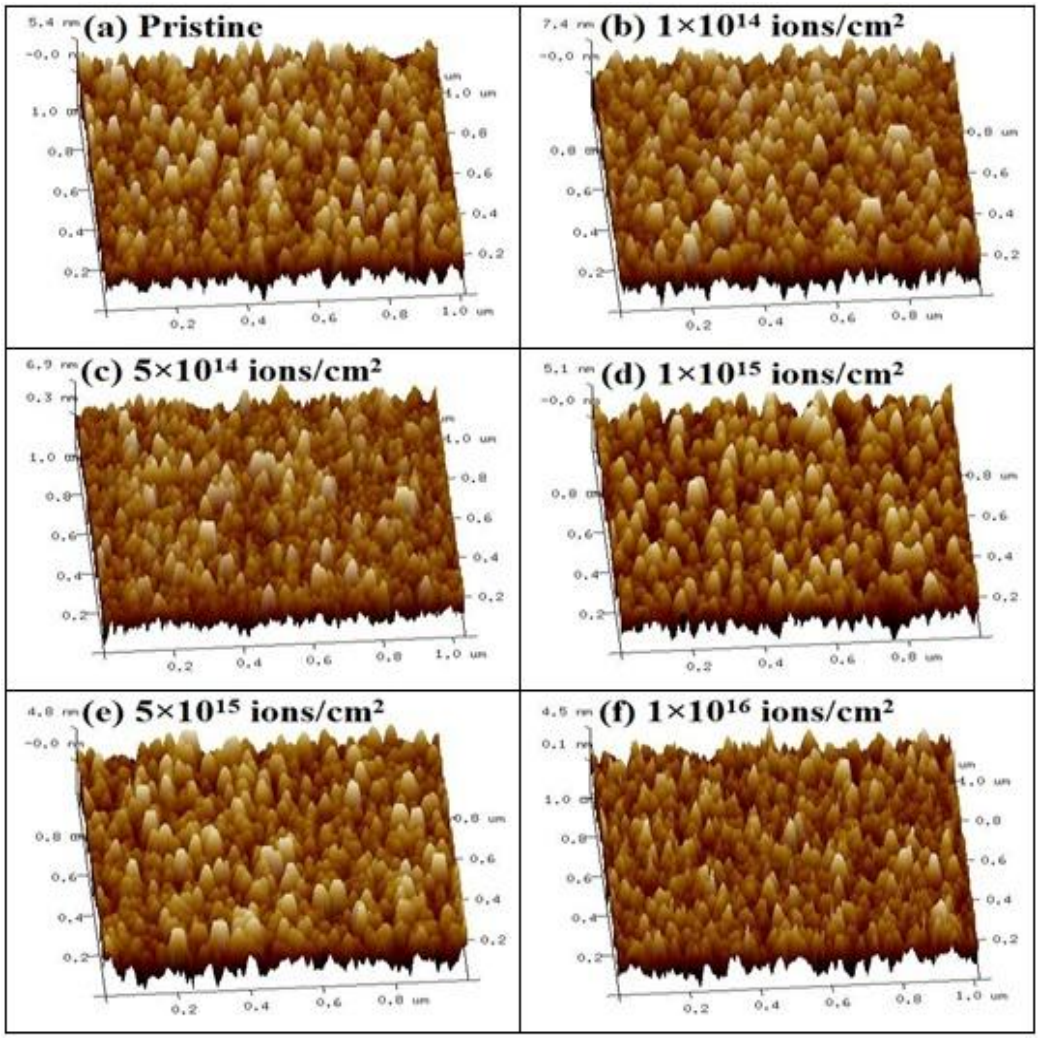

Figure 5.8: Three-dimensional AFM images of pristine and N^+ ion implanted TAT films.

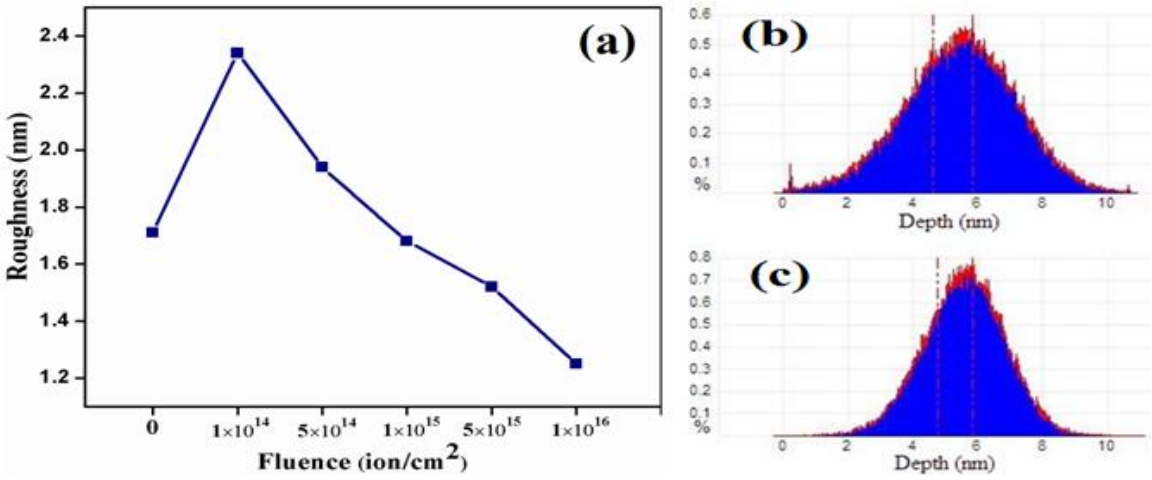

Figure 5.9: (a) Root mean square roughness of pristine and implanted films of TAT, (b) depth histogram of TAT pristine and (c) depth histogram of TAT- N^+ ion implanted films with fluence of 1×10^{16} ions/cm^2.

5.5.5 Optical analysis

Figure 5.10 (a) and (b) show the optical transmittance and absorbance spectra of TAT multilayer films as a function of wavelength in the visible region (400 nm<λ<800 nm) for different ion fluence. Optical transmittance of the pristine and N^+ ion implanted TAT films increases with wavelength initially, reaches a maximum value around 530 nm and then gradually decreases with increasing wavelength. Pristine sample exhibits an average transmittance of ~80% which reduces to ~70% for the implanted films as the ion fluence increases. Figure 5.10 (b) depicts the absorbance of the TAT films. It can be observed from the graph that all films show high absorbance for shorter wavelength (λ< 400 nm) and a low absorbance for longer wavelengths (λ> 400 nm). Ion implantation leads to band gap narrowing of the films which increases the absorbance, and consequently, the transmittance is decreasing. It is observed that transmittance and absorbance spectra of a TAT film exhibit an inverse relationship.

The optical band gap of the TAT films has been calculated using the standard expression [196].

$$\alpha h\nu = B(h\nu - E_g)^n \qquad (5.2)$$

Where hν the photon energy, Eg is optical band gap, α is absorption coefficient and B is a constant. The value of n is taken as 2, accounts for the fact that TiO_2 has indirect band gap transition mechanism.

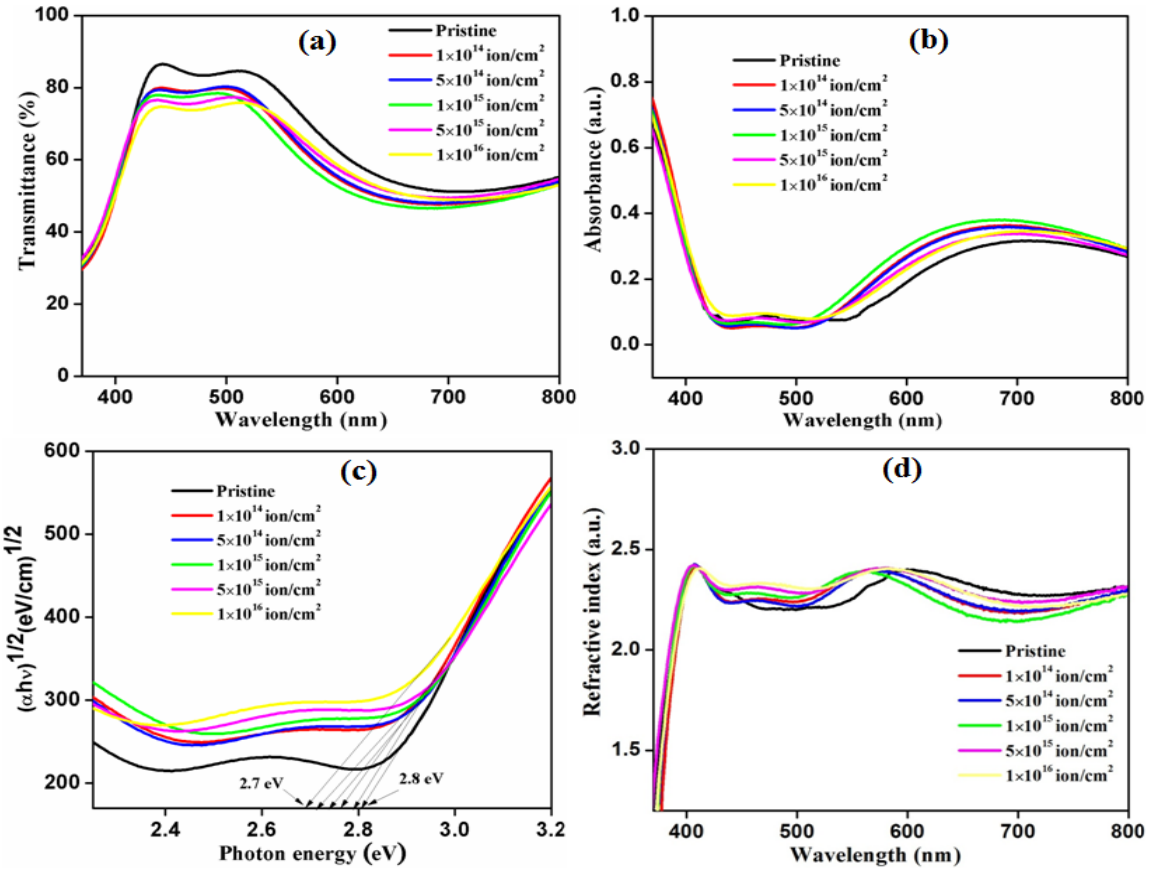

Figure 5.10: Pristine and implanted films of TAT: (a) Transmittance, (b) Absorbance, (c) Tauc plot and (d) refractive index.

Absorption coefficient (α) has been calculated using the Beer–Lambert's law [222].

$$\alpha = \frac{1}{d}\ln\frac{1}{T} = \frac{2.303}{d}A \qquad (5.3)$$

Where d is thickness of the multilayer structure, T is transmittance, and A is absorbance of TAT film. Figure 5.10 (c) shows the Tauc plot between photon energy (hν) and $(\alpha h\nu)^{1/2}$ for the TAT films; a band gap of 2.8 eV is obtained for the pristine film by the intersection of the fitted straight line and the abscissa. The band gap of the samples decreases as the fluence increases and attains a minimum value of 2.7 eV for the fluence of 1×10^{16} ions/cm^2. The band gap reduction of the TAT films suggests that N ions occupy

some of the oxygen positions in the lattice. Asahi *et al.* [211] reported that in N-doped TiO_2 film, substitutional doping with N provided an effective band-gap reduction mechanism. These authors explained it by mixing of 2p states of N with O 2p states, which causes band-gap reduction.

Refractive index is a fundamental parameter for optical materials, which regulate the antireflective effect, packing densities and transmittance property of the TCO materials. The refractive index can be calculated using the following formula [223].

$$n = \sqrt{\frac{4R}{(1-R^2)} - k^2} + \left(\frac{1+R}{1-R}\right) \quad (5.4)$$

Where R is reflectivity of the film and k is the extinction coefficient defined as-

$$k = \frac{\alpha\lambda}{4\pi} \quad (5.5)$$

Where α is absorption coefficient and λ is wavelength. Figure 5.10 (d) shows the refractive index of the TAT films. The refractive index of the pristine and implanted films with ion fluences of 1×10^{14}, 5×10^{14}, 1×10^{15}, 5×10^{15} and 1×10^{16} ions/cm^2 are estimated as 2.27, 2.25, 2.26, 2.25, 2.3 and 2.28, respectively. The RMS surface roughness, transmittance, refractive index, extinction coefficient and band gap have been calculated for pristine and implanted TAT films and are shown in table 5.2.

Table 5.2: RMS surface roughness, transmittance, refractive index, extinction coefficient and the band gap of pristine and implanted TAT films as a function of ion fluence.

S. No.	Fluence (ion cm^{-2})	RMS (nm)	Transmittance (%) at 530 nm	Refractive index (n)	Extinction coefficient (k)	Band gap (eV)
1	0	1.71	81	2.27	0.245	2.80
2	1×10^{14}	2.34	75	2.25	0.282	2.79
3	5×10^{14}	1.94	76	2.26	0.278	2.76
4	1×10^{15}	1.68	72	2.25	0.292	2.74
5	5×10^{15}	1.52	74	2.3	0.271	2.72
6	1×10^{16}	1.25	75	2.28	0.277	2.70

5.5.6 Electrical analysis

Figure 5.11 shows the carrier concentration and Hall mobility of the TAT multilayer films as a function of fluence. The pristine TAT carrier concentration is 3.9×10^{21} cm^{-3}, which increases to 7.06×10^{21} cm^{-3} as the fluence increases to 1×10^{16} ions/cm^2. Mobility also increases from 7.8 to 9.2 cm^2/V-s as fluence increases from 0 to 1×10^{16} ions/cm^2. Figure

5.12 shows the electrical resistivity and sheet resistance of the TAT multilayer films as a function of ion fluence. Electrical resistivity for the pristine sample was 2.04×10^{-4} Ω cm, and it minimized to 9.62×10^{-5} Ω cm for the highest fluence of 1×10^{16} ions/cm^2, which is lower than the resistivity of ITO films (31.2×10^{-4} Ω cm) studied by Lee *et al.* [224]. On the other hand, the sheet resistance decreases 20.4 Ω/□ to 9.6 Ω/□ as ion fluence increases from 0 to 1×10^{16} ions/cm^2. The reduction in resistivity to 9.62×10^{-5} Ω cm at 1×10^{16} ions/cm^2 fluence indicates that nitrogen is replacing the O sites of TiO_2. The substitutional N ion would add the new electronic states above the valence band edge of a pure TiO_2. The additional electronic states would be responsible for the band gap reduction as shown in figure 5.10 (c) giving less resistivity. Apart from occupying electrically active lattice sites, ion implantation in metal oxides is known to create or anneal the defects and thus lead to change in resistivity [133,225,226]. The resistivity (ρ) of TiO_2 can be tuned by ion implantation [133,225]. In the present study, N implantation and annealing of oxygen vacancies may be responsible for decrease in the resistivity. In addition, this results in decrease in band gap and change in microstructure. The increasing grain size with ion fluence causes low grain boundary. This reduces the scattering of charge carriers in crystal [226]. Consequently, the mobility and carrier concentration further increased and leads to reduction in electrical resistivity. XPS analysis of N 1s and Ti 2p spectra also revealed that substitutional N^+ ions into the TiO_2 lattice results in new electronic states just above the valence band which is responsible for the narrowing of band gap and the enhancement in electrical conductivity. The variation in electrical resistivity with the N^+ implantation can be understood by the following relation:

$$\rho = \frac{1}{n_e \mu e} \tag{5.6}$$

Where ρ is resistivity, μ is the mobility, n_e is carrier concentration and e is charge on the carrier. The resistivity is slightly decreasing up to the ion fluence 5×10^{15} ions/cm^2 due to a small variation of mobility and carrier concentration up to that fluence, but for the ion fluence 1×10^{16} ions/cm^{2,} a large decrement in resistivity is observed, dominated by large variation in carrier concentration. The total resistance of this multilayer configuration is found by considering a parallel combination of resistances of the three consecutive layers of the film.

$$\frac{1}{R_{total}} = \frac{1}{R_{metal}} + \frac{2}{R_{oxide}}$$

since $R_{oxide} \approx 1000R_{metal}$

so $R_{total} \approx R_{metal}$

The resistance of Ag (R_{Ag}) is very low compared to the oxide resistance, the total resistance of stacked multilayer would have a resistance nearly equal to that of Ag. Therefore the high conductivity of the TAT multilayer films is especially because of embedded Ag layer. A continuous film of Ag is required for good electrical conduction as below a critical film thickness the resistivity of the film suddenly increases due to aggregated state or islands of metal atoms [227]. The obtained results of electrical resistivity and sheet resistance of all TAT films indicate the formation of continuous metal inter layer. The figure of merit (FOM) is a significant factor that relates the sheet resistance and transmittance. Figure of merit (Ψ_{TC}) given by Haacke [76] is as follows-

$$\Psi_{TC} = \frac{T_{av}{}^{10}}{R_s} \quad (5.7)$$

where T_{av} is average transmittance and R_s is the sheet resistance.

Table 5.3: Carrier concentration, mobility, resistivity, sheet resistance, and Haacke FOM of pristine and N^+ ion implanted TAT films.

S. No.	Fluence (ion cm^{-2})	Carrier concentration (cm^{-3})	Mobility (cm^2/V-s)	Resistivity (Ω.cm)	Sheet resistance (Ω/□)	Haacke FOM (10^{-3} Ω^{-1})
1	0	3.94×10^{21}	7.77	2.04×10^{-4}	20.4	5.2
2	1×10^{14}	4.34×10^{21}	6.79	2.12×10^{-4}	21.2	2.1
3	5×10^{14}	3.60×10^{21}	8.75	1.98×10^{-4}	19.81	2.5
4	1×10^{15}	4.40×10^{21}	8.15	1.74×10^{-4}	17.41	1.6
5	5×10^{15}	4.17×10^{21}	8.10	1.85×10^{-4}	18.48	2.3
6	1×10^{16}	7.06×10^{21}	9.20	9.62×10^{-5}	9.62	5.7

FOM (Ψ_{TC}) calculated for the TAT pristine and implanted films are shown in figure 5.13. Figure of merit calculated for the pristine film comes out to be 5.2×10^{-3} Ω^{-1}. FOM for the samples first decreases with increase in fluence and increases for higher fluence and attain a value of 5.7×10^{-3} Ω^{-1} for fluence of 1×10^{16} ions/cm^2. This change is a consequence of variation in transmittance and sheet resistance with the fluence. These values of FOM indicate the suitability of these TAT films to be used as a transparent conductive

electrode. The nuclear and electronic energy losses for N^+ ion implantation films are shown in the inset of figure 5.13. It can be observed from the graph that nuclear energy loss is dominant over the electronic energy loss. The carrier concentration, mobility, resistivity, sheet resistance and Haacke figure of merit (FOM) have been calculated for pristine and implanted TAT films and shown in table 5.3.

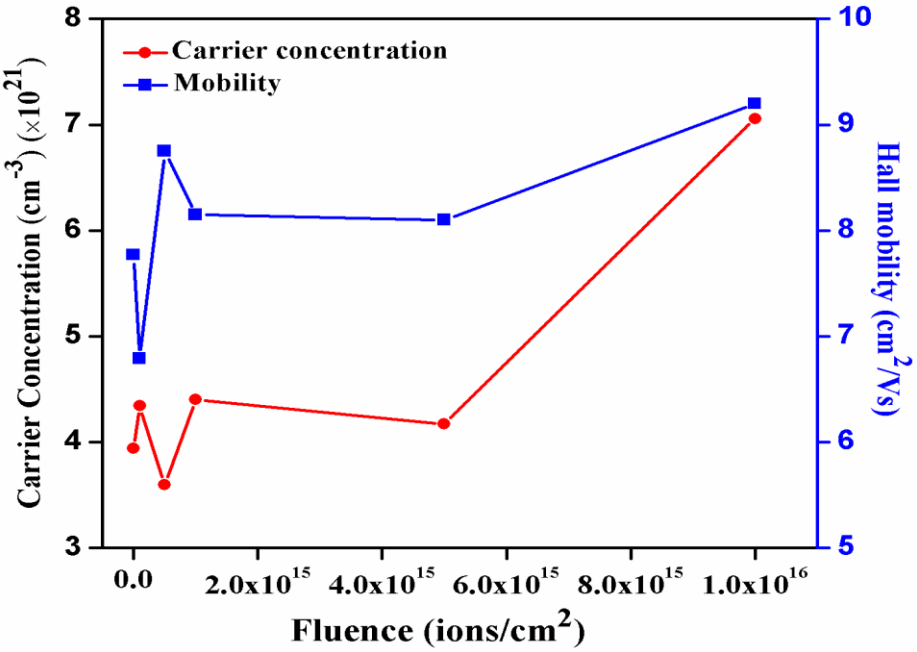

Figure 5.11: Carrier concentration and Hall mobility of pristine and N^+ ion implanted films of TAT.

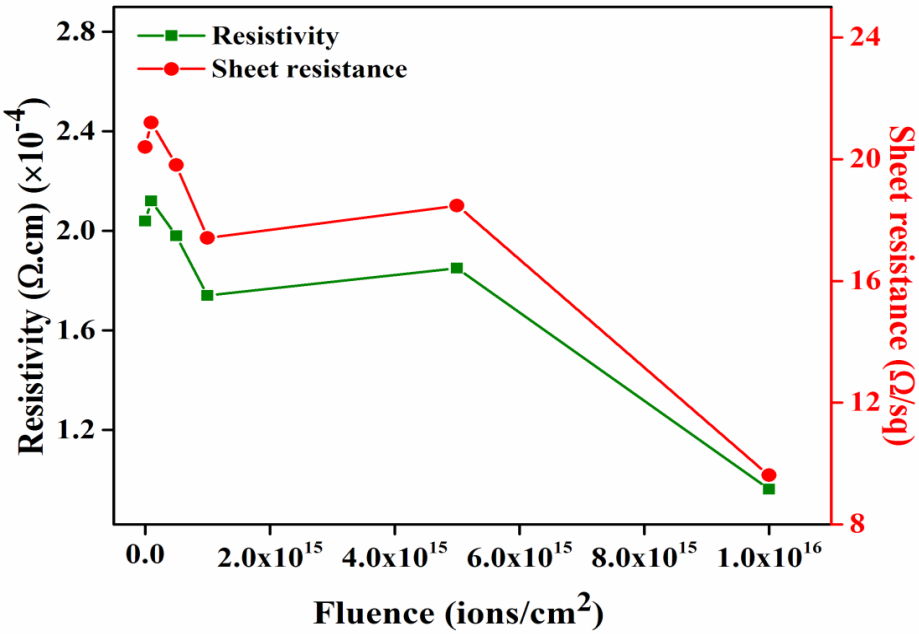

Figure 5.12: Resistivity (which is decreasing with increasing fluence) and sheet resistance of pristine and N^+ ion implanted films of TAT.

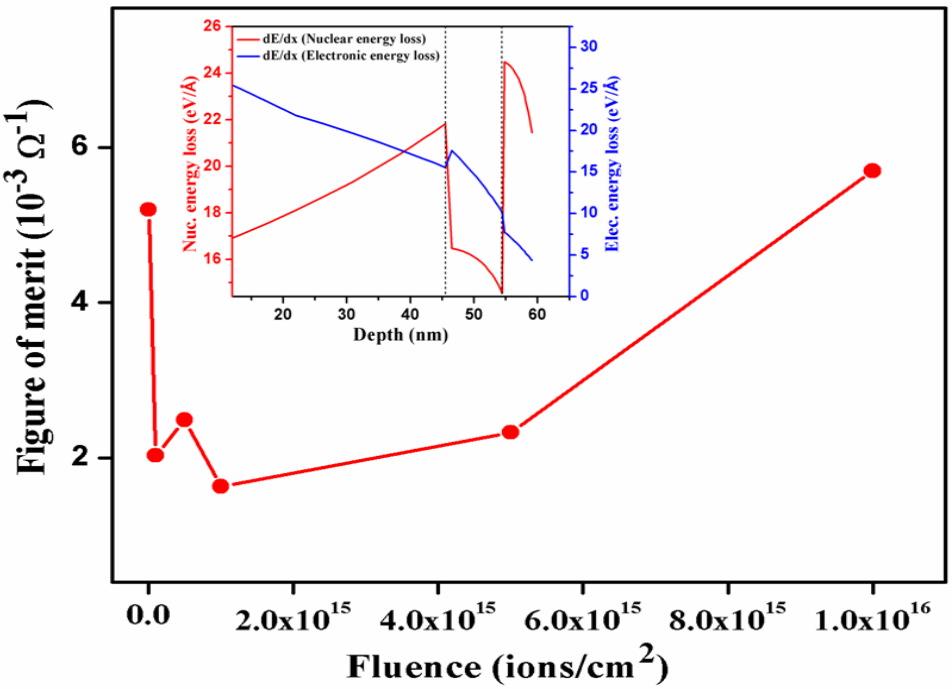

Figure 5.13: Haacke FOM (Ψ_{TC}) of pristine and N^+ ion implanted films of TAT. Inset shows the nuclear energy loss (S_n) and electronic energy loss (S_e) as a function of depth.

5.6 Ar^+ (100 keV) Ion Implantation in TiO_2/Ag/TiO_2 Multilayer Thin Films

The optimized as-prepared TAT (45 nm/9 nm/45 nm) films were implanted with 100 keV Ar^+ ions with fluence range (1×10^{14}– 1×10^{16} ions/cm^2) at room temperature. The Ar^+ implanted TAT multilayer films at 1×10^{16} ions/cm^2 fluence will be referred hereafter as A-TAT films. The objective of this study was to investigate the effect of 100 keV Ar^+ ion implantation on structural, electrical and optical properties of TiO_2/Ag/TiO_2 films. Ar is an inert gas and it does not make bonds with host material. However, Ar ions are most suitable for creating or annealing the defects mainly in form of oxygen vacancies that are responsible for modifying the electrical and optical properties. It has been reported that the Ar^+ ion implantation leads to large increase in electrical conductivity [128]. The stopping range of Ar^+ ions was ~60 nm measured by the SRIM-2010 software, which is less than the total film thickness (100 nm). The nuclear energy loss (S_n) and electronic energy loss (S_e) values for 100 keV Ar^+ ions were obtained as 1.65 and 1.03 eV/Å respectively.

5.7 Results and discussion

5.7.1 Structural Properties

Figure 5.14 shows the X-ray diffraction pattern of pristine and implanted TAT films. Peaks in the XRD pattern of pristine and implanted films match well with the JCPDS data (card no. 04-0783). The intensity of Ag (111), (200) and (220) positioned at 2θ = 38.15˚, 44.3˚ and 64.6˚ slightly varies with the fluence. No peak related to anatase TiO_2 was observed as TiO_2 is amorphous at room temperature deposition. The amorphous structure of metal oxides film makes them more suitable for deposition of these films on a flexible plastic substrate [228]. The intensity of the Ag (111) peak for the film implanted with the highest fluence of 1×10^{16} ions/cm^2 exhibits slight increment. The full width at half maximum FWHM (β) of this peak increases to 0.9106˚ at 1×10^{15} ions/cm^2 as fluence and then decreases to 0.6785˚ as the fluence increases. The crystallite size calculated using Debye–Scherrer formula decreases from 13.3 nm to 12.9 nm with increasing fluence. The lattice constant (*c*) and residual stress were calculated and are shown in table 5.4. The negative sign of obtained residual stress represent that stress for the TAT films is compressive.

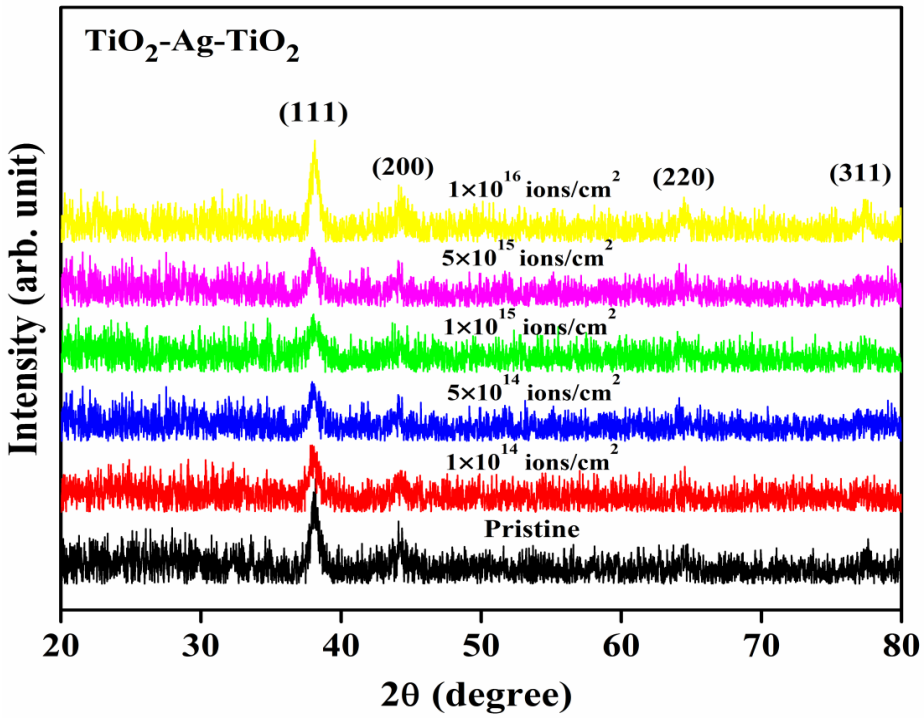

Figure 5.14: XRD pattern of pristine and Ar^+ ion implanted TiO_2/Ag/TiO_2 multilayer films with fluence.

The stress induced by implantation process hinders the growth of crystallites and it can be observed that as stress increases the crystallite size is decreasing and vice versa. Reports [229,230] indicate that Ar^+ ions can be used to control stress in the specimen. In our specimen, initial implantation of Ar^+ ions has generated stress which increases with increasing fluence up to 5×10^{14} ions/cm^2. On further increase of fluence, stress decreases. The decrement of stress in the TAT multilayer structure may be assigned to changes in microstructures induced by higher dose of Ar^+ ion implantation. Pienkos *et al.* [231] reported that structure changes, reduction of grain boundary voids and amorphization may influence the stress of the film. In present study, stress may also be reducing by reduction of grain boundary voids [232].

Table 5.4: FWHM, crystallite size, lattice constants and residual stress of pristine and Ar^+ implanted TAT multilayer films.

Fluence (ion cm^{-2})	FWHM (deg.) with error	Crystallite size (nm) with error	Lattice constant *c* (Å)	Residual Stress (GPa)
0	0.6605±0.03	13.3±0.6	4.093±0.003	-0.401
1×10^{14}	0.8132±0.07	10.9±0.9	4.096±0.004	-0.571
5×10^{14}	0.7815±0.05	11.2±0.6	4.098±0.005	-0.684
1×10^{15}	0.9106±0.04	09.6±0.3	4.088±0.004	-0.114
5×10^{15}	0.7962±0.06	11.1±0.8	4.090±0.001	-0.228
1×10^{16}	0.6785±0.03	12.9±0.5	4.091±0.002	-0.285

5.7.2 Rutherford Backscattering Spectrometry

The thickness and stoichiometry of TiO_2/Ag/TiO_2 multilayer structure were measured using Rutherford Backscattering Spectrometry (RBS). RBS spectrum with SIMNRA-fitted graph of TAT multilayer structure is shown in figure 5.15. The elemental peaks of Ag, Ti and O ions are seen in the RBS spectra. The thickness of individual layer was calculated using fitted data and found to be TiO_2 (45±5 nm)/Ag (9±1 nm)/TiO_2 (45±5 nm). RBS data confirms the formation of TiO_2 and Ag, which is consistent with XPS results given in next section. RBS provides the thickness of the different layers of the TAT film including the middle layer of Ag. Numerous reports [51,233] indicate that Ag film became continuous at ~9 nm. The FESEM image of middle Ag layer (shown in inset of figure 5.15) confirms the formation of continuous layer and also indicates that the

sputtering deposited Ag layer is smooth. The transport property results of the multilayer with 9 nm thick Ag layer are also supporting the formation of a continuous Ag layer.

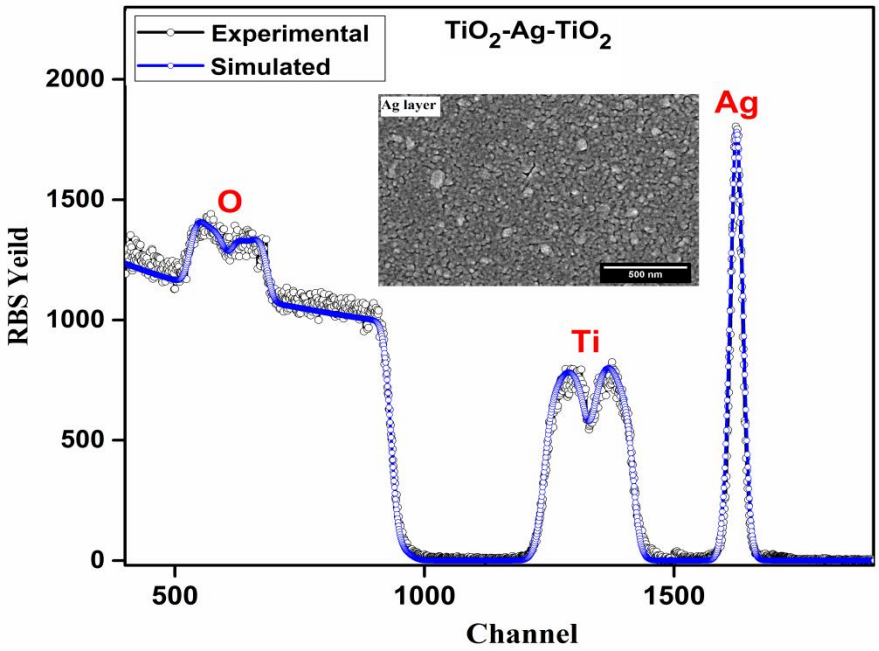

Figure 5.15: RBS spectrum of pristine TiO_2/Ag/TiO_2 multilayer film with fitted profile.

5.7.3 X-ray Photoelectron Spectroscopy

X-ray photoelectron spectroscopy was performed to analyze the chemical compositions of the TiO_2/Ag/TiO_2 pristine and Ar^+ implanted (fluence of 1×10^{16} ions/cm^2) (A−TAT) films. Figure 5.16 shows the XPS spectra of TAT films. Figure 5.16 (a) shows survey scan of TAT and A−TAT films containing dominant signals from Ti and O and weak signals from Ar and C. The low intensity C signal arises because of ex-situ transfer of samples to UHV chamber. Figure 5.16 (b) shows the Ti 2p core level spectra of top surface of TAT and A−TAT films. The Ti-$2p_{3/2}$ and Ti-$2p_{1/2}$ peaks of pristine films appearing at 458.9 and 464.6 eV are assigned to Ti^{4+} oxidation state of TiO_2 and match well with reported data [203]. The binding energy difference between Ti-$2p_{1/2}$ and Ti-$2p_{3/2}$ peak is 5.7 eV which is consistent with +4 oxidation state [200]. Meanwhile, peaks of Ti-$2p_{3/2}$ and Ti-$2p_{1/2}$ for A−TAT sample are positioned at 458.8 and 464.5 eV respectively and a peak corresponding to reduced specie of Ti ion (Ti^{3+}) is created at binding energy of 457 eV on Ar^+ implantation. The appearance of Ti^{3+} has been reported by other researchers also on Ar^+ bombardment [202]. This appearance of Ti^{3+} state leads

to band gap decrement that is validated by Tauc plot shown in figure 5.20 (b), producing reduced electrical resistivity, giving the highest figure of merit for the A−TAT sample. Hashimoto *et al.* [234] studied Ar bombardment on the TiO_2 single crystal and reported presence of Ti^{4+} component appeared for as-received TiO_2. Two additional peaks at 456.6 and 454.4 eV appeared after 30 s and 2 min of sputtering, respectively. The observed peaks at 456.6 and 454.4 eV are assigned to Ti^{3+} and Ti^{2+}, respectively. The reduced species of TiO_2 arise due to recombination of the O and Ti atoms. The recoiled atoms from Ar bombardment process are not able to recombine in accurate coordination of TiO_2.

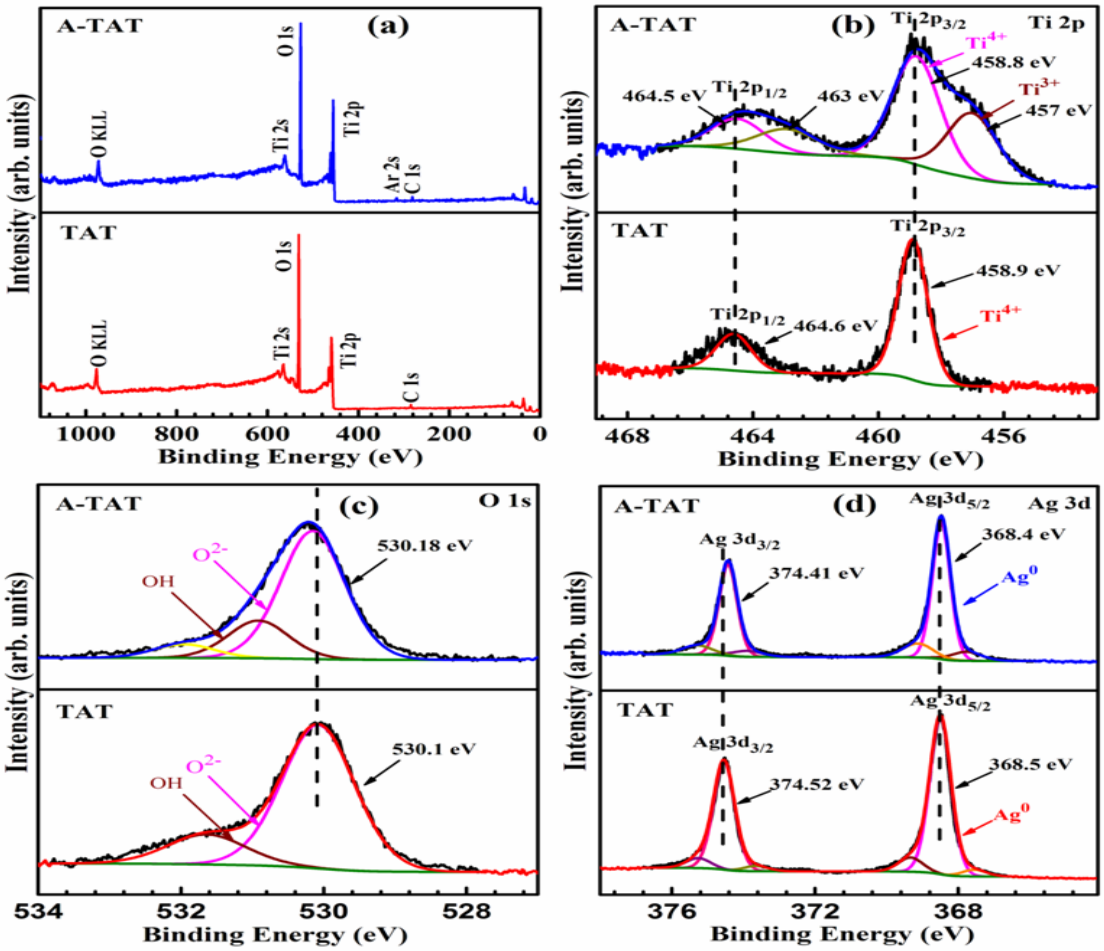

Figure 5.16: XPS spectra of pristine and Ar^+ ion implanted (1×10^{16} ions/cm^2) TiO_2/Ag/TiO_2 multilayer films (a) survey scan, (b) Ti 2p, (c) O 1s and (d) Ag 3d.

Figure 5.16 (c) shows the core level spectra of O 1s for TAT and A-TAT samples. The O 1s signal of pristine samples appears at 530.1 eV, and after deconvolution, another peak is seen at 531.6 eV which indicates the presence of OH groups on the surface. The O 1s

spectrum of A-TAT sample shows peak positioned at 530.18 eV, and the other peak at 531.1 eV assigned to OH species, present on the surface of sample. The O 1s peak of both TAT and A-TAT samples is at the same position suggesting similar nature of oxygen. Nitrogen doped TiO_2 [216] studies also suggest the similar nature of oxygen 1s, with peak positioned at around 530 eV. Lie *et al.* [235] reported the three components of O 1s of TiO_2 films: first component at 530.6 eV assigned to titanium dioxide; second component at 531.5±0.5 eV may be due to defective oxides or hydroxyl groups and other component at 533±1 eV because of adsorbed water. Figure 5.16 (d) shows the core spectra of Ag 3d for both samples. Ag signals from the sandwich layer were obtained using the depth profile mode XPS. Ag $3d_{5/2}$ and Ag $3d_{3/2}$ peaks appear at binding energies of 368.5 and 374.52 eV showing the presence of metallic Ag^0 as middle layer. After Ar^+ implantation peaks of Ag $3d_{3/2}$ and Ag $3d_{5/2}$ appear at 368.4 and 374.41 eV, respectively. A small shift towards lower binding energy is observed which could be due to interaction of Ti and O ions with Ag at the interface [236]. Harifi *et al.* [237] studied Ag/TiO_2 and found Ag $3d_{5/2}$ and Ag $3d_{3/2}$ peaks at 368.8 eV and 374.8 eV, respectively. No peak corresponding to Ag_2O (367.8 eV) or AgO (367.4 eV) was found, reinforcing the presence of metallic silver.

5.7.4 Surface characterization

TAT pristine and implanted multilayer films were characterized by FESEM for surface morphology and images are shown in figure 5.17. All films were observed at the 100*k*× magnification. SEM images show growth of spherical shape particles on the top surface. It can be seen that there is no major morphological change on implantation. The particle size has been calculated using surface morphology and found to vary in the range of 20–30 nm. Similar SEM micrographs of TiO_2 surface have been reported by other studies [191].

Surface topography of the TAT pristine and implanted multilayer films as observed by AFM is shown in figure 5.18 (a) – (f). The scan area of measurement was taken 1×1 μm^2. The average surface roughness of films as a function of fluence is shown in figure 5.19. The pristine film exhibits roughness of 1.71 nm and it becomes 3.31 nm for fluence of

5×10^{14} ions/cm^2 and then decreases to 0.87 nm for the highest fluence (1×10^{16} ions/cm^2). Surface roughness increment on initial ion implantation is caused by sputtering of surface by energetic Ar^+ ions incident on the sample [220]. High energy ions etch the surface and roughen the surface. Further increasing the fluence leads to the lower roughness which is due to ion implantation induced emission of atoms from the top surface [233].

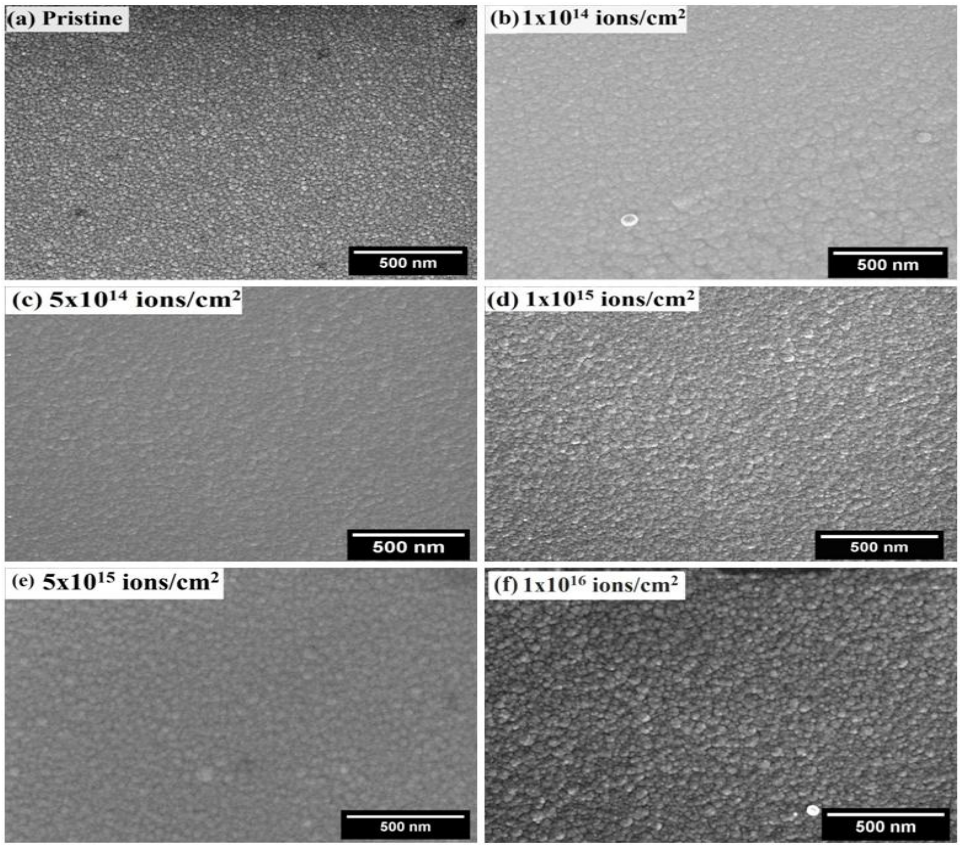

Figure 5.17: SEM images of pristine and Ar^+ ion implanted $TiO_2/Ag/TiO_2$ multilayer films.

The morphology of films exhibits similar shaped grains at different fluences. The peak height of the grains of the top surface as seen through AFM image varies with implantation fluence with no observation of cluster formation. Smooth TAT films with surface roughness of ~2 nm which is nearly equal to ITO films (~2–3 nm) makes them a good choice as TCEs and makes them suitable for optoelectronic devices.

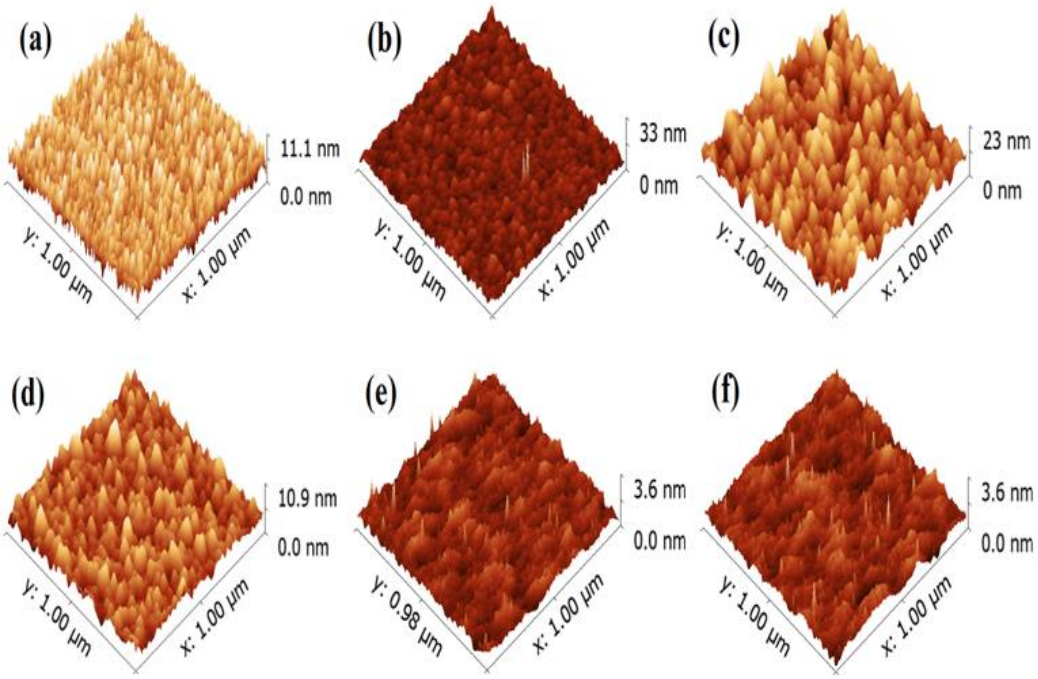

Figure 5.18: Three-dimensional AFM images of pristine and Ar^+ implanted $TiO_2/Ag/TiO_2$ multilayer films (a) pristine, (b) 1×10^{14}, (c) 5×10^{14}, (d) 1×10^{15}, (e) 5×10^{15} and (f) 1×10^{16} ions/cm^2.

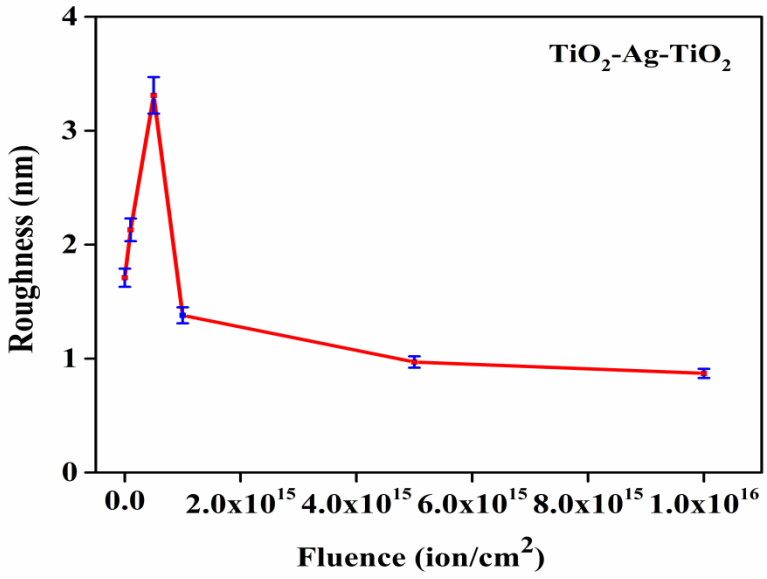

Figure 5.19: Average surface roughness of $TiO_2/Ag/TiO_2$ multilayer films with fluence.

5.7.5 Optical analysis

The optical transmittance spectra of TAT multilayer films in the visible region (400 nm<λ<800 nm) for different ion fluence are shown in figure 5.20 (a). Average transmittance of pristine film is observed ~80% which reduces to ~73% for the highest

fluence (1×10^{16} ions/cm^2). Transmittance for all samples shows a similar trend. An initial increase in transmittance is seen with increase in wavelength, attaining a maximum at a particular wavelength and then a decrease with further increase in wavelength. Increasing fluence leads to degradation in optical transmittance suggesting creation of defects in the system and removal of oxygen, on Ar^+ implantation. Higher surface roughness of 3.31 nm at 5×10^{14} ions/cm^2 fluence causes more scattering of light and as a result transmittance decreases. Further increasing fluence results in lower roughness and scattering of light decreases but reflection increases due to smooth top surface and it may degrade the transmittance. The film becomes oxygen deficient, which is also confirmed by XPS analysis seen by appearance of Ti^{3+} state (reduced species of Ti ions). The absorption of visible light depends upon the oxygen vacancies and could increase by the presence of oxygen vacancies in the system. The optical transition in visible region (400 nm<λ<800 nm) is because of electronic transition from valence band to localized mid-gap states and then to conduction band edge. The removal of oxygen from the system leads to increase the Ti/O ratio or more metallic content in the metal oxide layer which would absorb more light and consequently transmittance decreases. The XPS study also supports the reduction of band gap (i.e more absorption) by showing the reduced species of Ti (Ti^{3+}).

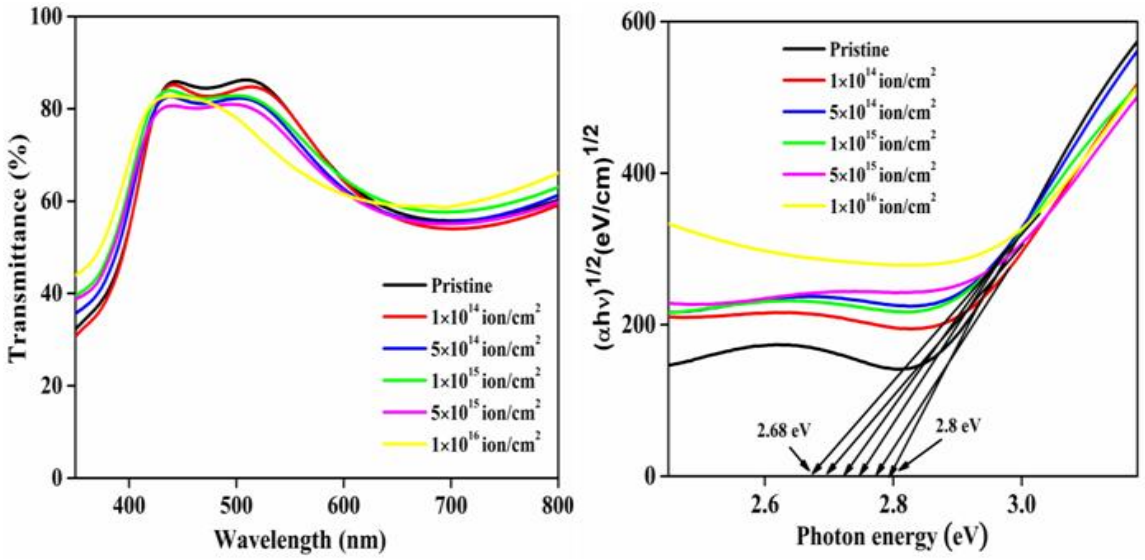

Figure 5.20: (a) Transmittance and (b) Tauc plot of pristine and Ar^+ ion implanted $TiO_2/Ag/TiO_2$ multilayer films with fluence.

The optical band gap of samples was estimated using the standard formula [196].

$$\alpha h\nu = B(h\nu - E_g)^n \qquad (5.8)$$

Where α is absorption coefficient, $h\nu$ the photon energy, B is a constant and E_g is optical band gap. Here the value of n is 2, because TiO_2 is indirect band gap material.

Absorption coefficient (α) was estimated using the Beer–Lambert's expression [222].

$$\alpha = \frac{2.303}{d} A \tag{5.9}$$

Where d is total thickness of the multilayer film and A is absorbance of TAT films. Optical band gap of TAT films was calculated using Tauc plot between $(\alpha h\nu)^{1/2}$ and photon energy ($h\nu$) and shown in figure 5.20 (b). Pristine film exhibits band gap of 2.8±0.01 eV and it decreases to 2.68±0.01 eV for the 1×10^{16} ions/cm^2 fluence. Band gap reduction for the highest fluence sample is supported by XPS results by showing creation of Ti^{3+} state at lower binding energy [238]. The average surface roughness, transmittance, band gap, extinction coefficient and refractive index have been calculated for pristine and implanted TAT films and are shown in table 5.5.

Table 5.5: RMS surface roughness, transmittance, band gap, extinction coefficient and refractive index of pristine and implanted TiO_2/Ag/TiO_2 multilayer films as a function of ion fluence.

Ion fluence (cm^{-2})	RMS (nm)	Transmittance (%) at 530 nm	Band gap (eV)	Extinction coefficient (k)	Refractive index (n)
0	1.71	83	2.80±0.01	0.245	2.27
1×10^{14}	2.13	81	2.77±0.01	0.247	2.19
5×10^{14}	3.31	79	2.75±0.01	0.287	2.17
1×10^{15}	1.38	80	2.72±0.01	0.264	2.12
5×10^{15}	0.97	77	2.70±0.01	0.282	2.15
1×10^{16}	0.87	74	2.68±0.01	0.297	2.16

5.7.6 Electrical analysis

Figure 5.21 shows the variation of Hall mobility and carrier concentration of TAT multilayer films with varying ion fluences. The carrier concentration of pristine TAT film is 3.94×10^{21} cm^{-3}, which increases to 6.63×10^{21} cm^{-3} with ion fluence. Simultaneously, Hall mobility increases from 7.8 to 10.32 cm^2/V-s with increasing fluence. Figure 5.22 shows the variation of electrical resistivity and sheet resistance of the TAT films with fluence. Pristine film exhibits electrical resistivity of 2.04×10^{-4} Ω cm and it decreases to 9.14×10^{-5} Ω cm for the highest fluence (1×10^{16} ions/cm^2). Meanwhile, sheet resistance varied from 20.4 Ω/□ to 9.14 Ω/□ with increase in fluence. The reduction in electrical

resistivity is mainly due to enhancement in carrier mobility from 7.8 to 10.32 cm^2/V-s, caused by decreasing grain boundary effects which were acting as scattering centres [134,239]. It has been reported that oxygen vacancies generated through implantation increase the electrical conductivity of TiO_2 by many fold [128,133]. Moreover, defects created by noble gas implantation results in enhancement of the electrial conductivity. The band gap is narrowing with increasing ion fluence which is responsible for the better conductivity of the specimens. The variation in electrical resistivity can be explained by the following expression:

$$\rho = \frac{1}{n_e \mu e} \tag{5.10}$$

Where ρ is resistivity, n_e is carrier concentration, μ is the mobility, and e is charge on the carrier.

The slight variation in resistivity at lower fluence is due to small variation in carrier concentartion and mobilty values but significant change in resistivity at highest fluence is mainly dominated by considerable increase in carrier concentartion and mobilty values. A continuous film of silver is essential for good electrical conduction [227]. The electrical resistivity and sheet resistance of this study suggest the formation of continuous Ag inter layer. Haacke [76] figure of merit (Ψ_{TC}) was calculated using the following formula:

$$\Psi_{TC} = \frac{{T_{av}}^{10}}{R_s} \tag{5.11}$$

where R_s is the sheet resistance and T_{av} is average transmittance.

Figure 5.23 shows the FOM (Ψ_{TC}) for the TAT pristine and implanted films. Figure of merit measured for the pristine film is 5.2×10^{-3} Ω^{-1}. This changes with fluence due to variation in the charge carriers and mobility and shows a maximum value of 5.6×10^{-3} Ω^{-1} at fluence of 1×10^{16} ions/cm^2. This change was observed because of variation in sheet resistance and transmittance with the fluence. The present figure of merit indicates acceptability of TAT films to be used as a transparent conductive electrode. The electronic and nuclear energy losses produced after Ar implantation in TAT films, measured by SRIM-2010 software are shown in inset of figure 5.23. It can be observed that nuclear energy loss is higher than electronic energy loss. The carrier concentration, mobility, resistivity, sheet resistance and Haacke figure of merit (FOM) have been calculated for TAT pristine and implanted films and are shown in table 5.6.

Table 5.6: Carrier concentration, mobility, resistivity, sheet resistance, transmittance and Haacke figure of merit (FOM) of pristine and implanted TAT multilayer films as a function of fluence.

Ion fluence (cm^{-2})	Carrier concentration (cm^{-3})	Mobility (cm^2/V-s)	Resistivity (Ω cm)	Sheet resistance ($\Omega/\square$)	Haacke FOM ($10^{-3}\ \Omega^{-1}$)
0	3.94×10^{21}	7.77	2.04×10^{-4}	20.4	5.2
1×10^{14}	4.09×10^{21}	7.96	1.92×10^{-4}	19.2	4.3
5×10^{14}	4.24×10^{21}	6.46	2.28×10^{-4}	22.8	3.0
1×10^{15}	4.73×10^{21}	8.63	1.53×10^{-4}	15.3	4.2
5×10^{15}	3.34×10^{21}	9.54	1.96×10^{-4}	19.6	3.1
1×10^{16}	6.63×10^{21}	10.32	9.14×10^{-5}	9.14	5.6

N^+ ion implantation in TAT multilayer films demonstrated that N ions replaces the O sites in TiO_2 lattice and added new electronic states just above the valence band by narrowing the band gap. This consequently increases the electrical conductivity but decreases the optical transmittance. Ar^+ ion implantation also leads to increases in electrical conductivity and reduction in transmittance. The Ar^+ ion implantation causes enhancement of mobility due to reduction in the grain boundary effects and the electrical conductivity increases due to annealing of oxygen vaccancies. While, the N^+ ion implantation in TiO_2 gives the maximum carrier mobility of 9.2 cm^2/V-s, the Ar^+ implantation it is 10.32 cm^2/V-s.

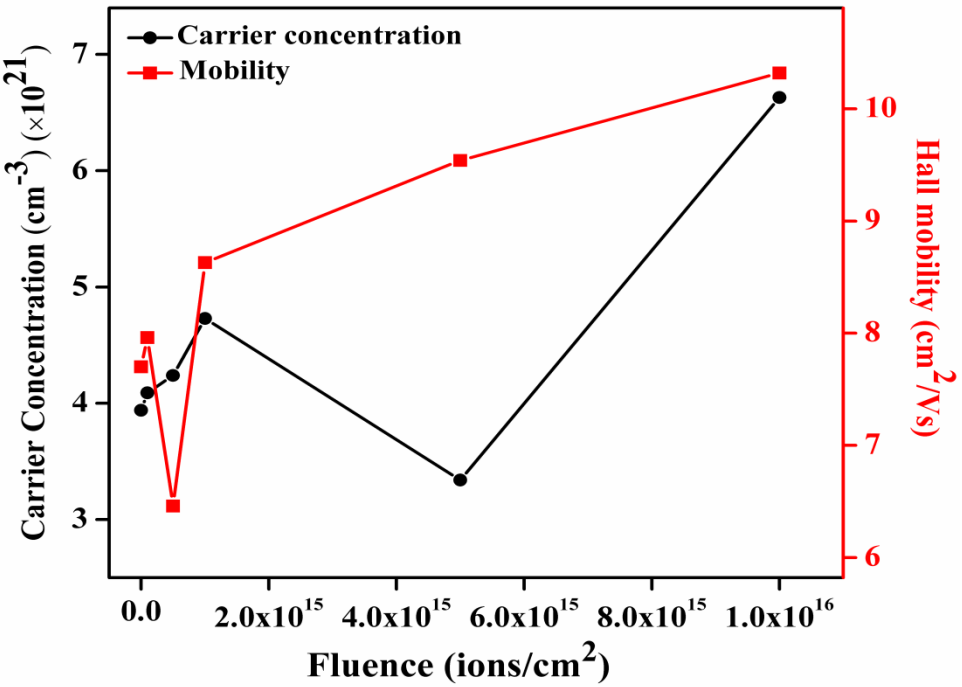

Figure 5.21: Carrier concentration and Hall mobility of pristine and Ar^+ ion implanted TiO_2/Ag/TiO_2 multilayer films with fluence.

The optical transmittance at 1×10^{16} ions/cm^2 fluence, increases from 70% (in case of N^+ implantation) to 73% for Ar^+ implantation. Based on the XPS studies, it is also evident that implanting N results in occuping O site and modifies the electronic structure [238]. On the other hand implanting Ar ions affect the Ti sites and reduces Ti^{4+} to Ti^{3+} which also causes modification in the electronic structure.

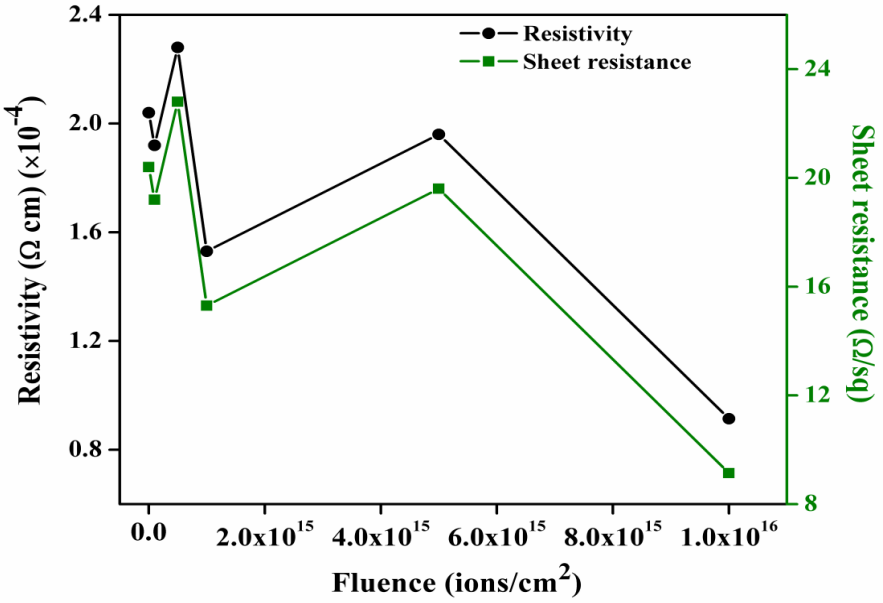

Figure 5.22: Resistivity and sheet resistance of pristine and Ar^+ ion implanted TiO_2/Ag/TiO_2 multilayer films with fluence.

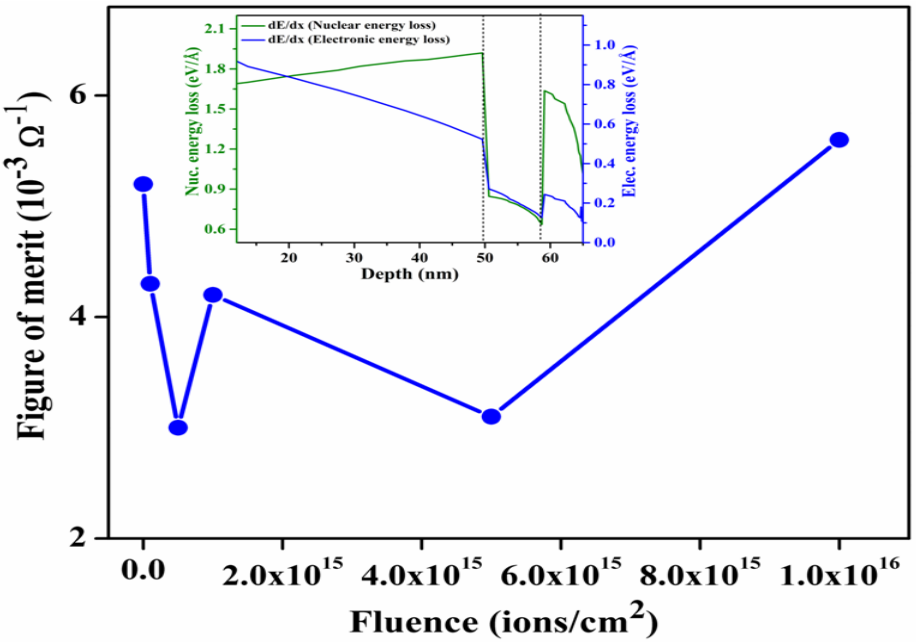

Figure 5.23: Haacke FOM (Ψ_{TC}) of pristine and Ar^+ ion implanted TiO_2/Ag/TiO_2 multilayer films with fluence. Inset exhibit the electronic energy loss (S_e) and nuclear energy loss (S_n) with depth.

5.8 Conclusion

Present investigation demonstrates that it is possible to enhance the electrode properties of TAT films by N^+ ion and Ar^+ ion implantation. The structural, optical and electrical properties of TAT films were investigated as a function of N^+ and Ar^+ ion fluence. For N^+ ion implantation, the replacement of O ions by N^+ ions results in the band gap narrowing and improvement in the electrical conduction. This is evidenced by the shift in Ti 2p peak and the position of N 1s peak in the XPS spectra. XRD shows amorphous nature of TiO_2 and a crystalline peak of Ag (111), SEM images indicate a smooth flat surface of the upper layer. Pristine film had surface roughness of 1.71 nm which decreases to 1.25 nm at the highest fluence of 1×10^{16} ions/cm^2. Implantation with higher fluences of N^+ ions smoothens the top surface. On ion implantation, average optical transmittance degraded from ~80% to ~70%, but there is a simultaneous improvement in electrical resistivity from 2.04×10^{-4} to 9.62×10^{-5} Ω cm as the ion fluence is increased. Results indicated that electrical conductivity of TAT films is primarily due to Ag interlayer which showed further improvement on N^+ ion implantation. Such high quality transparent conducting electrode can be used as an alternative to ITO for optoelectronic devices.

The as prepared TAT films were also implanted with 100 keV Ar^+ ions to modify optical and electrical properties for their use as transparent conducting electrode with enhanced figure of merit. While XRD shows the amorphous nature of TiO_2, the XPS analysis implies the presence of peak due to Ti^{3+} ions on implantation indicating lower binding energy of Ti state and consequent band gap reduction confirmed by optical measurement result. Lower band gap leads to decrease in the electrical resistivity which was the main objective of this study. The FESEM and AFM show homogeneous deposition of films with small roughness values. The optical transmittance was found to decrease from ~80% to ~73% after implantation. The electrical resistivity of pristine film was 2.04×10^{-4} Ω cm, which decreased to 9.14×10^{-5} Ω cm at the highest fluence of 1×10^{16} ions/cm^2. The sheet resistance decreased from 20.4 Ω/□ to 9.14 Ω/□. The Haacke figure of merit have been calculated for all samples and highest FOM (Ψ_{TC}) was found to 5.6×10^{-3} Ω^{-1} for the highest fluence of 1×10^{16} ions/cm^2. Our results demonstrate that Ar implantation is a favourable method to develop TAT multilayer based transparent conducting electrode with enhanced properties and hence FOM.

Chapter-6

Fabrication and Characterization of NTO-Ag-NTO Multilayer Thin Films and Their Ion Implantation Effects

6.1 Introduction

This chapter reports the investigation on fabrication and characterization of multilayer structures with Nb (3.7 at.%) doped TiO_2 (NTO) having the layers as NTO/Ag/NTO (NAN) to obtain high optical transmittance and low electrical resistivity TCE that could be a suitable replacement of the conventional transparent conducting electrode used in energy conversion and optoelectronics devices. The thickness of NTO layers was changed from 25 nm to 65 nm to establish optimum thickness and thickness of middle Ag layer was taken ~9 nm. Subsequently, optimized NAN multilayer films were implanted with N^+ and Ar^+ ions (as taken for TAT films) for alteration of their properties. Researchers have proposed different methods viz. doping and tracing of impurities in TiO_2 using chemical mixing, sol-gel method, ion assisted sputtering, ion implantation etc to improve properties of TiO_2. Nb doped TiO_2 has shown enhanced performance as TCE [113]. A single layer Nb doped TiO_2 (NTO) used as TCE in optoelectronic applications has shown less working efficiency in terms of electrical conductivity and the films are thicker than the multilayer structure [115]. The multilayer structure with Nb doped TiO_2 embedded with metal layer gives higher electrical conductivity with nearly same transmittance while having lower total thickness (~80 nm). Ion implantation has been used for modification of TiO_2, due to its reported good process control and restoring capacity of vacant oxygen sites in a TiO_2 lattice [109,211].

6.2 Experimental details

Nb powder (Strem Chemicals, 99.9% purity) and TiO_2 powder (Alfa-Aesar, 99.98% purity) were used to fabricate the Nb doped TiO_2 (NTO) sputtering target. These powders were mixed by solid state method and pressed into a 2-inch diameter pellet and then sintered at 1200 ˚C for 12 hrs. The first and third NTO layers of multilayer structure were

deposited by RF sputtering (120 W) at room temperature. Middle layer of Ag was deposited by DC sputtering (16 W) using silver target (99.98% purity). Initially the vacuum chamber was evacuated to 5×10^{-6} mbar and chamber pressure during deposition was 5×10^{-3} mbar for NTO layer and 1.5×10^{-2} mbar for Ag layer with constant Ar flow at 15 sccm. The distance of target to substrates was 100 mm and deposition rate for NTO and Ag layers were obtained as 1 Å/sec. and 6 Å/sec, respectively. The NTO/Ag/NTO multilayer structures were consecutively deposited on cleaned corning glass substrates. The thickness of top and bottom NTO layers was varied from 25 nm to 65 nm keeping the same sputtering conditions to find optimum value of thickness, in terms of maximum FOM. The thickness of Ag layer was kept constant at ~9 nm. The optimized as-deposited NAN films were implanted with 40 keV N^+ and 100 keV Ar^+ ions of fluence ranging from 1×10^{14} ions/cm^2 to 1×10^{16} ions/cm^2 at room temperature using the low energy ion beam facility (LEIBF) at the Inter-University Accelerator Centre (IUAC), New Delhi, India.

The electrical properties of pristine and implanted films were measured using ECOPIA-5000 low-temperature Hall Measurement unit using a magnetic field of 0.57 T for temperature range of 80 to 340 K. The optical transmittance and absorbance were obtained from LAMBDA 750 (Perkin Elmer) UV-Vis-NIR Spectrophotometer with bare glass as a reference in the visible range (300 nm–800 nm) of light. The crystalline properties of pristine and implanted films of NAN structure were probed by X-Ray Diffractometer (Panalytical X-Pert Pro) with CuKα radiation. The morphology of the films was examined by Nova Nano FE-SEM 450 (FEI) and topography was observed by using atomic force microscopy Multimode Scanning Probe Microscope (Bruker). Detailed study of chemical states of elements and the interfacial stability of NAN films were carried out by X-ray photoelectron spectroscopy (XPS, Omicron ESCA). Monochromatic source Al Kα (1486.7 eV) of 124 mm mean radius and X-ray resolution of 0.6 eV and 3×10^{-10} mbar chamber pressure has been used for XPS measurement. The thickness and elemental composition of the films were studied by Rutherford Backscattering Spectrometry (RBS). These measurements were carried out using 2 MeV He^+ ions at a back scattering angle of 165^o with 1.7 MV tandem accelerator facility at IUAC, New Delhi.

6.3 Optimization of NTO thickness

Nb (3.7 at. %) doped TiO_2 (NTO) based multilayer structure was deposited at room temperature. Figure 6.1 (a) shows the XRD pattern of NAN multilayer films with varying NTO thickness. The thickness of NTO film was varied from 25 – 65 nm. The figure shows a dominant peak at 38.18˚, assigned to Ag (111) diffraction plane (JCPDS No. 04-0783). Other peaks at 44.28˚, 64.62˚ and 77.51˚ are attributed to Ag (200), (220) and (311), respectively. No peak is observed for TiO_2 as room temperature deposition results in an amorphous Nb doped TiO_2 layer. The XRD graph exhibits a similar pattern for all NAN multilayer structures. Figure 6.1 (b) demonstrates optical transmittance of NAN films for different NTO thickness for the visible region (350 nm<λ<800 nm). The average transmittance in the visible region for NTO thickness of 25, 35, 45, 55 and 65 nm was observed as 84%, 83%, 82%, 80% and 81%, respectively. The highest transmittance of ~94% was obtained for the 35 nm NTO thickness at 550 nm wavelength, which is most preferred operating wavelength for the optoelectronic devices so the NAN structure with (~35 nm/~9 nm/~35 nm) exhibits the best optical results. The transmittance of these specimens initially increases with wavelength and attains a maximum and then decreases with further increasing wavelength.

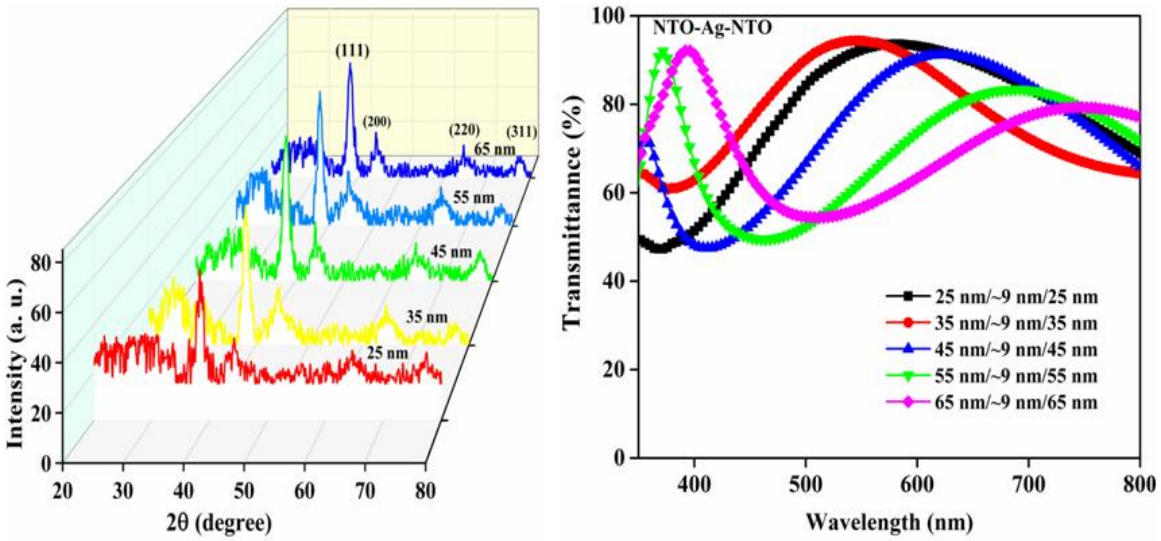

Figure 6.1: (a) XRD pattern and (b) Transmittance spectra of NAN multilayer films with different NTO thickness.

It can be also seen that; transmittance peaks of NAN structures are red-shifted with increasing NTO thickness. Transmission window broadens and is shifted to lower

energies with the NTO thickness. However, the increasing thickness of NTO layers in NTO/Ag/NTO multilayer structure leads to more absorbance of light intensity and consequently the transparency reduces. Large difference in the refractive indices of oxide layer and Ag may produce a plasmon coupling to give higher transmittance (> 80%) [240]. Therefore, good transmittance (~84%) of our specimen may be attributed to surface plasmon resonance in silver layer with optimized NTO thickness of 35 nm.

The top layer added on the metal layer serves as an antireflective coating. The optical properties of such a stacked layer depend on the film thickness and the peak of transmittance curve representing minimum reflectance is obtained by adjusting the thickness of the film [45,241]. As the film thickness increases, the peak shifts towards the longer wavelengths [104,242,243]. Material of high refractive index coated on the metal layer enhances its antireflective properties. Initial decrease in refractive index of NTO with wavelength (shown in figure 6.9 (d)) could be a reason for initial increase of transmittance with wavelength. Further, the transmittance enhances due to the screening effect of the bound electrons with an increase in wavelength. At higher wavelengths or for low energy region, the free charge carrier absorption is dominant and causes decrease in transmittance [244,245]. Similar transmittance behavior for transparent conducting electrodes has been reported in previous studies [104,246,247]. The role of NTO layers in NAN multilayer system is to increase the transmittance by reducing the reflection of light from the Ag surface. The transmittance value is limited by the Ag layer mainly due to reflection losses, which can be boosted by adding two NTO layers and behave as antireflective coatings. The intention is to tune the interference phenomena that happen between multiple reflections from the interfaces and to obtain the minimum reflectance or maximum transmittance. To fulfill this condition, the thickness of NTO layers is varied and finely tuned to get maximum transmittance at a particular wavelength say 550 nm [52,248]. It is reported that the shape of the transmittance curve depends upon the amount of oxygen in metal oxide film and its thickness. Therefore, an improvement in transmittance for particular wavelength region can be obtained by adjusting the film thickness of metal oxide [241,243,248].

Figure 6.2 (a) shows the electrical resistivity, carrier mobility and carrier concentration of NAN multilayer films for different NTO thickness. Resistivity for 25 nm NTO thickness was obtained 9.9×10^{-5} Ω cm, which reduces to 9.7×10^{-5} Ω cm for 35 nm and increases to 2.1×10^{-4} Ω cm as the NTO thickness increases. Figure 6.2 (b) illustrates the sheet resistance and Haacke figure of merit for NAN films. The sheet resistance varied from 16.5 Ω/□ to 15 Ω/□ with NTO thickness and a minimum value of 12.12 Ω/□ was obtained for 35 nm. The decrease in resistivity can be explained in terms of change carrier concentration and their mobility values. NAN multilayer system consists of a continuous Ag layer between two doped dielectric layers so interfacial scattering and ionized-impurity scattering would be dominant here. NAN multilayer structure was prepared by using two different materials (NTO and Ag) having different refractive indices and electronic structures. The refractive indices of NTO (~35 nm) and Ag (~9 nm) layers in the NAN multilayer system are ~2.1 and ~1.3 respectively. Therefore, the interfaces between NTO and Ag in the NAN structure are responsible for interfacial scattering [249,250]. The schematic diagram of the Fermi energy level (E_f) alignment in the electronic structure of the interfaces in NAN multilayer structure is shown in figure 6.15.

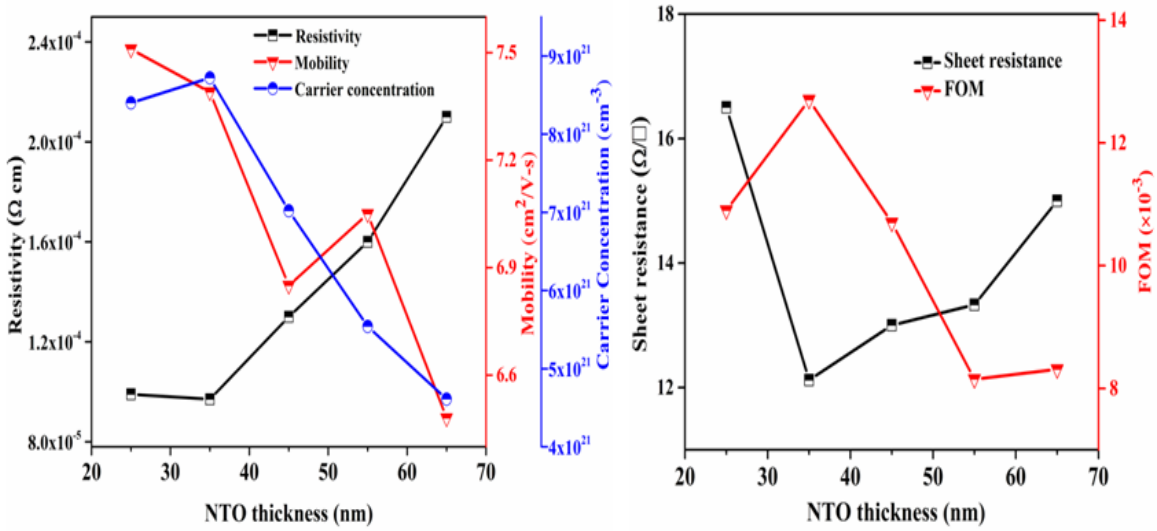

Figure 6.2: (a) Resistivity, mobility and carrier concentration and (b) Sheet resistance and the Haacke figure of NAN multilayer films with different NTO thickness.

The NAN multilayer structure was fabricated using sputtering method. During the stacked multilayer deposition, the Ag atoms are expected to diffuse into NTO matrix and this is evident in the RBS spectra. These diffused Ag ions are present in the top and bottom of

the NTO matrix and causes ionized impurity scattering [249,250]. The schematic diagram of diffused ions of Ag, Ti and O in NTO and Ag layers of NAN structure is shown in figure 6.3 (b).

The Haacke FOM [76] has been calculated using the following formula.

$$\Psi_{TC} = \frac{{T_{av}}^{10}}{R_s} \quad (6.1)$$

As observed from figure 6.2 (b) giving variation of FOM with NTO film thickness, highest FOM of 12.7 Ω^{-1} is obtained for 35 nm thickness. Hence the multilayer structure with this thickness of NTO layers was chosen for N ion implantation to modify the properties. The optimized NAN structure with 35 nm NTO layers and 9 nm thick Ag layer implanted using 40 keV nitrogen ions with different ion fluences and investigated for change in its structural, optical and electrical behavior. The ion implantation parameters viz. range and energy loss were measured by SRIM calculations.

6.4 N^+ (40 keV) Ion Implantation in NTO/Ag/NTO Multilayer Thin Films

An optimized thickness for NTO layer was obtained and the structure with NTO/Ag/NTO (35 nm/9 nm/35 nm) shows highest figure of merit of 12×10^{-3} Ω^{-1}. These multilayer films were further implanted with 40 keV N^+ ions to improve the properties with the fluence ranging from 1×10^{14} to 1×10^{16} ions/cm^2. It is seen that doping Nb in TiO_2 and the N^+ implantation both contribute in enhancement of electrical conductivity. There is decrement in optical transmittance but the overall figure of merit has significantly increased to 18×10^{-3} Ω^{-1}. We have also measured the work function of pristine NAN films using ultravoilet photoemission spectroscopy (UPS). Work functon of the TCE is a key factor and have significant impact on the performance of the solar cell because it affects the band alignment of TCE and the next active layer [251]. Lee *et al.* [252] have reported improved power conversion efficiency (3.6%) with MoO_3 graded ITO anodes. Lei *et al.* [253] increased the work function of ITO using CuS to gain higher power conversion efficiency (7.4 %).

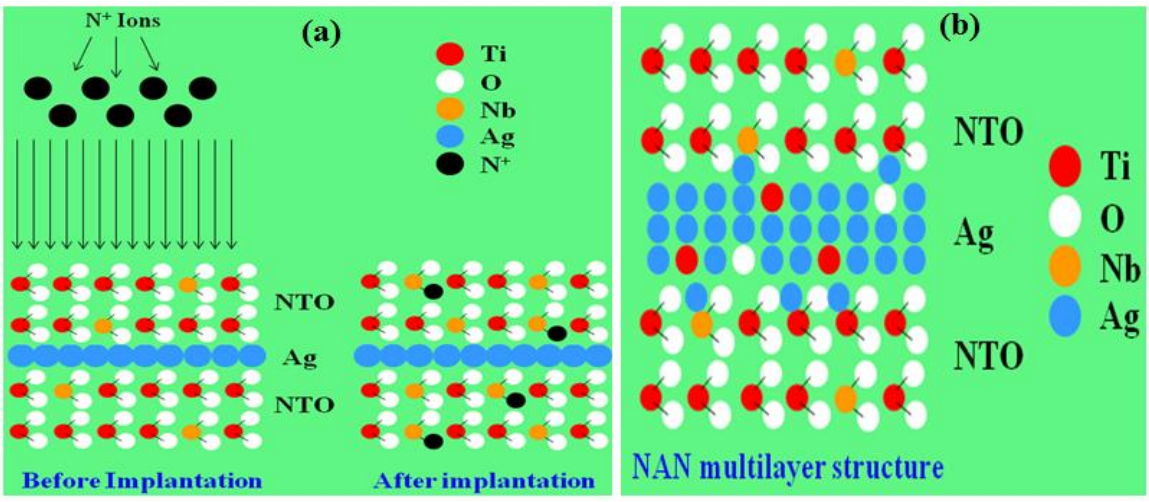

Figure 6.3: (a) Schematic diagram shows the N^+ implantation process and (b) Schematic representation of ion diffusion of Ag, Ti and O in NTO and Ag layers.

The electronic and nuclear energy loss values for this implantation were 12.1 and 25.6 eV/Å, respectively, showing that nuclear energy loss dominates over electronic energy loss. The stopping range as calculated by the SRIM-2010 software was obtained as 58 nm which is less than 80 nm, the total thickness of the film meaning there by that the ions have been implanted in the film. Figure 6.3 (a) shows the schematic diagram of N^+ ion implantation.

6.5 Results and discussion

6.5.1 Structural Properties

Figure 6.4 shows the XRD patterns of the pristine NAN and N^+ ion implanted NAN (referred as N-NAN) multilayer structures for the fluence range of 1×10^{14} ions/cm^2 to 1×10^{16} ions/cm^2. It can be observed from the graph; the diffraction planes of Ag (111), (200), (220) and (311) produce peaks at 38.18˚, 44.28˚, 64.62˚ and 77.51˚ positions respectively, matching well with JCPDS No. 04-0783. The crystallite size of the Ag particles was calculated using Debye–Scherrer formula ($0.9\lambda/\beta\cos\theta$) and found to be 8.1 nm for pristine film which decreases to 7.1 nm with increase in fluence to 1×10^{16} ions/cm^2. The variation in crystallite size of Ag is due to the annealing effect produced by ion implantation and may be explained by the thermal spike model [254]. The calculated lattice parameters were found to be identical with standard value (4.086 Å). The implantation process generates residual stress in the system and it changes from -0.108 to

-0.570 with increase in fluence. The negative sign of residual stress shows that the stress in the system is compressive. The increased intensity of Ag peaks indicates that implantation causes improvement in the crystallinity and it may contribute to get lower resistivity in the specimen. The crystallite size, lattice constant and residual stress of pristine and N-NAN multilayer films is given in table 6.1.

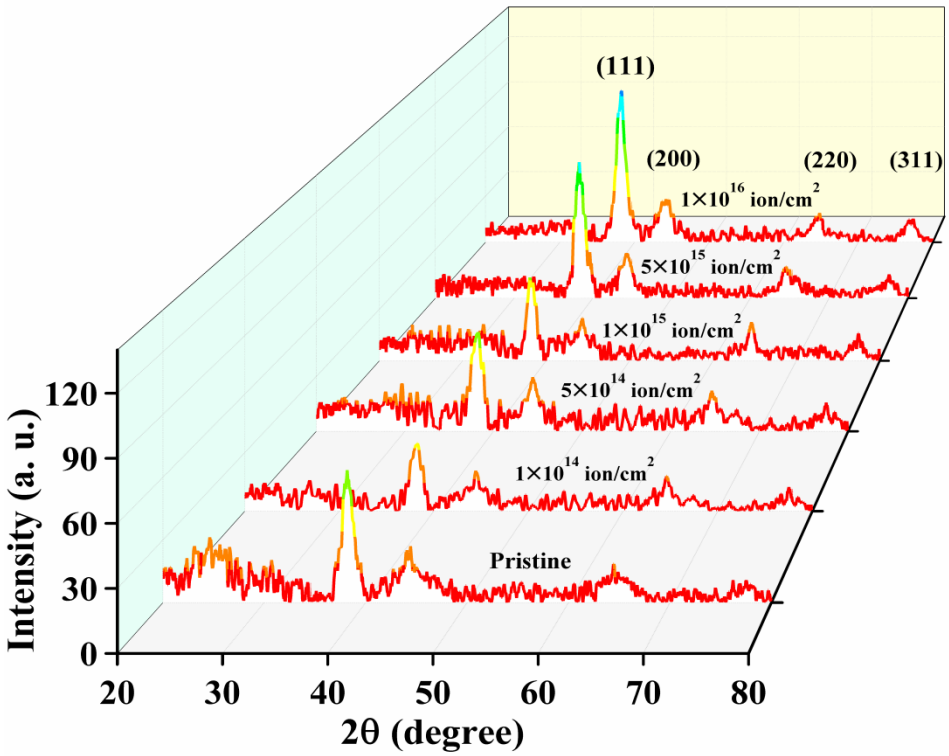

Figure 6.4: XRD pattern of NAN multilayer films with different ion fluences.

Table 6.1: FWHM, crystallite size, lattice constant and residual stress of Ag (111) plane of pristine NAN and N-NAN multilayer films with different ion fluences.

Samples details	FWHM (deg.)	Crystallite size (nm)	Lattice constant c (Å)	Residual Stress (GPa)
0	1.084±0.06	8.1±0.5	4.088±0.007	-0.108
1×10^{14}	1.098±0.05	8.0±0.4	4.089±0.004	-0.172
5×10^{14}	1.141±0.09	7.7±0.6	4.091±0.003	-0.284
1×10^{15}	1.156±0.07	7.6±0.5	4.095±0.007	-0.513
5×10^{15}	1.203±0.12	7.3±0.7	4.094±0.005	-0.456
1×10^{16}	1.237±0.11	7.1±0.6	4.096±0.006	-0.570

The XRD results show the amorphous behavior of oxide layer which generally appears in the films deposited at room temperature and it is advantageous for electrode when deposited on plastic substrates. The crystalline peak of metal layer confirms the good quality continuous metal layer, which enhances the overall electrical behavior of NAN structure in pristine and implanted samples. Negligible variation in the XRD of NAN structures also confirms the structural stability of the films in low energetic ion environment.

6.5.2 Rutherford Backscattering Spectrometry

RBS measurements were carried out for pristine NAN and N-NAN multilayer films deposited on Si substrates to evaluate the thickness of each layer. Figure 6.5 shows the RBS spectra of pristine NAN and N-NAN multilayer structures. SIMNRA software has been used for the simulation of these two samples. The primary purpose of this measurement was to determine the stoichiometry and thickness of the multilayer films. Both fitted spectra exhibit distinct elemental peaks corresponding to Ti, O, Nb and Ag ions.

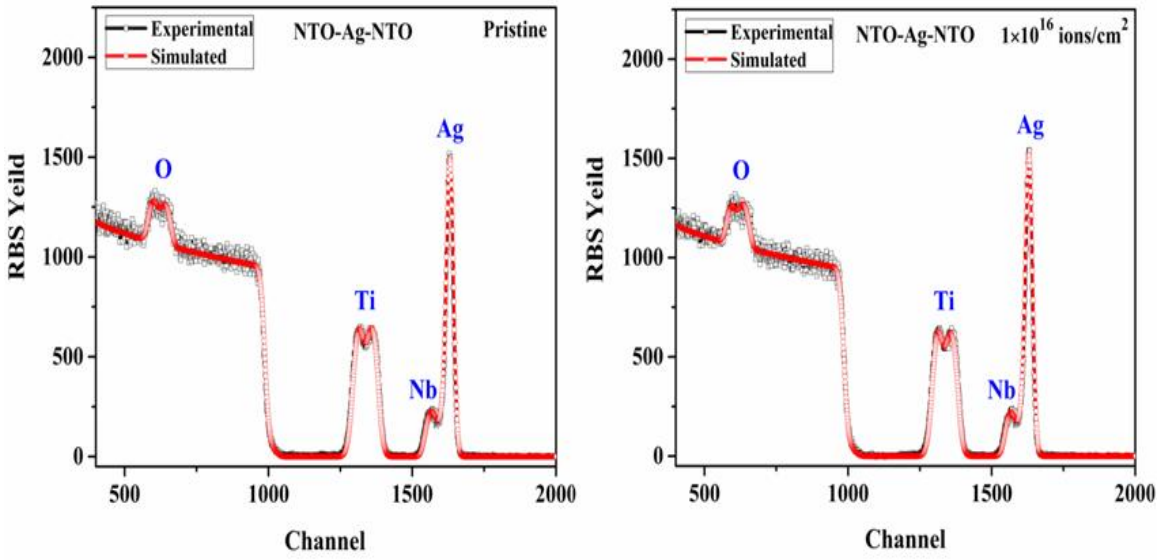

Figure 6.5: RBS spectra of pristine NAN and N-NAN multilayer films, with fitted profile.

The Nb concentration of ~3.7 at.% in TiO_2 matrix was estimated from RBS results. The thickness of first, second and third layers have been calculated from the fitted curves and found to be NTO (35±4 nm)/Ag (9±1 nm)/NTO (35±4 nm). These RBS results indicate

the formation of Nb doped TiO_2 lower and upper layers with pure Ag middle layer. Some of the energetic Ag ions are diffused in to adjacent TiO_2 layers during the film deposition process. The implantation leads to slight increase in the diffusion length due to transfer of source ion energy to the host multilayer films, which is confirmed by RBS measurements [249].

6.5.3 Surface characterization

A smooth and homogeneous deposition of top surface of the multilayer films was observed by FESEM, which is essential for the device formation on the electrode. Figure 6.6 illustrates the FESEM micrographs of NAN multilayer structures for pristine and N ion implanted films with 1×10^{14}, 5×10^{14}, 1×10^{15}, 5×10^{15} and 1×10^{16} ions/cm^2.

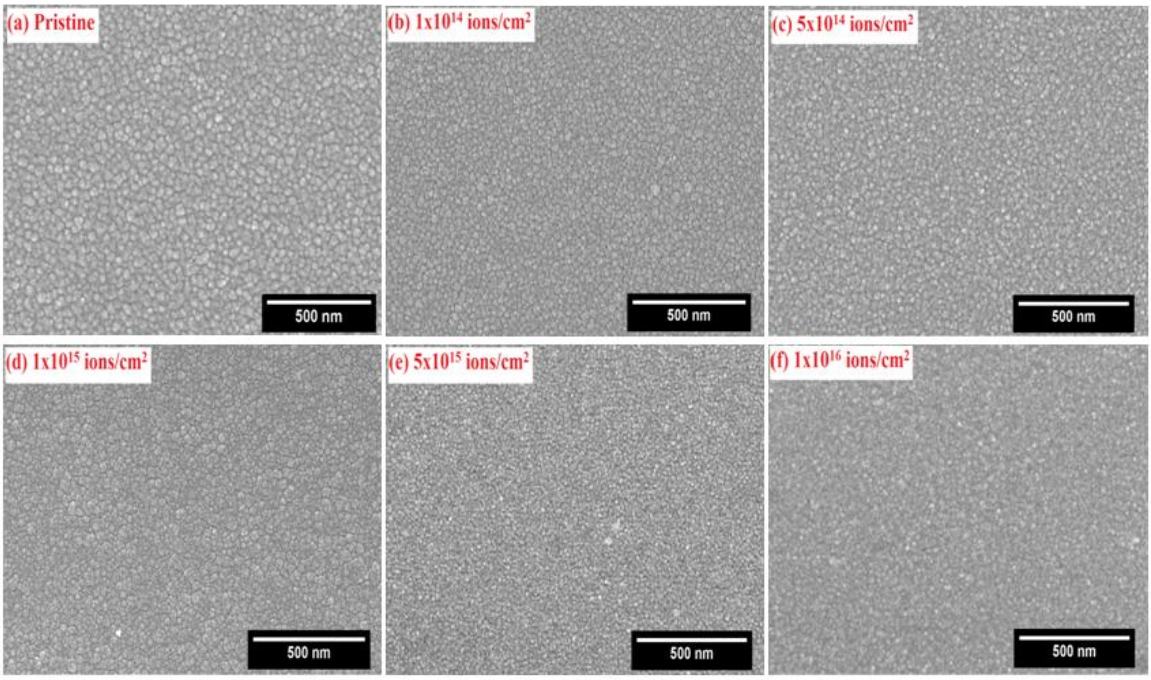

Figure 6.6: SEM images of the pristine NAN and N-NAN multilayer films with different ion fluences.

All images were recorded at 100k× magnification. It can be noticed from the images that films are composed of spherical shape nanoparticles with 15−30 nm size. The top surface of the pristine film shows regularly arranged particles with smooth surface. On ion implantation, the surface roughens with reduction in particle size. This phenomenon can be understood by existing studies that suggest sputtering of atoms during implantation process. The sputtering causes the removal of atoms from the upper surface and resulting

in decrease in particle size and consequently the surface is also becoming rougher. Similar morphology has been observed for the Nb doped TiO_2 films [190].

Figure 6.7 exhibits a three dimensional AFM images of the pristine NAN and N-NAN multilayer films. The scanning area for these measurements was taken as 2×2 μm^2. The top surface depicts continuous multilayer films. The obtained surface roughness are 1.6 nm, 1.6 nm, 1.7 nm, 1.4 nm, 1.1 nm and 0.7 nm for the pristine, 1×10^{14}, 5×10^{14}, 1×10^{15}, 5×10^{15} and 1×10^{16} ions/cm^2 respectively. The root mean square (rms) roughness of the pristine sample was observed as 1.6 nm, which first increases to 1.7 nm for 1×10^{15} ions/cm^2 fluence and then decreases to 0.7 nm at 1×10^{16} ions/cm^2 fluence. Initially, when the energetic N^+ ions are incident on the top surface of NAN multilayer structure they sputter the atoms from the NTO layer, which causes slight increase in rms roughness. As the energy of N^+ ions further increases, they behave as a cutting tool for the irregularities and microstructures which exist on the surface and consequently the surface roughness decreases. Ion beam interaction, both irradiation and implantation, modifies the surface roughness of film. It results in the smoothening of the surface of specimen and this has been reported by many research groups [233,255,256].

Thomas *et al.* [256] observed the smoothening of surface after irradiation and explained that the roughness can be reduced due to irradiation induced surface diffusion or volume diffusion. The material transport in ion beam interactions leads to the surface diffusion and hence the reduction in roughness. Hence, the development of NAN electrodes with use of ion implantation leads to smoother surface, which promotes their applicability in radiation environment [50]. NAN films show an average surface roughness of approximately 1.5 nm which is lower than that of a commercial ITO film (≈2.5 nm) and hence is more suitable for TCE applications in optoelectronic devices because higher roughness leads to more scattering of light from the top surface and may reduce flow of current between anode and cathode [257].

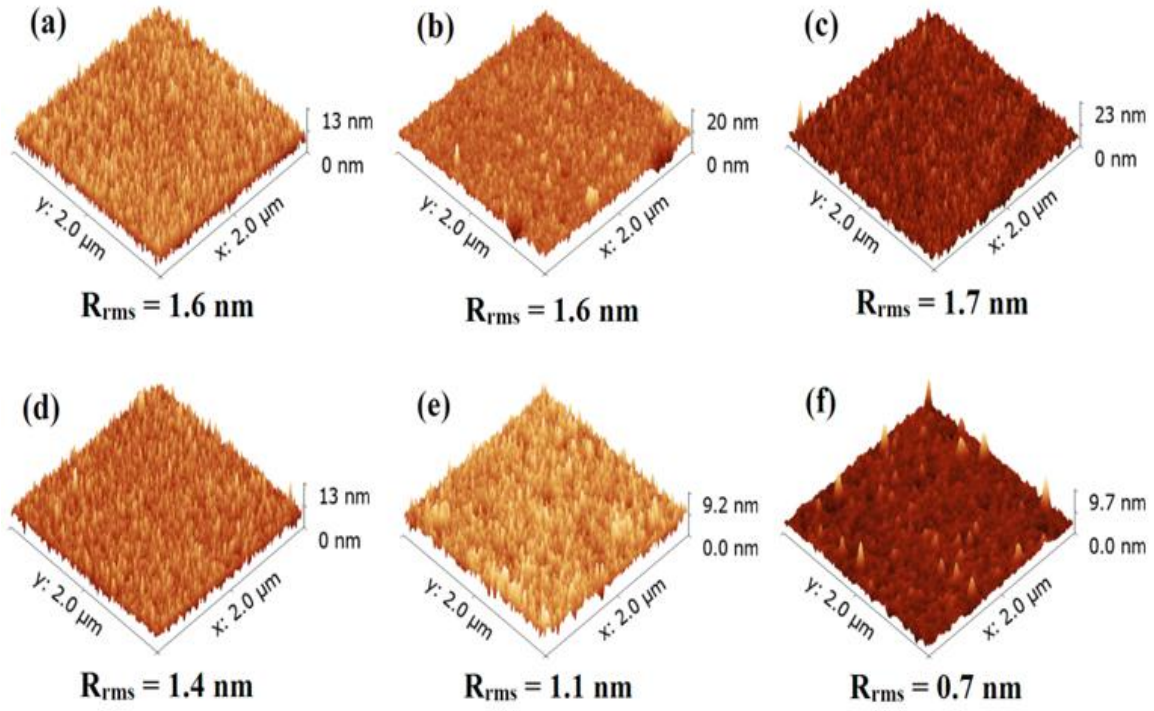

Figure 6.7: Three dimensional AFM images of the NAN multilayer films: (a) pristine, and N ion implanted with fluence of (b) 1×10^{14} , (c) 5×10^{14}, (d) 1×10^{15}, (e) 5×10^{15} and (f) (1×10^{16} ions/cm^2 fluence.

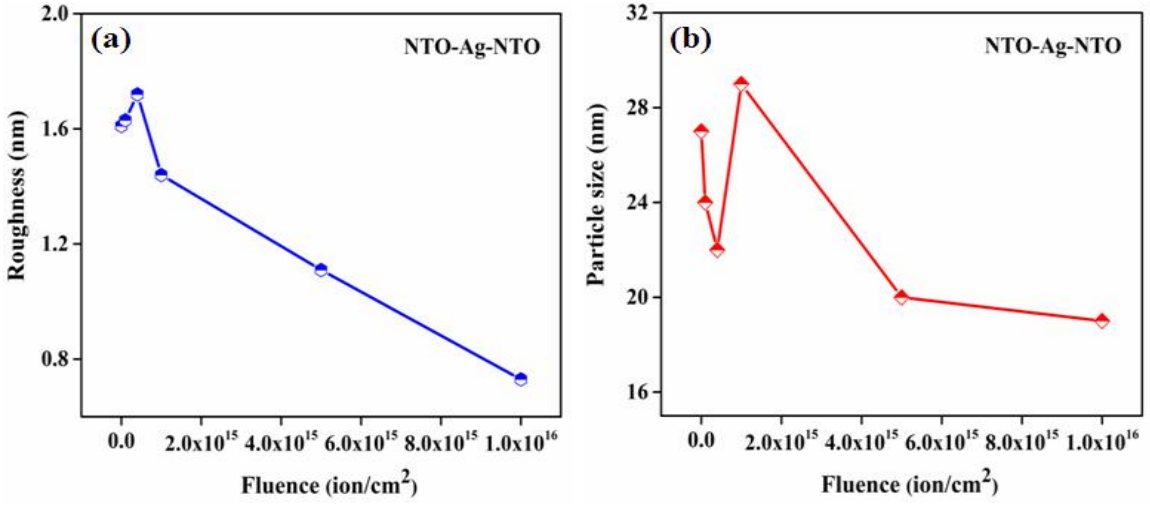

Figure 6.8: Morphology of NAN multilayer structure with N^+ ion implantations: (a) Ion fluence vs Surface roughness and (b) ion fluence vs particle size.

The surface roughness measured from AFM and particle size calculated from SEM micrographs of NAN multilayer structures at various ion fluences are shown in figure 6.8 (a) and (b) respectively. It is clear from the roughness curve and particle size distribution that higher particle sizes of specimen correspond to higher roughness and lower particle

size correspond to lower roughness. A small shift was observed in the flat region of transmittance of NAN films and is mainly attributed to variation in surface morphology. Initially, the optical transmittance reduced by the increased optical scattering of light is due to higher surface roughness [258] and for higher fluences it dominated by the decreasing band gap.

6.5.4 Optical analysis

The optical transmittance is an important parameter for the transparent electrode and it should be as much as high to transmit visible light. Figure 6.9 (a) shows the transmittance spectra of pristine and N ion implanted NAN multilayer structures in the visible range (350 nm<λ<800 nm) of light with varying fluence. The transmittance of pristine film is ~83% and it decreases to ~81% as the fluence increases to 1×10^{16} ions/cm^2. A standard ITO film (Sigma-Aldrich, Product Number: 703192, CAS Number: 50926-11-9 with sheet resistance of 8−12 Ω/□) shows an optical transmittance of ~81%. Therefore, the results of NAN films with implantation are comparable with commercial available ITO and ITO/Ag/ITO [259] and AZO/Ag/AZO [260].

The optical band gap of the NAN multilayer structure is determined by using the following standard relation [196].

$$\alpha h\nu = B(h\nu - E_g)^n \quad (6.2)$$

Where α is absorption coefficient, hν photon energy, B is a constant and Eg is the optical band gap. The value of n is chosen as 2, because TiO_2 is an indirect band gap semiconductor.

Absorption coefficient (α) was measured by the Beer–Lambert's relation [222].

$$\alpha = \frac{1}{d}\ln\frac{1}{T} = \frac{2.303}{d}A \quad (6.3)$$

Where A is absorbance of NAN multilayer film, T is transmittance and d is thickness of the film.

Using the absorption coefficient the band gap of NAN films has been calculated.

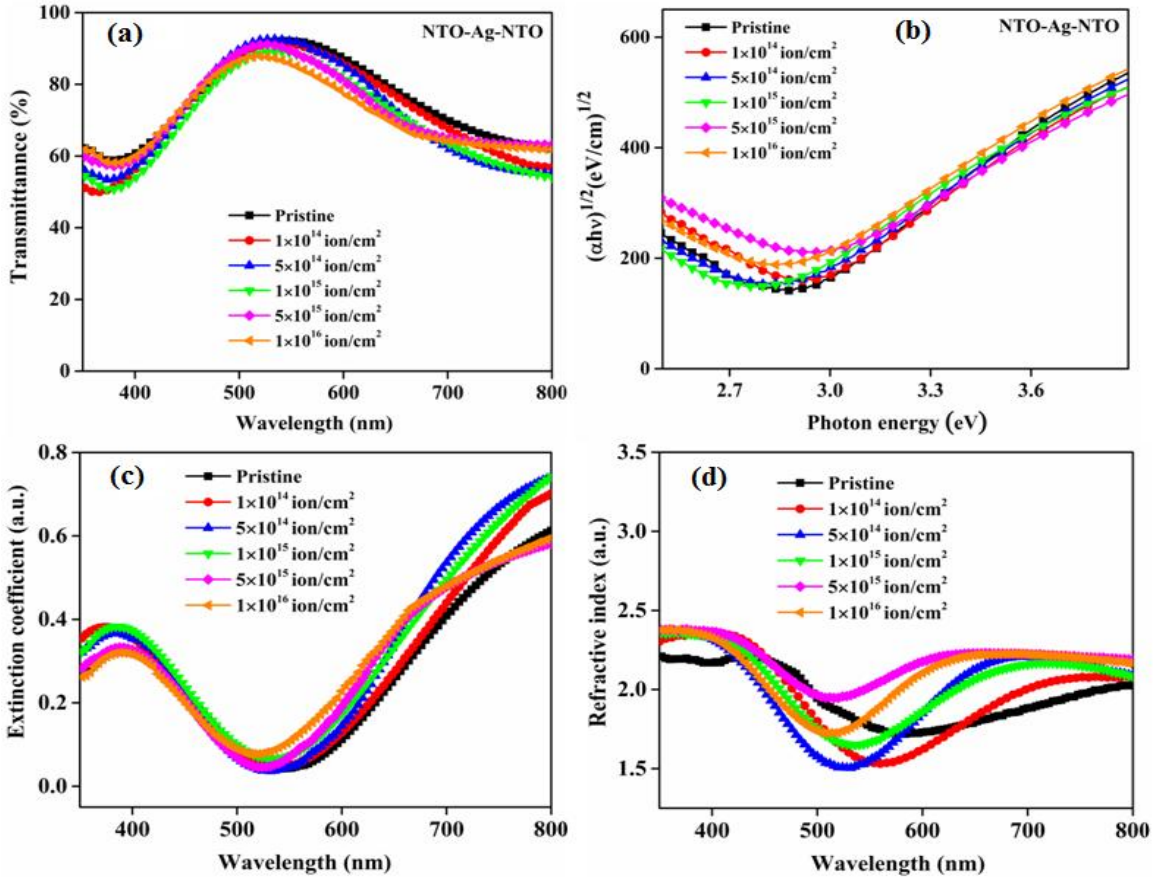

Figure 6.9: (a) Transmittance, (b) Tauc plot, (c) extinction coefficient and (d) refractive index of pristine NAN and N-NAN multilayer films with different ion fluences.

Figure 6.9 (b) depict the Tauc plot between $(\alpha h\nu)^{1/2}$ and incident photon energy ($h\nu$) for NAN films. The band gap of the pristine film is 2.71 eV and decreases to 2.57 eV at 1×10^{16} ions/cm^2. Generally, the band gap decreases on ion implantation which leads to improve the electrical conductivity. Appearance of Ti^{3+} state of TiO_2 in NTO on substitutional doping of N and increased grain size on implantation are responsible for band gap narrowing for N-NAN system. Morikawa *et al.* [261], Wu *et al.* [262] and Asahi *et al.* [211] have investigated N doping in TiO_2 and found that band gap is narrowing with increasing N concentration and it was suggested that band gap is decreasing due to merging of N 2p states with 2p states of O. Normally, ion implantation causes sputtering of Ag ions from the mid layer to the oxide layers which generates scattering centres for the incident light and implantation also creates defects resulting in more absorption and decreased transparency. The refractive index plays an important role for tuning the

transmittance and antireflective effect in optical materials and can be calculated by following relation [223].

$$n = \sqrt{\frac{4R}{(1-R^2)} - k^2} + \left(\frac{1+R}{1-R}\right) \tag{6.4}$$

Where k is the extinction coefficient and R is reflectivity of multilayer structure. Extinction coefficient is defined by:

$$k = \frac{\alpha\lambda}{4\pi} \tag{6.5}$$

Where λ is wavelength and α is absorption coefficient of NAN films. The extinction coefficient of NAN films vary from 0.27 to 0.32 as shown in table 2. The refractive index of pristine specimen is obtained as 2.11 and it increases to 2.21 for 5×10^{15} ions/cm^2 and then decreases to 2.18 for 1×10^{16} ions/cm^2 fluence. The RMS surface roughness, transmittance at wavelength of 550 nm, extinction coefficient, refractive index and band gap of pristine and implanted NAN films are give in table 6.2. Extinction coefficient and refractive index curves are presented in the figure 6.9 (c) and (d) respectively.

Table 6.2: Surface roughness (RMS), transmittance (at 550 nm), extinction coefficient, refractive index and band gap of pristine NAN and N-NAN multilayer films with different ion fluences.

Samples details	RMS (nm)	Transmittance (%) at 550 nm	Extinction coefficient (k)	Refractive index (n)	Band gap (eV)
0	1.61±0.08	92	0.27	2.11	2.71±0.01
1×10^{14}	1.63±0.08	91	0.29	2.12	2.68±0.01
5×10^{14}	1.72±0.09	90	0.32	2.15	2.65±0.01
1×10^{15}	1.44±0.07	88	0.32	2.16	2.63±0.01
5×10^{15}	1.11±0.05	89	0.30	2.21	2.59±0.01
1×10^{16}	0.73±0.03	86	0.31	2.18	2.57±0.01

6.5.5 Electrical analysis

Electrical performance of the proposed alternative TCE was compared with the standard ITO films and was found to be stable in a broad temperature range. The transport properties of as prepared films were investigated by using the Hall measurement with Vander Pauw method [198]. The pristine NAN film exhibits resistivity of 9.7×10^{-5} Ω cm and sheet resistance of 12.12 Ω/□ at room temperature, and these results are better than commercial ITO film (Product Number: 576360, CAS Number: 50926-11-9). The

resistivity of a conductor is given by: $\rho = 1/n_e \mu e$, where n_e is carrier concentration density, μ is mobility; e is charge on the electron. The resistivity of specimen decreases with increase in charge carrier density and the mobility. For the OMO structure, the lower resistivity of the order of ~10^{-4} or ~10^{-5} Ω cm is mainly obtained because of inter metal layer (Ag). This metal layer needs to be thick enough to provide structural continuity and it should be thin as possible to reduce absorption of light. This thickness is 8−9 nm, as discussed in the introduction part. The oxide layer thickness should be chosen as to minimize the surface plasmon coupling absorption [263]. Hence, the selection of thickness for both layers oxide and metal is crucial to obtain low resistivity and high transparency. Therefore, in the present case, the multilayer was adopted as 35 nm/9 nm/35 nm to address both issues and tuning of thickness of both metal and metal oxide layers, which helped us to achieve higher FOM for the prepared TCE. The total resistance for the multilayer structure is obtained by using parallel connection method of three resistances and is given as below:

$$\frac{1}{R_{total}} = \frac{1}{R_{metal}} + \frac{1}{R_{oxide}} + \frac{1}{R_{oxide}}$$

As the two oxide layers are deposited using same parameters, so their resistance can be taken as equal. Hence, above equation can be written as;

$$\frac{1}{R_{total}} = \frac{1}{R_{metal}} + \frac{2}{R_{oxide}}$$

Since $R_{oxide} \geq 1000 R_{metal}$ so $R_{total} \approx R_{metal}$ [45].

The resistance of the oxide layer is much higher than the Ag layer, thus the total resistance of embedded multilayer would be equal to middle Ag layer. Hence, the high conductivity of the NAN multilayer films comes entirely from the middle metal layer. The results of resistivity and sheet resistance confirm the continuous formation of Ag layer.

Charge carrier concentration, mobility and sheet resistance have been measured for the specimens in temperature ranging from 80 K to 340 K at an interval of 20 K and shown in figure 6.10. Resistivity and sheet resistance were found to increase with temperature

which is a characteristic of degenerate semiconductors. Since, the upper and lower layers in NAN structure is Nb doped TiO_2 (NTO), this gives the system a degenerate semiconductor behavior. Many studies have reported the n-type degenerate semiconductor behavior in Nb doped TiO_2 [264], B-doped ZnO films [265] and SnO_2/Ag [266] systems. In this study, Nb doping in TiO_2 and diffusion of Ag atoms into NTO, both are responsible for variation in resistivity and sheet resistance. A slight variation in carrier concentration and mobility was observed with temperature. The mobility in NAN system is a combined effect of mobility in NTO and Ag layer thickness. The variation in mobility occurs due to grain boundary effect; interface and ionized impurity scattering [249]. Charge carrier density and mobility in degenerate semiconductors do not change with temperature but changes occur due to scattering from interface and ionized impurities. For our films, small variation in n_e and μ is observed at low temperatures, indicating small grain boundary scattering and less thermally activated conductance [267] but at high temperatures n_e and μ change irregularly [268].

Figure 6.11 shows resistivity, carrier concentration and mobility of pristine and N^+ ion implanted NAN mutilayer films for 1×10^{14}, 5×10^{14}, 1×10^{15}, 5×10^{15} and 1×10^{16} ions/cm^2 flence at room temperature. The resistivity changes from 9.7×10^{-5} Ω cm to 5.52×10^{-5} Ω cm as the fluence increase from 0 to 1×10^{16} ions/cm^2. Simultaneously, carrier concentration increases from 7.48×10^{21} cm^{-3} to 9.72×10^{21} cm^{-3} and mobility values improve from 8.6 cm^2/V-s to 11.67 cm^2/V-s. Figure 6.12 illustrates the sheet resistance and Haacke's FOM variation as a function of ion fluence. It can be seen from the curves that sheet resitance for the prstine specimen is 12.12 Ω/□ and it is reducing to 6.9 Ω/□ at the maximum fluence of 1×10^{16} ions/cm^2. Meanwhile, FOM for as deposited sample was found to 12.7×10^{-3} Ω^{-1} and it is increasing with the fluence and reaches to a maximum of 18×10^{-3} Ω^{-1} for highest fluence of 1×10^{16} ions/cm^2. Implantation of N^+ and Ar^+ ions in optimized TiO_2/Ag/TiO_2 (45 nm/9 nm/45 nm) multilayer structure with improved electrical conductivity and FOM is given in chapter 5.

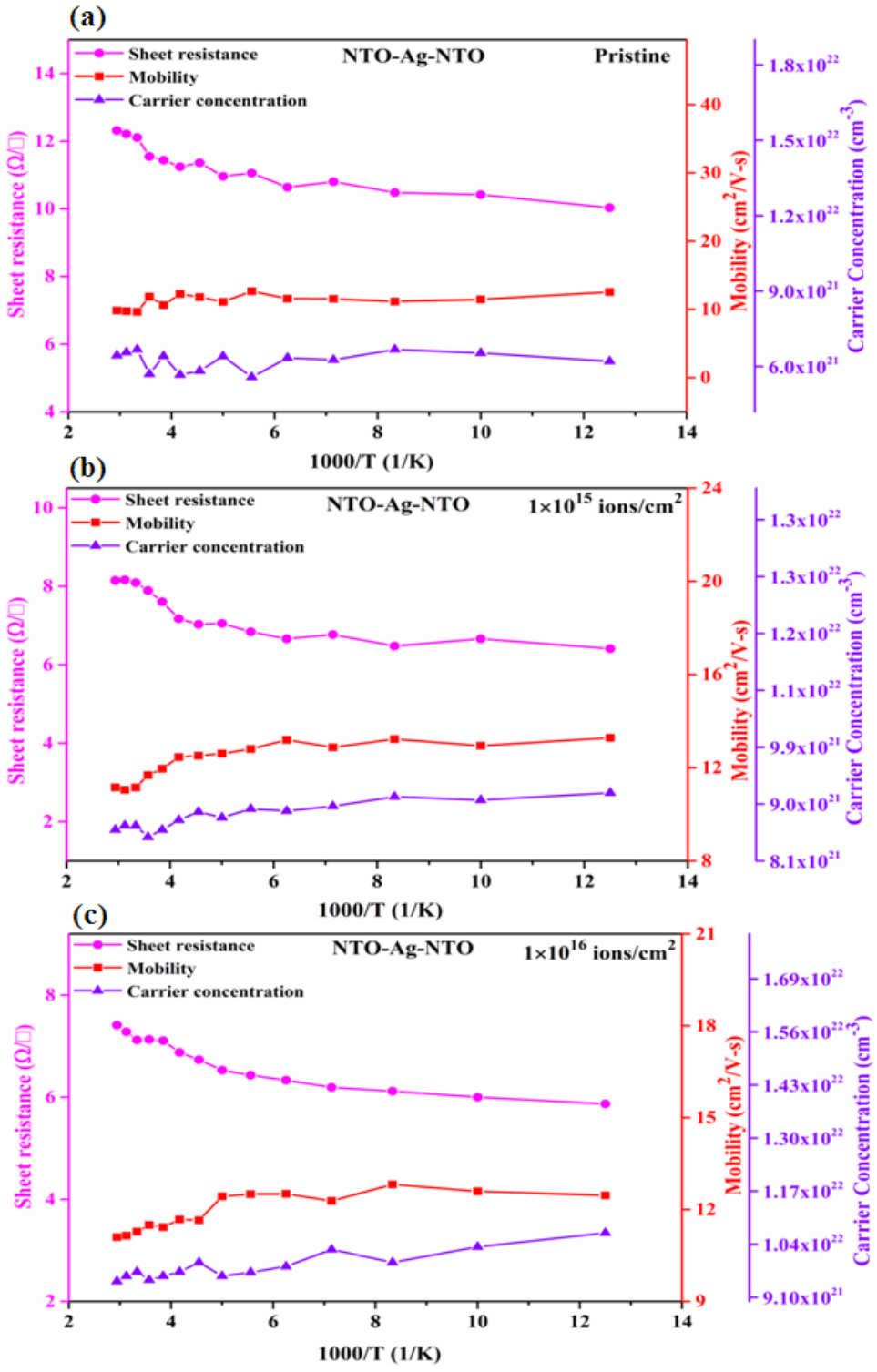

Figure 6.10: Resistivity, carrier concentration and Hall mobility of pristine NAN and N-NAN multilayer films for different fluence with temperature variation (a) pristine, (b) 1×10^{15} and (c) 1×10^{16} ions/cm^2.

Table 6.3: Room temperature mobility, Carrier concentration, resistivity, sheet resistance and Haacke FOM of pristine NAN and N-NAN multilayer films with different ion fluences.

Samples details	Mobility (cm^2/V-s)	Carrier concentration (cm^{-3})	Resistivity (Ω.cm)	Sheet resistance (Ω/□)	Haacke FOM (10^{-3} $Ω^{-1}$)
0	8.61	7.48×10^{21}	9.69×10^{-5}	12.12	12.7
1×10^{14}	8.29	6.82×10^{21}	1.10×10^{-4}	13.75	10.8
5×10^{14}	9.11	7.95×10^{21}	8.65×10^{-5}	10.81	12.9
1×10^{15}	9.92	8.73×10^{21}	7.22×10^{-5}	9.01	14.7
5×10^{15}	10.53	9.53×10^{21}	6.23×10^{-5}	7.79	16.4
1×10^{16}	11.67	9.72×10^{21}	5.52×10^{-5}	6.92	18.0

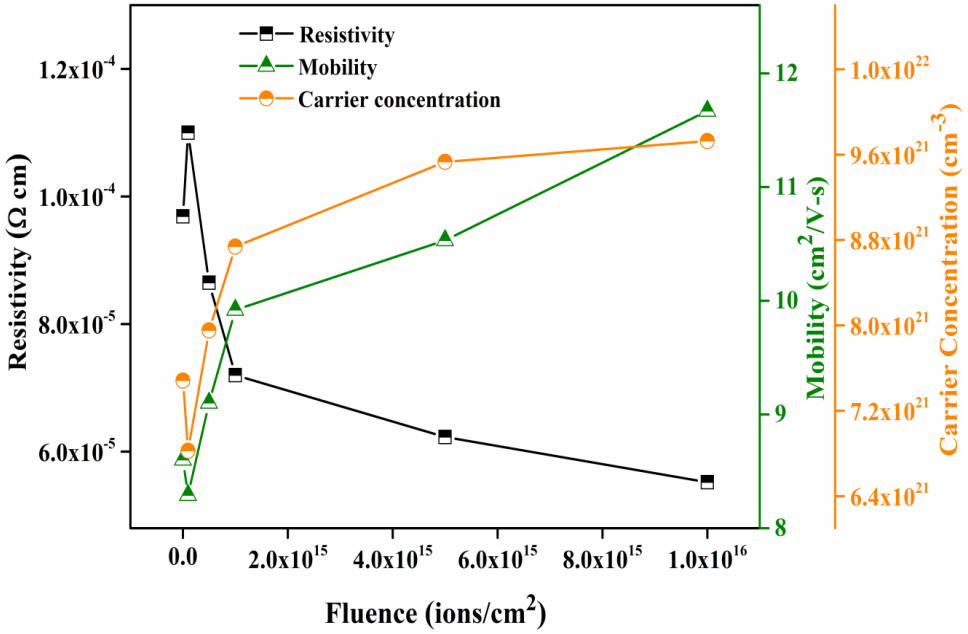

Figure 6.11: Resistivity, carrier concentration and Hall mobility of pristine NAN and N-NAN multilayer films with different ion fluences.

There are many factors which are responsible to get such superior electrical properties like resistivity of 5.52×10^{-5} Ω cm and sheet resistance of 6.9 Ω/□ with >81% optical transmittance for N-NAN films. The Nb doped TiO_2 (NTO) layers were chosen as upper and lower layers of NAN structure, which causes to appear Ti^{3+} chemical state of Ti and as a result the band gap is reduced. Then, these specimens were exposed to N^+ ion implantation to further enhance the electrical conductivity. The main effect of this implantation was, N^+ ions substituted the oxygen ions into the TiO_2 lattice and inserting new electronic states above the valance band.

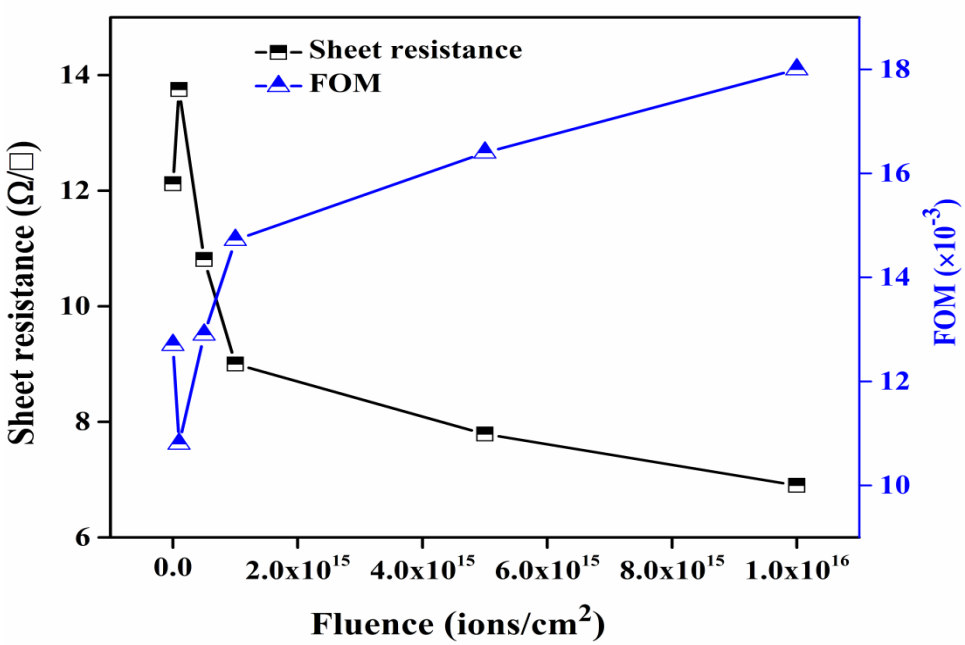

Figure 6.12: Sheet resistance and Haacke FOM of pristine NAN and N-NAN multilayer films with different ion fluences.

Appearance of Ti^{3+} states of TiO_2 on Nb doping and arising of new electronic states just the valance band after N^+ implantation, both are responsible for band gap narrowing that is confirmed by Tauc's plot shown in figure 6.9 (b). The lower band gap leads to lower resistivity and sheet resistance of NAN films. XPS measurements studies confirm that the N^+ ions replaces the O sites by showing the N peak at ~396 eV, reported by many researchers [211,217] and existence of Ti^{3+} state, positioned at 457 eV binding energy. Besides the substitutional impurity or capturing of electrical active lattice sites, ion implantation generates or anneals the defects and hence causing the changes in carrier density and mobility [128,133]. The structural, optical and electrical properties of metal oxides can be altered by implantation [128,133,226]. It has been suggested that, besides N implantation, creation and annealing of charged oxygen vacancies may also help to get lower resistivity. Apart from this, the change in microstructure and decreasing surface roughness on ion implantation may also contribute to improve electrical conductivity. The absorption of oxide donors [226] decreases due to reduced grain boundaries and resulting in higher carrier concentration and mobility. Table 6.3 gives the mobility, carrier concentration, resistivity, sheet resistance and Haacke FOM measured at room temperature for pristine and implanted NAN films.

6.5.6 X-ray Photoelectron Spectroscopy

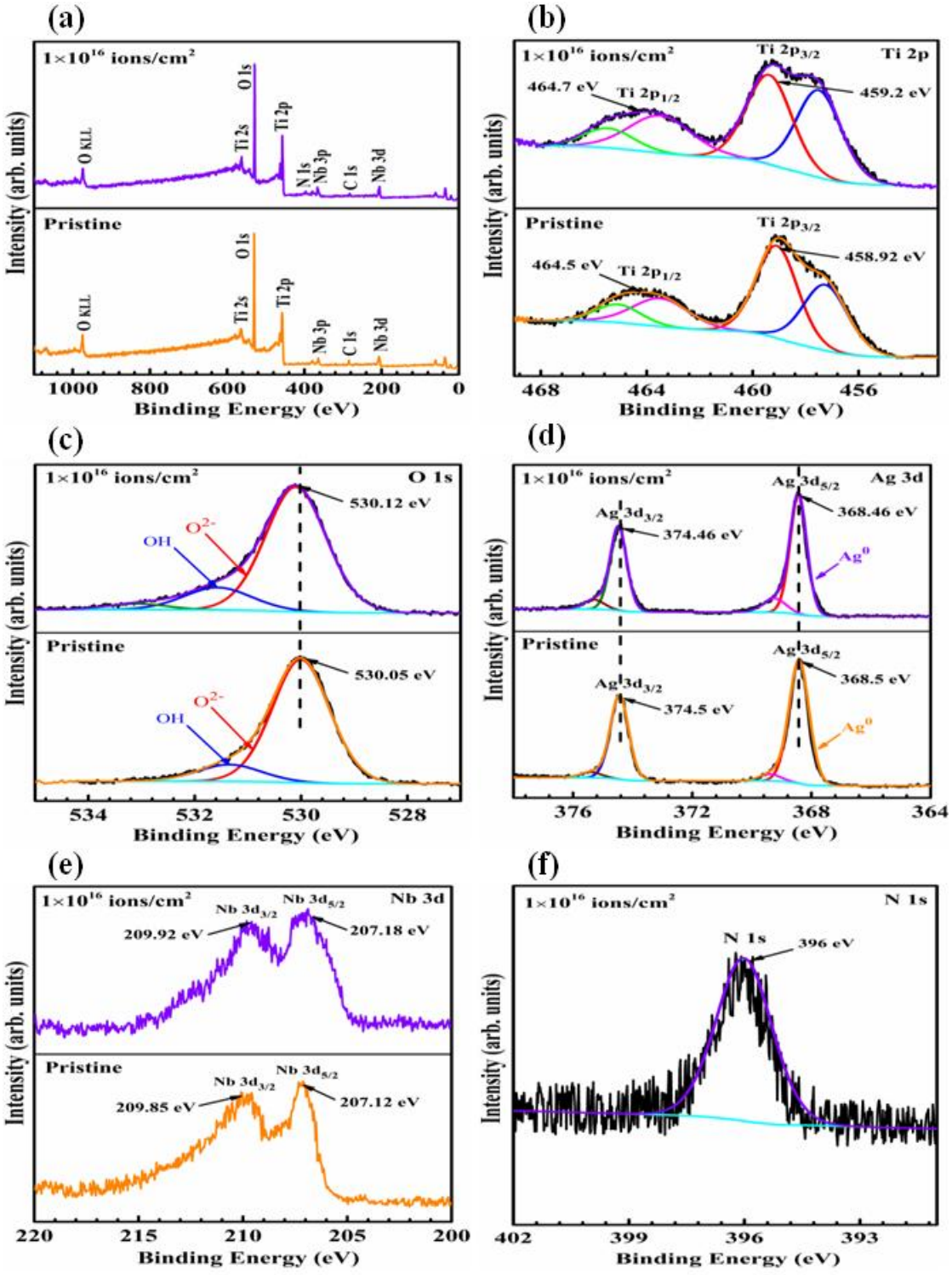

Figure 6.13: XPS spectra of pristine NAN and N^+ implanted NAN multilayer films with the fluence of 1×10^{16} ions/cm^2 (a) survey scan, (b) Ti 2p, (c) O 1s, (d) Ag 3d, (e) Nb 3d and (f) N 1s.

XPS measurements have been performed on pristine NAN and N-NAN multilayer structures to study the chemical states and stoichiometry using surface scan and depth profiling mode. The specific elemental signals were taken from all three layers by etching of previous layers and existence of Ti, Nb, O, Ag and N elements were confirmed in the respective layers. Figure 6.13 (a) illustrates the survey scan of NAN pristine and N-NAN films, which exhibit high intensity signals of Ti, O and Ag and low intensity signals of Nb, N and C. The C peak arises due to ex-situ transfers of sample to XPS chamber.

Figure 6.13 (b) represents the high resolution scan of Ti 2p for first layer (top) of pristine NAN and N-NAN films. The peak of Ti-$2p_{3/2}$ of pristine film appeared at 458.92 eV [200,201] The peak positions of Ti-$2p_{3/2}$ and Ti-$2p_{1/2}$ for first NTO layer of pristine sample agreed with the fact of substitution of Ti atom by Nb^{5+} in TiO_2 lattice [269]. On implantation the Ti 2p peak shows peak asymmetry and is deconvoluted in two peaks; one at 459.2 eV (Ti^{4+}) and another at 457 eV, a low energy shoulder assigned to Ti^{3+} peak [202]. The binding energies difference of Ti-$2p_{3/2}$ peak shifted by 0.3 eV on implantation due to change in nature of interaction of Ti with anions in case of pristine NAN and N-NAN structures. The N ion implantation produces considerable modifications in NTO due to dopant-induced strain. The observed binding energy shifts in N implanted NTO is assigned to enhancement of covalent behavior of bond between N and Ti [214].

Figure 6.13 (c) represents the high resolution scan of O 1s of pristine NAN and N-NAN films. The peak fitting of O 1s of pristine film results in two consecutive peaks, one positioned at 530.05 eV, assigned to O^{2-}, bulk oxygen in TiO_2 [270] and another peak positioned at 531.5 eV, corresponds to OH groups existing on the surface. The peaks of O 1s of N-NAN positioned at 530.12 eV and 530.6 eV correspond to O^{2-} and OH groups respectively. No significant change was observed in O 1s peaks, which indicates that the behavior of the oxygen is not changing on implantation. Figure 6.13 (d) represents the core level spectra of Ag 3d of pristine NAN and N-NAN multilayer films. The XPS signals of Ag were taken from middle layer of NAN multilayer structure after etching of first layer by Ar sputtering. The peaks observed at 368.5 eV and 374.5 eV in the Ag spectra are assigned to pristine Ag $3d_{5/2}$ and Ag $3d_{3/2}$ respectively. These peaks were slightly shifted towards lower binding energy for N-NAN films and appear at 368.46 eV

(Ag $3d_{5/2}$) and 374.46 eV (Ag $3d_{3/2}$). This shift may occur because of interaction of Ag atoms with Ti, Nb and O ions at the interface [219]. The XPS spectra of Ag confirm the metallic nature of the middle metal layer ensuring the stability of silver layer against the oxidation. This stability of Ag layer will contribute to electrical behavior of both pristine and implanted samples. Figure 6.13 (e) illustrates the high resolution scans of XPS spectra of Nb 3d for the both samples. Pristine film exhibits two peaks at 207.12 eV and 209.85 eV, are attributed to Nb $3d_{5/2}$ and Nb $3d_{3/2}$, respectively. The spin-orbit splitting between these two peaks is 2.73 eV. The Nb in NTO of the upper and lower films is found to be in Nb^{5+} state [176]. Figure 6.13 (f) exhibits the high resolution scan of N 1s that was obtained from N implanted NAN films at the highest fluence 1×10^{16} ions/cm^2. For this specimen the N peak appeared at ~396 eV suggesting replacement of O sites in the TiO_2 lattice by N [217]. This XPS study of NAN pristine and implanted films confirmed the presence of Ti, O, Nb, Ag and N in multilayer structure. The Nb core level spectra revealed the substitution of Ti atoms by Nb atoms and formation of Nb-O bond. The N core level spectra explain the substitution of O ions by N ions, resulting in the decrease in the band gap and improving the electrical conductivity with higher FOM.

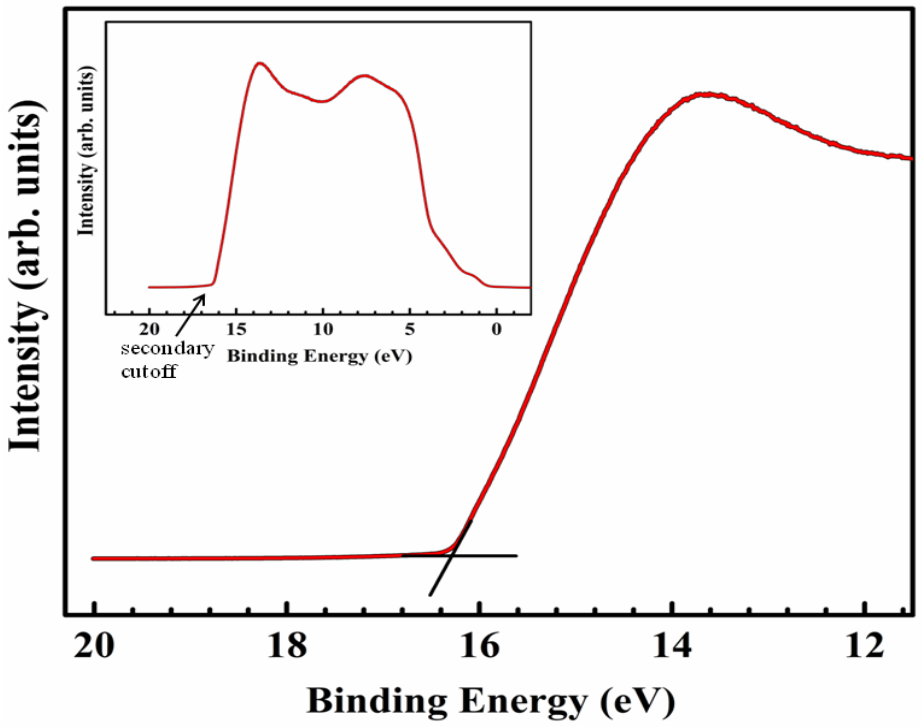

Figure 6.14: UPS measurements of pristine NAN multilayer films.

Figure 6.14 exhibits the UPS spectrum for the pristine NTO/Ag/NTO films. The binding energy of the electrons right at secondary cutoff is found using the secondary edge. The work function of the films has been determined directly from the graph by taking the difference of the energy of the UV photons (21.2 eV in this case) and the binding energy of secondary cutoff (16.57 eV in the case of NAN films), i.e.

Φ_{NAN} = 21.2 eV-16.57 eV = 4.63 eV.

The work function of NAN films to be used as transparent electrode in photovoltaics can be tuned according to work function of active layer and hence the efficiency of device can be improved. It has been reported that high work function of TCO leads to higher efficiency; higher open circuit voltage and larger photo generated current [271].

The conducting mechanism of NAN multilayer structure can be understood by the energy level diagram of NTO and Ag. Figure 6.15 shows the E_f alignment at the interface in multilayer structure. NAN films are prepared using two materials with different work functions NTO (4.8 eV) and Ag (4.4 eV). Before contact the E_f of both materials are not aligned but when two materials come into contact at interface the electrons are transferred from Ag to NTO due to band bending as alignment of E_f occurs. This explains the conduction in the multilayer through the middle Ag layer.

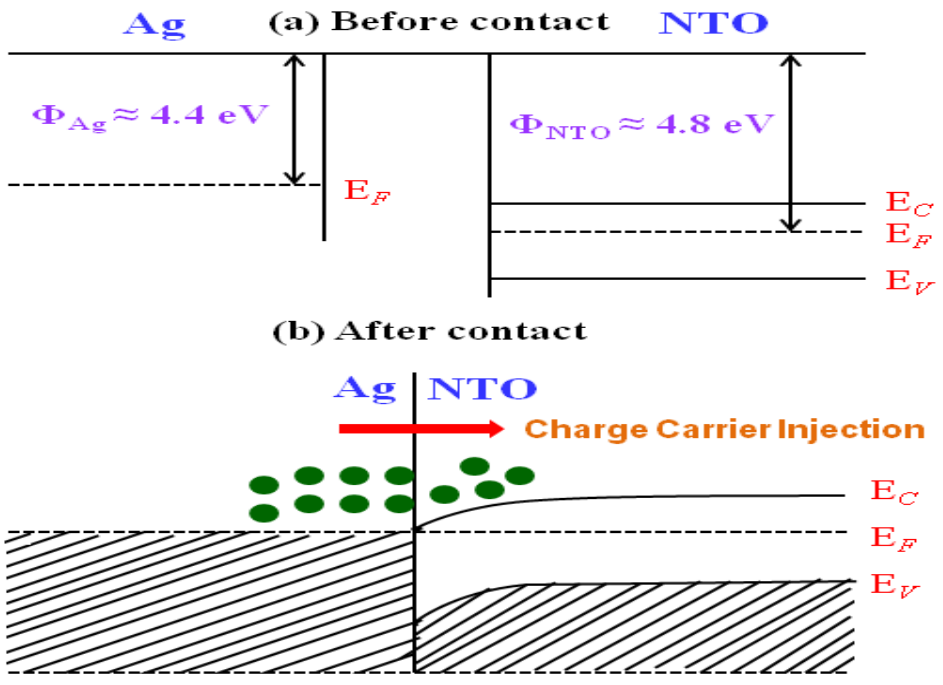

Figure 6.15: The energy level diagrams of NTO and Ag before and after contact and show the E_f alignment at the interface.

6.6 Ar^+ (100 keV) Ion Implantation in NTO/Ag/NTO Multilayer Thin Films

The optimized pristine NAN (35 nm/9 nm/35 nm) films were implanted with 100 keV Ar^+ ions with fluence range (1×10^{14}– 1×10^{16} ions/cm^2) at room temperature. The Ar^+ implanted NAN multilayer films will be referred hereafter as A-NAN films. The stopping range of Ar^+ ions was ~58 nm measured by the SRIM-2010 software, which is less than the total film thickness (100 nm). The nuclear energy loss (S_n) and electronic energy loss (S_e) values for 100 keV Ar^+ ions were obtained as 1.54 and 0.97 eV/Å respectively.

6.7 Results and discussion

6.7.1 Structural Properties

Figure 6.16 illustrates the X-ray diffraction pattern of NTO/Ag/NTO (NAN) multilayer structure with varying Ar^+ ion fluences. From the pattern it can be seen that the TiO_2 diffraction planes are absent due to room temperature deposition of NAN structures. Ag diffraction planes of (111), (200), (220) and (311) are present at 38.16˚, 44.25˚, 64.65˚ and 77.53˚ positions respectively, matching well with the JCPDS No. 04-0783. The intensity of XRD peaks first decreases with the fluence and then increases later. Thus we can say that the crystallinity of the silver middle layer has increased for highest fluence of 1×10^{16} ions/cm^2 due to annealing effect of ion implantation process. Debye–Scherrer formula ($0.9\lambda/\beta\cos\theta$) has been used to determine the crystallite size of the silver particles and it varies from 8.1 nm to 7.1 nm as the fluence increased from 0 to 1×10^{16} ions/cm^2. Meanwhile, the lattice parameters changes from 4.088 Å to 4.095 Å which is closely matches with the standard value of 4.086 Å. The compressive residual stress varies from -0.108 to -0.570 with the fluence. The crystallite size, lattice constants and residual stress of pristine and N-NAN multilayer films are given in table 6.4. Implantation causes stress in the system which can obstruct the growth of crystallites. From table 1 it can observed that more the stress, less the particle size and vice versa. Reports have revealed [229,230] that Ar^+ ion implantation can be used to regulate the stress in the sample.

Table 6.4: FWHM, crystallite size, lattice constants and residual stress of Ag (111) plane of pristine NAN and A-NAN multilayer films with different ion fluences.

Samples details	FWHM (deg.)	Crystallite size (nm)	Lattice constant c (Å)	Residual Stress (GPa)
0	1.084±0.06	8.1±0.5	4.088±0.007	-0.108
1×10^{14}	1.252±0.06	7.0±0.4	4.090±0.005	-0.228
5×10^{14}	1.103±0.07	8.0±0.5	4.089±0.005	-0.171
1×10^{15}	1.163±0.05	7.6±0.3	4.092±0.006	-0.342
5×10^{15}	1.216±0.11	7.3±0.6	4.093±0.006	-0.401
1×10^{16}	1.241±0.14	7.1±0.8	4.095±0.004	-0.513

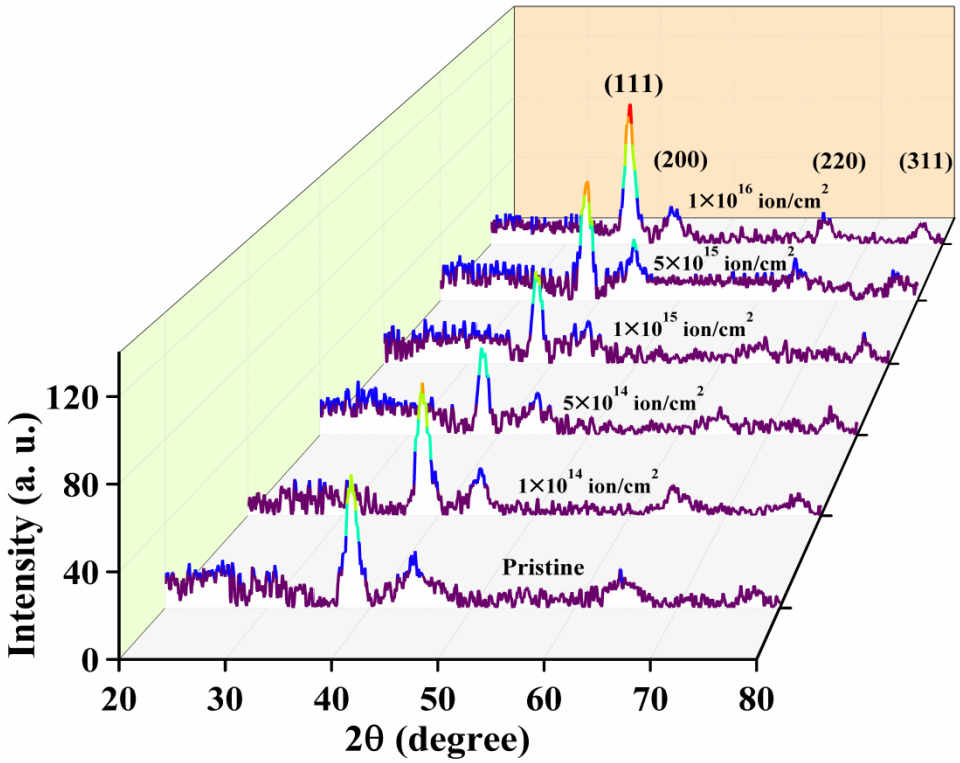

Figure 6.16: XRD pattern of NAN multilayer films with different ion fluences.

6.7.2 Rutherford Backscattering Spectrometry

Rutherford Backscattering Spectrometry (RBS) is technique which is used to determine the thickness, composition and structure of the material by analyzing the backscattered beam of alpha particles (~2 MeV) impinging on the material. Figure 6.17 demonstrate the RBS spectrum of pristine NAN and Ar^+ implanted NAN (A-NAN) film with highest fluence of 1×10^{16} ions/cm^2. RBS spectrum revealed that the Ti, O, Nb and Ag elements

were present in the pristine NAN and A-NAN multilayer films. The concentration of Nb which is used as dopant in TiO_2 was estimated ~3.7 at.% from RBS data. The thickness of top, middle and bottom layer have been measured using simulated curve and obtained as NTO (35±4 nm)/Ag (9±1 nm)/NTO (35±4 nm). The layer formation of NAN multilayer films with top and bottom NTO and middle Ag was confirmed by RBS results. At the interface of NTO and Ag layers some of Ag ions get diffused in to NTO layers and implantation causes slight variation in this diffusion length [249].

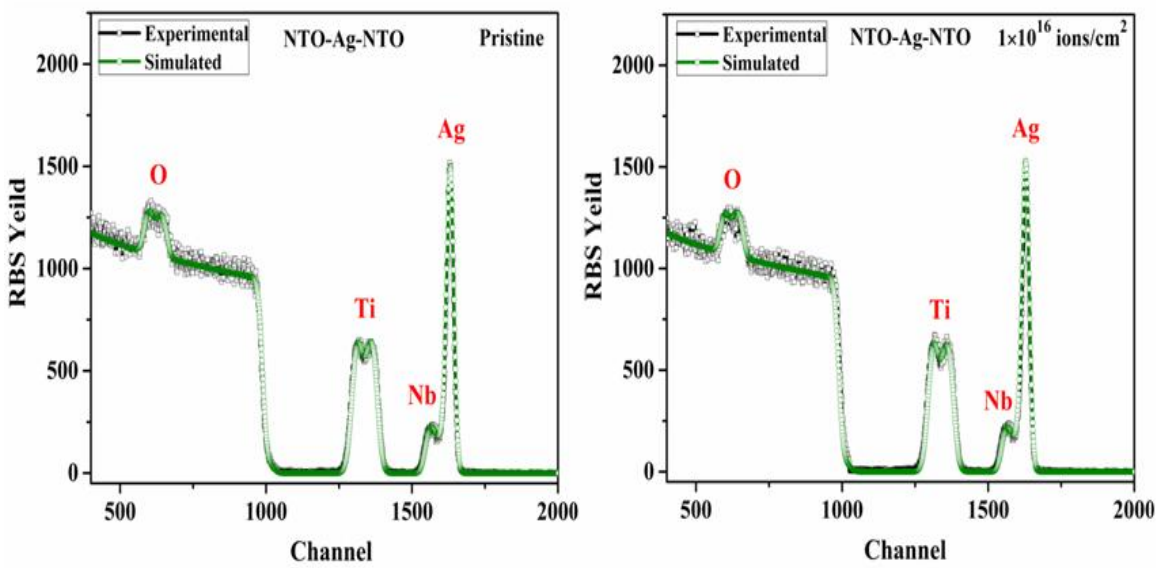

Figure 6.17: RBS spectra of pristine NAN and A-NAN multilayer films, with fitted profile.

6.7.3 Surface characterization

Field emission scanning electron microscopy (FESEM) gives the morphological information of specimen at high magnifications up to ~500,000×, with high depth of field than conventional scanning electron microscopy (SEM). Figure 6.18 shows the FESEM images of pristine NAN and A-NAN multilayer films taken at the 100k× magnification. A uniform and smooth fabrication of top layers of NAN multilayer structures has been observed which one of the favored characteristics for an electrode. The size of the round shape particles has been calculated using ImageJ software and found to vary from 17−30 nm. After implantation the surface of the NAN films becomes rough because atoms are sputtered from the top surface during implantation. The particle size measured using SEM

images is shown in figure 6.20 (b). This morphology is similar to our previous reports on Nb doped TiO_2 (NTO) thin films [190].

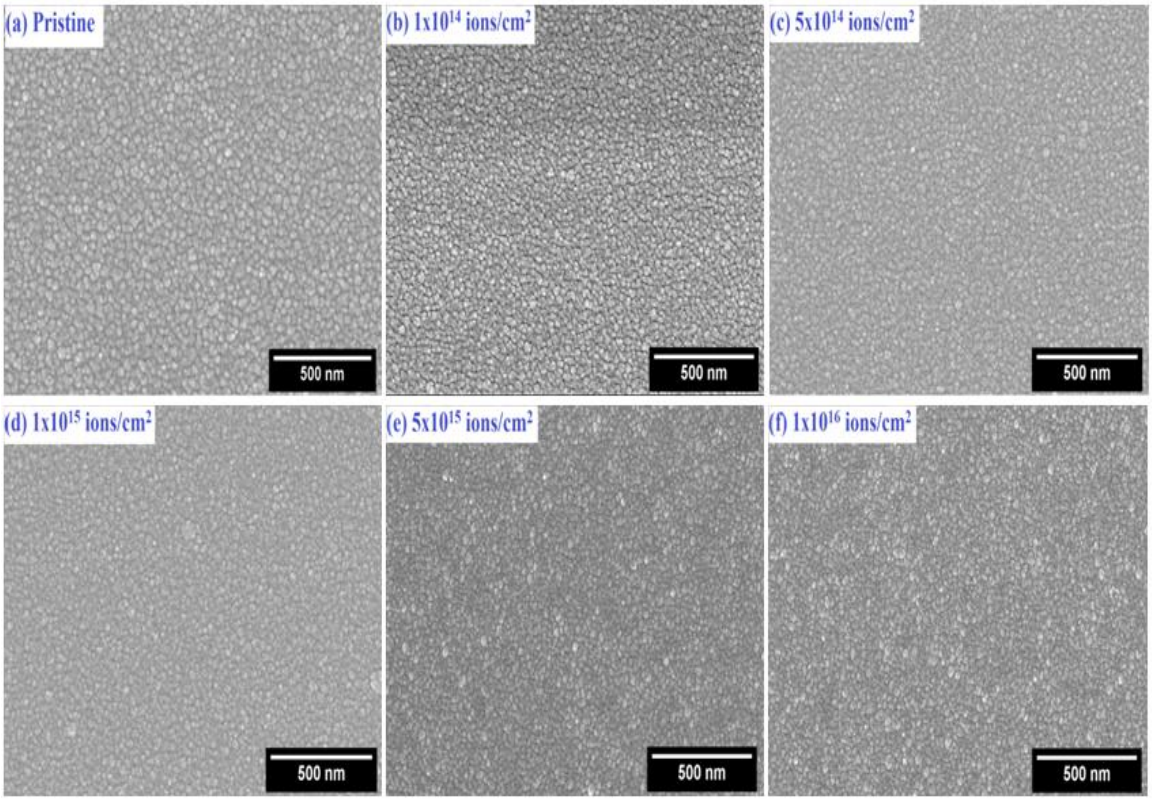

Figure 6.18: SEM images of the pristine NAN and A-NAN multilayer films with different ion fluences.

Atomic force microscopy (AFM) is a very-high-resolution microscopy based on scanning probe microscopy (SPM) and shows resolution of the order of fractions of a nanometer which is far better than the optical microscope. Figure 6.19 shows topography of NAN multilayer structures measured by the AFM. The scan area for the 3-dimensional AFM measurements was taken as 2×2 μm^2. The root mean square (rms) surface roughness were observed as 1.6 nm, 1.7 nm, 1.4 nm, 0.8 nm, 3.6 nm and 3.7 nm for fluence of 0, 1×10^{14}, 5×10^{14}, 1×10^{15}, 5×10^{15} and 1×10^{16} ions/cm^2 respectively. Surface roughness for pristine sample was 1.6 nm and initially it is decreases to 0.8 nm up to 1×10^{15} ions/cm^2 fluence and then it is increases as the fluence increases to 1×10^{16} ions/cm^2. A decrease in roughness up to 1×10^{15} ions/cm^2 may be due to high sputtering rate during ion implantation and this leads to deformation on the surface.

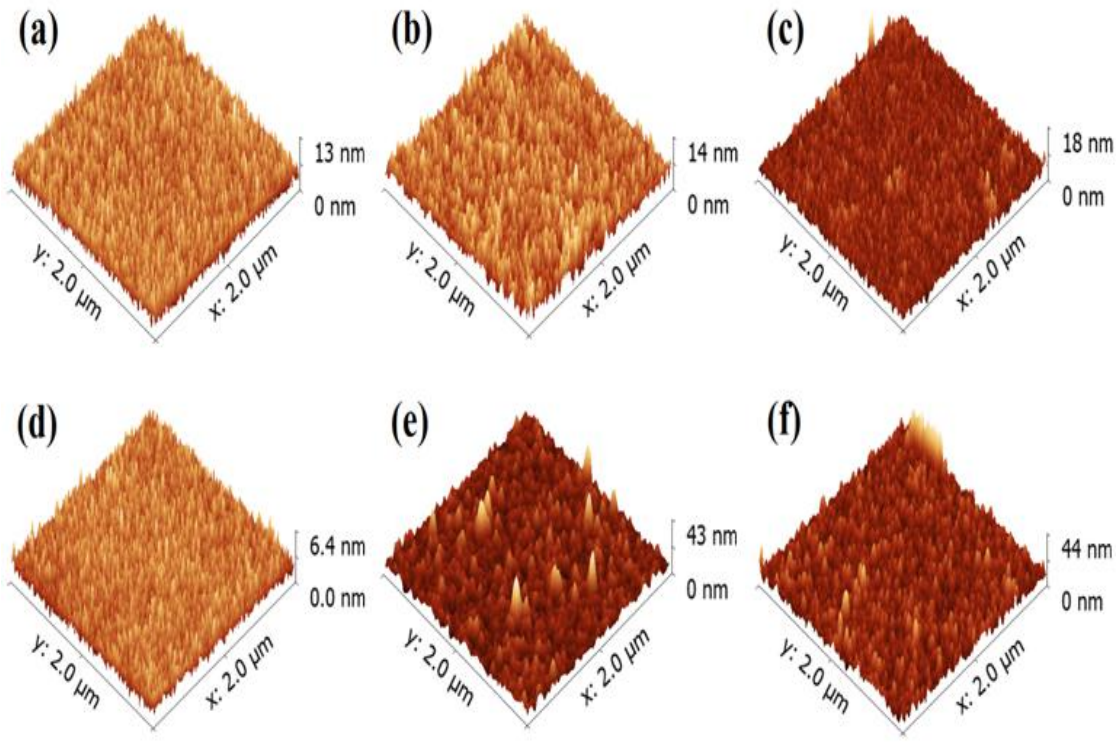

Figure 6.19: Three dimensional AFM images of the (a) pristine, (b) 1×10^{14} ions/cm^2, (c) 5×10^{14} ions/cm^2, (c) 1×10^{15} ions/cm^2, (d) 5×10^{15} ions/cm^2 and 1×10^{16} ions/cm^2 fluence, NAN multilayer films.

Furthermore, roughness increase at 5×10^{15} and 1×10^{16} ions/cm^2 fluences may be due to surface diffusion caused by ion bombardment, implantation-produced sputter cones which make the surface disordered [272]. The roughness of NAN multilayer structures is below than 5 nm. Figure 6.20 (a) shows the surface roughness curve with increasing fluence.

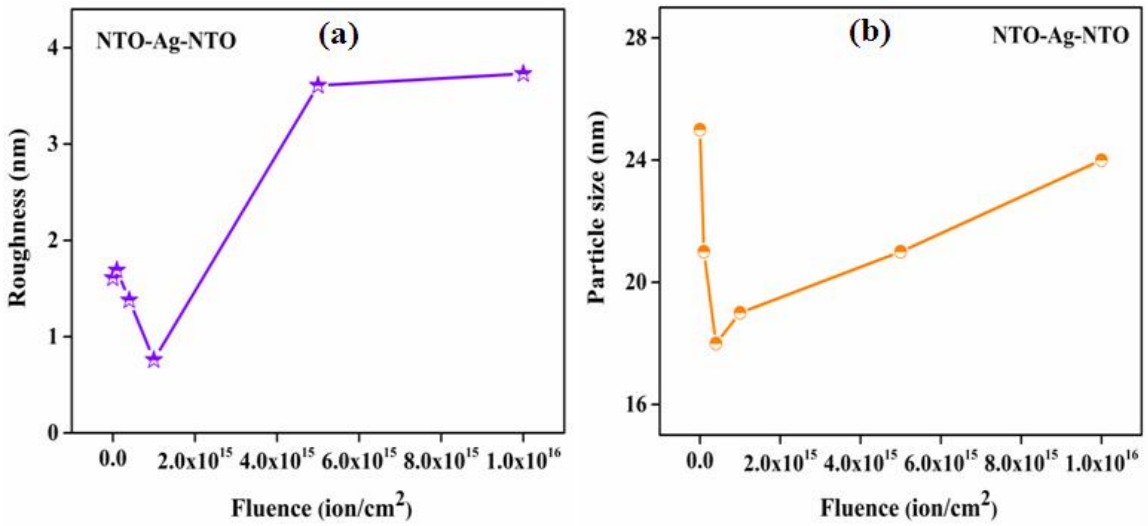

Figure 6.20: (a) Surface roughness graph and (b) particle size graph of NAN multilayer structure with different ion fluences.

6.7.4 Optical analysis

A high transmittance in a large wavelength region is an essential property for TCE. Figure 6.21 (a) shows the optical transmittance of pristine and Ar^+ implanted NAN multilayer structures with the fluence of 1×10^{14}, 5×10^{14}, 1×10^{15}, 5×10^{15} and 1×10^{16} ions/cm^2 in the visible region of light (400 nm<λ<800 nm). It can be noticed from the curves that transmittance increases with increasing wavelength, reaches a maximum and then gradually decreases. The pristine NAN multilayer films exhibit transmittance of ~83% which reduces to ~77% at 5×10^{14} ions/cm^2 fluence and then increases to ~79% at 1×10^{16} ions/cm^2 fluence. Initial reduction in transmittance indicates that Ar^+ implantation generates defects in the system mainly in the form of oxygen vacancies. Removal of oxygen from the system increases the metallic content and as a result it becomes less transparent. In addition to this lower transmittance may be attributed to the lower surface roughness because smoother surface reflects more light and higher roughness leads to more scattering. Incident light undergoes a strong absorption in NAN films below the 370 nm wavelength. NTO/Ag/NTO multilayer structures with implantation exhibit good transparency in the visible region of light and such structures can be a promising TCE in solar cells and other energy conversion devices.

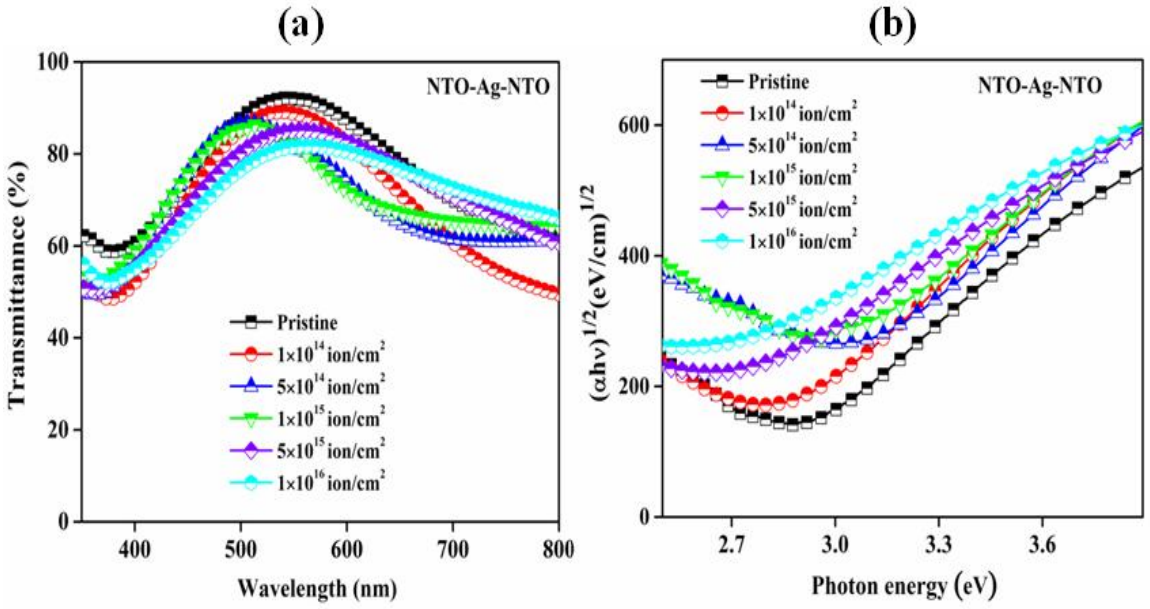

Figure 6.21: (a) Transmittance and (b) Tauc plot of pristine NAN and A-NAN multilayer films with different ion fluences.

Band gap measurement is very essential to study the electrical properties. The optical band gap of NAN and A-NAN films with different fluences has been calculated by the following relation [196].

$$\alpha h\nu = B(h\nu - E_g)^n \quad (6.6)$$

Where hν is photon energy, Eg is the optical band gap, α is absorption coefficient, B is a constant and n is taken as 2 due to indirect band gap of TiO_2. Absorption coefficient (α) was determined using Beer–Lambert's relation [222].

$$\alpha = \frac{1}{d}\ln\frac{1}{T} = \frac{2.303}{d}A \quad (6.7)$$

Where T is transmittance, d is thickness of the films and A is absorbance of the films. The band gap (figure 6.21 (b)) was measured using Tauc plot between photon energy (hν) and $(\alpha h\nu)^{1/2}$. Pristine NAN films show the band gap of 2.71 eV which reduces to 2.5 eV at the highest fluence of 1×10^{16} ions/cm^2. Narrowing of band gap of NAN films may occur because of generation of oxygen vacancies in the films introducing defect states.

6.7.5 Electrical analysis

Electrical properties play important role and affect the performance of a transparent conductor. These properties were examined by Hall measurement unit. Figure 6.22 shows the electrical resistivity, carrier mobility and carrier concentration of the NAN multilayer structures with varying Ar^+ fluence from 0 to 1×10^{16} ions/cm^2 measured at room temperature. Carrier density of specimen changes from 7.48×10^{21} cm^{-3} to 9.96×10^{21} cm^{-3} with increasing fluence. Simultaneously, carrier mobility enhances form 8.6 cm^2/V-s to 11.76 cm^2/V-s as the fluence increases. The resitivity is defined by $\rho = 1/n_e\mu e$; inversely proportional to the carrier density (n_e) and carrier mobility (μ). The resistivity of the pristine samples was 9.7×10^{-5} Ω cm and it minimized to 5.31×10^{-5} Ω cm for the highest fluence of 1×10^{16} ions/cm^2. In implantation process the concentration of implanted ions on O and Ti sites may be higher than achieved by conventional doping and hence creates interest for preference of implantation to get enhanced electrical conductivity. It was reported that the electrical conductivity (σ) of TiO_2 can be increased by many order due to radiation damage produced by ion implantation of non reactive gases like Kr and Ar [109]. For Kr σ saturated at about 1 Ω^{-1}cm^{-1} and for Ar at about 0.3 Ω^{-1}cm^{-1} with fluence.

Figure 6.23 illustrates the sheet resistance and Haacke figure of merit (FOM) of the NAN multilayer structures with varying ion fluence from 0 to 1×10^{16} ions/cm^2. Sheet resistance of the specimen decreases from 12.12 Ω/□ to 6.65 Ω/□ with increasing ion fluence. This change in sheet resitance is because of change in resistivity on implanation. Figure of merit is one of the methods to analyze the performance of the TCE because it includes both the key properties viz, transmittance and sheet resistance. Figure of merit given by Haacke is:

$$\Psi_{TC} = \frac{{T_{av}}^{10}}{R_s} \tag{6.8}$$

where Ψ_{TC} is FOM and T_{av} is average transmittance and R_s is sheet resistance of the specimen. The FOM increases from 12.7×10^{-3} Ω^{-1} to 14.4×10^{-3} Ω^{-1} as the fluence increase from 0 to 1×10^{16} ions/cm^2; although the transmittance lowers with incresing fluence but improvement in electrical conductivity after implantation leads to overall increase in FOM. This enhancement of FOM is dominated by low sheet resistance of 6.65 Ω/□ at highest fluence.

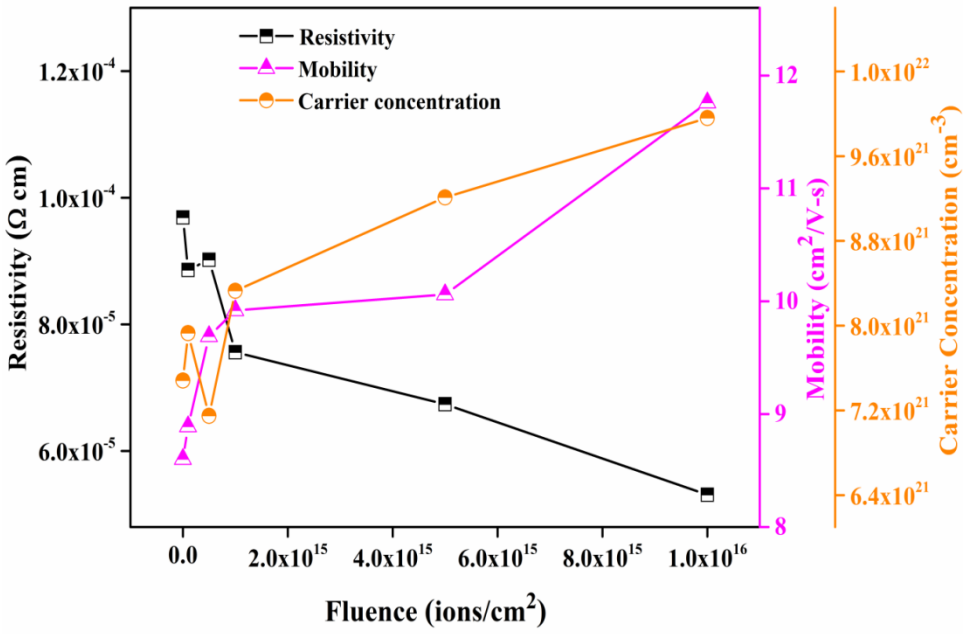

Figure 6.22: Resistivity, carrier concentration and the Hall mobility of pristine NAN and A-NAN multilayer films with different ion fluences.

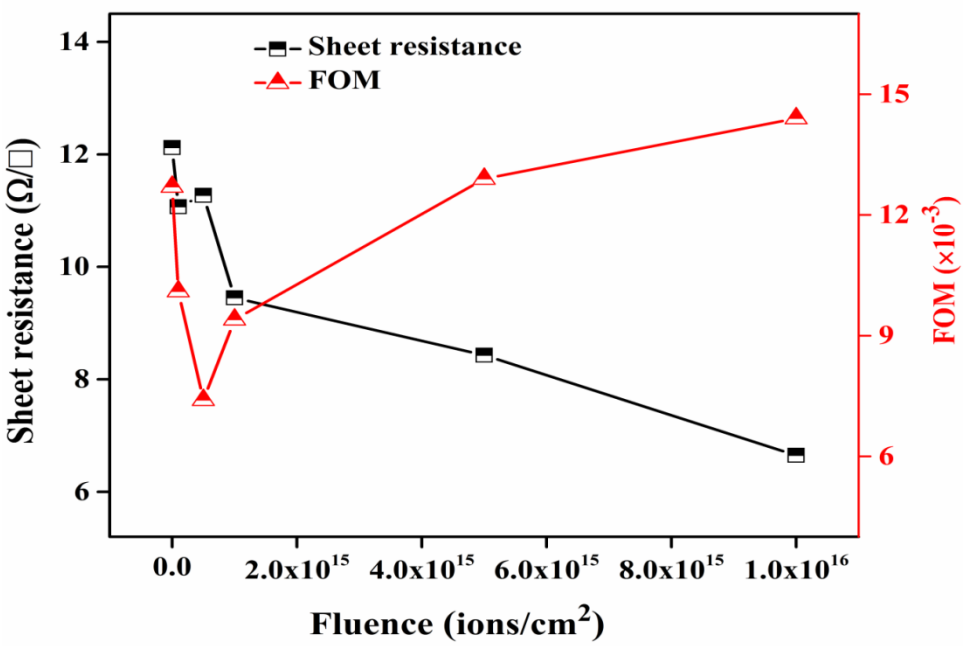

Figure 6.23: Sheet resistance and Haacke FOM of pristine NAN and A-NAN multilayer films with different ion fluences.

Figure 6.24 shows the sheet resistance, carrier concentration and carrier mobility variation of pristine, 1×10^{15} and 1×10^{16} ions/cm^2 fluence implanted NAN multilayer structures with the temperature variation from 80–340 K at an interval of 20 K. The low temperature Hall measurements were performed on the specimen to check the stability of the electrical properties at low temperatures. From the curves it can be observed that the carrier density (n_e), mobility (μ) and sheet resistance (R_s) are approximately constant up to the temperature of 240 K. After this temperature the n_e, μ and R_s slightly increase with increasing temperature. Generally in degenerate (heavily doped) semiconductors the sheet resistance and resistivity increases with temperature and these implanted NAN films exhibit the same behavior. Several investigations have shown Al doped ZnO [273], Nb doped TiO_2 [38], Ta doped TiO_2 [274] and SnO_2/Ag [266] having n-type degenerate semiconductor behavior. In our study, the top and bottom layer of NAN structure are Nb doped TiO_2 with middle Ag layer which makes it a degenerate system. Hence, this system shows metallic behavior on temperature variation.

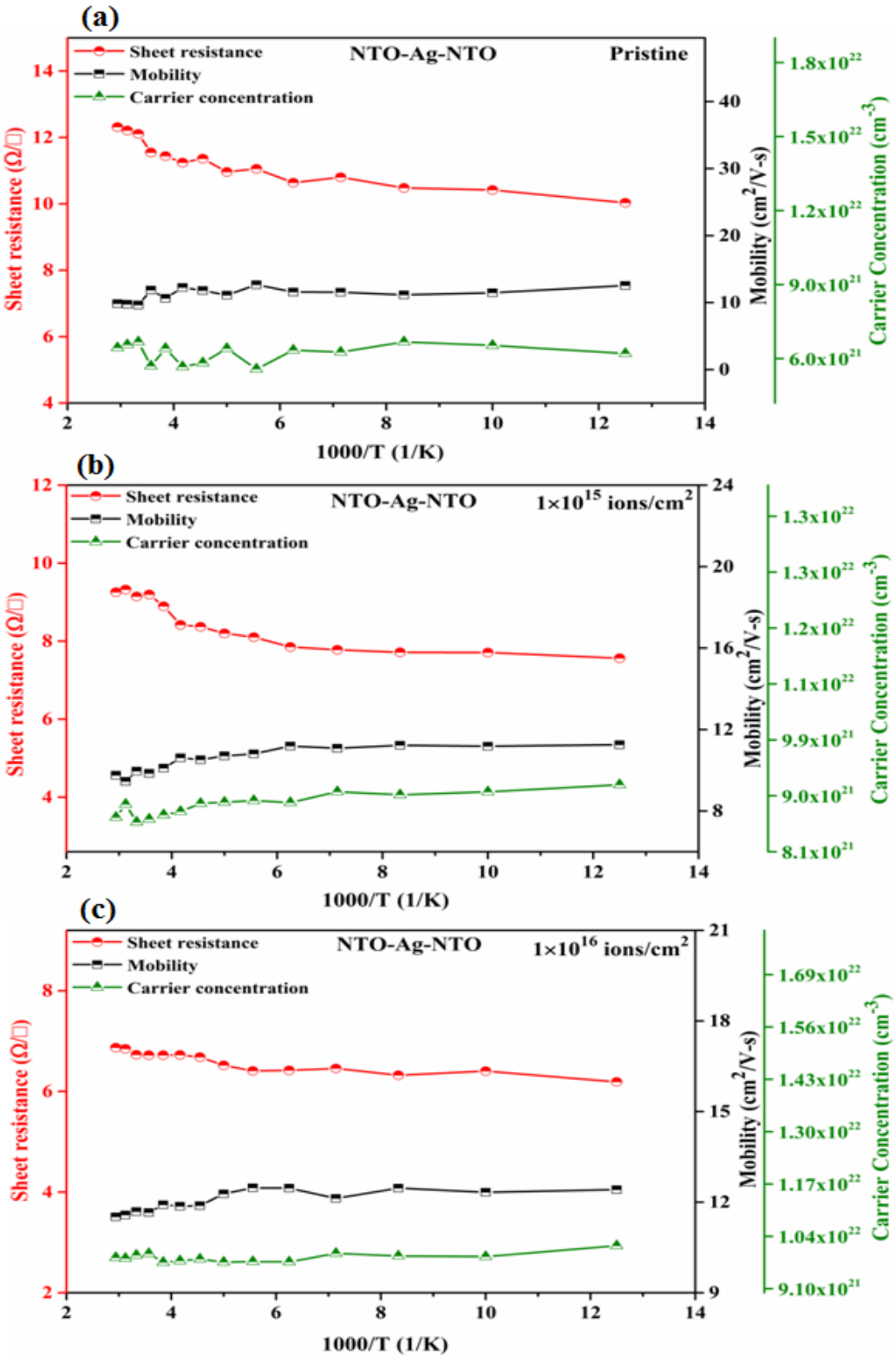

Figure 6.24: Resistivity, carrier concentration and Hall mobility of pristine NAN and A-NAN multilayer films for different fluence with temperature variation (a) pristine, (b) 1×10^{15} and (c) 1×10^{16} ions/cm^2 fluence.

6.7.6 X-ray photoelectron spectroscopy

We performed the XPS to study the chemical states and surface composition of the specimens by surface scan and depth profiling mode. Figure 6.25 (a) shows the survey scans of the top surface of pristine NAN and NAN films implanted with highest fluence of 1×10^{16} ions/cm^2 flence and named as A-NAN. The elemental peaks of Ti, Nb, O and C can be seen from the survey spectrums. The carbon signals (C 1s) in our samples observed from the envionmental carbon which appear through sample transfer process. The Ag signals and interface studies have been measured using the depth profile mode of XPS. Figure 6.25 (b) shows the short range scan of the Ti 2p of both the specimens. The peak positioned at 458.92 eV is attributed to Ti-$2p_{3/2}$ of pristine film [200,201]. The peaks of Ti-$2p_{3/2}$ and Ti-$2p_{1/2}$ pristine NAN and A-NAN films suggest that Nb^{5+} replaces the Ti atoms in the TiO_2 system [269]. It is revealed from the XPS results that the Ti-$2p_{3/2}$ peak of pristine NAN consist two components. One component appears at 459.2 eV which can be assigned to Ti^{4+} state and another component at 457.03 eV can be explained by the existence of Ti^{3+} state of titanium [202]. The peak of Ti-$2p_{3/2}$ of A-NAN appeared at 459.17 eV on implantation. A shift of 0.025 eV in binding energies of Ti-$2p_{3/2}$ was observed on Ar^+ implantation. This shift is attributed to defect creation mainly oxygen vacancies on implantation and different interactions behavior of Ti with Nb and with Ag at the interface of the NAN multilayer structures.

Figure 6.25 (c) shows the short range scan of the O 1s of pristine NAN and A-NAN multilayer structure. The O 1s peak of pristine specimen is deconvoluted in two peaks. One peak positioned at 530.05 eV is attributed to bulk oxygen (O^{2-}) of the TiO_2. Another component appeared at 531.5 eV can be understood by the existence of the hydroxyl group (OH) on the top surface of the samples. But in case of A-NAN films the O 1s is deconvoluted in two components; one is positioned at 530.1 eV corresponding to bulk oxygen (O^{2-}) of TiO_2 and another at 531.15 eV corresponding to OH group.

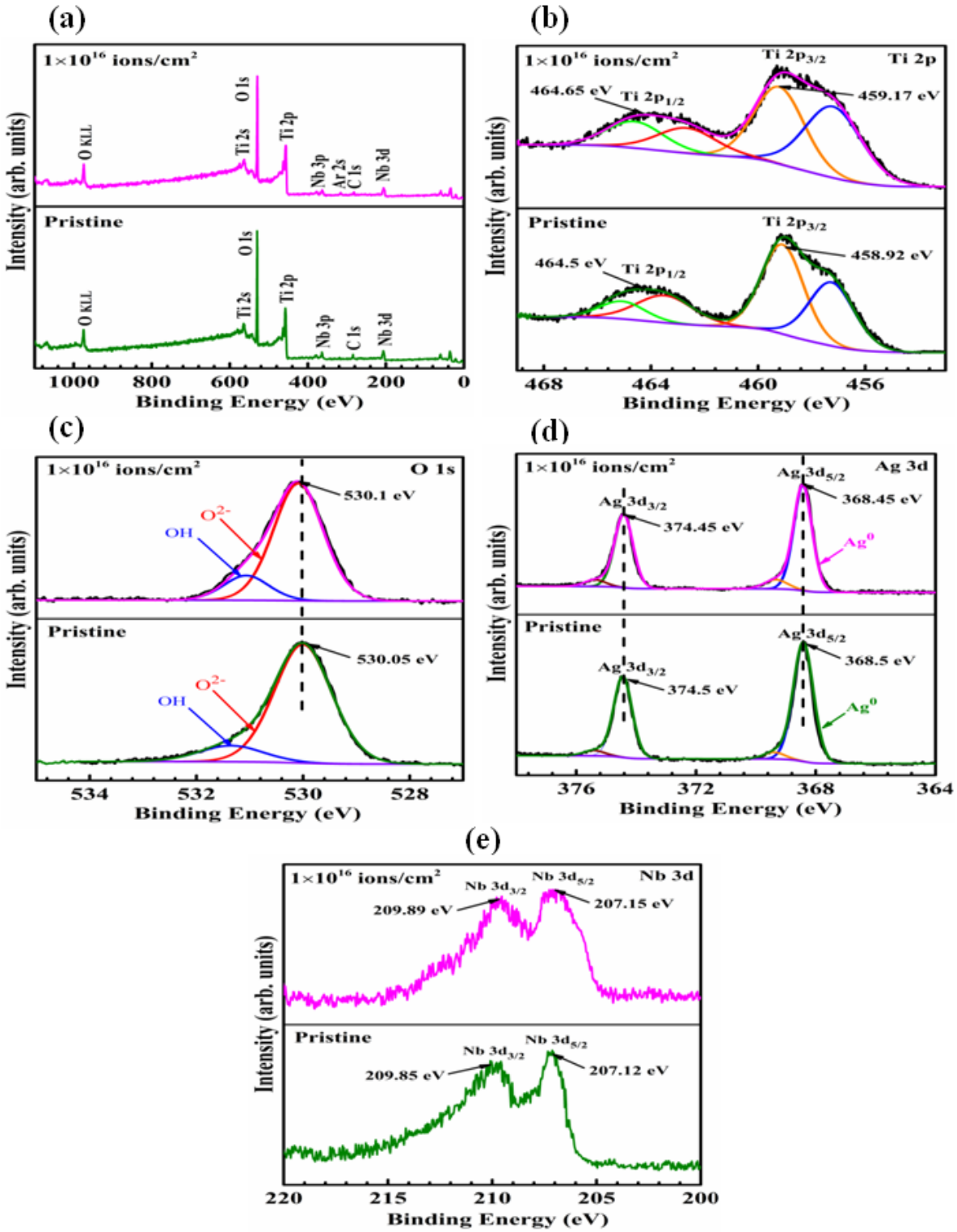

Figure 6.25: XPS spectra of pristine NAN and Ar^+ implanted NAN multilayer films with 1×10^{16} ions/cm^2 fluence (a) survey scan, (b) Ti 2p, (c) O 1s, (d) Ag 3d and (e) Nb 3d.

Figure 6.25 (d) demonstrates the short range scan of Ag 3d of the pristine NAN and A-NAN multilayer structures. The Ag signals from the middle layer of the multilayer structure were obtained through the depth profile mode of XPS, after etching of the first layer using sputtering. The peaks appeared at 368.5 eV and 374.5 eV for the pristine film are assigned to Ag $3d_{5/2}$ and Ag $3d_{3/2}$ respectively. After implantation a small shift in the peaks was observed toward lower angle and the peaks appeared at 368.45 eV (Ag $3d_{5/2}$) and 374.45 eV (Ag $3d_{3/2}$). Figure 6.25 (e) exhibits the short range scan of Nb 3d of pristine NAN and A-NAN multilayer films. The binding energy of Nb $3d_{5/2}$ and Nb $3d_{3/2}$ are 207.12 eV and 209.85 eV for pristine sample. The spin-orbit splitting (binding energy difference) of Nb $3d_{5/2}$ and Nb $3d_{3/2}$ is 2.73 eV which confirm the existence of the Nb^{5+} state [176] of Nb used in top and bottom layers in NAN structures as dopant.

6.8 Conclusion

In this work, the effect of N^+ and Ar^+ ion implantation on the electrical and optical properties of NTO/Ag/NTO multilayer films has been explored. Incorporation of N^+ ions in the NTO matrix lead to the oxygen replacement by N^+ ions and this influences the physical properties of the system. The XRD confirms the amorphous nature of TiO_2 and crystalline Ag with dominant peak at 38.2˚. The optimization of the NTO thickness has been reported and NTO/Ag/NTO (~35 nm/~9 nm/~35 nm) with highest FOM (12.7×10^{-3} Ω^{-1}) chosen for N^+ ion implantation. The chemical states of N ions measured using XPS exhibit that the N^+ replaces O sites by showing the peak position at 396 eV. The UPS results suggest that the work function of NAN films matches well with that of the active layer of the photovoltaic and TCE with proper work function can be used to fabricate a photovoltaic cell with better performance. The smooth morphology and low surface roughness (<2 nm) make them suitable for TCE applications. The optical transmittance varies from ~83% to ~81% as the ion fluence increases from 0 to 1×10^{16} ions/cm^2, the band gap of the NAN films decreases from 2.71 to 2.57 eV with fluence. The main motivation of N^+ ion implantation in this study was to reduce the band gap and lower the resistivity with optimum transparency. The electrical resistivity is found to decrease from 9.69×10^{-5} Ω cm to 5.52×10^{-5} Ω cm and sheet resistance also varies from 12.12 Ω/□ to 6.9

Ω/□ with increasing fluence. The maximum FOM of 18×10^{-3} Ω^{-1} is obtained for the fluence of 1×10^{16} ions/cm^2. The N^+ ion implanted NAN multilayer films with low sheet resistance and high transmittance provide an alternate to ITO and can be used as futuristic TCE with enhanced performance.

In the second part of the chapter, we investigated the influence of 100 keV Ar^+ ion implantation on properties of NAN multilayer structures. The crystallinity of Ag was slightly improved on implantation. Morphology of the films indicates the homogeneous deposition of the films. The optical transmittance of the pristine NAN films was reduced from ~83% to ~79% on implantation. Meanwhile, sheet resistance of NAN films was decreased from 12.12 Ω/□ to 6.65 Ω/□ at the highest fluence (1×10^{16} ions/cm^2). XPS studies confirm the creation of oxygen vacancies in the TiO_2 system and a low shoulder peak was observed. The band gap of the specimens was reduced after implantation and electrical resistivity decreased. The figure of merit was enhanced to 14.4×10^{-3} Ω^{-1}. Hence the Ar^+ implantation produces good results with sufficient transmittance and low sheet resistance in the NAN films.

Chapter-7

Synthesis and Characterization of Transparent Resistive Switching Random Access Memory Device Based on Al_2O_3 Layer with Multilayer TAT and NAN Electrodes

7.1 Introduction

In recent times, transparent resistive switching memory devices have emerged due to their human-friendly interfaces, portable and light weight. These novel device technologies have shown many advantages over the conventional flash memories and bulk silicon devices [42,275]. They provide high endurance, high density storage, fast speed, high retention and simple structure [275]. Widely used electronic devices such as transparent transistors [276], e-paper [277] and diodes [278] have generated the demand of the transparent devices. This transparent memory device can be a key component in electronic devices for data storage and fast processing and will help to develop a new generation of electronic devices. Generally, silicon based flash memory devices made from field effect transistors using additional floating gate, has limited data storage capacity [279]. Researchers are working on development of advanced devices such as magnetic random-access memory (MRAM) [280], dynamic random access memory (DRAM) [281], ferroelectric random-access memory (FeRAM) [282] and resistive switching memory (ReRAM). The resistive switching memory (ReRAM) fabricated with a simple structure of an insulating layer embedded between two metals exhibits fast switching, scalability to nanometer regime [283] and high endurance and retention capabilities, therefore it can be a good choice for nonvolatile memory devices. Numerous study reports say that the ReRAM are compatible with the silicon CMOS based technology [284,285].

In ReRAMs the switching phenomenon occurred due to formation and rupture of nanosize conductive filaments (CFs). These CFs mainly contains the metal precipitates and oxygen vacancies [286,287]. The device is operated through two processes namely

set and reset process. In set process it switches from high-resistance state (HRS) to low-resistance state (LRS) due to creation of oxygen ions/vacancies; on the other hand in reset process it changes from LRS to HRS due to annihilation of oxygen ions/vacancies [288,289]. In recent times, different materials have been studied for memory applications to get better device characteristics. Various metal oxide materials such as Al_2O_3 [290], HfO_2 [291], Cu_2O [292] and Ta_2O_5 [293] have been investigated for ReRAMs devices due to their low cost processing. Among these materials Al_2O_3 and HfO_2 are popularly used in memory devices. Al_2O_3 is widely used due to its wide band gap, resistive switching properties and good thermal stability. To fabricate the transparent resistive switching memory, transparent conducting electrodes (TCE) are needed. The most commonly used TCE is indium tin oxide (ITO) and looking at its limitations we have replaced it by TAT and NAN films. We have used the TiO_2/Ag/TiO_2 (TAT) and NTO/Ag/NTO (NAN) as the transparent and conducting top and bottom electrodes and fabricated TAT/Al_2O_3/TAT and NAN/Al_2O_3/NAN transparent device structures for resistive switching memory applications and characterized them with UV-Vis, XPS and I-V measurements.

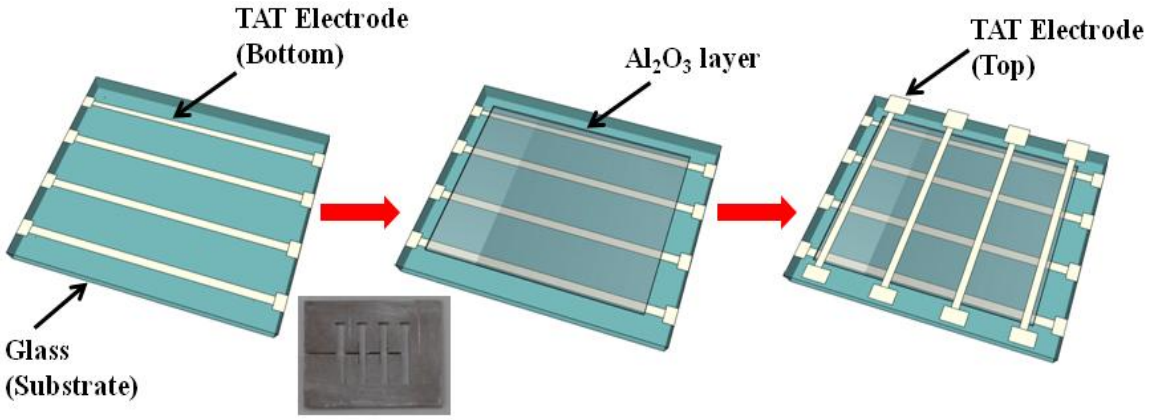

Figure 7.1: Schematic diagram of the method adopted for RRAM device fabrication with TAT electrodes.

7.2 Experimental details

A resistive switching memory device structure of TiO_2/Ag/TiO_2/Al_2O_3/TiO_2/Ag/TiO_2 (TAT/Al_2O_3/TAT) (as shown in figure 7.1) and NTO/Ag/NTO/Al_2O_3/NTO/Ag/NTO (NAN/Al_2O_3/NAN) (as shown in figure 7.2) were fabricated using rf/dc magnetron sputtering on clean glass substrates at room temperature. The TiO_2 target was prepared by

pressing the powder in to 2 inch diameter pellet and then sintered at 1100 ˚C for 10 hrs. Commercial targets of silver and Al_2O_3 have been used for the deposition of their films. Before deposition, the sputtering chamber was evacuated to 5×10^{-6} mbar. The Ar flow was kept constant at 15 sccm for the deposition of TiO_2, Ag and Al_2O_3 films. A 100 W power was applied to rf source to deposit the oxide films of TiO_2 and Al_2O_3. The power of dc source was kept 16 W to deposit the silver films. Working pressure for TiO_2 and Ag films deposition was 6×10^{-3} mbar and 1.7×10^{-2} mbar respectively. The thickness of top and bottom transparent conducting electrodes of TiO_2/Ag/TiO_2 and NTO/Ag/NTO were 45±5 nm/9±1 nm/45±5 nm and 35±4 nm/9±1 nm/35±4 nm as taken in our earlier studies. The insulating layer of Al_2O_3 thickness of 35±5 nm was deposited by rf sputtering at 3×10^{-3} mbar working pressure. Initially 100 nm thick TAT and 80 nm thick NAN electrodes (bottom) were deposited using a metal mask (inset of figure 7.1) composed of four lines on the transparent glass substrate and then 35 nm thick continuous Al_2O_3 insulating layer was deposited on the bottom electrodes. And finally the TAT and NAN electrodes of same thickness were deposited on top insulating layer. LAMBDA 750 (Perkin Elmer) UV-Vis-NIR Spectrophotometer was used to measure the transmittance of the devices. Chemical states and surface stoichiometry of the device structure were measured using X-ray photoelectron spectroscopy (XPS, Omicron ESCA). XPS was operated with monochromatic Al K_α (1486.7 eV) source having mean radius of 124 mm and FWHM of 0.6 eV. I-V characteristics of the devices were obtained using Semiconductor Device Analyzer (Agilent B1500A) integrated with probe station.

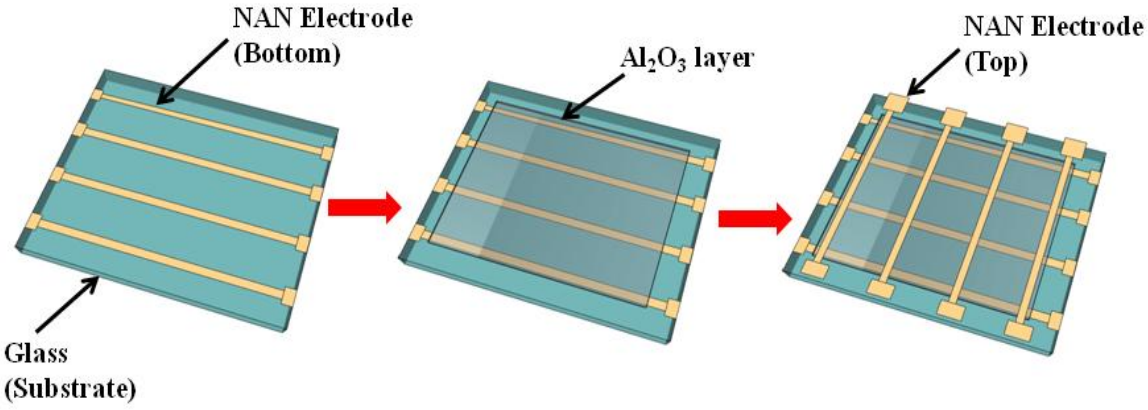

Figure 7.2: Schematic diagram of the method adopted for ReRAM fabrication with NAN electrodes.

7.3 Resistive Switching Memory using TiO_2-Ag-TiO_2 Electrodes

In the digital and internet era, the data has increased tremendously and therefore there is a need of scalable and fast memory technologies which can store large data with easy computation. Transparent electronics is an emerging technology for optoelectronic devices and next generation electronics generating considerable impact in industrial and consumer products. Transparent device circuitry needs transparent memory cells with simple structure and layout and hence highly transparent material is desirable. A transparent resistive switching memory with top and bottom electrodes of TAT and insulating layer of Al_2O_3; have been fabricated by sputtering on glass substrates. The data storage in resistive switching memories is understood by its two resistance states i.e. high resistance state and low resistance state.

7.4 Results and Discussion

7.4.1 UV-Vis Transmittance

A transparent nonvolatile memory device which is transparent for visible light would be advantageous for the realization of transparent electronics and invisible circuits [294]. Employing transparent conducting electrodes, large band gap switching (insulating) materials and transparent substrate is needed to fabricate the invisible ReRAM device. FTO [295], ITO and AZO [296] have been used as TCE in transparent electronics but in this work, the stacked multilayer TCE has been used to prepare the ReRAM.

Figure 7.3 shows the optical transmittance spectrum of ReRAM device with TAT electrodes deposited on the glass substrates. The transmittance of the memory device was >85% in the visible region of light. The high transmittance of the device structure was due to large band gap of thin Al_2O_3 layer, transparent TAT electrodes and transparent glass substrate. The name of MNIT can be clearly seen through memory device which is shown in inset of Fig. 7.3. The obtained transmittance of >85% makes it obvious that this memory device can be used as transparent ReRAM.

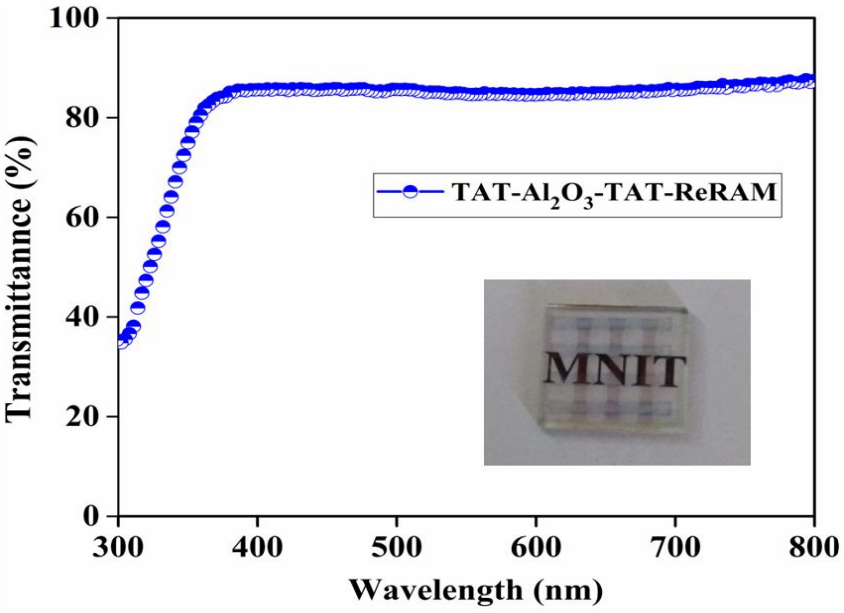

Figure 7.3: Transmittance spectrum of ReRAM device with TAT electrodes and inset shows the TAT/Al_2O_3/TAT ReRAM device.

7.4.2 X-ray Photoelectron Spectroscopy

The stoichiometry of constituent elements, elemental composition and chemical state of oxygen of Al_2O_3 layer in ReRAM device has been analyzed by X-ray Photoelectron Spectroscopy. Figure 7.4 (a) shows the survey scan spectra of memory device and the elemental peaks of Ti 2p, Al 2s, Al 2p, Ag 3d and O 1s are clearly seen in the graph. Inset of figure 7.4 (a) shows the elemental composition of device with 55.96% O, 6.45% Ti, 18% Al and 7.2% Ag. To gain better insight into the conduction mechanism which gives the resistive switching behavior of Al_2O_3 based ReRAM, chemical state of O 1s have been investigated by XPS using depth profile mode. The O 1s signals from Al_2O_3 layer were obtained after etching the TAT layer by Ar sputtering.

Figure 7.4 (b) exhibits the core level spectra of O 1s which obtained from insulating Al_2O_3 layer. The asymmetric spectra of O 1s of Al_2O_3 can be deconvoluted into two peaks after the Gaussian fitting. The peak positioned at 530.15 eV is assigned to the oxygen that is bound with Al_2O_3 lattice. Another peak positioned at 531.35 eV is attributed to oxygen vacancies, present in the Al_2O_3 layer. Many researchers [297,298] have investigated chemical state of oxygen in oxides and established a correlation between the formation of

oxygen vacancies and non lattice oxygen. The role of oxygen vacancies in the switching of the device is discussed later.

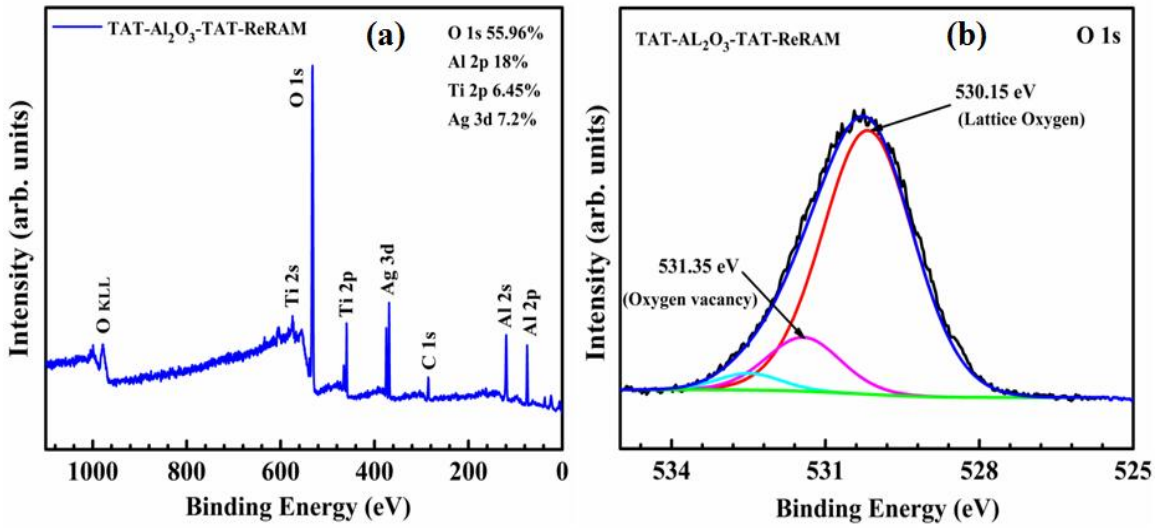

Figure 7.4: (a) XPS survey spectrum and (b) O 1s short range spectrum of ReRAM device with TAT electrodes.

7.4.3 I-V Characteristics

Computer reads the data using binary numbers viz. "1" and "0". Similarly, in resistive memories the data are differentiated by its resistance states such as high resistance state (HRS) or "OFF" and low resistance state (LRS) or "ON". These states are switched from one state to another using electric impulse. The switching phenomenon from LRS to HRS and HRS to LRS are called as "reset" and "set", respectively. The electrical properties of Al_2O_3 based ReRAM device were analyzed by I-V characteristics using semiconductor device analyzer. Figure 7.5 (a) shows the typical I-V characteristics of transparent ReRAM device fabricated using TAT electrodes. The bottom TAT electrode was grounded and a bias was applied to top TAT electrode during I-V measurements. Initially a forming voltage was applied to the ReRAM memory device because the as prepared device was in high resistance state. In the forming process a negative bias voltage from 0 to −5V was applied and consequently a rapid increase in the current was noticed till about ~4.6 V and it is known as $V_{Forming}$. This forming of device was done to activate the device and to convert it from HRS to LRS. I-V curve of forming process is shown in inset of

figure 7.5 (a). During the forming (set) process compliance current (I_{comp}) is generally applied to prevent the device from breakdown, because in switching process the current increases abruptly.

To determine the current-voltage characteristics, the voltage sweep of 0V → 5V → 0V → -5V → 0V have been followed. After forming process the device was in LRS and hence current was maintained in LRS till subjected to a certain positive voltage (V_{RESET}). Above 4.5V of positive voltage the device was switched from LRS to the HRS. Similarly, the device remained in HRS before applying a particular negative voltage (V_{SET}) and the transparent ReRAM device converted from HRS to the LRS on application of the specific negative voltage. I-V curves were plotted in the LRS and HRS states to study the switching process of the Al_2O_3 based transparent ReRAM device. Before applying V_{RESET} a logarithmic scale curve of LRS was replotted between current and voltage to study the conduction mechanism. Figure 7.5 (b) exhibits I-V graph for LRS which is linear. The linear slope confirms that conduction process in the LRS is governed by ohmic conduction [299]. Moreover, the conduction mechanism of device in HRS can be understood by Poole–Frenkel emission [300]. Poole–Frenkel emission equation explained that the current-voltage characteristics can be examined in terms of $V^{1/2}$ and ln (I/V). Figure 7.5 (c) shows the I-V curves of the device in HRS which is plotted between $V^{1/2}$ and ln (I/V) to investigate the dominant conduction mechanism. It can be seen from the graph that conduction process is well fitted with that given by Poole–Frenkel emission.

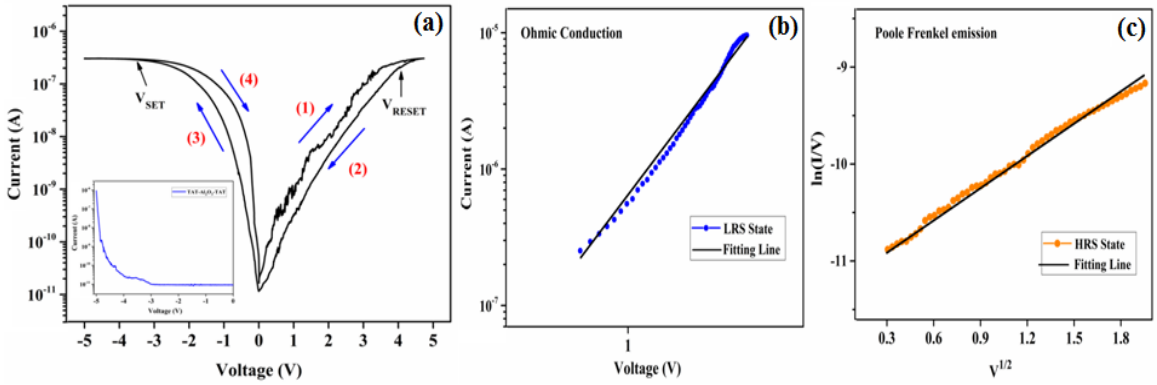

Figure 7.5: (a) I-V characteristics of ReRAM device with TAT electrodes, (b) I-V characteristics in LRS described by ohmic conduction and (c) ln (I/V) vs. $V^{1/2}$ described by Poole Frenkel emission.

The nonlinear resistance changes have been observed in different metal oxides [301]. Gibbons *et al.* [302] reported the existence of conducting filaments (CFs) in Ag/NiO/Ni device, responsible for variation in resistance. The switching mechanism in oxide based ReRAMs is dominated by generation and recombination of oxygen vacancies [284,303]. In our work also, the resistive switching phenomena can be understood by oxygen vacancies present in Al_2O_3 layer. The high resistance state given by Poole–Frenkel emission suggest that oxygen vacancies, traps the injected electrons in the Al_2O_3 layer. These oxygen ions removed from the Al_2O_3 lattice when negative bias was applied on the top electrode as shown in figure 7.6 (a). The removal of oxygen ions creates the vacancies in Al_2O_3 layer. The oxygen ion moves towards the TAT/Al_2O_3 interface and are accumulate there and this process generates the conductive filaments in the Al_2O_3 layer. These ions migrate from interface to Al_2O_3 layer as the positive bias was applied on the top electrode as shown in figure 7.6 (b). Due to the migration of ions to Al_2O_3 layer the oxygen vacancies again filled up and consequently conductive filaments are ruptured. Therefore, in our ReRAM device the switching phenomenon is mainly due to migration of oxygen ions from Al_2O_3 layer to interface and vice versa on applying the negative and positive voltage to the electrodes, respectively.

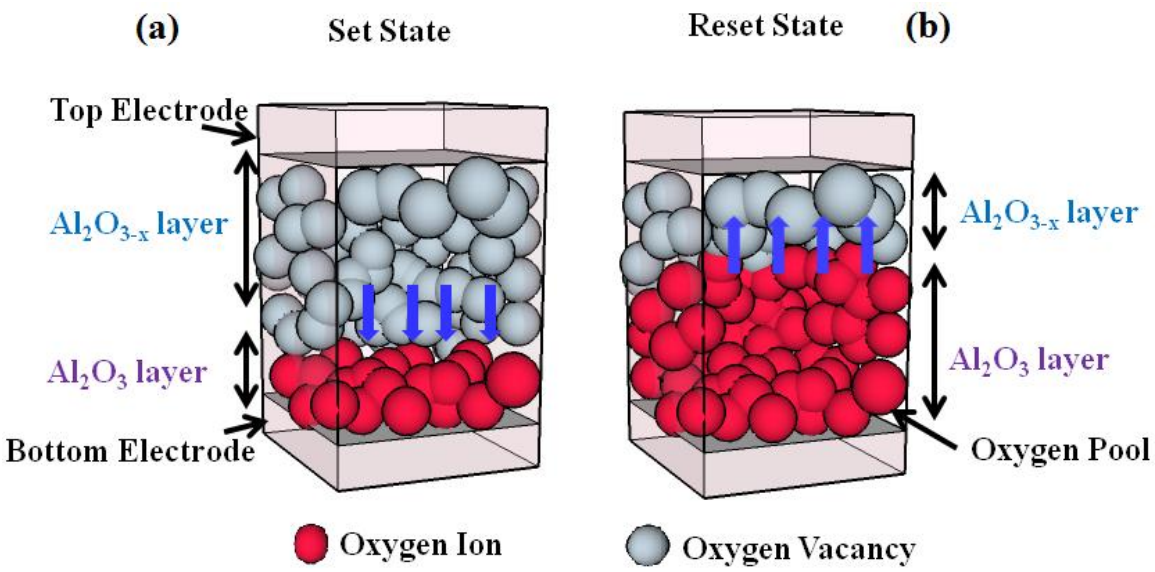

Figure 7.6: Schematic diagrams of (a) oxygen vacancies creation in set state and (b) oxygen vacancies recombination in reset state of ReRAM device with TAT electrode.

The state of Al_2O_3 layer can be denoted as Al_2O_{3-x} layer after migration of oxygen ions from lattice. Due to these oxygen ions transfers from lattice to interface the resistive states of device changes from HRS to LRS and this is called set process. Conversely, when ions come back to the Al_2O_{3-x} layer, resulting Al_2O_3 layer and device comes to HRS and this is called reset process.

7.5 Resistive Switching Memory using NTO-Ag-NTO Electrodes

These days several class of memories are available to fulfill the present need of large data storage. Generally some physical phenomenons are involved in the switching of the memory devices from the OFF (reset) state to ON (set) state and vice versa. In magnetic memories or magnetoresistive random access memories (MRAM), magnetic field is involved in the process of switching. In case of phase-change RAM (PCRAM), the state switches when material switches from amorphous to crystalline state and this phase transition is controlled by thermal processes [304]. There is another category of resistive switching based on electrical stimulus which changes its resistance from high resistance to low resistance and vice versa. These memory devices usually called resistive switching RAM of ReRAM for short. A transparent resistive switching memory device using top and bottom electrodes of NAN film and insulating layer of Al_2O_3; have been fabricated by sputtering on glass substrates. The data storage in resistive switching memories is given by its resistance state i.e. high resistance state and low resistance state. In previous section, we have discussed the resistive switching memory device using TAT electrodes; these electrodes were replaced with NAN electrodes to fabricate the same device structure.

7.6 Results and Discussion

7.6.1 UV-Vis Transmittance

Large band gap, optically-transparent and electrically-switchable materials are essential to fabricate the transparent ReRAM [305]. In this regard, the silicon based semiconductors which are opaque; are not eligible to fabricate transparent memories. Therefore metal oxides have been used to develop invisible electronic devices and provide an alternative opportunity [306]. Normally, the higher dielectric constants in high-k materials come at

the cost of narrower band gap, but Al_2O_3 has a large band gap with high-k value. Therefore, in our work a thin layer of Al_2O_3 is used to make the ReRAM. Figure 7.7 exhibits the optical transmittance spectrum of ReRAM device with NAN electrodes. The device stricture was fabricated on glass substrates. The obtained transmittance of ReRAM device was >83% in the visible region of light. The wide band gap of thin Al_2O_3 layer, transparent electrodes and transparent substrate together provide the good transmittance in the device. Inset of figure 7.7 clearly indicates the high transparency of the device. The obtained transmittance of >83% makes this memory device applicable as transparent ReRAM.

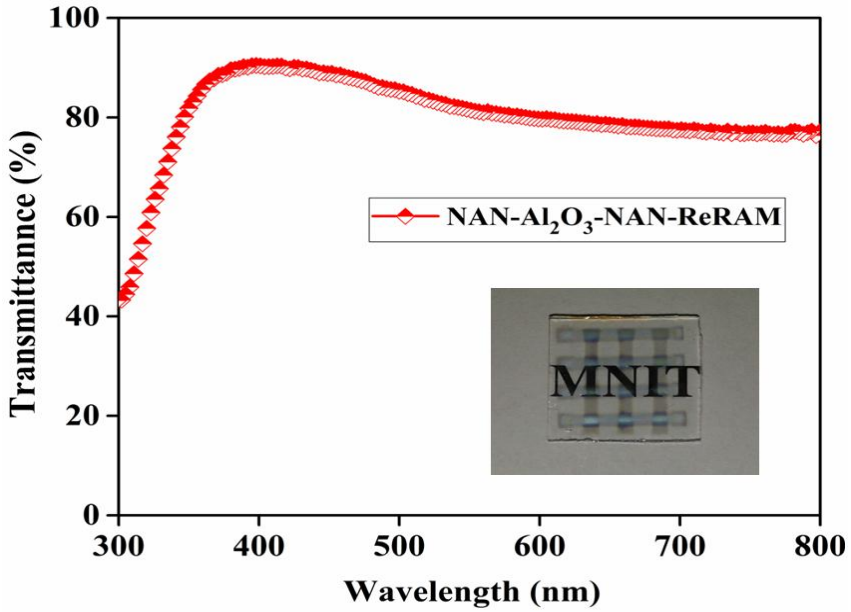

Figure 7.7: Transmittance spectrum of ReRAM device with NAN electrodes and inset shows the NAN/Al_2O_3/NAN ReRAM device.

7.6.2 X-ray Photoelectron Spectroscopy

The XPS measurements have been performed to determine the elemental composition, stoichiometry and chemical state of oxygen of Al_2O_3 layer of ReRAM device. The elemental peaks corresponding to Ti 2p, Al 2s, Al 2p, Ag 3d, Nb 3d and O 1s were observed in survey scan spectra (figure 7.8 (a)) of ReRAM device. Elemental composition of device with 55.96% O, 6.45% Ti, 18% Al, 7.2% Ag and 1.2% Nb is shown in inset of figure 7.8 (a). Depth profile mode of XPS was used to etch the NAN layer and get the signal for O 1s from the Al_2O_3 layer. Oxygen vacancies play key role to understand the

switching phenomenon in ReRAMs hence it is important to investigate the chemical state of oxygen in Al_2O_3. The core level spectra of O 1s acquired from Al_2O_3 layer is shown in figure 7.8 (b). After Gaussian fitting the O 1s spectra is deconvoluted into two peaks. The peak at 530.12 eV is attributed to metallic oxygen bound with Al_2O_3 lattice. Another peak at 530.32 eV appeared due to oxygen vacancies existing in the Al_2O_3 layer. Correlation between the formation of oxygen vacancies and non lattice oxygen in oxides has been reported in previous studies [297,298]. The oxygen vacancies play significant role in the switching process of device as explained later.

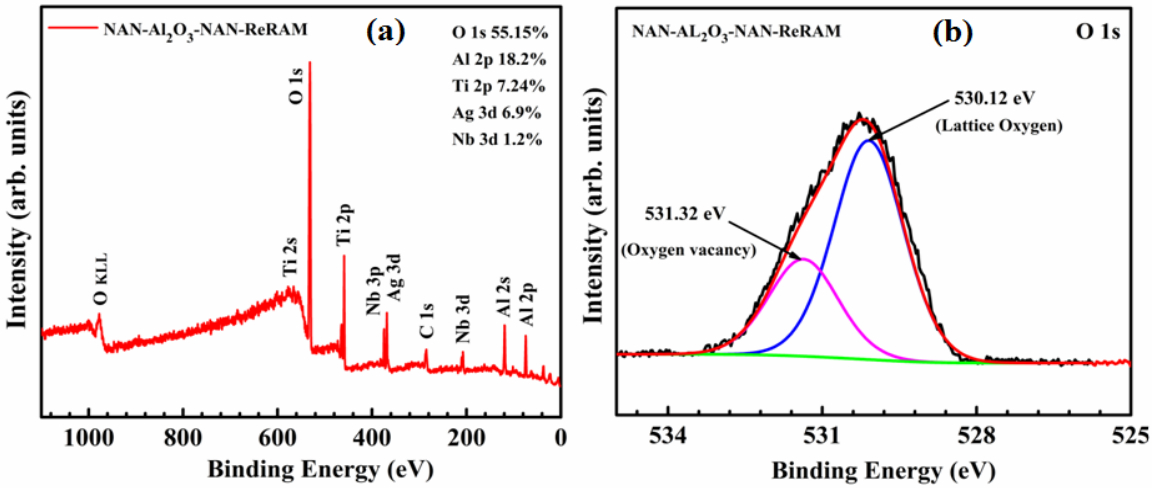

Figure 7.8: (a) XPS survey spectrum and (b) O 1s short range spectrum of ReRAM device with NAN electrodes.

7.6.3 I-V Characteristics

Typical current-voltage (I-V) measurements of transparent ReRAM device are shown in figure 7.9 (a). During the measurements the bottom NAN electrode was grounded and a bias voltage was applied to the top NAN electrode. The as prepared device was in HRS and a forming process was done to bring the device in LRS. When a negative bias voltage from 0 to −5V was applied an abrupt increase in current was observed about ~4.7V and it is known as $V_{Forming}$. Forming process makes the device active and changes it from HRS to LRS. I-V curve of forming process is shown in inset of figure 7.9 (a). Compliance current (I_{comp}) is applied in forming process to prevent the device from breakdown. This is necessary because in the switching process the current increases rapidly. The device remains in LRS only until a certain positive voltage (V_{RESET}) is applied.

A voltage sweep of 0V → 5V → 0V → -5V → 0V has been performed to measure the I-V characteristics of the device. The status of device has been changed from LRS to HRS above the 4.6V of positive voltage. Likewise, the device remained in HRS until a particular negative bias voltage (V_{SET}) was applied. When a specific negative bias voltage (V_{SET}) was applied, the device switched from HRS to the LRS. Figure 7.9 (b) shows the current-voltage graph for LRS is a linear slope line. The conduction process in the LRS is controlled by ohmic conduction, which confirmed by linear slope line of I-V curve [299]. In HRS, the conduction mechanism of device can be described by Poole–Frenkel emission [300]. I-V curves of the device in HRS which is plotted between $V^{1/2}$ and ln (I/V) to study the main conduction mechanism is shown in figure 7.9 (c). It can be observed from the graph that conduction in HRS is well fitted with Poole–Frenkel emission.

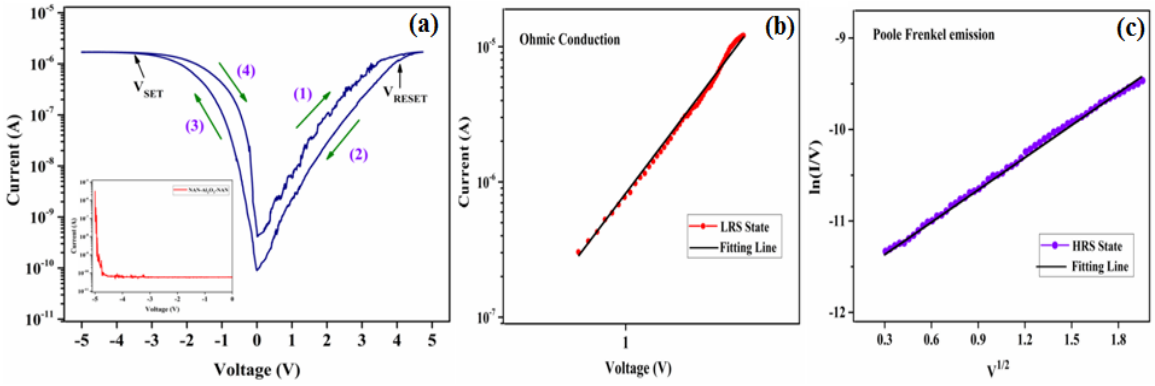

Figure 7.9: (a) I-V characteristics of ReRAM device with NAN electrodes, (b) I-V characteristics in LRS described by ohmic conduction and (c) ln (I/V) vs. $V^{1/2}$ described by Poole Frenkel emission.

It was reported that conducting filaments (CFs) are present in the oxide based device and are responsible for the change in its resistance [302]. Switching process is controlled by creation and recombination of oxygen vacancies on applying the bias voltage to device [284,303]. For our ReRAM device, the switching is accomplished by generation and recombination of oxygen vacancies in Al_2O_3 layer. According to Poole–Frenkel emission, in the Al_2O_3 layer the oxygen vacancies traps the injected electrons and result in high resistance. When negative bias voltage was applied on the top electrode the oxygen ions removed from the Al_2O_3 lattice which is shown in figure 7.10 (a) (Al_2O_{3-x}). The vacancies have been created in Al_2O_3 layer as the oxygen ions removed. The oxygen ions go to

NAN/Al_2O_3 interface and stay there and consequently conductive filaments in the Al_2O_3 layer are created. The oxygen ions move back to Al_2O_{3-x} layer when positive bias voltage was applied to the top electrode as shown in figure 7.10 (b) (Al_2O_3). Because of migration of ions to Al_2O_3 layer the oxygen vacancies are again filled up and as a result conductive filaments are ruptured. Thus, in this memory device the switching process is dominated by creation and annihilation of oxygen vacancies on applying the bias voltage to the top electrodes and consequent switching of device between LRS and HRS. When the device switches from HRS to LRS, this is known as set process and is called reset when the device switches from LRS to HRS.

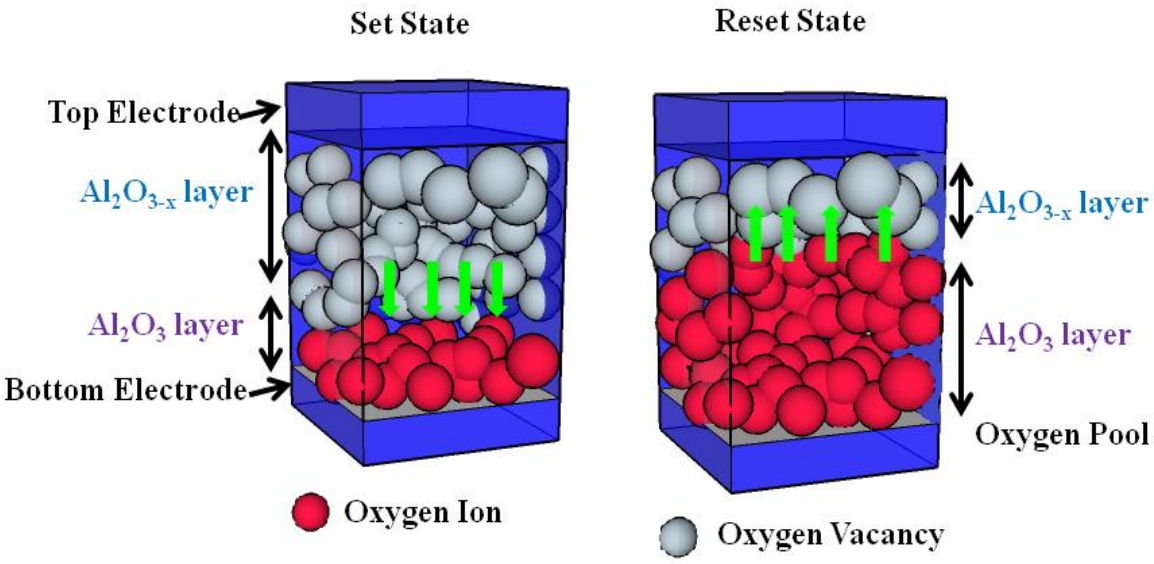

Figure 7.10: Schematic diagrams of (a) oxygen vacancies creation in set state and (b) oxygen vacancies recombination in reset state of ReRAM device with NAN electrode.

Shang *et al.* [307] prepared transparent RRAM devices of ITO/HfO_x/ITO sandwiched structure. The device demonstrated ≈75% − 88% transmittance in the visible region. The RRAM device showed a high retention period of over 10^6 second and an excellent endurance of ≈5×10^7 cycles. Cheon *et al.* [308] have reported the resistive switching behavior of metal–insulator–metal (MIM) structure of amorphous ZnO sandwiched between Al electrode and Ga-doped ZnO. The device (Al/a-ZnO/GZO) exhibited the transmittance of ~90% in visible range. Current–voltage curves showed the bipolar resistive switching behavior and resistive switching phenomenon was assigned to the

employment of amorphous ZnO as an insulating layer and the use of GZO and Al as electrodes. Kim *et al.* [309] have reported on flexible and transparent RRAM using multi thin layer electrodes. The top and bottom electrodes were formed with ZnS/Ag/ZnS, a Ti (2 nm) layer was sequentially evaporated using a metal mask and then Al_2O_3 and MgO layers were deposited as dielectric layers. The transmittance of device was over 70% in visible region on PET substrates. The device has shown successful switching from high resistance to low resistance state and vice versa. Yeom *et al.* [42] fabricated transparent and flexible RRAM based on Al_2O_3 layer using indium zinc oxide (IZO) top and bottom electrodes on flexible substrates. The device demonstrated >80% transmittance for visible wavelength region. The device showed by good on/off ratio, long retention and excellent endurance.

7.7 Conclusion

We fabricated fully transparent ReRAM devices based on TAT/Al_2O_3/TAT and NAN/Al_2O_3/NAN sandwich structures by sputtering on glass substrates at room temperature. The prepared device structures were characterized by UV-Vis, XPS and I-V measurements. Both devices have shown good transmittance over the visible region of solar radiation and device based on TAT electrode exhibited slightly higher transmittance (>85%) than the NAN electrodes based device (>83%). The chemical states of oxygen of Al_2O_3 and elemental compositions of both devices were analyzed using XPS. The transparent resistive switching random access memory devices exhibited good on–off ratio with low-voltage operation. The obtained current value of memory device with NAN electrodes was slightly higher than that with TAT electrodes. The conduction process of the ReRAM devices was described by Poole–Frenkel emission and ohmic conduction. Switching of devices from HRS to LRS was assigned to formation of conductive filaments due to creation of oxygen vacancies after applying the biasing voltage to top electrodes during the set process. We believe that fabrication of transparent ReRAM devices based on Al_2O_3 will impart to the development of transparent memory devices and next generation invisible electronic devices.

Chapter-8

Conclusions and Scope of Future Work

8.1 Conclusions

The investigations and the results obtained thereof presented in the thesis deal with fabrication of single and multilayer thin films for transparent conducting electrodes applications. The optimized multilayer transparent electrodes have been used to synthesize Al_2O_3 based ReRAM devices. The conclusions made from this study are given below:

1. Nb doped TiO_2 thin films were prepared on glass substrates with varying Nb content (0−2 at. %) using sol-gel spin coating method. Annealing of as deposited amorphous films at 550 ˚C in air led to good crystallinity and increase in electrical conduction.
2. Transmittance of these films were decreased from 85% to 70% with increasing Nb content and electrical resistivity decreased with increase in Nb and minimum resistivity of 3.56 Ω cm was observed at 2 at. % Nb.
3. $Ti_{0.97}Nb_{0.03}O_2$ thin films prepared by rf sputtering were investigated for effect of post deposition annealing on the structural, optical and electrical properties of the films.
4. Transmittance of $Ti_{0.97}Nb_{0.03}O_2$ thin films decreased from 75% to 70% with annealing temperature. The electrical resistivity of films decreased to 3.2×10^{-2} Ω cm on annealing at 450 ˚C. Hence it was concluded that 450 ˚C is the optimum annealing temperature for these films to enhance their conductivity.
5. Deposition of TiO_2/Ag/TiO_2 multilayer structure by rf/dc sputtering was done on glass substrates at room temperature. Optimization of TiO_2 top and bottom layer thickness was done by changing them from 25 nm to 65 nm.
6. Optimized TiO_2/Ag/TiO_2 hybrid film was exposed to low energy ion implantation of 40 keV N^+ and 100 keV Ar^+ ions of various fluences.
7. Nitrogen ion implantation in TAT films leads to improvement in electrical conductivity due to replacement of O by N ions and decrement in optical transmittance. However figure of merit improved from 5.2×10^{-3} Ω^{-1} to 5.7×10^{-3} Ω^{-1} with increasing fluence.

8. Argon implantation in TAT films generates oxygen vacancies in the system thereby leading to change in optical and electrical properties and a better figure of merit.
9. Synthesis of sandwich multilayer structure of NTO/Ag/NTO was done on glass substrates by sputtering at room temperature. The optimization was carried out by changing the upper and lower NTO thicknesses. The obtain results indicated that the NAN structure of 35 nm/9 nm/35 nm had maximum figure of merit.
10. The optimized pristine NAN films were also subjected to ion implantation of 40 keV N^+ and 100 keV Ar^+ at fluence ranging from 1×10^{14} to 1×10^{16} ions/cm^2 to obtain modifications in their structural, optical and electrical properties.
11. Implantations of ions lead to improvement in electrical conductivity but simultaneously transmittance decreases with increasing ion fluence. The overall figure of merit for N implantation increased from 12.7×10^{-3} Ω^{-1} to 18×10^{-3} Ω^{-1} and for Ar it increases from 12.7×10^{-3} Ω^{-1} to 14.4×10^{-3} Ω^{-1} with the increasing fluence.
12. The optimized NTO/Ag/NTO multilayer structure with N implantation was concluded to be the best among all structures developed under the scope of the thesis work. The obtained figure of merit for the NAN structure was highest among all the structures.
13. The TAT and NAN multilayer films exhibit superior electrical and optical properties and hence can be an alternative to indium tin oxide (ITO) for futuristic TCE applications in optoelectronic devices.
14. The transparent resistive switching random access memory (ReRAMs) devices based on Al_2O_3 layer were fabricated with TAT and NAN electrodes. The device prepared with TAT electrodes, show a little higher transmittance. Meanwhile, device with NAN electrodes show higher current than the device prepared with TAT electrodes.
15. We believe that successful fabrication of transparent ReRAM devices based on Al_2O_3 is an important to the development for transparent memory devices and next generation invisible electronic devices.

8.2 Scope of Future Work

Based on the present investigations and results, there is a wide scope for further extension of this work. Some of the points of future work are given below:

1. The multilayer transparent conducting electrodes can be used in development of solar cells, flat panel displays, light emitting diodes and other optoelectronic devices to obtain higher efficiencies and more applications.
2. In oxide/metal/oxide multilayer structures, the oxide layer can be replaced by polymer and the middle metal layer can be replaced by metal grids and networks for the development of organic devices with better compatibility. Polymer based TCE in flexible organic devices gives better matching of work function and mechanical stability for bending.
3. Wide band gap oxide materials may be used in oxide/metal/oxide multilayer structures to extend the transmittance window to near UV range light spectrum.
4. Retention and endurance test may be done for ReRAM devices to test their reliability and performance.
5. There is a huge scope to understand and predict the electrical conduction phenomenon in these oxide/metal/oxide multilayer structures theoretically.

References

[1] K.L. Chopra, S. Major, D.K. Pandya, Transparent conductors-A status review, Thin Solid Films. 102 (1983) 1–46. doi:10.1016/0040-6090(83)90256-0.

[2] A. Stadler, Transparent Conducting Oxides—An Up-To-Date Overview, Materials. 5 (2012) 661–683. doi:10.3390/ma5040661.

[3] T.O.M. T.J. Coutts, J.D. Perkins, and D.S. GinleyMason, Transparent Conducting Oxides : Status and Opportunities in Basic, 195th Meeting of the Electrochemical Society. (1999) 1–15.

[4] R.G. Gordon, Criteria for choosing transparent conductors, MRS Bulletin. 25 (2000) 52–57. doi:10.1557/mrs2000.151.

[5] K. Ellmer, Past achievements and future challenges in the development of optically transparent electrodes, Nature Photonics. 6 (2012) 809–817. doi:10.1038/nphoton.2012.282.

[6] K. Badeker, Ann Phys. 22 (1907) 749.

[7] G. Rupprecht, Z. Phys. 139 (1954) 504.

[8] M. Mizuhashi, Electrical properties of vacuum-deposited indium oxide and indium tin oxide films, Thin Solid Films. 70 (1980) 91–100. doi:10.1016/0040-6090(80)90415-0.

[9] Y. Song, W. Fang, R. Brenes, J. Kong, Challenges and opportunities for graphene as transparent conductors in optoelectronics, Nano Today. 10 (2015) 681–700. doi:10.1016/j.nantod.2015.11.005.

[10] F. Guo, X. Zhu, K. Forberich, J. Krantz, T. Stubhan, M. Salinas, M. Halik, S. Spallek, B. Butz, E. Spiecker, T. Ameri, N. Li, P. Kubis, D.M. Guldi, G.J. Matt, C.J. Brabec, ITO-free and fully solution-processed semitransparent organic solar cells with high fill factors, Advanced Energy Materials. 3 (2013) 1062–1067. doi:10.1002/aenm.201300100.

[11] J. Mass, P. Bhattacharya, R.S. Katiyar, Effect of high substrate temperature on Al-doped ZnO thin films grown by pulsed laser deposition, Materials Science and Engineering B: Solid-State Materials for Advanced Technology. 103 (2003) 9–15. doi:10.1016/S0921-5107(03)00127-2.

[12] M. Liang, B. Luo, L. Zhi, Application of graphene and graphene-based materials in clean energy-related devices, International Journal of Energy Research. 33 (2009) 1161–1170. doi:10.1002/er.1598.

[13] C. Zhang, D. Zhao, D. Gu, H. Kim, T. Ling, Y.K.R. Wu, L.J. Guo, An ultrathin, smooth, and low-loss Al-doped Ag film and its application as a transparent electrode in organic photovoltaics, Advanced Materials. 26 (2014) 5696–5701.

doi:10.1002/adma.201306091.

[14] D.S. Hecht, L. Hu, G. Irvin, Emerging transparent electrodes based on thin films of carbon nanotubes, graphene, and metallic nanostructures, Advanced Materials. 23 (2011) 1482–1513. doi:10.1002/adma.201003188.

[15] J.Y. Lee, S.T. Connor, Y. Cui, P. Peumans, Solution-processed metal nanowire mesh transparent electrodes, Nano Letters. 8 (2008) 689–692. doi:10.1021/nl073296g.

[16] J.H. Park, D.Y. Lee, Y.H. Kim, J.K. Kim, J.H. Lee, J.H. Park, T.W. Lee, J.H. Cho, Flexible and transparent metallic grid electrodes prepared by evaporative assembly, ACS Applied Materials and Interfaces. 6 (2014) 12380–12387. doi:10.1021/am502233y.

[17] P.C. Wang, L.H. Liu, D. Alemu Mengistie, K.H. Li, B.J. Wen, T.S. Liu, C.W. Chu, Transparent electrodes based on conducting polymers for display applications, Displays. 34 (2013) 301–314. doi:10.1016/j.displa.2013.05.003.

[18] P.C. Lansåker, J. Backholm, G.A. Niklasson, C.G. Granqvist, TiO_2/Au/TiO_2 multilayer thin films: Novel metal-based transparent conductors for electrochromic devices, Thin Solid Films. 518 (2009) 1225–1229. doi:10.1016/j.tsf.2009.02.158.

[19] M. Girtan, Comparison of ITO/metal/ITO and ZnO/metal/ZnO characteristics as transparent electrodes for third generation solar cells, Solar Energy Materials and Solar Cells. 100 (2012) 153–161. doi:10.1016/j.solmat.2012.01.007.

[20] B.G. Lewis, D.C. Paine, Applications and processing of transparent conducting oxides, MRS Bulletin. 25 (2000) 22–27. doi:10.1557/mrs2000.147.

[21] T.C. Yeh, Q. Zhu, D.B. Buchholz, A.B. Martinson, R.P.H. Chang, T.O. Mason, Amorphous transparent conducting oxides in context : Work function survey , trends , and facile modification, Applied Surface Science. 330 (2015) 405–410. doi:10.1016/j.apsusc.2015.01.026.

[22] C. Wang, J. Li, J. Dho, Post-deposition annealing effects on the transparent conducting properties of anatase Nb:TiO_2 films on glass substrates, Materials Science and Engineering B: Solid-State Materials for Advanced Technology. 182 (2014) 1–5. doi:10.1016/j.mseb.2013.11.021.

[23] D.B. Buchholz, Q. Ma, D. Alducin, A. Ponce, M. Jose-yacaman, R. Khanal, J.E. Medvedeva, R.P.H. Chang, The Structure and Properties of Amorphous Indium Oxide, Chemistry of Materials. 26 (2014) 5401-5411. doi:10.1021/cm502689x.

[24] A. Klein, K. Christoph, Transparent Conducting Oxides for Photovoltaics: Manipulation of Fermi Level, Work Function and Energy Band Alignment, Materials. 3 (2010) 4892–4914. doi:10.3390/ma3114892.

[25] C.J.M. Emmott, A. Urbina, J. Nelson, Solar Energy Materials & Solar Cells Environmental and economic assessment of ITO-free electrodes for organic solar

cells, Solar Energy Materials and Solar Cells. 97 (2012) 14–21. doi:10.1016/j.solmat.2011.09.024.

[26] G.S. Chae, A Modified Transparent Conducting Oxide for Flat Panel Displays Only, Japanese Journal of Applied Physics. 40 (2001) 1282-1286. doi.org/10.1143/JJAP.40.1282.

[27] R.D. Rauh, Electrochromic windows : an overview, Electrochimica Acta .44 (1999) 3165–3176.

[28] Z. Zhang, Y. Gao, H. Luo, L. Kang, Z. Chen, J. Du, M. Kanehira, Y. Zhang and Z.L. Wang Solution-based fabrication of vanadium dioxide on F : SnO_2 substrates with largely enhanced thermochromism and low-emissivity for energy-saving, Energy and Environmental Science. (2011). doi:10.1039/c1ee02092g.

[29] S. Kiruthika, R. Gupta, G.U. Kulkarni, Large area defrosting windows based on electrothermal heating of highly conducting and transmitting Ag wire mesh, RSC Advances. 4 (2014) 49745–49751. doi:10.1039/C4RA06811D.

[30] J.W. Seo, J. Park, K.S. Lim, J. Yang, S.J. Kang, J.W. Seo, J. Park, S. Lim, J. Yang, S.J. Kang, Transparent resistive random access memory and its characteristics for nonvolatile resistive switching, Applied Physics Letters. 93 (2011) 223505. doi:10.1063/1.3041643.

[31] H. Kawazoe, M. Yasukawa, H. Hyodo, M. Kurita, H. Yanagi, H. Hosono, P-type electrical conduction in transparent thin films of $CuAlO_2$, Letters to Nature. 389 (1997) 939–942.

[32] H. Ohta, K. Kawamura, M. Orita, M. Hirano, N. Sarukura, H. Hosono, Current injection emission from a transparent p–n junction composed of p- $SrCu_2O_2$/n-ZnO, Applied Physics Letters. 77 (2004) 475–477. doi:10.1063/1.127015.

[33] K.H.L. Zhang, K. Xi, M.G. Blamire, R.G. Egdell, P -type transparent conducting oxides, Journal of Physics: Condensed Matter. 28 (2016) 383002. doi:10.1088/0953-8984/28/38/383002.

[34] N. Xia, R.A. Gerhardt, Fabrication and characterization of highly transparent and conductive indium tin oxide fi lms made with different solution-based methods, Materials Research Express. 3 (2016) 116408. doi:10.1088/2053-1591/3/11/116408.

[35] B.H. Lee, I.G. Kim, S.W. Cho, S. Lee, Effect of process parameters on the characteristics of indium tin oxide thin film for flat panel display application, Thin Solid Films. 302 (1997) 25-30. doi.org/10.1016/S0040-6090(96)09581-8.

[36] Y. Ogawa, A.J. Waldau, Y. Hashimoto, K. Ito, In_2O_3/CdS/$CuInS_2$ Thin-Film Solar Cell with 9.7 % Efficiency, Japanese Journal of Applied Physics. 33 (1994) 1775-1777.

[37] H. Kim, J.S. Horwitz, G.P. Kushto, Z.H. Kafafi, D.B. Chrisey, H. Kim, J.S. Horwitz, G.P. Kushto, Z.H. Kafafi, D.B. Chrisey, Indium tin oxide thin films

grown on flexible plastic substrates by pulsed-laser deposition for organic light-emitting diodes, Applied Physics Letters. 79 (2001) 284-286. doi:10.1063/1.1383568.

[38] S. Okazaki, J. Ohkubo, S. Nakao, Y. Hirose, T. Hitosugi, T. Hasegawa, Fabrication of Nb-doped TiO_2 transparent conducting films by postdeposition annealing under nitrogen atmosphere, Japanese Journal of Applied Physics. 51 (2012) 118003. doi:10.1143/JJAP.51.118003.

[39] T. Minami, H. Nanto, S. Takata, Highly Conductive and Transparent Aluminum Doped Zinc Oxide Thin Films Prepared by RF Magnetron Sputtering, Jap. J. Appl. Phys. 23 (1984) L280. doi:10.1143/JJAP.23.L280.

[40] L. Pereira, E.Ã. Fortunato, L. Raniero, L. Silva, A. Gonc, A. Pimentel, P. Barquinha, G. Gonc, I. Ferreira, E. Elangovan, R. Martins, Highly stable transparent and conducting gallium-doped zinc oxide thin films for photovoltaic applications, Solar Energy Materials & Solar Cells. 92 (2008) 1605–1610. doi:10.1016/j.solmat.2008.07.009.

[41] H. Kim, R.C.Y. Auyeung, A. Piqué, Transparent conducting F-doped SnO_2 thin films grown by pulsed laser deposition, Thin Solid Films. 516 (2008) 5052–5056. doi:10.1016/j.tsf.2007.11.079.

[42] S. Yeom, S. Shin, T. Kim, H.J. Ha, Transparent resistive switching memory using aluminum oxide on a fl exible substrate, Nanotechnology. 27 (2016) 1-6. doi:10.1088/0957-4484/27/7/07LT01.

[43] A. Hadi, A. Shuhaimi, Z. Hassan, Structural, optical and electrical characterization of ITO , ITO/Ag and ITO/Ni transparent conductive electrodes, Applied Surface Science. 288 (2014) 599–603. doi:10.1016/j.apsusc.2013.10.079.

[44] T. Minami, T. Miyata, T. Yamamoto, Work function of transparent conducting multicomponent oxide thin films prepared by magnetron sputtering, Surface and Coatings Technology. 108–109 (1998) 583–587.

[45] C. Guillén, J. Herrero, TCO/metal/TCO structures for energy and flexible electronics, Thin Solid Films. 520 (2011) 1–17. doi:10.1016/j.tsf.2011.06.091.

[46] K.H. Choi, J.Y. Kim, Y.S. Lee, H.J. Kim, ITO/Ag/ITO multilayer Films for the application of a very low resistance transparent electrode, Thin Solid Films. 341 (1999) 152–155.

[47] A. Kloppel, W. Kriegseis, B.K. Meyer, A. Scharmann, C. Daube, J. Stollenwerk, J. Trube, Dependence of the electrical and optical behaviour of ITO-silver-ITO multilayers on the silver properties, Thin Solid Films. 365 (2000) 139–146.

[48] C. Charton, M. Fahland, Optical properties of thin Ag films deposited by magnetron sputtering, Surface and Coatings Technology. 174-175 (2003) 181–186. doi:10.1016/S0257-8972.

[49] C. Charton, M. Fahland, Electrical properties of Ag films on polyethylene terephthalate deposited by magnetron sputtering, Thin Solid Films. 449 (2004) 100–104. doi:10.1016/S0040-6090.

[50] H.J. Lee, J.W. Kang, S.H. Hong, S.H. Song, S.J. Park, $Mg_xZn_{1-x}O$/Ag/$Mg_xZn_{1-x}O$ Multilayers As High-Performance Transparent Conductive Electrodes, ACS Applied Materials and Interfaces. 8 (2016) 1565–1570. doi:10.1021/acsami.5b09974.

[51] A. Dhar, T.L. Alford, High quality transparent TiO_2/Ag/TiO_2 composite electrode films deposited on flexible substrate at room temperature by sputtering, APL Materials. 1 (2014) 012102 1-7 doi:10.1063/1.4808438.

[52] K. Koike, S. Fukuda, Multilayer transparent electrode consisting of silver alloy layer and metal oxide layers for organic luminescent electronic display device, Journal of Vacuum Science & Technology A 26 (2008) 444-454. doi:10.1116/1.2897315.

[53] Y. Choi, K. Choi, H. Lee, H. Lee, J. Kang, H. Kim, Nano-sized Ag-inserted amorphous $ZnSnO_3$ multilayer electrodes for cost-efficient inverted organic solar cells, Solar Energy Materials and Solar Cells. 95 (2011) 1615–1623. doi:10.1016/j.solmat.2011.01.013.

[54] Y. Park, K. Choi, H. Kim, Room temperature flexible and transparent ITO/Ag/ITO electrode grown on flexile PES substrate by continuous roll-to-roll sputtering for flexible organic photovoltaics, Journal of Physics D: Applied Physics. 42 (2009) 235109. doi:10.1088/0022-3727/42/23/235109.

[55] J.W. Seo, J. Park, K.S. Lim, S.J. Kang, Y.H. Hong, J.H. Yang, L. Fang, G.Y. Sung, H. Kim, J.W. Seo, J. Park, K.S. Lim, S.J. Kang, Y.H. Hong, Transparent flexible resistive random access memory fabricated at room temperature, Applied Physics Letters. 95 (2009) 133508 1-3. doi:10.1063/1.3242381.

[56] N. Ren, J. Zhu, S. Ban, N. Ren, J. Zhu, S. Ban, Highly transparent conductive ITO/Ag/ ITO trilayer films deposited by RF sputtering at room temperature, AIP Advances. 7 (2017) 055009 1-7. doi:10.1063/1.4982919.

[57] B. Sarma, B.K. Sarma, Role of residual stress and texture of ZnO nanocrystals on electro- optical properties of ZnO/Ag/ZnO multilayer transparent conductors, Journal of Alloys and Compounds. 734 (2018) 210–219. doi:10.1016/j.jallcom.2017.11.028.

[58] A.I.N. Press, Growth of highly conducting epitaxial ZnO–Pt–ZnO heterostructure on α-Al_2O_3 (0 001), Journal of Crystal Growth. 291 (2006) 212–217. doi:10.1016/j.jcrysgro.2006.02.010.

[59] S. Yu, W. Zhang, L. Li, D. Xu, H. Dong, Y. Jin, Optimization of SnO_2/Ag/SnO_2 tri-layer fi lms as transparent composite electrode with high figure of merit, Thin Solid Films. 552 (2014) 150–154. doi:10.1016/j.tsf.2013.11.109.

[60] Y. Yin, C. Lan, H. Guo, C. Li, Reactive Sputter Deposition of WO_3/Ag/WO_3 Film

for Indium Tin Oxide (ITO)-Free Electrochromic Devices, Applied Materials & Interfaces. 8 (2016) 3861-3867. doi:10.1021/acsami.5b10665.

[61] S. Calnan, A.N. Tiwari, High mobility transparent conducting oxides for thin film solar cells, Thin Solid Films. 518 (2010) 1839–1849. doi:10.1016/j.tsf.2009.09.044.

[62] K. Choi, H. Nam, J. Jeong, S. Cho, H. Kim, K. Choi, H. Nam, J. Jeong, S. Cho, H. Kim, Highly flexible and transparent $InZnSnO_x$/Ag/$InZnSnO_x$ multilayer electrode for flexible organic light emitting diodes, Applied Physics Letters. 9 (2008) 223302 1-3. doi:10.1063/1.2937845.

[63] A.R Madaria, A. Kumar and C. Zhou, Large scale , highly conductive and patterned transparent films of silver nanowires on arbitrary substrates and their appllications in touch screens, Nanotechnology. 22 (2011) 245201. doi:10.1088/0957-4484/22/24/245201.

[64] C.M. Lampert, Heat mirror coatings for energy conserving windows, Solar Energy Materials. 6 (1981) 1-41.

[65] S. Kiruthika, R. Gupta, G.U. Kulkarni, RSC Advances electrothermal heating of highly conducting and, RSC Advances. 4 (2014) 49745–49751. doi:10.1039/C4RA06811D.

[66] E.O. Filatova, Transparent-conductive-oxide (TCO) buffer layer effect on the resistive switching process in metal/TiO_2/TCO/metal assemblies, New Journal of Physics. 16 (2014) 113014. doi:10.1088/1367-2630/16/11/113014.

[67] H. Park, J. Kang, S. Na, D. Kim, H. Kim, Characteristics of indium-free GZO / Ag / GZO and AZO/Ag/AZO multilayer electrode grown by dual target DC sputtering at room temperature for low-cost organic photovoltaics, Solar Energy Materials and Solar Cells. 93 (2009) 1994–2002. doi:10.1016/j.solmat.2009.07.016.

[68] Y.M. Yang, Q. Chen, Y. Hsieh, T. Song, N. De Marco, Multilayer Transparent Top Electrode for Solution Processed Perovskite/Cu(In, Ga)(Se, $S)_2$ Four Terminal Tandem Solar Cells, ACS Nano. 9 (2015) 7714–7721. doi:10.1021/acsnano.5b03189.

[69] Y. Shim, H. Gyu, D. Hong, H. Won, C. Kang, Y. Soo, S. Yoon, Sensors and Actuators B : Chemical Transparent conducting oxide electrodes for novel metal oxide gas sensors, Sensors & Actuators: B. Chemical. 160 (2011) 357–363. doi:10.1016/j.snb.2011.07.061.

[70] H. Hajibabaei, O. Zandi, T.W. Hamann, Tantalum Nitride Films Integrated with Transparent Conductive Oxide Substrates via Atomic Layer Deposition for Photoelectrochemical Water Splitting, Chemical Science. (2016). doi:10.1039/C6SC02116F.

[71] H. Hosono, Recent progress in transparent oxide semiconductors : Materials and device application, Thin Solid Films. 515 (2007) 6000–6014.

doi:10.1016/j.tsf.2006.12.125.

[72] T. Minami, Transparent conducting oxide semiconductors for transparent electrodes, Semicond. Sci. Technol. 20 (2005) S35–S44. doi:10.1088/0268-1242/20/4/004.

[73] G. Bauer, Elektrisches und optisches Yerhalten von Ealbleitern. XI11, Ann. Phys. (Paris). 30 (1937) 433.

[74] T.M. Ratcheva, M.D. Nanova, L.V. Vassilev and M.G. Mikhailov, Properties of In_2O_3: Te films prepared by the spraying method, Thin Solid Films. 139 (1986) 189-199.

[75] L. Holland, Vacuum Deposition of Thin Films, Wiley, New York, (1958) 492.

[76] G. Haacke, New figure of merit for transparent conductors, Journal of Applied Physics. 47 (1976) 4086–4089. doi:10.1063/1.323240.

[77] J.L. Vossen, Abstract : Transparent conducting films, Journal of Vacuum Science & Technology. 13 (1976.) 116. doi:10.1116/1.568875.

[78] Z.M. Jabzrbski, Preparation and Physical Properties of Transparent Conducting Oxide Films, Physica Status Solidi (a) 71, (1982) 13-41.

[79] S. Major, S. Kumar, M. Bhatnagar, K.L. Chopra, S. Major, S. Kumar, M. Bhatnagar, K.L. Chopra, Effect of hydrogen plasma treatment on transparent conducting oxides, Applied Physics Letters. 49 (1986) 394-396. doi:10.1063/1.97598.

[80] A. Yamada, B. Sang, M. Konagai, Atomic layer deposition of ZnO transparent conducting oxides, Applied Surface Science. 112 (1997) 216–222.

[81] G. Gustafsson, Y. Cao, G.M. Treacy, F. Klavetter, N. Colaneri and A.J. Heeger, Flexible light emitting diodes made from soluble conducting polymer, Nature. 357 (1992) 477–478.

[82] UK Pat. (1952).

[83] J.M. Ward, Appl. 1nd, 16 (1955) 408.

[84] J.C. Manifacier, L. Szepessy, J. F. Bresse, M. Perotin and R. Stuck, Mater. Res. Bull., 14 (1979) 163.

[85] D.L. White and M. Feldman, Electron. Lett. 6 (1970) 837.

[86] E. Ando, S. Suzuki, N. Aomine, M. Miyazaki, M. Tada, Sputtered silver-based low-emissivity coatings with high moisture durability, Vacuum. 59 (2000) 792–799.

[87] R.R. Mehta, S.F. Vogel, Sputtered Cadmium Oxide and Indium Oxide/Tin Oxide Films as Transparent Electrodes to Cadmium Sulfide, Journal of The

Electrochemical Society. 119 (1972) 752. doi:10.1149/1.2404320.

[88] T.S. Films, Thin Solid Films, 91 (1982) 71-79, 91 (1982) 71–79.

[89] A. Pan, T.P. Ma, evaporation High-quality transparent conductive indium oxide films prepared by thermal evaporation, Applied Physics Letters. 37 (1980) 163-165. doi:10.1063/1.91809.

[90] T. Maruyama, K. Tabata, Indium-Tin Oxide Thin Films Prepared by Chemical Vapor Deposition from Metal Acetates, Japanese Journal of Applied Physics. 29 (1990) L355-L357.

[91] D. Burgard, C. Goebbert and R. Nass, Synthesis of Nanocrystalline, Redispersable Antimony-Doped SnO_2 Particles for the Preparation of Conductive, Transparent Coatings, Journal of Sol-Gel Science and Technology. 13 (1998) 789–792.

[92] L. Zhao, X. Zhao, J. Liu, A. Zhang, D. Wang, B. Wei, Fabrications of Nb-doped TiO2 (TNO) transparent conductive oxide polycrystalline films on glass substrates by sol–gel metho, Journal of Sol-Gel Sci Technology. 53 (2010) 475–479.

[93] K.L . Chopra , R.C. Kainthla , D.K. Pandya , and A.P. Thakoor, Chemical Solution Deposition of Inorganic Films, Physics of Thin Films. 12 (1982) 167–235. doi:10.1016/S0079-1970(13)70010-0.

[94] A. V Singh, R.M. Mehra, N. Buthrath, A. Wakahara, A. Yoshida, Highly conductive and transparent aluminum-doped zinc oxide thin films prepared by pulsed laser deposition in oxygen ambient, Journal of Applied Physics. 90 (2001) 5661-5665. doi:10.1063/1.1415544.

[95] D.C. Olson and D.S. Ginley, in Handb. Transparent Conduct. (Springer US, Boston, MA, 2011) 425 – 457.

[96] H. Ohta, M. Orita, M. Hirano, H. Tanji, H. Kawazoe, H. Hosono, Highly electrically conductive indium-tin-oxide thin films epitaxially grown on yttria-stabilized zirconia (100) by pulsed-laser deposition, Applied Physics Letters. 76 (2000) 2740–2742. doi:10.1063/1.126461.

[97] M.T.J. Facchetti, Antonio, Transparent Electronics: From Synthesis to Applications, First (Wiley, 2010).

[98] B. Bissig, T. Jäger, L. Ding, A.N. Tiwari, Y.E. Romanyuk, Limits of carrier mobility in Sb-doped SnO_2 conducting films deposited by reactive sputtering, APL Materials. 3 (2015) 62802. doi:10.1063/1.4916586.

[99] W.J. Li, C.Y. Kong, H.B. Ruan, G.P. Qin, G.J. Huang, T.Y. Yang, W.W. Liang, Y.H. Zhao, X.D. Meng, P. Yu, Y.T. Cui, L. Fang, Electrical properties and Raman scattering investigation of Ag doped ZnO thin films, Solid State Communications. 152 (2012) 147–150. doi:10.1016/j.ssc.2011.10.006.

[100] Y.M. Hu, J.Y. Li, N.Y. Chen, C.Y. Chen, T.C. Han, C.C. Yu, Effect of sputtering

power on crystallinity, intrinsic defects, and optical and electrical properties of Al-doped ZnO transparent conducting thin films for optoelectronic devices, Journal of Applied Physics. 121 (2017). doi:10.1063/1.4977104.

[101] K. Safeen, V. Micheli, R. Bartali, G. Gottardi, A. Safeen, H. Ullah, N. Laidani, Synthesis of conductive and transparent Nb-doped TiO_2 films: Role of the target material and sputtering gas composition, Materials Science in Semiconductor Processing. 66 (2017) 74–80. doi:10.1016/j.mssp.2017.04.012.

[102] A. Dhar, T.L. Alford, Optimization of TiO_2/Cu/TiO_2 Multilayer as Transparent Composite Electrode (TCE) Deposited on Flexible Substrate at Room Temperature, ECS Solid State Letters. 3 (2014) N33–N36. doi:10.1149/2.0061411ssl.

[103] J. Ho Kim, J. Hwan Lee, S.W. Kim, Y.Z. Yoo, T.Y. Seong, Highly flexible ZnO/Ag/ZnO conducting electrode for organic photonic devices, Ceramics International. 41 (2015) 7146–7150. doi:10.1016/j.ceramint.2015.02.031.

[104] Z. Zhao, T.L. Alford, The optimal TiO_2/Ag/TiO_2 electrode for organic solar cell application with high device-specific Haacke figure of merit, Solar Energy Materials and Solar Cells. 157 (2016) 599–603. doi:10.1016/j.solmat.2016.07.044.

[105] D. Kim, Characterization of TiO_2/Au/TiO_2 films deposited by magnetron sputtering on polycarbonate substrates, Applied Surface Science. 257 (2010) 704–707. doi:10.1016/j.apsusc.2010.07.038.

[106] A. El Hajj, B. Lucas, M. Chakaroun, R. Antony, B. Ratier, M. Aldissi, Optimization of ZnO/Ag/ZnO multilayer electrodes obtained by Ion Beam Sputtering for optoelectronic devices, Thin Solid Films. 520 (2012) 4666–4668. doi:10.1016/j.tsf.2011.10.193.

[107] J. Ho Kim, Y.J. Moon, S.K. Kim, Y.Z. Yoo, T.Y. Seong, Al-doped ZnO/Ag/Al-doped ZnO multilayer films with a high figure of merit, Ceramics International. 41 (2015) 14805–14810. doi:10.1016/j.ceramint.2015.08.001.

[108] S. Yu, L. Li, X. Lyu, W. Zhang, Preparation and investigation of nano-thick FTO/Ag/FTO multilayer transparent electrodes with high figure of merit, Scientific Reports. 6 (2016) 1–8. doi:10.1038/srep20399.

[109] A.L. Stepanov, Applications of ion implantation for modification of TiO_2: A review, Reviews on Advanced Materials Science. 30 (2012) 150–165.

[110] A. Zaleska, Doped-TiO_2: A Review, Recent Patents on Engineering 2008, 2, 157-164. (2008) 157–164. doi:1872-2121/08.

[111] T. Hitosugi, TiO_2-based Transparent Conducting Oxide, (2008) 1–10.

[112] J. Liu, X. Zhao, L. Duan, M. Cao, H. Sun, J. Shao, S. Chen, H. Xie, X. Chang, C. Chen, Influence of annealing process on conductive properties of Nb-doped TiO_2 polycrystalline films prepared by sol-gel method, Applied Surface Science. 257

(2011) 10156–10160. doi:10.1016/j.apsusc.2011.07.009.

[113] T. Hitosugi, N. Yamada, S. Nakao, Y. Hirose, T. Hasegawa, Properties of TiO_2-based transparent conducting oxides, Physica Status Solidi (a). 207 (2010) 1529–1537. doi:10.1002/pssa.200983774.

[114] Y. Furubayashi, T. Hitosugi, Y. Yamamoto, K. Inaba, G. Kinoda, Y. Hirose, T. Shimada, T. Hasegawa, A transparent metal: Nb-doped anatase TiO_2, Applied Physics Letters. 86 (2005) 1–3. doi:10.1063/1.1949728.

[115] R.T. Tucker, N.A. Beckers, M.D. Fleischauer, M.J. Brett, Electron beam deposited Nb-doped TiO_2 toward nanostructured transparent conductive thin films, Thin Solid Films. 525 (2012) 28–34. doi:10.1016/j.tsf.2012.10.075.

[116] K.H. Hung, P.W. Lee, W.C. Hsu, H.C. Hsing, H.T. Chang, M.S. Wong, Transparent conducting oxide films of heavily Nb-doped titania by reactive co-sputtering, Journal of Alloys and Compounds. 509 (2011) 10190–10194. doi:10.1016/j.jallcom.2011.08.020.

[117] C.M. Maghanga, J. Jensen, G.A. Niklasson, C.G. Granqvist, M. Mwamburi, Transparent and conducting TiO_2:Nb films made by sputter deposition: Application to spectrally selective solar reflectors, Solar Energy Materials and Solar Cells. 94 (2010) 75–79. doi:10.1016/j.solmat.2009.02.023.

[118] V. Brinzari, G. Korotcenkov, J. Schwank, Y. Boris, Chemisorptional approach to kinetic analysis of SnO 2 :Pd-based thin film gas sensors, Journal of Optoelectronics and Advanced Materials. 4 (2002) 147–150.

[119] S.-H. Chan, M.-C. Li, H.-S. Wei, S.-H. Chen, C.-C. Kuo, The Effect of Annealing on Nanothick Indium Tin Oxide Transparent Conductive Films for Touch Sensors, Journal of Nanomaterials. 2015 (2015) 1–5. doi:10.1155/2015/179804.

[120] M. Warzecha, J.I. Owen, M. Wimmer, F. Ruske, J. Hotovy, J. Hüpkes, High mobility annealing of transparent conductive oxides, IOP Conference Series: Materials Science and Engineering. 34 (2012) 012004 1-15. doi:10.1088/1757-899X/34/1/012004.

[121] M.S. Dabney, M.F.A.M. van Hest, C.W. Teplin, S.P. Arenkiel, J.D. Perkins, D.S. Ginley, Pulsed laser deposited Nb doped TiO_2 as a transparent conducting oxide, Thin Solid Films. 516 (2008) 4133–4138. doi:10.1016/j.tsf.2007.10.093.

[122] H.T. Sun, X.P. Wang, Z.Q. Kou, L.J. Wang, J.Y. Wang, Y.Q. Sun, Optimization of TiO_2/Cu/TiO_2 multilayers as a transparent composite electrode deposited by electron-beam evaporation at room temperature, Chinese Physics B. 24 (2015) 2–7. doi:10.1088/1674-1056/24/4/047701.

[123] S.J. Kim, E.A. Stach, C.A. Handwerker, Silver layer instability in a SnO_2/Ag/SnO_2 trilayer on silicon, Thin Solid Films. 520 (2012) 6189–6195. doi:10.1016/j.tsf.2012.05.033.

[124] A. Alyamani, N. Mustapha, Effects of high dose gamma irradiation on ITO thin film properties, Thin Solid Films. 611 (2016) 27–32. doi:10.1016/j.tsf.2016.05.022.

[125] C.J. McHargue, Ion beam modification of ceramics, Materials Science and Engineering: A. 253 (1998) 94–105. doi:10.1016/S0921-5093(98)00714-X.

[126] D. K. Avasthi, G. K. Mehta, Swift Heavy Ions for Materials Engineering and Nanostructuring, Springer Series in Materials Science. (2011).

[127] N.E. Sosa, C. Chen, J. Liu, T.J. Marks, M.C. Hersam, N.E. Sosa, C. Chen, J. Liu, T.J. Marks, and M.C. Hersam, 1 (2012) 22110.

[128] R. Fromknecht, R. Auer, I. Khubeis, O. Meyer, Lattice location and electrical conductivity in ion implanted TiO_2 single crystals, Nuclear Instruments and Methods in Physics Research Section B: Beam Interactions with Materials and Atoms. 120 (1996) 252–256. doi:10.1016/s0168-583x(96)00520-4.

[129] H. Hosono, Ionic amorphous oxide semiconductors: Material design, carrier transport, and device application, Journal of Non-Crystalline Solids. 352 (2006) 851–858. doi:10.1016/j.jnoncrysol.2006.01.073.

[130] C.H. Hong, Y.J. Jo, H.A. Kim, I.H. Lee, J.S. Kwak, Effect of electron beam irradiation on the electrical and optical properties of ITO/Ag/ITO and IZO/Ag/IZO films, Thin Solid Films. 519 (2011) 6829–6833. doi:10.1016/j.tsf.2011.01.220.

[131] Surbhi, Sharma, V., Singh, S., Garg, P., Asokan, K., Sachdev, 2018. Enhanced Electrical Conductivity in Xe Ion Irradiated CNT Based Transparent Conducting Electrode on PET Substrate, Materials Research Express. 5 (2018) 025037 1-10. https://doi.org/10.1088/2053-1591/aaaele.

[132] S. Keshri, A. Kumar, D. Kabiraj, Tailoring of optical and gas sensitivity behaviors of WO_3 films by low energy Ar^+ ion implantation, Thin Solid Films. 526 (2012) 50–58. doi:10.1016/j.tsf.2012.10.101.

[133] R. Fromknecht, I. Khubeis, S. Massing, O. Meyer, Ion implantation in TiO_2: damage production and recovery, lattice site location and electrical conductivity, Nuclear Instruments and Methods in Physics Research Section B: Beam Interactions with Materials and Atoms. 147 (1999) 191–201. doi:10.1016/S0168-583X(98)00551-5.

[134] M. Miyakawa, K. Ueda, H. Hosono, Carrier generation in highly oriented WO_3 films by proton or helium implantation, Journal of Applied Physics. 92 (2002) 2017–2022. doi:10.1063/1.1496120.

[135] J.S. Preston, Constitution and mechanism of the selenium rectifier photocell, Proc. R. Soc. Lond. A. 202 (1950) 449–466. doi:10.1098/rspa.1950.0112.

[136] H.A. McMaster, Electrically conducting films and method of application, UK patent (1947).

[137] A.R. Hutson, Piezoelectricity and conductivity in ZnO and CdS, Physical Review Letters. 4 (1960) 505–507.

[138] H.J.J. van Boort, R. Groth, Low-pressure sodium lamps with indium oxide filters, Phil. Tech. Rev. 29 (1968) 47–48.

[139] G.C. Temes, R.N. Gadenz, Liqiud-Crystal Light Valves, Electronic Letters. 6 (1970) 837–839.

[140] J. Müller, B. Rech, J. Springer, M. Vanecek, TCO and light trapping in silicon thin film solar cells, Solar Energy. 77 (2004) 917–930. doi:10.1016/j.solener.2004.03.015.

[141] K.-H. Hwang, S.-H. Nam, W.S. Jung, Y.M. Lee, H.-S. Yang, J.-H. Boo, Wet Chemical Etching of Al-doped ZnO Film Deposited by RF Magnetron Sputtering Method on Textured Glass Substrate for Energy Application, Bulletin of the Korean Chemical Society. 36 (2015) 850–854. doi:10.1002/bkcs.10159.

[142] J. Lewis, S. Grego, B. Chalamala, E. Vick, D. Temple, Highly flexible transparent electrodes for organic light-emitting diode-based displays, Applied Physics Letters. 85 (2004) 3450–3452. doi:10.1063/1.1806559.

[143] M. Chen, Z.L. Pei, C. Sun, J. Gong, R.F. Huang, L.S. Wen, ZAO: An attractive potential substitute for ITO in flat display panels, Materials Science and Engineering B: Solid-State Materials for Advanced Technology. 85 (2001) 212–217. doi:10.1016/S0921-5107(01)00584-0.

[144] R. Cinnsealach, G. Boschloo, S.N. Rao, D. Fitzmaurice, Electrochromic windows based on viologen-modified nanostructured TiO_2 films, Solar Energy Materials and Solar Cells. 55 (1998) 215–223. doi:10.1016/S0927-0248(98)00096-8.

[145] J. Shang, W. Xue, Z. Ji, G. Liu, X. Niu, X. Yi, L. Pan, Q. Zhan, X.-H. Xu, R.-W. Li, Highly flexible resistive switching memory based on amorphous-nanocrystalline hafnium oxide films, Nanoscale. 9 (2017) 7037–7046. doi:10.1039/C6NR08687J.

[146] Y. Hu, X. Diao, C. Wang, W. Hao, T. Wang, Effects of heat treatment on properties of ITO films prepared by rf magnetron sputtering, Vacuum. 75 (2004) 183–188. doi:10.1016/j.vacuum.2004.01.081.

[147] T.L. Thompson, J.T. Yates, Surface science studies of the photoactivation of TIO_2-New photochemical processes, Chemical Reviews. 106 (2006) 4428–4453. doi:10.1021/cr050172k.

[148] U. Diebold, The surface science of titanium dioxide, Surface Science Reports. 48 (2003) 53–229. doi:10.1016/S0167-5729(02)00100-0.

[149] F.A. Grant, Properties of rutile (titanium dioxide), Reviews of Modern Physics. 31 (1959) 646–674. doi:10.1103/RevModPhys.31.646.

[150] L.S. Dubrovinsky, N.A. Dubrovinskaia, V. Swamy, J. Muscat, N.M. Harrison, R. Ahuja, B. Holm, B. Johansson, The hardest known oxide, Nature. 410 (2001) 653–654. doi:10.1038/35070650.

[151] C.H. Heo, S.-B. Lee, J.-H. Boo, Deposition of TiO_2 thin films using RF magnetron sputtering method and study of their surface characteristics, Thin Solid Films. 475 (2005) 183–188. doi:10.1016/j.tsf.2004.08.033.

[152] I. Dima, B. Popescu, F. Iova, G. Popescu, Influence of the silver layer on the optical properties of the TiO_2/Ag/TiO_2 multilayer, Thin Solid Films. 200 (1991) 11–18. doi:10.1016/0040-6090(91)90026-T.

[153] K. Hashimoto, H. Irie, A. Fujishima, TiO_2 Photocatalysis: A Historical Overview and Future Prospects, Japanese Journal of Applied Physics. 44 (2005) 8269–8285. doi.org/10.1143/JJAP.44.8269.

[154] J. Nowotny, T. Bak, M.A. Alim, Defect Disorder of TiO_2. Equilibrium Constant for the Formation of Oxygen Vacancies, ECS Solid State Letters. 3 (2014) Q71–Q75. doi:10.1149/2.0011411ssl.

[155] R.M. Pasquarelli, D.S. Ginley, R. O'Hayre, Solution processing of transparent conductors: from flask to film, Chemical Society Reviews. 40 (2011) 5406. doi:10.1039/c1cs15065k.

[156] X. Liu, X. Cai, J. Qiao, J. Mao, N. Jiang, The design of ZnS/Ag/ZnS transparent conductive multilayer films, Thin Solid Films. 441 (2003) 200–206. doi:10.1016/S0040-6090(03)00141-X.

[157] W. Wang, M. Song, T.S. Bae, Y.H. Park, Y.C. Kang, S.G. Lee, S.Y. Kim, D.H. Kim, S. Lee, G. Min, G.H. Lee, J.W. Kang, J. Yun, Transparent ultrathin oxygen-doped silver electrodes for flexible organic solar cells, Advanced Functional Materials. 24 (2014) 1551–1561. doi:10.1002/adfm.201301359.

[158] C.J. Brinker, G.W. Scherer. Sol--Gel Science: The Physics and Chemistry of sol-gel processing, Academic Press. Inc. (1990).

[159] A.C. Pierre, Introduction to Sol-Gel Processing, (1998). doi:10.1007/978-1-4615-5659-6.

[160] S. Swann, Magnetron Sputtering, Physics in Technology. 19 (1988) 67–75.

[161] L. Holland, G. Siddall, Reactive Sputtering and Associated Plant Design, Vacuum III (1953) 245–253. doi:10.1016/0042-207X(53)90563-6.

[162] Y.H. Kim, J.W. Lee, R.I. Murakami, Dependences of sputtering times on the structural and electrical properties of ZnO/Ag/ZnO thin films on PET by DC sputtering, IEEE Transactions on Nanotechnology. 12 (2013) 991–995. doi:10.1109/TNANO.2013.2274596.

[163] W. Shockey, N.J. Madison, Forming semconductive devices by onic bombardment,

United States Patent Office. 2,787,564 (1957).

[164] C.A. Straede, Application of ion implantation in tooling industry, Nuclear Instruments and Methods in Physics Research Section B: Beam Interactions with Materials and Atoms. 113 (1996) 161–166. doi:http://dx.doi.org/10.1016/0168-583X(95)01380-6.

[165] J. Perriere, Rutherford Backscattering Spectrometry, Vacuum. 37 (1987) 429–432.

[166] W.E. Swartz, X-Ray Photoelectron Spectroscopy, Analytical Chemistry. 45 (1973) 788A–800A. doi:10.1021/ac60331a001.

[167] N.J. Unakar, J. Jane, Y. Tsui, C. V. Harding, Scanning Electron Microscopy, Ophthalmic Research. 13 (1981) 20–35. doi:10.1159/000265104.

[168] O.P. Choudhary, P. ka, Scanning Electron Microscope: Advantages and Disadvantages in Imaging Components, International Journal of Current Microbiology and Applied Sciences. 6 (2017) 1877–1882. doi:10.20546/ijcmas.2017.605.207.

[169] E. Meyer, Atomic force microscopy, Progress in Surface Science. 41 (1992) 3-49.

[170] D.B. Williams and C.B. Carter, in Transm. Electron Microsc. (Springer US, Boston, MA, 1996), 3 – 17.

[171] A.B. Djuris, UV-VIS and Photoluminescence Spectroscopy for Nanomaterials Characterization (2013).

[172] R. Green, Hall Effect Measurements in Materials Characterization, Keithley White Paper. 3111 (2011) 1–11.

[173] C.M. Maghanga, G.A. Niklasson, C.G. Granqvist, Optical properties of sputter deposited transparent and conducting TiO_2:Nb films, Thin Solid Films. 518 (2009) 1254–1258. doi:10.1016/j.tsf.2009.06.064.

[174] H. Tang, K. Prasad, R. Sanjinès, P.E. Schmid, F. Lévy, Electrical and optical properties of TiO_2 anatase thin films, Journal of Applied Physics. 75 (1994) 2042–2047. doi:10.1063/1.356306.

[175] J.K. Lee, H.S. Jung, J.A. Valdez, M.F. Hundley, J.D. Thompson, K.E. Sickafus, M. Nastasi, D.W. Hamby, D.A. Lucca, Room temperature ferromagnetism of Co doped TiO_2 using ion implantation and defect engineering, Nuclear Instruments and Methods in Physics Research, Section B: Beam Interactions with Materials and Atoms. 250 (2006) 279–282. doi:10.1016/j.nimb.2006.04.171.

[176] H. Su, Y.T. Huang, Y.H. Chang, P. Zhai, N.Y. Hau, P.C.H. Cheung, W.T. Yeh, T.C. Wei, S.P. Feng, The Synthesis of Nb-doped TiO_2 Nanoparticles for Improved-Performance Dye Sensitized Solar Cells, Electrochimica Acta. 182 (2015) 230–237. doi:10.1016/j.electacta.2015.09.072.

[177] E. Uyanga, A. Gibaud, P. Daniel, D. Sangaa, G. Sevjidsuren, P. Altantsog, T.

Beuvier, C.H. Lee, A.M. Balagurov, Structural and vibrational investigations of Nb-doped TiO_2 thin films, Materials Research Bulletin. 60 (2014) 222–231. doi:10.1016/j.materresbull.2014.08.035.

[178] W.F. Zhang, Y.L. He, M.S. Zhang, Z. Yin, Q. Chen, Raman scattering study on anatase TiO_2 nanocrystals, Journal of Physics D: Applied Physics. 33 (2000) 912–916. doi:10.1088/0022-3727/33/8/305.

[179] L. De Trizio, R. Buonsanti, A.M. Schimpf, A. Llordes, D.R. Gamelin, R. Simonutti, D.J. Milliron, Nb-Doped Colloidal TiO_2 Nanocrystals with Tunable Infrared Absorption, Chemistry of Materials. 25 (2013) 3383–3390. doi:10.1021/cm402396c.

[180] J.C. Parker, R.W. Siegel, Raman microprobe study of nanophase TiO_2 and oxidation-induced spectral changes, Journal of Materials Research. 5 (1990) 1246–1252. doi:10.1557/JMR.1990.1246.

[181] J.C. Parker, R.W. Siegel, Calibration of the Raman spectrum to the oxygen stoichiometry of nanophase TiO_2, Applied Physics Letters. 57 (1990) 943–945. doi:10.1063/1.104274.

[182] P. Mazzolini, V. Russo, C.S. Casari, T. Hitosugi, S. Nakao, T. Hasegawa, A. Li Bassi, Vibrational-Electrical Properties Relationship in Donor-Doped TiO_2 by Raman Spectroscopy, Journal of Physical Chemistry C. 120 (2016) 18878–18886. doi:10.1021/acs.jpcc.6b05282.

[183] J. Yang, X. Zhang, C. Wang, P. Sun, L. Wang, B. Xia, Y. Liu, Solar photocatalytic activities of porous Nb-doped TiO_2 microspheres prepared by ultrasonic spray pyrolysis, Solid State Sciences. 14 (2012) 139–144. doi:10.1016/j.solidstatesciences.2011.11.010.

[184] M. Yang, C. Hume, S. Lee, Y.-H. Son, J.-K. Lee, Correlation between Photocatalytic Efficacy and Electronic Band Structure in Hydrothermally Grown TiO_2 Nanoparticles, The Journal of Physical Chemistry C. 114 (2010) 15292–15297. doi:10.1021/jp103764n.

[185] S. Perumal, G.C. Sambandam, M.K. Prabu, S. Ananthakumar, Synthesis and characterization studies of nano TiO_2 prepared via sol-gel method, International Journal of Research in Engineering and Technology. 3 (2014) 651–657.

[186] G. Battiston, R. Gerbasi, M. Porchia, Influence of substrate on structural properties of TiO_2 thin films obtained via MOCVD, Thin Solid Films. 239 (1994) 186–191. doi.org/10.1016/0040-6090(94)90849-4.

[187] C.G. Sambandam, A.P. Mohamed, Synthesis and Characterization Studies of Solvothermally Synthesized Undoped and Ag-Doped TiO_2 Nanoparticles Using Toluene as a Solvent, Journal of Engineering Research and Applications. 4 (2014) 184–187.

[188] S.S. Al-taweel, H.R. Saud, New route for synthesis of pure anatase TiO_2

nanoparticles via utrasound- assisted sol-gel method, Journal of Chemical and Pharmaceutical Research. 8 (2) (2016) 620-626.

[189] T. Nikolay, L. Larina, O. Shevaleevskiy, B.T. Ahn, Electronic structure study of lightly Nb-doped TiO_2 electrode for dye-sensitized solar cells, Energy & Environmental Science. 4 (2011) 1480-1486. doi:10.1039/c0ee00678e.

[190] S. Singh, V. Sharma, K. Sachdev, Investigation of Post Annealing Effects on Nb:TiO_2 Transparent Conducting Thin Films, Advanced Science Letters. 22 (2016) 3773–3776. doi:10.1166/asl.2016.8069.

[191] L. Gan, C. Wu, Y. Tan, B. Chi, J. Pu, L. Jian, Oxygen sensing performance of Nb-doped TiO_2 thin film with porous structure, Journal of Alloys and Compounds. 585 (2014) 729–733. doi:10.1016/j.jallcom.2013.09.161.

[192] M. Wang, Y. Gao, Z. Chen, C. Cao, J. Zhou, L. Dai, X. Guo, Transparent and conductive W-doped SnO_2 thin films fabricated by an aqueous solution process, Thin Solid Films. 544 (2013) 419–426. doi:10.1016/j.tsf.2013.02.088.

[193] Y. Wang, B.M. Smarsly, I. Djerdj, Niobium doped TiO_2 with mesoporosity and its application for lithium insertion, Chemistry of Materials. 22 (2010) 6624–6631. doi:10.1021/cm1020977.

[194] C.P. Sibu, S.R. Kumar, P. Mukundan, K.G.K. Warrier, Structural modifications and associated properties of lanthanum oxide doped sol-gel nanosized titanium oxide, Chemistry of Materials. 14 (2002) 2876–2881. doi:10.1021/cm010966p.

[195] T. Potlog, P. Dumitriu, M. Dobromir, A. Manole, D. Luca, Nb-doped TiO_2 thin films for photovoltaic applications, Materials & Design. 85 (2015) 558–563. doi:10.1016/j.matdes.2015.07.034.

[196] J. Tauc, Optical Properties of Amorphous Semiconductors, Amorphous and Liquid Semiconductors. (1974) 159–220. doi:10.1007/978-1-4615-8705-7_4.

[197] M. Chen, Z.L. Pei, X. Wang, Y.H. Yu, X.H. Liu, C. Sun, Intrinsic limit of electrical properties of transparent conductive oxide films, Journal of Physics D: Applied Physics. 33 (2000) 2538–2548.

[198] O.N. Lamellae, O.F. Arbitrary, A Method of Measuring the Resistivity and Hall Coefficient on Lamellae of Arbitrary Shape, Phillps Technical Review. 20 (1958) 220–224. http://www.extra.research.philips.com/hera/people/aarts/_Philips Bound Archive/PTechReview/PTechReview-20-1958_59-220.pdf.

[199] L. Zhao, X. Zhao, J. Liu, A. Zhang, D. Wang, B. Wei, Fabrications of Nb-doped TiO_2 (TNO) transparent conductive oxide polycrystalline films on glass substrates by sol-gel method, Journal of Sol-Gel Science and Technology. 53 (2010) 475–479. doi:10.1007/s10971-009-2102-3.

[200] R. Sanjinés, H. Tang, H. Berger, F. Gozzo, G. Margaritondo, F. Lévy, Electronic structure of anatase TiO_2 oxide, Journal of Applied Physics. 75 (1994) 2945–2951.

doi:10.1063/1.356190.

[201] C.N.R. Rao, D.D. Sarma, S. Vasudevan, M.S. Hegde, Study of Transition Metal Oxides by Photoelectron Spectroscopy, Proceedings of the Royal Society A: Mathematical, Physical and Engineering Sciences. 367 (1979) 239–252. doi:10.1098/rspa.1979.0085.

[202] A. Berko, I. Ulrych, K.C. Prince, Encapsulation of Rh nanoparticles supported on TiO_2 (110)-(1x1) surface: XPS and STM studies, Journal of Physical Chemistry B. 102 (1998) 3379–3386. doi:10.1021/jp973255g.

[203] Z. Song, J. Hrbek, R. Osgood, Formation of TiO_2 nanoparticles by reactive-layer-assisted deposition and characterization by XPS and STM, Nano Letters. 5 (2005) 1327–1332. doi:10.1021/nl0505703.

[204] M.Z. Atashbar, H.T. Sun, B. Gong, W. Wlodarski, R. Lamb, XPS study of Nb-doped oxygen sensing TiO_2 thin films prepared by sol-gel method, Thin Solid Films. 326 (1998) 238–244.

[205] Z. Dohcevic-Mitrovic, Z. V. Popović, M. Šćepanović, Anharmonicity effects in nanocrystals studied by Raman scattering spectroscopy, Acta Physica Polonica A. 116 (2009) 36–41. doi:10.12693/APhysPolA.116.36.

[206] M.J. Šćepanović, M. Grujić-Brojčin, Z.D. Dohčević-Mitrović, Z. V. Popović, Characterization of anatase TiO_2 nanopowder by variable-temperature raman spectroscopy, Science of Sintering. 41 (2009) 67–73. doi:10.2298/SOS0901067S.

[207] C.F. Yu, S.J. Sun, J.M. Chen, Magnetic and electrical properties of TiO_2:Nb thin films, Applied Surface Science. 292 (2014) 773–776. doi:10.1016/j.apsusc.2013.12.047.

[208] A. V. Manole, M. Dobromir, M. Gîrtan, R. Mallet, G. Rusu, D. Luca, Optical properties of Nb-doped TiO_2 thin films prepared by sol-gel method, Ceramics International. 39 (2013) 4771–4776. doi:10.1016/j.ceramint.2012.11.066.

[209] Y. Sato, H. Akizuki, T. Kamiyama, Y. Shigesato, Transparent conductive Nb-doped TiO2films deposited by direct-current magnetron sputtering using a TiO_{2-x} target, Thin Solid Films. 516 (2008) 5758–5762. doi:10.1016/j.tsf.2007.10.047.

[210] S. Keshri, A. Kumar, D. Kabiraj, Tailoring of optical and gas sensitivity behaviors of WO_3 films by low energy Ar^+ ion implantation, Thin Solid Films. 526 (2012) 50–58. doi:10.1016/j.tsf.2012.10.101.

[211] R. Asahi, T. Mikawa, T. Ohwaki, K. Aoki, Y. Taga, Visible Light Photocatalysis in Nitrogen-Doped Titanium Oxides, Science. 293 (2001) 269–271. doi:10.1126/science.1061051.

[212] W. Choi, A. Termin, M.R. Hoffmann, The Role of Metal Ion Dopants in Quantum-Sized TiO_2: Correlation between Photoreactivity and Charge Carrier Recombination Dynamics, Journal of Physical Chemistry. 98 (1994) 13669–13679.

doi:10.1021/j100102a038.

[213] J. Zhang, Q. Sun, J. Zheng, X. Zhang, Y. Cui, P. Wang, W. Li, Y. Zhu, The characterization of nitrogen doped TiO_2 photoanodes and its application in the dye sensitized solar cells, Journal of Renewable and Sustainable Energy. 3 (2011). doi:10.1063/1.3599840.

[214] T.C. Jagadale, S.P. Takale, R.S. Sonawane, H.M. Joshi, S.I. Patil, B.B. Kale, S.B. Ogale, N-doped TiO_2 nanoparticle based visible light photocatalyst by modified peroxide sol-gel method, Journal of Physical Chemistry C. 112 (2008) 14595–14602. doi:10.1021/jp803567f.

[215] C. Burda, Y. Lou, X. Chen, A.C.S. Samia, J. Stout, J.L. Gole, Enhanced Nitrogen Doping in TiO_2 Nanoparticles, Nano Letters. 3 (2003) 1049–1051. doi:10.1021/nl034332o.

[216] M. Sathish, B. Viswanathan, R.P. Viswanath, C.S. Gopinath, Synthesis, characterization, electronic structure, and photocatalytic activity of nitrogen-doped TiO_2 nanocatalyst, Chemistry of Materials. 17 (2005) 6349–6353. doi:10.1021/cm052047v.

[217] T. Yoshida, S. Niimi, M. Yamamoto, T. Nomoto, S. Yagi, Effective nitrogen doping into TiO_2 (N-TiO_2) for visible light response photocatalysis, Journal of Colloid and Interface Science. 447 (2014) 278–281. doi:10.1016/j.jcis.2014.12.097.

[218] N.C. Saha, H.G. Tompkins, Titanium nitride oxidation chemistry: An x-ray photoelectron spectroscopy study, Journal of Applied Physics. 72 (1992) 3072–3079. doi:10.1063/1.351465.

[219] R. Chen, C. Zou, J. Bian, A. Sandhu, W. Gao, Microstructure and optical properties of Ag-doped ZnO nanostructures prepared by a wet oxidation doping process., Nanotechnology. 22 (2011) 105706. doi:10.1088/0957-4484/22/10/105706.

[220] H. Liu, L. Li, T. Yao, W. Ding, D. Ju, W. Chai, The effect of ion source working power on the composition and optical properties of TiO_2 films bombarded by N ion beam, Surface and Coatings Technology. 219 (2013) 88–93. doi:10.1016/j.surfcoat.2013.01.009.

[221] M. Rizwan, A. Ahmad, K.M. Deen, W. Haider, Electrochemical behavior and biological response of Mesenchymal Stem Cells on cp-Ti after N-ions implantation, Applied Surface Science. 320 (2014) 718–724. doi:10.1016/j.apsusc.2014.09.169.

[222] B. Joseph, P.K. Manoj, V.K. Vaidyan, Studies on the structural, electrical and optical properties of Al-doped ZnO thin films prepared by chemical spray deposition, Ceramics International. 32 (2006) 487–493. doi:10.1016/j.ceramint.2005.03.029.

[223] M. Di Giulio, G. Micocci, R. Rella, P. Siciliano, A. Tepore, Optical Absorption of Tellurium Suboxide Thin Films, Physica Status Solidi (a). 136 (1993) K101–K104. doi:10.1002/pssa.2211360236.

[224] J.Y. Lee, J.W. Yang, J.H. Chae, J.H. Park, J.I. Choi, H.J. Park, D. Kim, Dependence of intermediated noble metals on the optical and electrical properties of ITO/metal/ITO multilayers, Optics Communications. 282 (2009) 2362–2366. doi:10.1016/j.optcom.2008.12.044.

[225] R. Fromknecht, R. Auer, I. Khubeis, O. Meyer, Lattice location and electrical conductivity in ion implanted TiO_2 single crystals, Nuclear Instruments and Methods in Physics Research Section B: Beam Interactions with Materials and Atoms. 120 (1996) 252–256. doi:10.1016/S0168-583X(96)00520-4.

[226] C.-H. Yang, S.-C. Lee, S.-C. Chen, T.-C. Lin, The effect of annealing treatment on microstructure and properties of indium tin oxides films, Materials Science and Engineering: B. 129 (2006) 154–160. doi:10.1016/j.mseb.2006.01.012.

[227] K. Seal, M.A. Nelson, Z.C. Ying, D.A. Genov, A.K. Sarychev, V.M. Shalaev, Growth, morphology, and optical and electrical properties of semicontinuous metallic films, Physical Review B. 67 (2003) 35318. doi:10.1103/PhysRevB.67.035318.

[228] N. Zhou, D.B. Buchholz, G. Zhu, X. Yu, H. Lin, A. Facchetti, T.J. Marks, R.P.H. Chang, Ultraflexible polymer solar cells using amorphous zinc-indium-tin oxide transparent electrodes., Advanced Materials. 26 (2014) 1098–1104. doi:10.1002/adma.201302303.

[229] S. Mohapatra, N. Bhardwaj, A. Pandey, MeV ion irradiation induced evolution of morphological, structural and optical properties of nanostructured SnO_2 thin films, Materials Research Express. 2 (2015) 45013. doi:10.1088/2053-1591/2/4/045013.

[230] H.-G. Boyen, P. Widmayer, D. Schwertberger, N. Deyneka, P. Ziemann, Sequential ion-induced stress relaxation and growth: A way to prepare stress-relieved thick films of cubic boron nitride, Applied Physics Letters. 76 (2000) 709. doi:10.1063/1.125869.

[231] T. Pieńkos, L. Gładyszewski, A. Prószyński, D. Chocyk, G. Gładyszewski, F. Martin, C. Jaouen, M. Drouet, B. Lamongie, Stress development during thin film growth and its modification under ion irradiation, Vacuum. 70 (2003) 243–248. doi:10.1016/S0042-207X(02)00650-4.

[232] S. Chandramohan, R. Sathyamoorthy, P. Sudhagar, D. Kanjilal, D. Kabiraj, K. Asokan, V. Ganesan, Influence of SHI irradiation on the structure and surface topography of CdTe thin films on flexible substrate, Journal of Materials Science: Materials in Electronics. 18 (2007) 1093–1098. doi:10.1007/s10854-007-9137-4.

[233] V. Sharma, P. Kumar, A. Kumar, Surbhi, K. Asokan, K. Sachdev, High-performance radiation stable ZnO/Ag/ZnO multilayer transparent conductive

electrode, Solar Energy Materials and Solar Cells. 169 (2017) 122–131. doi:10.1016/j.solmat.2017.05.009.

[234] S. Hashimoto, A. Tanaka, Alteration of Ti 2p XPS spectrum for titanium oxide by low-energy Ar ion bombardment, Surface and Interface Analysis. 34 (2002) 262–265. doi:10.1002/sia.1296.

[235] G. Liu, W. Jaegermann, J. He, V. Sundstro, L. Sun, XPS and UPS Characterization of the TiO_2/ZnPcGly Heterointerface: Alignment of Energy Levels, Journal of Physical Chemistry B. 106 (2002) 5814–5819.

[236] H. Chen, G. Liu, L. Wang, Switched photocurrent direction in Au/TiO_2 bilayer thin films, Scientific Reports. 5 (2015) 10852. doi:10.1038/srep10852.

[237] T. Harifi, M. Montazer, Fe^{3+}:Ag/TiO_2 nanocomposite: Synthesis, characterization and photocatalytic activity under UV and visible light irradiation, Applied Catalysis A: General. 473 (2014) 104–115. doi:10.1016/j.apcata.2014.01.005.

[238] M. Shirkhanzadeh, XRD and XPS characterization of superplastic TiO_2 coatings prepared on Ti6Al4V surgical alloy by an electrochemical method, Journal of Materials Science: Materials in Medicine. 6 (1995) 206–210. doi:10.1007/BF00146857.

[239] M. Miyakawa, K. Kawamura, H. Hosono, H. Kawazoe, Large electrical conductivity enhancement of WO_3 thin films produced by ion implantation, Journal of Applied Physics. 84 (1998) 5610. doi:10.1063/1.368608.

[240] L. Cattin, M. Morsli, F. Dahou, S.Y. Abe, A. Khelil, J.C. Bernède, Investigation of low resistance transparent MoO_3/Ag/MoO_3 multilayer and application as anode in organic solar cells, Thin Solid Films. 518 (2010) 4560–4563. doi:10.1016/j.tsf.2009.12.031.

[241] C. Guillén, J. Herrero, Transparent conductive ITO/Ag/ITO multilayer electrodes deposited by sputtering at room temperature, Optics Communications. 282 (2009) 574–578. doi:10.1016/j.optcom.2008.10.075.

[242] C. Guillén, J. Herrero, Transparent electrodes based on metal and metal oxide stacked layers grown at room temperature on polymer substrate, Physica Status Solidi (A) Applications and Materials Science. 207 (2010) 1563–1567. doi:10.1002/pssa.200983707.

[243] K. Koike, S. Fukuda, Multilayer transparent electrode consisting of silver alloy layer and metal oxide layers for organic luminescent electronic display device, Journal of Vacuum Science & Technology A: Vacuum, Surfaces, and Films. 26 (2008) 444–454. doi:10.1116/1.2897315.

[244] K. Sivaramakrishnan, N.D. Theodore, J.F. Moulder, T.L. Alford, The role of copper in ZnO/Cu/ZnO thin films for flexible electronics, Journal of Applied Physics. 106 (2009). doi:10.1063/1.3213385.

[245] H. Ehrenreich, H.R. Philipp, Optical properties of Ag and Cu, Physical Review. 128 (1962) 1622–1629. doi:10.1103/PhysRev.128.1622.

[246] J.H. Kim, D.H. Kim, T.Y. Seong, Realization of highly transparent and low resistance TiO_2/Ag/TiO_2conducting electrode for optoelectronic devices, Ceramics International. 41 (2015) 3064–3068. doi:10.1016/j.ceramint.2014.10.148.

[247] S.H. Mohamed, Effects of Ag layer and ZnO top layer thicknesses on the physical properties of ZnO/Ag/Zno multilayer system, Journal of Physics and Chemistry of Solids. 69 (2008) 2378–2384. doi:10.1016/j.jpcs.2008.03.019.

[248] M. Bender, W. Seelig, C. Daube, H. Frankenberger, B. Ocker, J. Stollenwerk, Dependence of film composition and thicknesses on optical and electrical properties of ITO–metal–ITO multilayers, Thin Solid Films. 326 (1998) 67–71. doi:10.1016/S0040-6090(98)00520-3.

[249] H. Han, N.D. Theodore, T.L. Alford, Improved conductivity and mechanism of carrier transport in zinc oxide with embedded silver layer, Journal of Applied Physics. 103 (2008). doi:10.1063/1.2829788.

[250] A. Indluru, T.L. Alford, Effect of Ag thickness on electrical transport and optical properties of indium tin oxide-Ag-indium tin oxide multilayers, Journal of Applied Physics. 105 (2009). doi:10.1063/1.3153977.

[251] R. Po, C. Carbonera, A. Bernardi, N. Camaioni, The role of buffer layers in polymer solar cells, Energy Environ. Sci. 4 (2011) 285–310. doi:10.1039/C0EE00273A.

[252] H.M. Lee, S.S. Kim, H.K. Kim, Artificially MoO_3 graded ITO anodes for acidic buffer layer free organic photovoltaics, Applied Surface Science. 364 (2016) 340–348. doi:10.1016/j.apsusc.2015.12.171.

[253] H. Lei, P. Qin, W. Ke, Y. Guo, X. Dai, Z. Chen, H. Wang, B. Li, Q. Zheng, G. Fang, Performance enhancement of polymer solar cells with high work function CuS modified ITO as anodes, Organic Electronics: Physics, Materials, Applications. 22 (2015) 173–179. doi:10.1016/j.orgel.2015.03.051.

[254] V. Kumar, F. Singh, O.M. Ntwaeaborwa, H.C. Swart, Effect of Br^{+6} ions on the structural, morphological and luminescent properties of ZnO/Si thin films, Applied Surface Science. 279 (2013) 472–478. doi:10.1016/j.apsusc.2013.04.145.

[255] S. Thomas, H. Thomas, D.K. Avasthi, A. Tripathi, R. V. Ramanujan, M.R. Anantharaman, Swift heavy ion induced surface modification for tailoring coercivity in Fe-Ni based amorphous thin films, Journal of Applied Physics. 105 (2009). doi:10.1063/1.3075581.

[256] H. Thomas, S. Thomas, R. V. Ramanujan, D.K. Avasthi, I.A. Al- Omari, S. Al-Harthi, M.R. Anantharaman, Swift heavy ion induced surface and microstructural evolution in metallic glass thin films, Nuclear Instruments and Methods in Physics Research, Section B: Beam Interactions with Materials and Atoms. 287 (2012) 85–

90. doi:10.1016/j.nimb.2012.05.039.

[257] Y.H. Tak, K.B. Kim, H.G. Park, K.H. Lee, J.R. Lee, Criteria for ITO (indium-tin-oxide) thin film as the bottom electrode of an organic light emitting diode, Thin Solid Films. 411 (2002) 12–16. doi:10.1016/S0040-6090(02)00165-7.

[258] J.H. Lee, B.O. Park, Transparent conducting ZnO:Al, In and Sn thin films deposited by the sol-gel method, Thin Solid Films. 426 (2003) 94–99. doi:10.1016/S0040-6090(03)00014-2.

[259] K.P. Sibin, G. Srinivas, H.D. Shashikala, A. Dey, N. Sridhara, A. Kumar Sharma, H.C. Barshilia, Highly transparent and conducting ITO/Ag/ITO multilayer thin films on FEP substrates for flexible electronics applications, Solar Energy Materials and Solar Cells. 172 (2017) 277–284. doi:10.1016/j.solmat.2017.08.001.

[260] L. Zhou, X. Chen, F. Zhu, X. Sun, Z. Sun, Improving temperature-stable AZO–Ag–AZO multilayer transparent electrodes using thin Al layer modification, Journal of Physics D: Applied Physics. 45 (2012) 505103. doi:10.1088/0022-3727/45/50/505103.

[261] T. Morikawa, R. Asahi, T. Ohwaki, K. Aoki, Y. Taga, Band-Gap Narrowing of Titanium Dioxide by Nitrogen Doping, Japanese Journal of Applied Physics. 40 (2001) L561–L563. doi:10.1143/JJAP.40.L561.

[262] P. Wu, C. Ma, J. Shang, Effects of nitrogen doping on optical properties of TiO_2 thin films, Applied Physics A: Materials Science & Processing 81 (2005) 1411–1417. doi:10.1007/s00339-004-3101-4.

[263] S. Kim, J.-L. Lee, Design of dielectric/metal/dielectric transparent electrodes for flexible electronics, Journal of Photonics for Energy. 2 (2012) 21215. doi:10.1117/1.JPE.2.021215.

[264] G. Sahasrabudhe, J. Krizan, S.L. Bergman, R.J. Cava, J. Schwartz, Million-fold Increase of the Conductivity in TiO_2 Rutile through 3% Niobium Incorporation, Chemistry of Materials. 28 (2016) 3630–3633. doi:10.1021/acs.chemmater.6b02031.

[265] S.Y. Myong, J. Steinhauser, R. Schlüchter, S. Faÿ, E. Vallat-Sauvain, A. Shah, C. Ballif, A. Rüfenacht, Temperature dependence of the conductivity in large-grained boron-doped ZnO films, Solar Energy Materials and Solar Cells. 91 (2007) 1269–1274. doi:10.1016/j.solmat.2007.04.022.

[266] S. Yu, W. Zhang, L. Li, D. Xu, H. Dong, Y. Jin, Transparent conductive Sb-doped SnO_2/Ag multilayer films fabricated by magnetron sputtering for flexible electronics, Acta Materialia. 61 (2013) 5429–5436. doi:10.1016/j.actamat.2013.05.031.

[267] D. Gaspar, L. Pereira, K. Gehrke, B. Galler, E. Fortunato, R. Martins, High mobility hydrogenated zinc oxide thin films, Solar Energy Materials and Solar Cells. 163 (2017) 255–262. doi:10.1016/j.solmat.2017.01.030.

[268] V. Sharma, R. Vyas, P. Bazylewski, G.S. Chang, K. Asokan, K. Sachdev, Probing the highly transparent and conducting SnO_x/Au/SnO_x structure for futuristic TCO applications, RSC Adv. 6 (2016) 29135–29141. doi:10.1039/C5RA24422F.

[269] S. Singh, V. Sharma, K. Sachdev, materials Investigation of effect of doping concentration in Nb-doped TiO_2 thin films for TCO applications, Journal of Materials Science. 52 (2017) 11580–11591. doi:10.1007/s10853-017-1328-7.

[270] S. Södergren, H. Siegbahn, H. Rensmo, H. Lindström, A. Hagfeldt, S.-E. Lindquist, Lithium Intercalation in Nanoporous Anatase TiO_2 Studied with XPS, The Journal of Physical Chemistry B. 101 (1997) 3087–3090. doi:10.1021/jp9639399.

[271] A. Chen, K. Zhu, Q. Shao, Z. Ji, Understanding the effects of TCO work function on the performance of organic solar cells by numerical simulation, Semiconductor Science and Technology. 31 (2016) 1–6. doi:10.1088/0268-1242/31/6/065025.

[272] A.H. Ramezani, M.R. Hantehzadeh, M. Ghoranneviss, E. Darabi, Structural modification of tantalum crystal induced by nitrogen ion implantation, Bulletin of Materials Science. 39 (2016) 633–640. doi:10.1007/s12034-016-1212-0.

[273] M. Mickan, U. Helmersson, H. Rinnert, J. Ghanbaja, D. Muller, D. Horwat, Room temperature deposition of homogeneous, highly transparent and conductive Al-doped ZnO films by reactive high power impulse magnetron sputtering, Solar Energy Materials and Solar Cells. 157 (2016) 742–749. doi:10.1016/j.solmat.2016.07.020.

[274] T. Hitosugi, Y. Furubayashi, A. Ueda, K. Itabashi, K. Inaba, Y. Hirose, G. Kinoda, Y. Yamamoto, T. Shimada, T. Hasegawa, Ta-doped Anatase TiO_2 Epitaxial Film as Transparent Conducting Oxide, Japanese Journal of Applied Physics. 44 (2005) L1063–L1065. doi:10.1143/JJAP.44.L1063.

[275] Y. Sun, D. Wen, X. Bai, J. Lu, C. Ai, Ternary Resistance Switching Memory Behavior Based on Graphene Oxide Embedded in a Polystyrene Polymer Layer, Scientific Reports. 7 (2017) 1–11. doi:10.1038/s41598-017-04299-z.

[276] E.M.C. Fortunato, P.M.C. Barquinha, A.C.M.B.G. Pimentel, A.M.F. Gonçalves, A.J.S. Marques, L.M.N. Pereira, R.F.P. Martins, Fully transparent ZnO thin-film transistor produced at room temperature, Advanced Materials. 17 (2005) 590–594. doi:10.1002/adma.200400368.

[277] D.Y. Kim, A.J. Steckl, Electrowetting on paper for electronic paper display, ACS Applied Materials and Interfaces. 2 (2010) 3318–3323. doi:10.1021/am100757g.

[278] A.N. Banerjee, S. Nandy, C.K. Ghosh, K.K. Chattopadhyay, Fabrication and characterization of all-oxide heterojunction p-$CuAlO_2$+x/n-Zn1-xAlxO transparent diode for potential application in "invisible electronics," Thin Solid Films. 515 (2007) 7324–7330. doi:10.1016/j.tsf.2007.02.087.

[279] C.Y. Lu, K.Y. Hsieh, R. Liu, Future challenges of flash memory technologies,

Microelectronic Engineering. 86 (2009) 283–286. doi:10.1016/j.mee.2008.08.007.

[280] S. Tehrani, J.M. Slaughter, E. Chen, M. Durlam, J. Shi, M. Deherrera, Progress and outlook for mram technology, IEEE Transactions on Magnetics. 35 (1999) 2814–2819. doi:10.1109/20.800991.

[281] Q.-D. Ling, F.-C. Chang, Y. Song, C.-X. Zhu, D.-J. Liaw, D.S.-H. Chan, E.-T. Kang, K.-G. Neoh, Synthesis and Dynamic Random Access Memory Behavior of a Functional Polyimide, Journal of the American Chemical Society. 128 (2006) 8732–8733. doi:10.1021/ja062489n.

[282] Y. Arimoto, H. Ishiwara, Current Status of Ferroelectric Random-Access Memory, MRS Bulletin. (2004) 823–828.

[283] S. Yu, Y. Wu, R. Jeyasingh, D. Kuzum, H.S.P. Wong, An electronic synapse device based on metal oxide resistive switching memory for neuromorphic computation, IEEE Transactions on Electron Devices. 58 (2011) 2729–2737. doi:10.1109/TED.2011.2147791.

[284] R. Waser, R. Dittmann, C. Staikov, K. Szot, Redox-based resistive switching memories nanoionic mechanisms, prospects, and challenges, Advanced Materials. 21 (2009) 2632–2663. doi:10.1002/adma.200900375.

[285] S.H. Jo, W. Lu, CMOS compatible nanoscale nonvolatile resistance switching memory, Nano Letters. 8 (2008) 392–397. doi:10.1021/nl073225h.

[286] M. Lee, S. Han, S.H. Jeon, B.H. Park, B.S. Kang, S. Ahn, K.H. Kim, C.B. Lee, C.J. Kim, D.H. Seo, J. Park, J. Lee, X. Li, Y. Park, Electrical manipulation of nano-filaments in metal oxides for resistance based memory, Materials Science. (2009) 1–7. doi:10.1021/nl803387q.

[287] D.-H. Kwon, K.M. Kim, J.H. Jang, J.M. Jeon, M.H. Lee, G.H. Kim, X.-S. Li, G.-S. Park, B. Lee, S. Han, M. Kim, C.S. Hwang, Atomic structure of conducting nanofilaments in TiO_2 resistive switching memory, Nature Nanotechnology. 5 (2010) 148–153. doi:10.1038/nnano.2009.456.

[288] U. Russo, D. Ielmini, C. Cagli, A.L. Lacaita, Filament conduction and reset mechanism in NiO-based resistive-switching memory (RRAM) devices, IEEE Transactions on Electron Devices. 56 (2009) 186–192. doi:10.1109/TED.2008.2010583.

[289] D.S. Jeong, H. Schroeder, R. Waser, Mechanism for bipolar switching in a $Pt/TiO_2/Pt$ resistive switching cell, Physical Review B-Condensed Matter and Materials Physics. 79 (2009) 1–10. doi:10.1103/PhysRevB.79.195317.

[290] C.-Y. Lin, C.-Y. Wu, C.-Y. Wu, C. Hu, T.-Y. Tseng, Bistable Resistive Switching in Al_2O_3 Memory Thin Films, Journal of The Electrochemical Society. 154 (2007) G189. doi:10.1149/1.2750450.

[291] W.K. Cheng, F. Wang, Y.M. Han, Z.C. Zhang, J.S. Zhao, K.L. Zhang, HfO_2-based

resistive switching memory with CNTs electrode for high density storage, Solid-State Electronics. 132 (2017) 19–23. doi:10.1016/j.sse.2017.03.004.

[292] M. Kumar, T. Som, Structural defect-dependent resistive switching in Cu-O/Si studied by Kelvin probe force microscopy and conductive atomic force microscopy, Nanotechnology. 26 (2015) 345702. doi:10.1088/0957-4484/26/34/345702.

[293] T. Breuer, A. Siemon, E. Linn, S. Menzel, R. Waser, V. Rana, Low-current operations in 4F2-compatible Ta_2O_5-based complementary resistive switches, Nanotechnology. 26 (2015) 415202. doi:10.1088/0957-4484/26/41/415202.

[294] G. Thomas, Invisible circuits, Nature. 389 (1997) 907–908. doi:10.1038/39999.

[295] D.P. Sahu, S.N. Jammalamadaka, Remote control of resistive switching in TiO_2 based resistive random access memory device, Scientific Reports. 7 (2017) 17224. doi:10.1038/s41598-017-17607-4.

[296] F.M. Simanjuntak, D. Panda, T.L. Tsai, C.A. Lin, K.H. Wei, T.Y. Tseng, Enhanced switching uniformity in AZO/ZnO_{1-x}/ITO transparent resistive memory devices by bipolar double forming, Applied Physics Letters. 107 (2015) 1–5. doi:10.1063/1.4927284.

[297] X. Zhang, J. Qin, Y. Xue, P. Yu, B. Zhang, L. Wang, R. Liu, Effect of aspect ratio and surface defects on the photocatalytic activity of ZnO nanorods, Scientific Reports. 4 (2014) 4–11. doi:10.1038/srep04596.

[298] Q. Mao, Z. Ji, J. Xi, Realization of forming-free ZnO-based resistive switching memory by controlling film thickness, Journal of Physics D: Applied Physics. 43 (2010) 395104 1-5. doi:10.1088/0022-3727/43/39/395104.

[299] Sze S M, Physics of Semiconductor Devices 2nd edn (New York: Wiley) (1981).

[300] W.-Y. Chang, Y.-C. Lai, T.-B. Wu, S.-F. Wang, F. Chen, M.-J. Tsai, Unipolar resistive switching characteristics of ZnO thin films for nonvolatile memory applications, Applied Physics Letters. 92 (2008) 22110 1-3. doi:10.1063/1.2834852.

[301] T.W. Hickmott, Low-frequency negative resistance in thin anodic oxide films, Journal of Applied Physics. 33 (1962) 2669–2682. doi:10.1063/1.1702530.

[302] J.F. Gibbons, W.E. Beadle, Switching properties of thin Nio films, Solid-State Electronics. 7 (1964) 785–790. doi:10.1016/0038-1101(64)90131-5.

[303] M.J. Kim, D.S. Jeon, J.H. Park, T.G. Kim, Bipolar resistive switching characteristics in tantalum nitride-based resistive random access memory devices, Applied Physics Letters. 106 (2015) 3–7. doi:10.1063/1.4921349.

[304] R. Waser, M. Aono, Nonoionics-based resistive switching memories, Nature Materials. 6 (2007) 833.

[305] F.M. Simanjuntak, D. Panda, K.-H. Wei, T.-Y. Tseng, Status and Prospects of ZnO-Based Resistive Switching Memory Devices, Nanoscale Research Letters. 11 (2016) 368. doi:10.1186/s11671-016-1570-y.

[306] K. Kinoshita, T. Okutani, H. Tanaka, T. Hinoki, H. Agura, K. Yazawa, K. Ohmi, S. Kishida, Flexible and transparent ReRAM with GZO memory layer and GZO-electrodes on large PEN sheet, Solid-State Electronics. 58 (2011) 48–53. [307]

[307] J. Shang, G. Liu, H. Yang, X. Zhu, X. Chen, H. Tan, B. Hu, L. Pan, W. Xue, R.W. Li, Thermally stable transparent resistive random access memory based on all-oxide heterostructures, Advanced Functional Materials. 24 (2014) 2171–2179.

[308] D. Cheon, M. Son, M.-H. Ham, W. Lee, Resistive switching in an amorphous ZnO dielectric film prepared on a Ga-doped ZnO transparent electrode, RSC Adv. 6 (2016) 103864–103871. doi:10.1039/C6RA21726E.

[309] M. Kim, K.C. Choi, Transparent and flexible resistive random access memory Based on Al_2O_3 film with multilayer electrodes, IEEE Transactions on Electron Devices. 64 (2017) 3508–3510.

Publications from the work

1. **Satyavir Singh**, Vikas Sharma, Surbhi, Dinesh Saini, K. Asokan, Kanupriya Sachdev, Fabrication of highly efficient $TiO_2/Ag/TiO_2$ multilayer transparent conducting electrode with N ion implantation for optoelectronic applications, **Ceramics International 43 (2017) 9759–9768**.

2. **Satyavir Singh**, Vikas Sharma, Kanupriya Sachdev, Investigation of effect of doping concentration in Nb doped TiO_2 thin films for TCO applications, **Journal of Material Science 52 (2017) 11580–11591**.

3. **Satyavir Singh**, Vikas Sharma, Dinesh Saini, Surbhi Shekhawat, K. Asokan, Kanupriya Sachdev, Influence of 100 keV Ar^+ implantation on electrical and optical properties of $TiO_2/Ag/TiO_2$ multilayer films, **Materials Science in Semiconductor Processing 75 (2018) 18–25**.

4. **Satyavir Singh**, Vikas Sharma, K. Sachdev, Investigation of Post Annealing Effects on Nb:TiO_2 Transparent Conducting Thin Films, **Advanced Science Letters 22 (2016), 3773–3776**.

5. **Satyavir Singh**, Vikas Sharma, K. Asokan, Kanupriya Sachdev, NTO/Ag/NTO multilayer transparent conducting electrodes for photovoltaic applications tuned by low energy ion implantation, **Solar Energy 173 (2018) 651-664**.

Bio-Data

Satyavir Singh

164/288, Pratap Nagar,

Sanganer, Jaipur (Raj.)-302033

Mobile: +918560932660

E-mail: satyavir84@gmail.com

Objectives:

- To strive for academic excellence and impart quality education with emphasis on Physics and research work.
- To establish myself in the field of education, to utilize my skills and experience to help students to achieve high improvements in academics.

Educational qualifications:

Ph.D.:	Thesis Title: "TiO_2 based Single and Multilayer Transparent Conducting Electrodes and ReRAMs" (Physics – Materials Science – Experimental) Year of Passing: 2018, CGPA 8.64/10.00 Malaviya National Institute of Technology Jaipur, Rajasthan (India)
Master of Engineering:	Computer Science & Engineering Year of passing 2010, CGPA 8.12/10.00 Thapar University Patiala, Punjab (India)
Master of Science:	Physics Year of passing 2005, Percentage: 61.50% University of Rajasthan Jaipur, Rajasthan (India)
Bachelor of Science:	Physics, Mathematics, Electronics Year of passing 2003, Percentage: 63.11% University of Rajasthan Jaipur, Rajasthan (India)

Research Interests:

Materials Science, Transparent Conducting Oxides, Ion Implantations, Resistive Switching Random Access Memories (ReRAMs) and Energy Conversion Devices.

Academic Achievements:

GATE: − Physics (2008): 95 percentiles, AIR: 292

NET (CSIR): − Physics (2007)

Ceramics International 43 (2017) 9759–9768

Contents lists available at ScienceDirect

Ceramics International

journal homepage: www.elsevier.com/locate/ceramint

Fabrication of highly efficient $TiO_2/Ag/TiO_2$ multilayer transparent conducting electrode with N ion implantation for optoelectronic applications

Satyavir Singh[a], Vikas Sharma[a], Surbhi[a], Dinesh Saini[a], K. Asokan[c], Kanupriya Sachdev[a,b,*]

[a] Department of Physics, Malaviya National Institute of Technology, Jaipur 302017, India
[b] Materials Research Centre, Malaviya National Institute of Technology, Jaipur 302017, India
[c] Inter-University Accelerator Centre, Aruna Asaf Ali Road, New Delhi 110067, India

ARTICLE INFO

Keywords:
Transparent conducting oxide
Multilayer
Implantation
Hall measurement

ABSTRACT

Fabrication of highly conductive and transparent $TiO_2/Ag/TiO_2$ (referred hereafter as TAT) multilayer films with nitrogen implantation is reported. In the present work, TAT films were fabricated with a total thickness of 100 nm by sputtering on glass substrates at room temperature. The as-deposited films were implanted with 40 keV N ions for different fluences (1×10^{14}, 5×10^{14}, 1×10^{15}, 5×10^{15} and 1×10^{16} ions/cm^2). The objective of this study was to investigate the effect of N^+ implantation on the optical and electrical properties of TAT multilayer films. X-ray diffraction of TAT films shows an amorphous TiO_2 film with a crystalline peak assigned to Ag (111) diffraction plane. The surface morphology studied by atomic force microscopy (AFM) and field emission scanning electron microscope (FESEM) revealed smooth and uniform top layer of the sandwich structure. The surface roughness of pristine film was 1.7 nm which increases to 2.34 nm on implantation for 1×10^{14} ions/cm^2 fluence. Beyond this fluence, the roughness decreases. The oxide/metal/oxide structure exhibits an average transmittance ~80% for pristine and ~70% for the implanted film at fluence of 1×10^{16} ions/cm^2 in the visible region. The electrical resistivity of the pristine sample was obtained as 2.04×10^{-4} Ω cm which is minimized to 9.62×10^{-5} Ω cm at highest fluence. Sheet resistance of TAT films decreased from 20.4 to 9.62 Ω/□ with an increase in fluence. Electrical and optical parameters such as carrier concentration, carrier mobility, absorption coefficient, band gap, refractive index and extinction coefficient have been calculated for the pristine and implanted films to assess the performance of films. The TAT multilayer film with fluence of 1×10^{16} ions/cm^2 showed maximum Haacke figure of merit (FOM) of 5.7×10^{-3} Ω^{-1}. X-ray photoelectron spectroscopy (XPS) analysis of N 1s and Ti 2p spectra revealed that substitutional implantation of nitrogen into the TiO_2 lattice added new electronic states just above the valence band which is responsible for the narrowing of band gap resulting in the enhancement in electrical conductivity. This study reports that fabrication of multilayer transparent conducting electrode with nitrogen implantation that exhibits superior electrical and optical properties and hence can be an alternative to indium tin oxide (ITO) for futuristic TCE applications in optoelectronic devices.

1. Introduction

Transparent conducting electrode (TCE) is a key component in any optoelectronic device including solar cells, flat panel displays, light emitting diodes (LED) [1,2] etc. A good TCE should exhibit low resistivity and high transparency in the visible region of the electromagnetic spectrum [3,4]. Indium tin oxide has been widely used as TCE due to its high conductivity, high transparency and ease of deposition. However, In is high-cost material due to its increasing demand and natural scarcity. Doped single layers and multilayers of TiO_2 with metal embedded between the two oxide layers have emerged as TCE with comparable optical and electrical properties for flat panel displays, LEDs and solar cells [5–7]. In addition, TiO_2 is a potential semiconductor material with technological importance because of high refractive index (2.7), wide band gap (~3.2 eV), high transmittance (~95%) in the visible region and high mechanical and chemical stability [8–10]. Doped metal oxides like Nb-doped TiO_2 (NTO) [11], Al-doped ZnO (AZO) [12], and F doped-SnO_2 (FTO) [13] have been commonly used as TCE in optoelectronic devices. In addition, electrical conductivity has been further increased by sandwiching a thin metal (M) film

* Corresponding author at: Department of Physics, Malaviya National Institute of Technology, Jaipur 302017, India.
E-mail addresses: satyavir84@gmail.com (S. Singh), ksachdev.phy@mnit.ac.in (K. Sachdev).

http://dx.doi.org/10.1016/j.ceramint.2017.04.152
Received 20 December 2016; Received in revised form 26 January 2017; Accepted 26 April 2017
Available online 29 April 2017

between these two dielectric (D) layers to form a DMD multilayer. Among metals, Ag is a good candidate because it exhibits low resistance and high transmittance (as a very thin layer) in the visible region, so Ag (< 20 nm thick) [14] is commonly used as the interlayer in DMD multilayers. Many advantages of the metal embedded multilayer structure have been reported over the single layer TCO [15,16]. Researchers have been investigating various multilayers employing the Ag layer as a middle layer with different oxides such as SnO_2/Ag/SnO_2 [17,18], SnO_x/Au/SnO_x [19], ZnO/Ag/ZnO [20], AZO/Ag/AZO [21], ITO/Ag/ITO [22] and TiO_2/Ag/TiO_2 [23] exhibiting low resistance and high transmittance in the visible region. Kim et al. [24] investigated the effect of Ag layer thickness on electrical and optical properties of TiO_2/Ag/TiO_2. Authors found highest transmittance of 86.3–97% at 591 nm for different Ag thicknesses, and sheet resistance slightly decreasing from 6.17 to 2.27 Ω/sq with increase in the Ag layer thickness. Dhar et al. [25] deposited TiO_2/Ag/TiO_2 by sputtering on the flexible substrate; Ag thickness was varied between 5 and 13 nm. It was reported that Ag layer became contiguous as it approaches the critical thickness of 9.5 nm and multilayer with Ag thickness 9.5 nm had the best figure of merit, 6.14×10^{-4} Ω^{-1}. Many other researchers [26,27] have also investigated the properties of the TiO_2/Ag/TiO_2 multilayer thin films. Tin dioxide based multilayer SnO_2/Ag/SnO_2 films studied by Yu et al. [28] as a function of Ag thickness varied between 0 and 9 nm showed an average transmittance of > 83%, sheet resistance of 9.61 Ω/sq and highest figure of merit (1.6×10^{-2} Ω^{-1}) for the SnO_2 (25 nm)/Ag (5 nm)/SnO_2 (25 nm) tri-layer film.

Ion doping is a unique method to restore the vacant oxygen sites in a TiO_2 lattice, and N-ion was taken as a particular choice [29]. It was reported that ion-doped TiO_2 causes band bending due to an alteration in electron concentration via charge transfer between a dopant and conduction band or valence band [30]. In N-doped TiO_2, new energy states are introduced above the valence band of the TiO_2, by increasing the electron density [31]. According to Asahi et al. [29] doping of N into TiO_2 contributes to band gap narrowing to provide visible-light response. Many research groups [29,32,33] have analyzed the N 1s XPS spectra and found that the peak at 396 was assigned to atomic β-N and substitutional N doping. Peaks at 400 and 402 eV are attributed to molecularly chemisorbed (γ-N_2) and organic impurities [34]. Jangheum et al. [35] reported smoothing of Cu film on N doping as indicated by surface morphological study using AFM & SEM.

In this work, we have fabricated TiO_2/Ag/TiO_2 multilayer films by sputtering and the pristine films were implanted by the N^+ 40 keV ions of various fluence. The thickness of upper and lower TiO_2 layer was kept constant at ~45 nm, and that of embedded Ag layer was taken ~9 nm to form a continuous layer, necessary for good electrical conduction.

2. Experimental details

2.1. Sample preparation

TiO_2 powder (Alfa-Aesar, 99.99% purity) was used for target preparation. This powder was pressed into 2-in. pellet and then sintered at 1100 °C for 10 h to get better structural stability for film deposition. Commercial Ag target (99.99% purity) was used for Ag layer deposition. Glass substrates of 1×1 cm^2 were cleaned using standard cleaning processes. Before deposition, TiO_2 and Ag targets were pre-sputtered for 15 min to remove contaminants. RF source for oxide layers and DC source for metal layer deposition were used in TAT structure preparation using sputtering method at 100 W and 16 W with 15 sccm Ar flow, respectively. The TiO_2/Ag/TiO_2 (45 ± 5 nm/9 ± 2 nm/45 ± 5 nm) structure was sequentially prepared at room temperature on glass substrates. The base pressure of the chamber was ~5×10^{-6} mbar and working pressure during TiO_2 deposition was ~6×10^{-3} mbar and ~1.6×10^{-2} mbar for Ag layer. The as-deposited TAT films were implanted with 40 keV N^+ ions with fluences of 1×10^{14}, 5×10^{14}, 1×10^{15}, 5×10^{15} and 1×10^{16} ions/cm^2 at room temperature using the low energy ion beam facility at the Inter-University Accelerator Centre (IUAC), New Delhi, India. The nuclear energy loss and electronic energy loss values for 40 keV N^+ ions were obtained as 20.13 and 13.3 eV/Å respectively; as calculated by the SRIM-2010 software. These values show that entire passage of these ions in the film is dominated by nuclear energy loss. The stopping range of N ions was 60 nm, which is less than the film thickness (100 nm). RBS was performed using 1.7 MV tandem accelerator facility with 2 MeV He^+ ions at scattering angle of 165° at IUAC, New Delhi for depth profiling and compositional studies.

2.2. Characterization

The crystal structure of the TAT multilayer was investigated by using an X-Ray Diffractometer (Panalytical X-Pert Pro) with CuKα radiation. The morphology and topography of the films were imaged from Nova Nano FE-SEM 450 (FEI) and atomic force microscopy done by Multimode Scanning Probe Microscope (Bruker). Optical transmittance and absorbance were measured using LAMBDA 750 (Perkin Elmer) UV–vis–NIR Spectrophotometer. Carrier concentration, carrier mobility and resistivity of TAT multilayer films were measured by HMS3000, Ecopia using a magnetic field of 0.57 T. Sheet resistance was evaluated using the four-point-probe technique. Composition, valence and chemical states of TAT films were analyzed by the X-ray photoelectron spectroscopy (XPS, Omicron ESCA). For XPS measurement monochromatic Al K_α (1486.7 eV) source with a mean radius of 124 mm was used and monochromatic X-ray resolution as confirmed by FWHM was 0.6 eV. The vacuum pressure of the chamber was ~4×10^{-10} mbar.

3. Results and discussion

3.1. Structural properties

The X-ray diffraction (XRD) pattern of the pristine and implanted TiO_2/Ag/TiO_2 multilayer films for different fluence is shown in Fig. 2. The absence of any peak for TiO_2 shows its amorphous behavior which is expected because the deposition was done at room temperature. Peaks at 2θ=38.15°, 44.3°, 64.6° and 77.5°, are assigned to the (111), (200), (220) and (311) planes of Ag (JCPDS No. 04-0783) respectively. After implantation, the intensity of the Ag (111) peak slightly increased with the ion fluences and the full width at half maximum FWHM (β) changed from 0.6605 to 0.5188 and crystallite size increased from 13.3 nm to 16.8 nm as the fluence changed from 0 to 1×10^{16} ions/cm^2. Residual stress and lattice constant calculated for pristine and N ion implanted films are shown in Table 1.

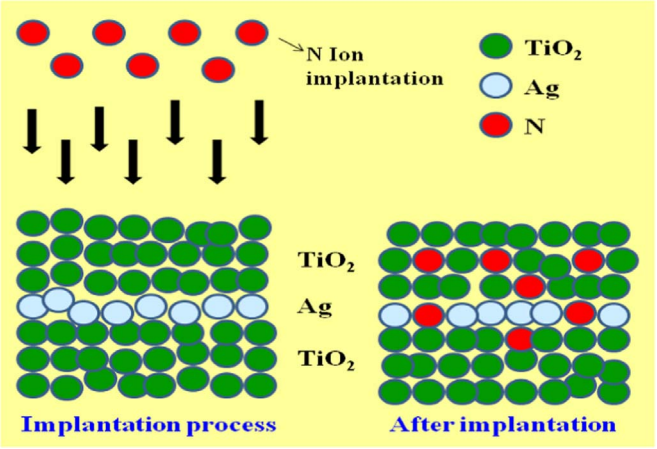

Fig. 1. Schematic showing the fabrication of nitrogen ion implanted TAT multilayer film.

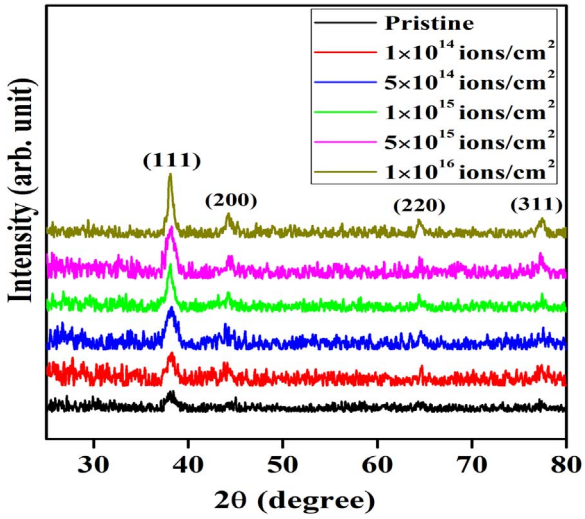

Fig. 2. XRD pattern of pristine and N ion implanted films of TAT.

Table 1
FWHM, crystallite size, stress and lattice constants of pristine and N ion implanted TAT films.

S. no.	Fluence (ion cm^{-2})	FWHM	Crystallite size (nm)	Residual stress	Lattice constant c (Å)
1	0	0.6605	13.3	−0.401	4.093
2	1×10^{14}	0.5144	16.9	−0.627	4.097
3	5×10^{14}	0.6318	13.9	−0.741	4.099
4	1×10^{15}	0.5401	16.3	−0.171	4.089
5	5×10^{15}	0.6116	14.4	−0.285	4.091
6	1×10^{16}	0.5188	16.8	−0.228	4.090

3.2. Rutherford back scattering

The RBS measurement was carried out to determine the thickness and stoichiometry of this TAT multilayer Fig. 3 shows the RBS spectrum along with the SIMNRA-fitted profile of TiO_2/Ag/TiO_2 multilayer structure. This spectra show the elemental peaks corresponding to Ti, O and Ag ions. The thickness of the each layer was measured using fitted curve and obtained as TiO_2 (45 ± 5 nm)/Ag (9 ± 1 nm)/TiO_2 (45 ± 5 nm). These results suggest the formation of TiO_2 with pure Ag layer as middle layer and are consistent with XPS data discussed in next section (Fig. 4).

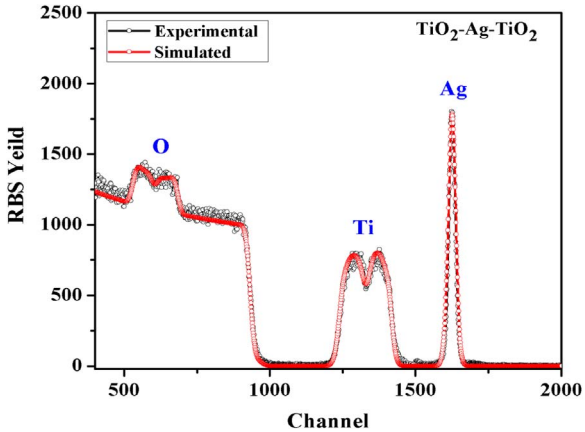

Fig. 3. RBS spectrum of TAT multilayer structure with fitted profile.

3.3. X-ray photoelectron spectroscopy

Fig. 4 shows the XPS spectra of TiO_2/Ag/TiO_2 pristine and N implanted (for fluence of 1×10^{16} ions/cm^2) films (N–TAT). Typical survey scans of TAT pristine and N–TAT films are shown in Fig. 4(a). Survey scans of pristine film and N ion implanted films consist of dominant signals from Ti, and O and a weak signal from C, which may be due to ex-situ process of the sample transfer to UHV chamber and N signal also appeared. Fig. 4(b) shows the Ti 2p core level spectra of top surfaces of the TAT pristine and N–TAT films. The pristine sample exhibits peaks of Ti-$2p_{3/2}$ and Ti-$2p_{1/2}$ at 458.9 and 464.6 eV attributed to Ti^{4+} oxidation state of TiO_2 which is consistent with reported data in literature [36]. The difference between the binding energies of Ti-$2p_{1/2}$ and Ti-$2p_{3/2}$ peak is 5.7 eV, which is also in good agreement with +4 oxidation state [37,38]. However, peaks due to Ti-$2p_{3/2}$ and Ti-$2p_{1/2}$ core levels of the N–TAT sample appear at 458.3 and 464 eV, respectively indicating differences in the binding energy after nitrogen implantation. A shift in binding energy of Ti 2p occurs due to different electronic interaction behavior of Ti with the anions for pure and N-doped TiO_2. N doping induces a significant modification in TiO_2 matrix possibly produced by dopant-induced strain. A shift towards lower side in binding energy of Ti 2p in N-doped TiO_2 is attributed to the improvement in covalent behavior of the bond between Ti and N [39]. These results are in good agreement with previous reports [40,41].

Fig. 4(c) shows the high-resolution O 1s core spectra of TAT and N-TAT samples. The O 1s signal of TAT samples appears at 530.1 eV, and on deconvolution, another peak resulted at 531.6 eV which is assigned to OH groups present on the surface. The O 1s spectra of N-TAT sample appear at 530.16 eV, and another peak is at 531.7 eV corresponding to OH species present on the surface of the sample. In both these samples, the O 1s peak appears at the same place indicating the nature of oxygen to be similar. Fig. 4(e) shows the N 1s spectra for the TAT films implanted with the fluence of 1×10^{16} ions/cm^2. It can be seen that there is a peak for N at 396 eV. The N 1s peak appearing at 396 eV is attributed to N substituting O sites of TiO_2 lattice [42]. This peak at 396 eV has been identified as the atomic β-N states by Saha et al. [32]. In order to determine chemical state of middle Ag layer, the depth profile mode of XPS has been used. The core level spectra of Ag of TAT pristine exhibits two peaks of Ag $3d_{5/2}$ and Ag $3d_{3/2}$ located at 368.5 and 374.52 eV binding energies respectively, indicating presence of metallic Ag^0 in TAT pristine films. Upon introduction of N in TAT sample, new peaks of Ag $3d_{3/2}$ and Ag $3d_{5/2}$ appear with binding energies of 368.3 and 374.3 eV. A shift to lower binding energy in Ag 3d was observed from the position of Ag $3d_{5/2}$ (368.5 eV) and Ag $3d_{3/2}$ (374.52 eV), may be due to the presence of Ag at the interface and interaction with Ti and O ions [43]. Fig. 4(a)–(e) indicate incorporation of N in TiO_2 and are suggestive of replacement of O by N ions in the TiO_2 lattice. Substitutional N ions would add electronic states above the valence band edge of TiO_2. The additional electronic states would be responsible for the band gap narrowing, resulting in reduction of electrical resistivity giving a high figure of merit (FOM) for N–TAT sample.

3.4. Surface characterization

Fig. 5(a)–(e) shows the surface FESEM images of top layer of TiO_2/Ag/TiO_2 multilayer films as a function of the ion fluences ranging from 1×10^{14} to 1×10^{16} ions/cm^2. All images were taken at the 100k× magnification. It can observe that the surface morphology of the as-grown TiO_2 film and implanted films are compact and uniform. All images demonstrate the flat surface composed of regular round grain structure with TiO_2 nanoparticles of size 20–40 nm. Similar images of TiO_2 were reported by other researchers [44]. Fig. 5(h) shows the FE-SEM cross sectional image of TAT multilayer structure and TiO_2 and Ag layers are distinctly visible. The ~10 nm Ag is embedded between

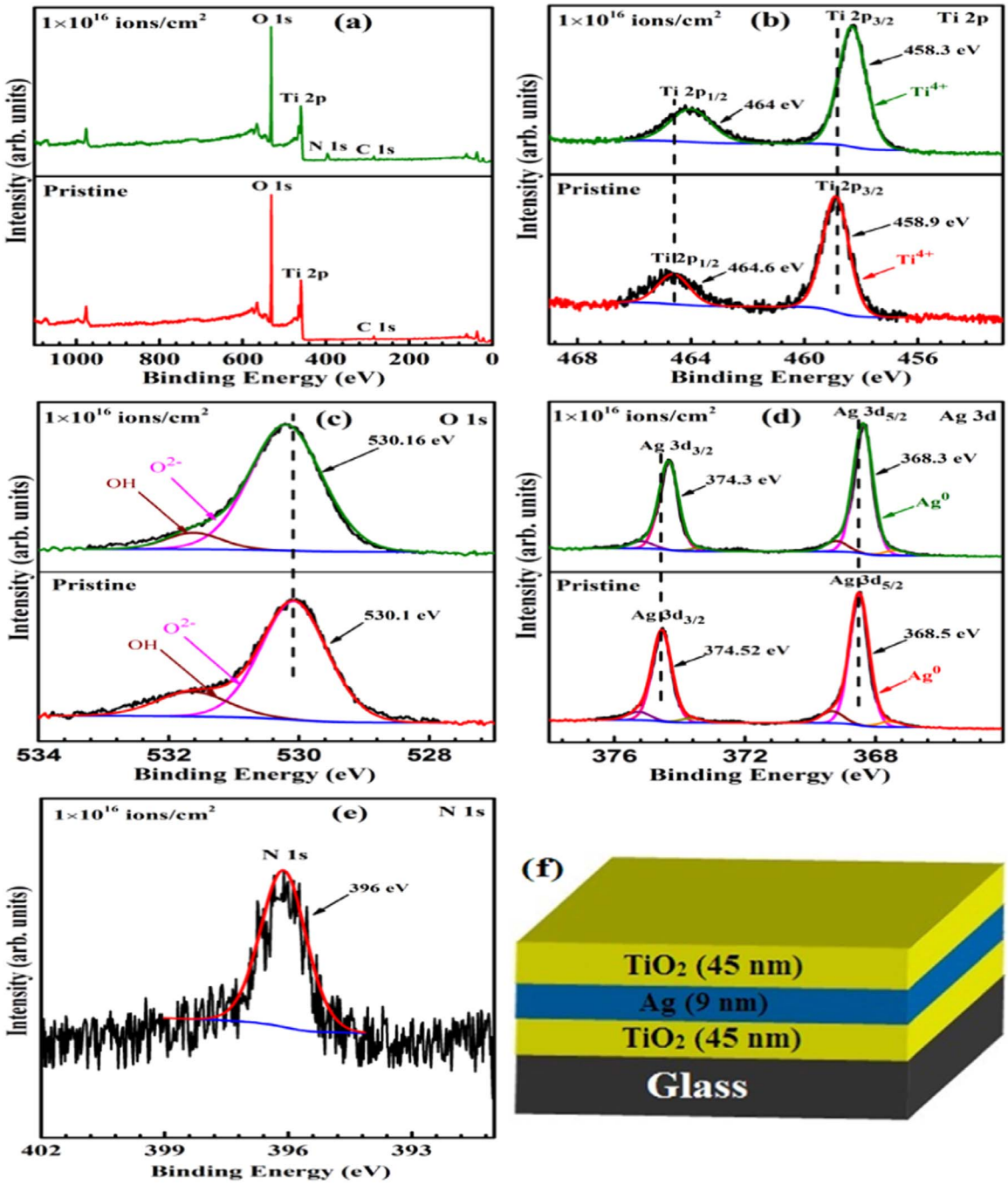

Fig. 4. XPS spectra of pristine and 1×10^{16} ions/cm^2 implanted films of TAT (a) survey scan, (b) Ti 2p, (c) O 1s, (d) Ag 3d, (e) N 1s and (f) schematic diagram of TAT film.

the upper TiO_2 layer (~50 nm) and lower TiO_2 layer (~50 nm). The TiO_2 and Ag layers are smooth and continuous in the deposited films.

Fig. 6 shows the surface morphology of the TAT multilayer films with varying fluences as observed by the AFM in a scanning area of 1×1 μm^2. Root mean square (rms) roughness of the TAT films as a function of ion fluence is shown in Fig. 5. The rms roughness of the pristine specimen and with ion fluences of 1×10^{14}, 5×10^{14}, 1×10^{15}, 5×10^{15} and 1×10^{16} ions/cm^2 are found to be 1.71, 2.34, 1.94, 1.68, 1.52 and 1.25 nm respectively. The average roughness of the pristine film is 1.71 nm and increases to 2.34 nm at N ion implantation fluence of 1×10^{14} ions/cm^2. Further increase in ion fluence results in a decrease of average surface roughness to a minimum value of 1.25 nm for highest fluence 1×10^{16} ions/cm^2. Increase in surface roughness for 1×10^{14} fluence implanted sample could be understood in terms of sputtering/etching process during implantation process [45]. High energy N ions used in implantation process etch the surface of the film, deteriorating the surface causing damage to the surface. For further increase in the N ion fluencies, the surface became smoother because higher fluence leads to erosion of existing microstructures on the surface [46]. Fig. 7(a) represents the roughness variation with fluence and Fig. 7(b) and (c) shows the depth histogram of TAT pristine and highest implanted films.

3.5. Optical analysis

Fig. 8(a) and (b) show the optical transmittance and absorbance spectra of TAT multilayer films as a function of wavelength in the visible region (400 nm < λ < 800 nm) for different ion fluence. Optical transmittance of the pristine and N ion implanted TAT films increases with wavelength initially, reaches a maximum value around 530 nm

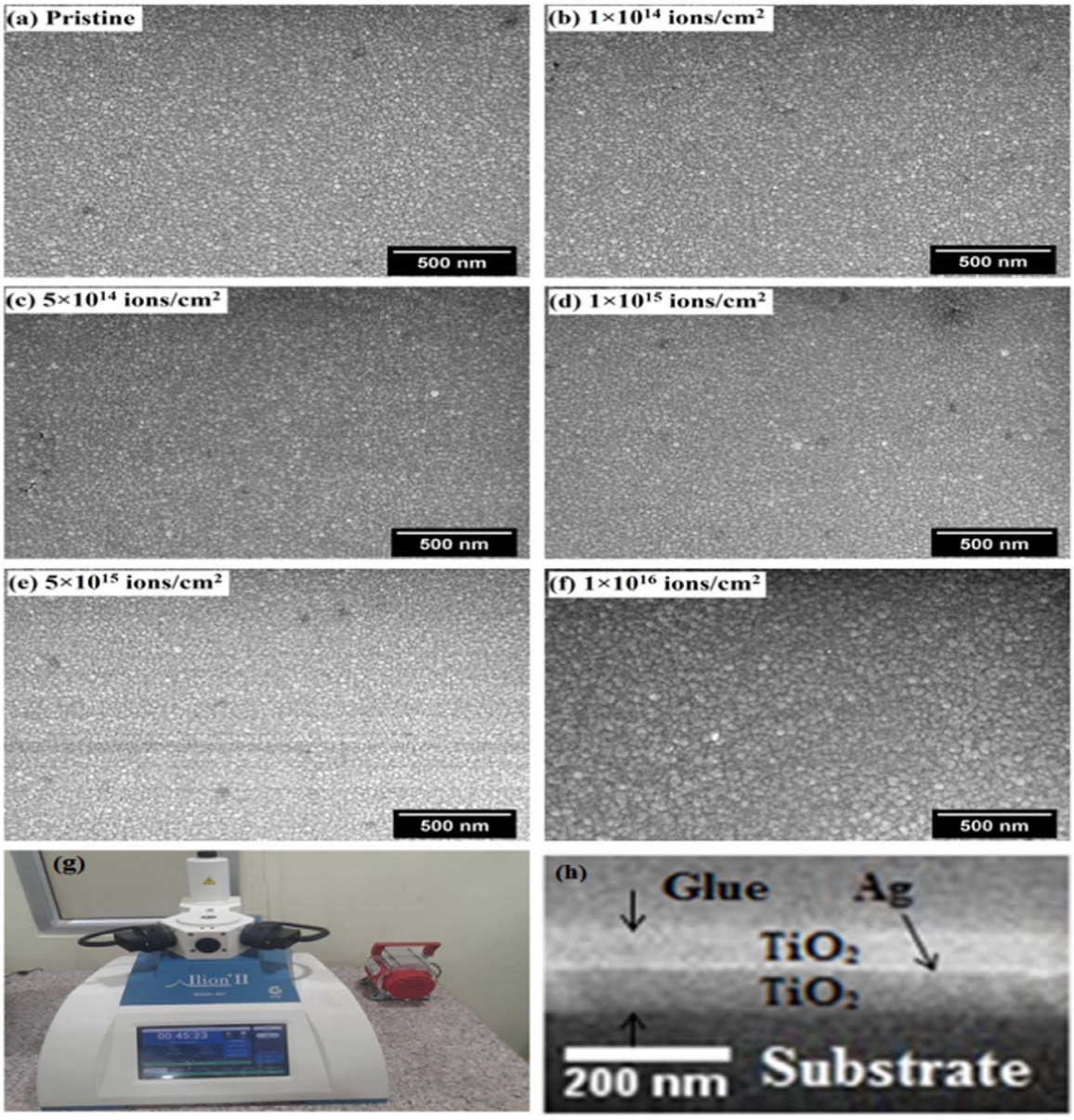

Fig. 5. (a) –(e) SEM images of the pristine and N ion implanted films of TAT, (g) sample polishing machine, Ilion II and (h) cross-sectional FE-SEM image of TAT multilayer film.

and then gradually decreases with increasing wavelength. Pristine sample exhibits an average transmittance of ~80% which reduces to ~70% as the ion fluence increases. Fig. 8(b) depicts the absorbance of the TAT films. It can be observed from the graph that all films show high absorbance for shorter wavelength ($\lambda < 400$ nm) and a low absorbance for longer wavelengths ($\lambda > 400$ nm). Ion implantation leads to band gap narrowing of the films which increases the absorbance, and consequently, the transmittance is decreasing. It can be observed that transmittance and absorbance spectra of a TAT film exhibit an inverse relationship.

The optical band gap of the TAT films has been calculated using the standard expression [47].

$$\alpha h\nu = B(h\nu - E_g)^n \quad (1)$$

where hν the photon energy, Eg is optical band gap, α is absorption coefficient and B is a constant. The value of n is taken as 2, accounts for the fact that TiO_2 has indirect band gap transition mechanism.

Absorption coefficient (α) has been calculated using the Beer–Lambert's law [48].

$$\alpha = \frac{1}{d}\ln\frac{1}{T} = \frac{2.303}{d}A \quad (2)$$

where d is thickness of the multilayer structure, T is transmittance, and A is absorbance of TAT film. Fig. 8(c) shows the Tauc plot between photon energy (hν) and $(\alpha h\nu)^{1/2}$ for the TAT films; a band gap of 2.8 eV is obtained for the pristine film by the intersection of the fitted straight line and the abscissa. The band gap of the samples decreases as the fluence increases and attains a minimum value of 2.7 eV for the fluence of 1×10^{16} ions/cm^2. The band gap reduction of the TAT films suggests that N ions occupy some of the oxygen positions in the lattice. Asahi et al. [29] reported that in N-doped TiO_2 film, substitutional doping with N proved the effective band-gap reduction mechanism. These authors explained it by mixing of 2p states of N with O 2p states, which causes band-gap reduction.

Refractive index is a fundamental parameter for optical materials, which regulate the antireflective effect, packing densities and transmittance property of the TCO materials. The refractive index can be calculated using the following formula [49].

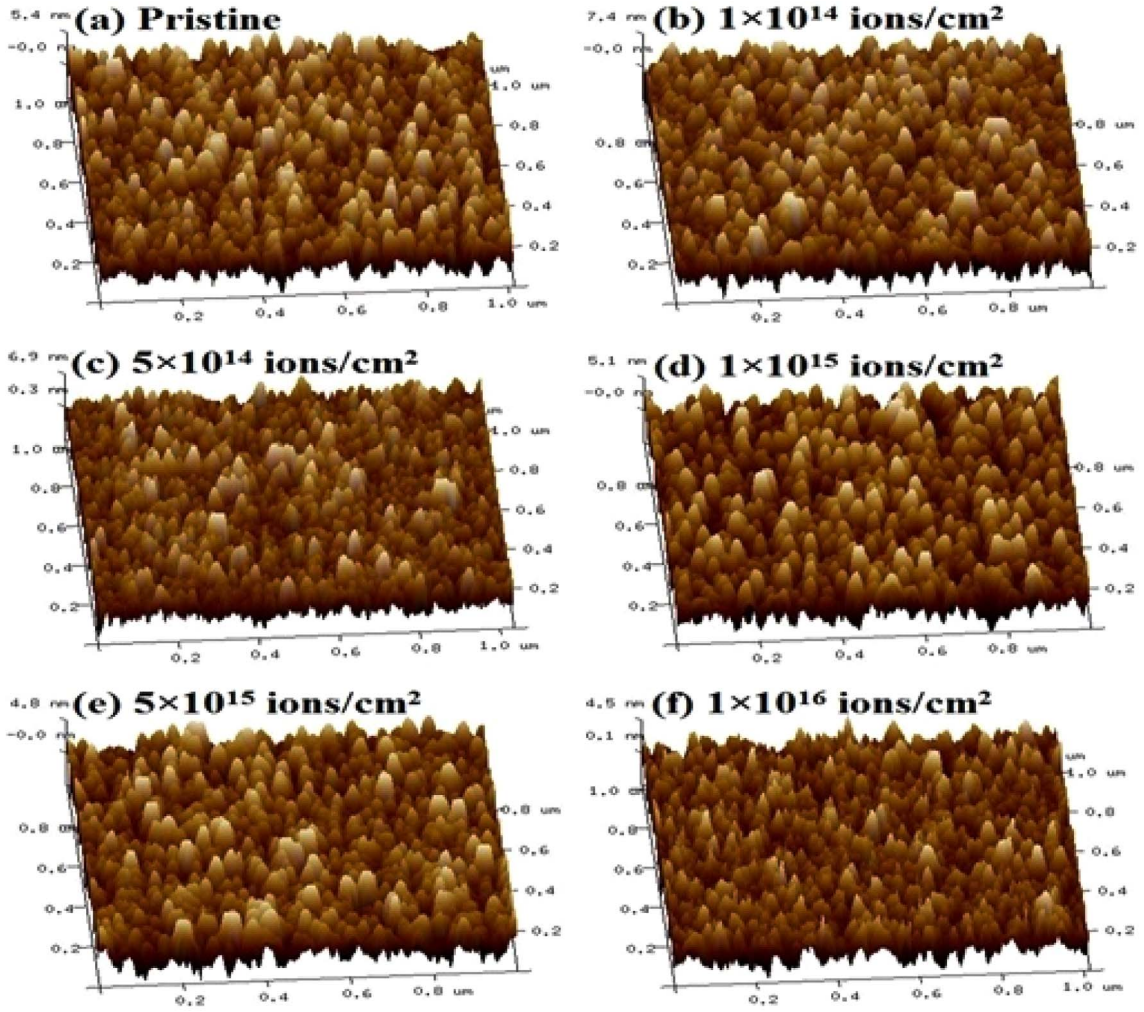

Fig. 6. Three-dimensional AFM images of pristine and N ion implanted TAT films.

$$n = \sqrt{\frac{4R}{(1-R^2)} - k^2 + \left(\frac{1+R}{1-R}\right)} \quad (3)$$

where R is reflectivity of the film and k is the extinction coefficient defined as-

$$K = \frac{\alpha\lambda}{4\pi} \quad (4)$$

where α is absorption coefficient and λ is wavelength. Fig. 8(d) shows the refractive index of the TAT films. The refractive index of the pristine, ion fluences of 1×10^{14}, 5×10^{14}, 1×10^{15}, 5×10^{15} and 1×10^{16} ions/cm^2 are estimated 2.27, 2.25, 2.26, 2.25, 2.3 and 2.28, respec-

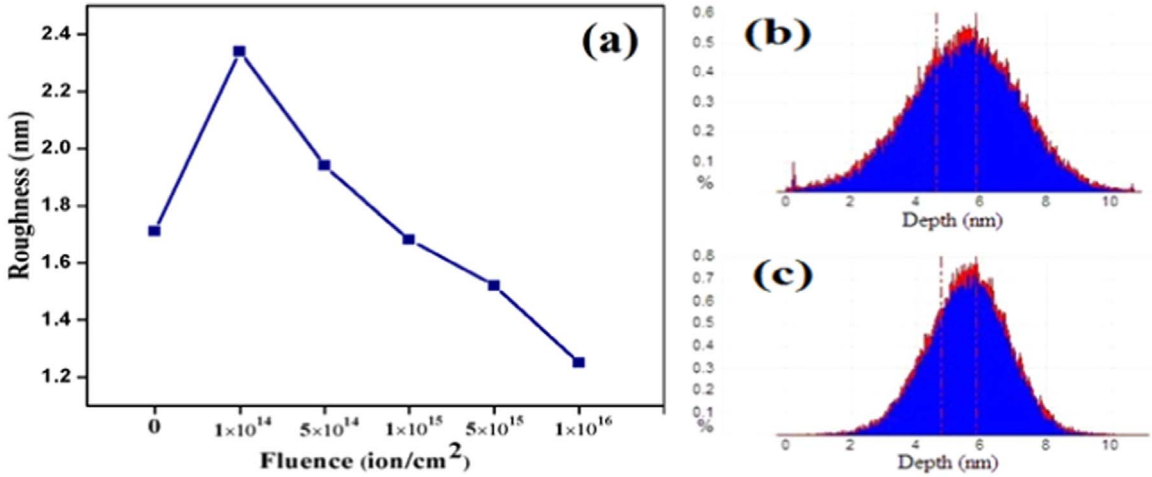

Fig. 7. (a) Root mean square roughness of pristine and implanted films of TAT, (b) depth histogram of TAT pristine and (c) depth histogram of TAT-N ion implanted films with fluence of 1×10^{16}.

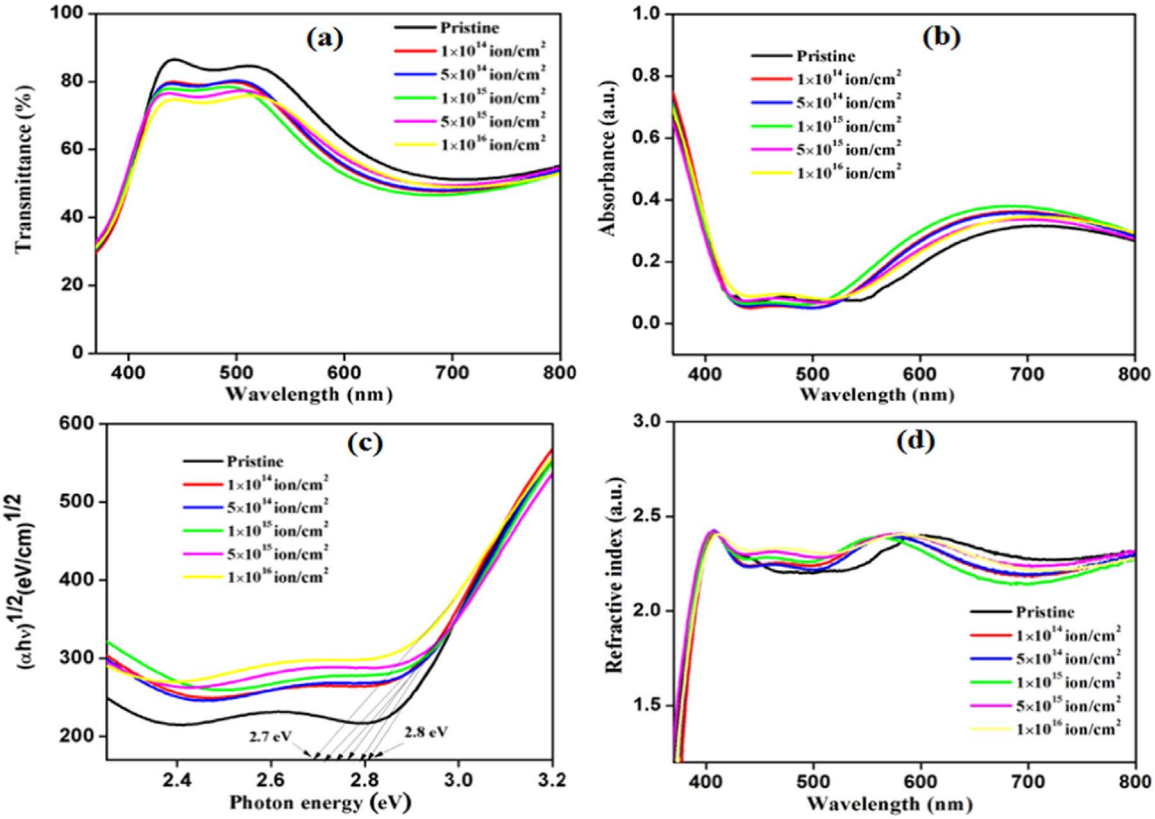

Fig. 8. Pristine and implanted films of TAT: (a) transmittance, (b) absorbance, (c) Tauc plot and (d) refractive index.

Table 2
RMS surface roughness, transmittance, refractive index, extinction coefficient and the band gap of pristine and implanted TAT films as a function of ion fluence.

S. no.	Fluence (ion cm^{-2})	RMS (nm)	Transmittance (%) at 530 nm	Refractive index (n)	Extinction coefficient (k)	Band gap (eV)
1	0	1.71	81	2.27	0.245	2.80
2	1×10^{14}	2.34	75	2.25	0.282	2.79
3	5×10^{14}	1.94	76	2.26	0.278	2.76
4	1×10^{15}	1.68	72	2.25	0.292	2.74
5	5×10^{15}	1.52	74	2.3	0.271	2.72
6	1×10^{16}	1.25	75	2.28	0.277	2.70

tively. The RMS surface roughness, transmittance, refractive index, extinction coefficient (Supplementary material Fig. S1) and band gap have been calculated for pristine and implanted TAT films and are shown in Table 2.

3.6. Electrical analysis

Fig. 9 shows the carrier concentration and Hall mobility of the TAT multilayer films as a function of fluence. The pristine TAT carrier concentration is 3.9×10^{21} cm^{-3}, which increases to 7.06×10^{21} cm^{-3} as the fluence increases to 1×10^{16} ions/cm^2. Mobility also increases from 7.8 to 9.2 cm^2/V-s as fluence increases from 0 to 1×10^{16} ions/cm^2. Fig. 10 shows the electrical resistivity and sheet resistance of the TAT multilayer films as a function of ion fluence. Electrical resistivity for the pristine sample was 2.04×10^{-4} Ω cm, and it minimized to 9.62×10^{-5} Ω cm for the highest fluence of 1×10^{16} ions/cm^2, which is lower than the resistivity of ITO films (31.2×10^{-4} Ω cm) studied by Lee et al. [50]. On the other hand, the sheet resistance decreases 20.4 Ω/□ to 9.6 Ω/□ as ion fluence increases from 0 to 1×10^{16} ions/cm^2. The reduction in resistivity to 9.62×10^{-5} Ω cm at 1×10^{16} ions/cm^2 fluence

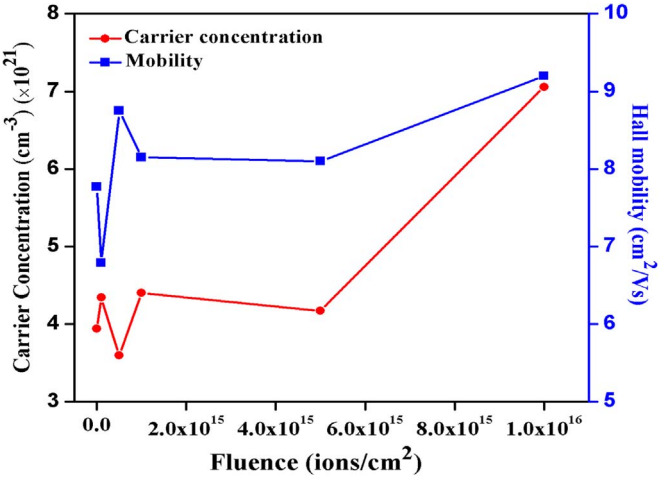

Fig. 9. Carrier concentration and Hall mobility of pristine and N ion implanted films of TAT.

indicates that nitrogen is replacing the O sites of TiO_2. The substitutional N ion would add the new electronic states above the valence band edge of a pure TiO_2. The additional electronic states would be responsible for the band gap reduction as shown in Fig. 8(c) giving less resistivity. Apart from occupying electrically active lattice sites, ion implantation in metal oxides is known to create or anneal the defects and thus lead to change in resistivity [51–53]. The resistivity (ρ) of TiO_2 can be tuned by ion implantation [51,52]. In the present study, N implantation and annealing of oxygen vacancies may be responsible for decrease in the resistivity. In addition, this results in decrease in band gap and change in microstructure. The increasing grain size with ion fluence causes low grain boundary. This reduces the absorption of metal oxide donors in crystal [53]. Consequently, the mobility and carrier concentration further increased and leads to reduction in

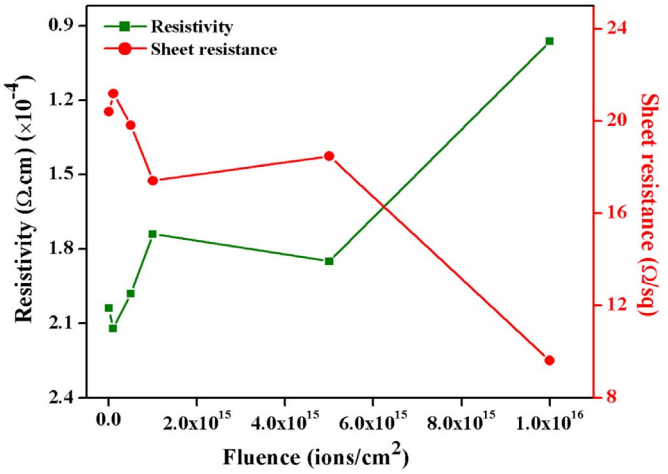

Fig. 10. Resistivity (which is decreasing with increasing fluence) and sheet resistance of pristine and N ion implanted films of TAT.

electrical resistivity. The trend of resistivity and sheet resistance after ion implantation may be attributable to surface roughness. XPS analysis of N 1s and Ti 2p spectra also revealed that substitutional N ions into the TiO_2 lattice results in new electronic states just above the valence band which is responsible for the narrowing of band gap and the enhancement in electrical conductivity. The variation in electrical resistivity with the N^+ implantation can be understood by the following relation:

$$\rho = \frac{1}{n_e \mu e} \tag{5}$$

where ρ is resistivity, μ is the mobility, n_e is carrier concentration and e is charge on the carrier. The resistivity is slightly decreasing up to the ion fluence 5×10^{15} ions/cm^2 due to a small variation of mobility and carrier concentration up to that fluence, but for the ion fluence 1×10^{16} ions/cm^{2,} a large decrement in resistivity is observed, dominated by large variation in carrier concentration. The total resistance of this multilayer configuration is calculated by considering a parallel combination of resistances of the three consecutive layers of the film.

$$\frac{1}{R_{total}} = \frac{1}{R_{metal}} + \frac{2}{R_{oxide}}$$

since $R_{oxide} \approx 1000 R_{metal}$

so $R_{total} \approx R_{metal}$

The resistance of Ag (R_{Ag}) is very low compared to the oxide resistance, the total resistance of stacked multilayer would have a resistance nearly equal to that of Ag. Therefore the high conductivity of the TAT multilayer films is especially because of embedded Ag layer. A continuous film of Ag is required for good electrical conduction as below a critical film thickness the resistivity of the film suddenly increases due to aggregated state or islands of metal atoms [54]. The obtained results of electrical resistivity and sheet resistance of all TAT films indicate the formation of continuous metal inter layer. The figure of merit (FOM) is a significant factor that relates the sheet resistance and transmittance. A figure of merit (Ψ_{TC}) given by Haacke [55] is as follows-.

$$_{TC} = \frac{T_{av}^{10}}{R_s} \tag{6}$$

where T_{av} is average transmittance and R_s is the sheet resistance.

FOM (Ψ_{TC}) calculated for the TAT pristine and implanted films are shown in Fig. 11. Figure of merit calculated for the pristine film comes out to be $5.2\times10^{-3}\ \Omega^{-1}$. FOM for the samples first decreases with increase in fluence and increases for higher fluence and attain a value

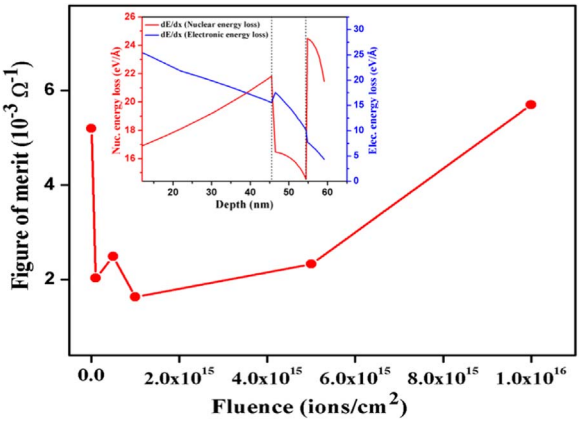

Fig. 11. Haacke FOM (Ψ_{TC}) of pristine and N ion implanted films of TAT. Inset shows the nuclear energy loss (S_n) and electronic energy loss (S_e) as a function of depth.

of $5.7\times10^{-3}\ \Omega^{-1}$ for fluence of 1×10^{16} ions/cm^2. This change is a consequence of variation in transmittance and sheet resistance with the fluence. These values of FOM indicate the suitability of these TAT films to be used as a transparent conductive electrode. Fraser and Cook [56] figure of merit (F_{FC}) is also calculated and showing similar trend for pristine and implanted samples (Supplementary material Fig. S2). The nuclear and electronic energy losses for N ion implantation films are shown in the inset of Fig. 11. It can be observed from the graph that nuclear energy loss is dominant over the electronic energy loss. The carrier concentration, mobility, resistivity, sheet resistance and Haacke figure of merit (FOM) have been calculated for pristine and implanted TAT films and shown in Table 3.

4. Conclusion

Present investigation demonstrates that it is possible to enhance the electrode properties of TAT films by N ion implantation. The structural, optical and electrical properties of TAT films were investigated as a function of N ion fluence. On implantation, the replacement of O ions by N ions results in the band gap narrowing and improvement in the electrical conduction. This is evidenced by the shift in Ti 2p peak and the position of N 1s peak in the XPS spectra. XRD shows amorphous nature of TiO_2 and a crystalline peak of Ag (111), SEM images indicate a smooth flat surface of the upper layer. Pristine film had surface roughness of 1.71 nm which decreases to 1.25 nm at the highest fluence of 1×10^{16} ions/cm^2. Implantation with higher fluences of N ions smoothens the top surface. On ion implantation, average optical transmittance degraded from ~80% to ~70%, but there is a simultaneous improvement in electrical resistivity from 2.04×10^{-4} to $9.62\times10^{-5}\ \Omega$ cm as the ion fluence is increased. Results indicated that electrical conductivity of TAT films is primarily due to Ag interlayer which showed further improvement on N ion implantation. Such high quality transparent conducting electrode can be used as an alternative to ITO for optoelectronic devices.

Acknowledgement

Authors are thankful to Materials Research Centre, MNITJ, India for the various fabrication and characterization facilities and Inter University Accelerator Center (IUAC), New Delhi, India for the low energy ion beam facility.

Appendix A. Supplementary material

Supplementary data associated with this article can be found in the online version at doi:10.1016/j.ceramint.2017.04.152.

Table 3
Carrier concentration, mobility, resistivity, sheet resistance, and Haacke FOM of pristine and N ion implanted TAT films.

S. no.	Fluence (ion cm^{-2})	Carrier concentration (cm^{-3})	Mobility (cm^2/V-s)	Resistivity (Ω cm)	Sheet resistance (Ω/□)	Haacke FOM (10^{-3} $Ω^{-1}$)
1	0	3.94×10^{21}	7.77	2.04×10^{-4}	20.4	5.2
2	1×10^{14}	4.34×10^{21}	6.79	2.12×10^{-4}	21.2	2.1
3	5×10^{14}	3.60×10^{21}	8.75	1.98×10^{-4}	19.81	2.5
4	1×10^{15}	4.40×10^{21}	8.15	1.74×10^{-4}	17.41	1.6
5	5×10^{15}	4.17×10^{21}	8.10	1.85×10^{-4}	18.48	2.3
6	1×10^{16}	7.06×10^{21}	9.20	9.62×10^{-5}	9.62	5.7

References

[1] K.L. Chopra, S. Major, D.K. Pandya, Transparent conductors-a status review, Thin Solid Films 102 (1983) 1–46. http://dx.doi.org/10.1016/0040-6090(83)90256-0.
[2] K. Ellmer, Past achievements and future challenges in the development of optically transparent electrodes, Nat. Photonics 6 (2012) 808–816. http://dx.doi.org/10.1038/nphoton.2012.282.
[3] S. Lany, A. Zunger, Dopability, intrinsic conductivity, and nonstoichiometry of transparent conducting oxides, Phys. Rev. Lett. 98 (2007) 2–5. http://dx.doi.org/10.1103/PhysRevLett.98.045501.
[4] T. Minami, Transparent conducting oxide semiconductors for transparent electrodes, Semicond. Sci. Technol. 20 (2005) 35–44. http://dx.doi.org/10.1088/0268-1242/20/4/004.
[5] A. Stadler, Transparent conducting oxides—an up-to-date overview, Materials 5 (2012) 661–683. http://dx.doi.org/10.3390/ma5040661.
[6] H. Liu, V. Avrutin, N. Izyumskaya, Ü. Özgr, H. Morkoç, Transparent conducting oxides for electrode applications in light emitting and absorbing devices, Superlattices Microstruct. 48 (2010) 458–484. http://dx.doi.org/10.1016/j.spmi.2010.08.011.
[7] D.S. Ginley, C. Bright, Transparent conducting oxides, MRS Bull. 25 (2000) 15–18. http://dx.doi.org/10.1557/mrs2000.256.
[8] I. Dima, B. Popescu, F. Iova, G. Popescu, Influence of the silver layer on the optical properties of the TiO2/Ag/TiO2 multilayer, Thin Solid Films 200 (1991) 11–18. http://dx.doi.org/10.1016/0040-6090(91)90026-T.
[9] C.H. Heo, S.-B. Lee, J.-H. Boo, Deposition of TiO2 thin films using RF magnetron sputtering method and study of their surface characteristics, Thin Solid Films 475 (2005) 183–188. http://dx.doi.org/10.1016/j.tsf.2004.08.033.
[10] K. Hashimoto, H. Irie, A. Fujishima, A. Historical, Overview and future prospects, AAPPS Bull. 17 (2007) 12–28. http://dx.doi.org/10.1007/BF00290457.
[11] C. Wang, J. Li, J. Dho, Post-deposition annealing effects on the transparent conducting properties of anatase Nb:TiO_2 films on glass substrates, Mater. Sci. Eng. B: Solid-State Mater. Adv. Technol. 182 (2014) 1–5. http://dx.doi.org/10.1016/j.mseb.2013.11.021.
[12] Z. Ben Ayadi, H. Mahdhi, K. Djessas, J.L. Gauf, L. El Mir, S. Alaya, Sputtered Al-Doped ZnO Transparent Conducting Thin Films Suitable for Silicon Solar Cells, 553. 2014. pp. 123–126.
[13] C.A. Amorim, C.J. Dalmaschio, E.R. Leite, A.J. Chiquito, Fluorine doped SnO_2 (FTO) nanobelts: some data on electronic parameters, J. Phys. D: Appl. Phys. 47 (2014) 45301. http://dx.doi.org/10.1088/0022-3727/47/4/045301.
[14] J. Ho Kim, J. Hwan Lee, S.W. Kim, Y.Z. Yoo, T.Y. Seong, Highly flexible ZnO/Ag/ZnO conducting electrode for organic photonic devices, Ceram. Int. 41 (2015) 7146–7150. http://dx.doi.org/10.1016/j.ceramint.2015.02.031.
[15] J.H. Kim, D.H. Kim, T.Y. Seong, Realization of highly transparent and low resistance TiO_2/Ag/TiO_2 conducting electrode for optoelectronic devices, Ceram. Int. 41 (2015) 3064–3068. http://dx.doi.org/10.1016/j.ceramint.2014.10.148.
[16] A. Indluru, T.L. Alford, Effect of Ag thickness on electrical transport and optical properties of indium tin oxide-Ag-indium tin oxide multilayers, J. Appl. Phys. 105 (2009). http://dx.doi.org/10.1063/1.3153977.
[17] L. Liu, S. Ma, H. Wu, B. Zhu, H. Yang, J. Tang, X. Zhao, Effect of the annealing process on electrical and optical properties of SnO2/Ag/SnO2 nanometric multi-layer film, Mater. Lett. 149 (2015) 43–46. http://dx.doi.org/10.1016/j.matlet.2015.02.093.
[18] V. Sharma, S. Singh, K. Asokan, K. Sachdev, A study on 100 MeV O^{7+} irradiated SnO_2/Ag/SnO_2 multilayer as transparent electrode for flat panel display application, Nucl. Instrum. Methods Phys. Res. B (2016) 2–6. http://dx.doi.org/10.1016/j.nimb.2016.04.059.
[19] V. Sharma, R. Vyas, P. Bazylewski, G.S. Chang, K. Asokan, K. Sachdev, Probing the highly transparent and conducting SnOx/Au/SnOx structure for futuristic TCO, RSC Adv., 2016, pp. 29135–29141. ⟨https://dx.doi.org/10.1039/C5RA24422F⟩.
[20] J.U.N.H.O. Kim, J. Na, S. Kim, Y. Yoo, Highly Transparent and Low-Resistance Indium-Free ZnO/Ag/ZnO Multilayer Electrodes for Organic Photovoltaic Devices, 44, 2015, pp. 3967–3972. ⟨https://dx.doi.org/10.1007/s11664-015-3811-8⟩.
[21] J.-H. Qi, Y. Li, T.-T. Duong, H.-J. Choi, S.-G. Yoon, Dye-sensitized solar cell based on AZO/Ag/AZO multilayer transparent conductive oxide film, J. Alloy. Compd. 556 (2013) 121–126. http://dx.doi.org/10.1016/j.jallcom.2012.12.127.
[22] H.J. Kim, K.W. Seo, Y.H. Kim, J. Choi, H.K. Kim, Direct laser patterning of transparent ITO-Ag-ITO multilayer anodes for organic solar cells, Appl. Surf. Sci. 328 (2015) 215–221. http://dx.doi.org/10.1016/j.apsusc.2014.12.017.
[23] M.-Q. Zhu, H.-D. Jin, P.-Q. Bi, F.-J. Zong, J. Ma, X.-T. Hao, Performance improvement of TiO_2/Ag/TiO_2 multilayer transparent conducting electrode films for application on photodetectors, J. Phys. D: Appl. Phys. 49 (2016) 115108. http://dx.doi.org/10.1088/0022-3727/49/11/115108.
[24] J.H. Kim, H. Lee, J. Na, S. Kim, Y. Yoo, T.-Y. Seong, Dependence of optical and electrical properties on Ag thickness in TiO_2/Ag/TiO_2 multilayer films for photovoltaic devices, Ceram. Int. 41 (2015) 8059–8063. http://dx.doi.org/10.1016/j.ceramint.2015.03.002.
[25] A. Dhar, T.L. Alford, High quality transparent TiO_2/Ag/TiO_2 composite electrode films deposited on flexible substrate at room temperature by sputtering, APL Mater. 1 (2013) 10–17. http://dx.doi.org/10.1063/1.4808438.
[26] K.D. Kim, T. Pfadler, E. Zimmermann, Y. Feng, J.A. Dorman, J. Weickert, L. Schmidt-Mende, Decoupling optical and electronic optimization of organic solar cells using high-performance temperature-stable TiO_2/Ag/TiO_2 electrodes, APL Mater. 3 (2015). http://dx.doi.org/10.1063/1.4933414.
[27] J. Kulczyk-Malecka, P.J. Kelly, G. West, G.C.B. Clarke, J.A. Ridealgh, K.P. Almtoft, A.L. Greer, Z.H. Barber, Investigation of silver diffusion in TiO2/Ag/TiO2 coatings, Acta Mater. 66 (2014) 396–404. http://dx.doi.org/10.1016/j.actamat.2013.11.030.
[28] S.H. Yu, C.H. Jia, H.W. Zheng, L.H. Ding, W.F. Zhang, High quality transparent conductive SnO_2/Ag/SnO_2 tri-layer films deposited at room temperature by magnetron sputtering, Mater. Lett. 85 (2012) 68–70. http://dx.doi.org/10.1016/j.matlet.2012.06.108.
[29] R. Asahi, T. Mikawa, T. Ohwaki, K. Aoki, Y. Taga, Visible light photocatalysis in nitrogen-doped titanium oxides, Science 293 (2001) 269–271. http://dx.doi.org/10.1126/science.1061051.
[30] W. Choi, A. Termin, M.R. Hoffmann, The role of metal ion dopants in quantum-sized TiO2: correlation between photoreactivity and charge carrier recombination dynamics, J. Phys. Chem. 98 (1994) 13669–13679. http://dx.doi.org/10.1021/j100102a038.
[31] J. Zhang, Q. Sun, J. Zheng, X. Zhang, Y. Cui, P. Wang, W. Li, Y. Zhu, The characterization of nitrogen doped TiO2 photoanodes and its application in the dye sensitized solar cells, J. Renew. Sustain. Energy 3 (2011). http://dx.doi.org/10.1063/1.3599840.
[32] N.C. Saha, H.G. Tompkins, Titanium nitride oxidation chemistry: an x-ray photoelectron spectroscopy study, J. Appl. Phys. 72 (1992) 3072–3079. http://dx.doi.org/10.1063/1.351465.
[33] H. Irie, Y. Watanabe, K. Hashimoto, Nitrogen-concentration dependence on photocatalytic activity of $TiO_{2-x}N_x$ Powders, J. Phys. Chem. B 107 (2003) 5483–5486. http://dx.doi.org/10.1021/jp030133h.
[34] T. Sano, N. Negishi, K. Koike, K. Takeuchi, S. Matsuzawa, Preparation of a visible light-responsive photocatalyst from a complex of Ti^{4+} with a nitrogen-containing ligand, J. Mater. Chem. 14 (2004) 380. http://dx.doi.org/10.1039/b311444a.
[35] G. Zhao, S.M. Kim, S.G. Lee, T.S. Bae, C. Mun, S. Lee, H. Yu, G.H. Lee, H.S. Lee, M. Song, J. Yun, Bendable solar cells from stable, flexible, and transparent conducting electrodes fabricated using a nitrogen-doped ultrathin copper film, Adv. Funct. Mater. (2016) 4180–4191. http://dx.doi.org/10.1002/adfm.201600392.
[36] Z. Song, J. Hrbek, R. Osgood, Formation of TiO_2 nanoparticles by reactive-layer-assisted deposition and characterization by XPS and STM, Nano Lett. 5 (2005) 1327–1332. http://dx.doi.org/10.1021/nl0505703.
[37] C.N.R. Rao, D.D. Sarma, S. Vasudevan, M.S. Hegde, Study of transition metal oxides by photoelectron spectroscopy, Proc. R. Soc. A: Math. Phys. Eng. Sci. 367 (1979) 239–252. http://dx.doi.org/10.1098/rspa.1979.0085.
[38] R. Sanjinés, H. Tang, H. Berger, F. Gozzo, G. Margaritondo, F. Lévy, Electronic structure of anatase TiO_2 oxide, J. Appl. Phys. 75 (1994) 2945–2951. http://dx.doi.org/10.1063/1.356190.
[39] T.C. Jagadale, S.P. Takale, R.S. Sonawane, H.M. Joshi, S.I. Patil, B.B. Kale, S.B. Ogale, N-doped TiO_2 nanoparticle based visible light photocatalyst by modified peroxide sol-gel method, J. Phys. Chem. C 112 (2008) 14595–14602. http://dx.doi.org/10.1021/jp803567f.
[40] M. Sathish, B. Viswanathan, R.P. Viswanath, C.S. Gopinath, Synthesis, characterization, electronic structure, and photocatalytic activity of nitrogen-doped TiO2 nanocatalyst, Chem. Mater. 17 (2005) 6349–6353. http://dx.doi.org/10.1021/cm052047v.
[41] C. Burda, Y. Lou, X. Chen, A.C.S. Samia, J. Stout, J.L. Gole, Enhanced nitrogen doping in TiO_2 nanoparticles, Nano Lett. 3 (2003) 1049–1051. http://dx.doi.org/10.1021/nl034332o.
[42] T. Yoshida, S. Niimi, M. Yamamoto, T. Nomoto, S. Yagi, Effective nitrogen doping into TiO_2 (N-TiO_2) for visible light response photocatalysis, J. Colloid Interface Sci. 447 (2014) 278–281. http://dx.doi.org/10.1016/j.jcis.2014.12.097.
[43] R. Chen, C. Zou, J. Bian, A. Sandhu, W. Gao, Microstructure and optical properties of Ag-doped ZnO nanostructures prepared by a wet oxidation doping process, Nanotechnology 22 (2011) 105706. http://dx.doi.org/10.1088/0957-4484/22/10/105706.
[44] Z. Zhao, T.L. Alford, The optimal TiO_2/Ag/TiO_2 electrode for organic solar cell

application with high device-specific Haacke figure of merit, Sol. Energy Mater. Sol. Cells 157 (2016) 599–603 https://dx.doi.org/10.1016/j.solmat.2016.07.044.
[45] H. Liu, L. Li, T. Yao, W. Ding, D. Ju, W. Chai, The effect of ion source working power on the composition and optical properties of TiO_2 films bombarded by N ion beam, Surf. Coat. Technol. 219 (2013) 88–93. http://dx.doi.org/10.1016/j.surfcoat.2013.01.009.
[46] M. Rizwan, A. Ahmad, K.M. Deen, W. Haider, Electrochemical behavior and biological response of mesenchymal stem cells on cp-Ti after N-ions implantation, Appl. Surf. Sci. 320 (2014) 718–724. http://dx.doi.org/10.1016/j.apsusc.2014.09.169.
[47] J. Tauc, Optical properties of amorphous semiconductors, Amorph. Liq. Semicond. (1974) 159–220. http://dx.doi.org/10.1007/978-1-4615-8705-7_4.
[48] B. Joseph, P.K. Manoj, V.K. Vaidyan, Studies on the structural, electrical and optical properties of Al-doped ZnO thin films prepared by chemical spray deposition, Ceram. Int. 32 (2006) 487–493. http://dx.doi.org/10.1016/j.ceramint.2005.03.029.
[49] M. Di Giulio, G. Micocci, R. Rella, P. Siciliano, A. Tepore, Optical absorption of tellurium suboxide thin films, Phys. Status Solidi (a) 136 (1993) K101–K104. http://dx.doi.org/10.1002/pssa.2211360236.
[50] J.Y. Lee, J.W. Yang, J.H. Chae, J.H. Park, J.I. Choi, H.J. Park, D. Kim, Dependence of intermediated noble metals on the optical and electrical properties of ITO/metal/ITO multilayers, Opt. Commun. 282 (2009) 2362–2366. http://dx.doi.org/10.1016/j.optcom.2008.12.044.
[51] R. Fromknecht, R. Auer, I. Khubeis, O. Meyer, Lattice location and electrical conductivity in ion implanted TiO2 single crystals, Nucl. Instrum. Methods Phys. Res. Sect. B: Beam Interact. Mater. At. 120 (1996) 252–256. http://dx.doi.org/10.1016/s0168-583x(96)00520-4.
[52] R. Fromknecht, I. Khubeis, S. Massing, O. Meyer, Ion implantation in TiO2: damage production and recovery, lattice site location and electrical conductivity, Nucl. Instrum. Methods Phys. Res. Sect. B: Beam Interact. Mater. At. 147 (1999) 191–201. http://dx.doi.org/10.1016/S0168-583X(98)00551-5.
[53] C.-H. Yang, S.-C. Lee, S.-C. Chen, T.-C. Lin, The effect of annealing treatment on microstructure and properties of indium tin oxides films, Mater. Sci. Eng. B 129 (2006) 154–160. http://dx.doi.org/10.1016/j.mseb.2006.01.012.
[54] K. Seal, M.A. Nelson, Z.C. Ying, D.A. Genov, A.K. Sarychev, V.M. Shalaev, Growth, morphology, and optical and electrical properties of semicontinuous metallic films, Phys. Rev. B 67 (2003) 35318. http://dx.doi.org/10.1103/PhysRevB.67.035318.
[55] G. Haacke, New Figure of Merit for Transparent Conductors*, 4086, 1976, pp. 1–5. ⟨https://dx.doi.org/10.1063/1.323240⟩).
[56] D.B. Fraser, H.D. Cook, Highly conductive, transparent films of sputtered $In_{2-x}Sn_xO_{3-y}$ x]O[sub 3–y], J. Electrochem. Soc. 119 (1972) 1368. http://dx.doi.org/10.1149/1.2403999.

J Mater Sci (2017) 52:11580–11591

Electronic materials

Investigation of effect of doping concentration in Nb-doped TiO_2 thin films for TCO applications

Satyavir Singh[1], Vikas Sharma[1], and Kanupriya Sachdev[1,2,*]

[1] Department of Physics, Malaviya National Institute of Technology, Jaipur 302017, India
[2] Materials Research Centre, Malaviya National Institute of Technology, Jaipur 302017, India

Received: 7 March 2017
Accepted: 27 June 2017
Published online: 5 July 2017

ABSTRACT

Nb-doped TiO_2 (referred hereafter as NTO) thin films were deposited by sol–gel spin coating method to investigate their use as transparent conducting electrode (TCE). A range of $Nb_xTi_{1-x}O_2$ ($x = 0$, 0.003, 0.005, 0.008, 0.01, 0.015, 0.02) compositions were synthesized and deposited as thin films via spin coating. The films were deposited at room temperature and showed crystallization on annealing at 550 °C for 1 h in air. The X-ray diffraction confirms formation of anatase TiO_2 by showing dominant peak at $2\theta \sim 25.5°$ corresponding to (101) reflection plane. Raman spectroscopy shows the characteristics modes of TiO_2. Surface topography and morphology measured by atomic force microscopy and field-emission scanning electron microscopy exhibit smooth and uniform deposition of films. Optical transmittance reduces from 85 to 70% as Nb content increases from 0 to 2 at.%. Meanwhile, electrical resistivity attained a minimum value of 3.65 Ω cm for 2 at.% Nb doping. X-ray photoelectron spectroscopy analysis exhibits shifting of Ti 2*p* peak which confirms substitution by Nb^{5+} in TiO_2 lattice and Nb–O–Ti bond formation. Transmission electron microscope and selected area electron diffraction patterns reveal that films consist of Nb and crystalline phase of TiO_2. All films were characterized by Fourier transmission infrared spectroscopy and thermogravimetric analysis. Present study reports low-cost and effective fabrication of TCE for optoelectronic applications.

Introduction

Transparent conducting oxides (TCOs) are electrically conductive materials with high transparency in the visible region. They are generally fabricated using thin film technologies and have wide applications. Solar cells, touch panel controls, light emitting diodes, optoelectronic devices; all devices need transparent conducting electrodes (TCEs) [1–3]. Most popular transparent conducting oxide is indium–tin oxide (ITO), which is commonly used in optoelectronic devices due to its high conductivity, high transparency and ease of deposition [4, 5]. However, due to the increasing demand and natural scarcity, researchers are interested to find indium-free TCOs with equivalent electrical resistivity and optical

Address correspondence to E-mail: ksachdev.phy@mnit.ac.in

DOI 10.1007/s10853-017-1328-7

transmittance [6–8]. Nb-doped TiO_2 (NTO) has emerged as promising TCO material for the replacement of ITO. Kasai et al. [9] prepared TNO films by rf sputtering method, and they showed that 170-nm-thick film exhibited a resistivity of 8×10^{-4} Ω cm with carrier concentration of $n_e = 1.5 \times 10^{21}$ cm^{-3} and transmittance of ~70%. Hung et al. [10] deposited niobium-doped TiO_2 (TNO) films with different Nb contents by reactive co-sputtering. Nb concentration in the TNO films was changed from 0 to ~13 at.%. TNO film with 9.7 at.% Nb showed a minimum resistivity of 9.2×10^{-4} Ω cm and average transmittance above 70% in the visible range.

The sol–gel method is a promising method for producing homogeneous and large area thin films at low cost. This method can also be used in fabrication of nano-particles, sheets and fibers at room temperature. Fallah et al. [11] reported electrical properties of Nb-doped TiO_2 ($Ti_{0.94}Nb_{0.06}O_2$) thin films prepared by sol–gel method. The films were dried in air at 100 °C and then annealed two times in vacuum for two different pressure and time. They showed that two-step annealing is more effective way to enhance the electrical properties of NTO thin films, which showed minimum resistivity of 4.4 Ω cm and more than 50% transmittance in the visible region for 36-nm-thick films. It also indicated that sol–gel technique is a cheap and feasible method to prepare NTO films. In this work, we have prepared and investigated Nb-doped TiO_2 thin films for low concentration of Nb (0–2 at.%). No reports in the literature are seen for this low concentration of Nb. As-prepared thin films were annealed at 550 °C for 1 h in air to achieve crystallinity, which shows anatase phase. Annealing of NTO films has been done to lower the resistivity of films. This is employed to increase the oxygen vacancies in the film which help in improving ion diffusion in the host matrix enhancing the electrical properties of the film [12]. The annealed films were then extensively investigated by XPS, FTIR and TGA to gain a better understanding of these films for TCO applications.

Experimental details

Sample preparation

NTO films were prepared by sol–gel spin coating method. The sources of titanium and niobium were tetrabutyl titanate (TBT) and niobium (V) chloride, respectively. Acetyl acetone (AcAc) was added as a chelating agent with acetic acid and ethanol as catalyst and solvent, respectively. TBT was dissolved in ethanol in a flask (flask A) and stirred for 1 h at room temperature. Niobium chloride with acetic acid and AcAc was dissolved in ethanol in a flask (flask B), which was also stirred for 2 h at room temperature. The niobium chloride solution was added into TBT solution, and the final solution was stirred for 2 h at room temperature. The obtained final light yellow solution used for coating was aged for 20 h at room temperature. The concentration of Nb for doping was taken as 0, 0.3, 0.5, 0.8, 1, 1.5 and 2 at.%. The corning glass substrates were cleaned using standard cleaning method. These slides were stored in ethanol to keep them clean and fresh. The films (~400 nm thick) were spin coated using aged sol with a fixed spin speed of 3000 rpm for 1 min. The deposited films were dried in air at 120 °C for 15 min and then annealed at 550 °C for 1 h in air. Photograph of pure TiO_2 and NTO films is shown in supplementary Fig. S1.

Characterization

X-ray diffractometer (Panalytical X-Pert Pro) was used to determine the crystal structure of NTO films. The Multimode Scanning Probe Microscope (Bruker) and Nova Nano FE-SEM 450 (FEI) were used to measure the topography and morphology of the NTO films. LAMBDA 750 (PerkinElmer) UV–Vis–NIR spectrophotometer was used to find the optical transmittance and absorbance. The resistivity and sheet resistance of NTO films were measured using four-probe method. Chemical states were analyzed by X-ray photoelectron spectroscopy (XPS, Omicron ESCA). HRTEM images and SAED pattern were obtained from T20 ST FEI Technai G^2 transmission electron microscope (TEM) operating at 200 keV. The Fourier transform infrared (FTIR) data were acquired using FTIR Spectrum 2 (PerkinElmer). Thermogravimetric (TG) behavior was studied using STA 6000 (PerkinElmer).

Results and discussion

X-ray diffraction measurements

Figure 1a shows the XRD pattern of the Nb-doped TiO_2 (NTO) thin films with Nb composition in the

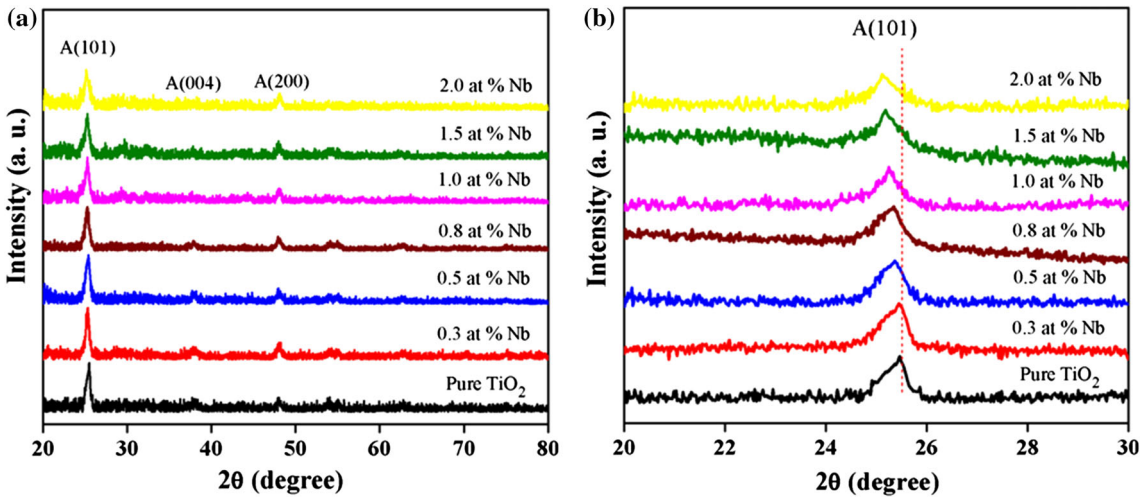

Figure 1 **a** XRD patterns of the pure TiO_2 and NTO films post-annealed at 550 °C, **b** magnified pattern in the range of 20°–30°.

Table 1 Crystallite size, lattice strain and lattice constants of pure TiO_2 and NTO films with different Nb concentration

S. no.	Nb concentration (at.%)	Angle (θ) (°)	d-spacing (Å) (±0.05)	Crystallite size (nm)	Lattice strain ($\times 10^{-2}$)	Lattice constant	
						a (Å)	c (Å)
1	0	12.755	3.487	15.2	1.001	3.771	9.17
2	0.3	12.725	3.496	15	1.097	3.781	9.19
3	0.5	12.695	3.504	14.9	1.102	3.787	9.25
4	0.8	12.672	3.511	14.7	1.129	3.798	9.29
5	1.0	12.625	3.523	14.2	1.156	3.792	9.52
6	1.5	12.585	3.534	13.4	1.211	3.796	9.67
7	2.0	12.555	3.542	12.6	1.468	3.813	9.79

range of 0–2 at.%. As-deposited pure TiO_2 and NTO films were amorphous due to room temperature preparation of films. Annealing of thin films at 550 °C led to good crystallinity. Annealed NTO films show a sharp peak at 2θ position of ~25.5°, which can be assigned to the (101) anatase Nb/TiO_2 reflection plane. The weak peaks at ~37.7° and 48.1° in the annealed samples are due to the (004) and (200) anatase reflection plane. Figure 1b shows a shift in the position of the (101) peak to lower angular side with increase in Nb content. Similar results were investigated by Su et al. [13], and the shift has been attributed to Nb atoms replacing Ti atoms in the crystal on doping.

Crystallite size has been calculated by using Debye–Scherrer formula (Eq. 1). Inter-planar spacing (d-spacing) between atoms was obtained using Bragg's Law (Eq. 2).

$$D = \frac{0.94\lambda}{\beta \cos\theta} \quad (1)$$

$$2d \sin\theta = n\lambda \quad (2)$$

where D is the diameter of the particle, θ is the diffraction angle, λ is the wavelength of X-rays, d is inter-planar spacing and β is the full width at half maximum of the XRD peak. The crystallite size of deposited NTO thin films in the anatase (101) direction is given in Table 1. It was observed that the crystallite size reduces with increasing Nb concentration. The substitution of Ti by Nb atoms in TiO_2 lattice produces some strain (as Nb atom is larger) which may hamper growth of TiO_2. The same characteristics were reported by Uyanga et al. [14].

Lattice strain and lattice constants have been calculated using Eqs. 3 and 4.

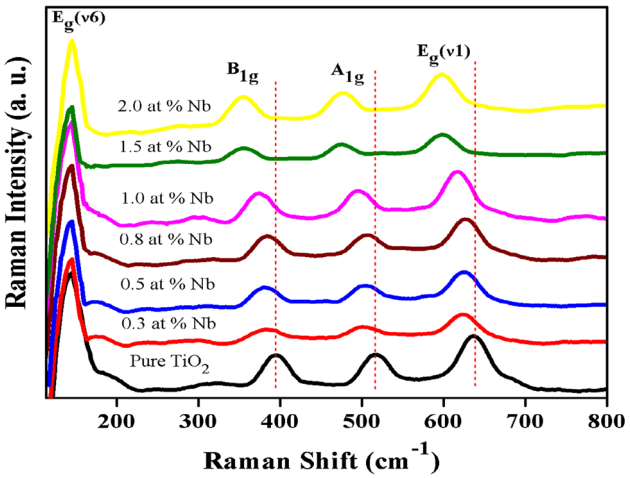

Figure 2 Raman spectra of pure TiO_2 and NTO films.

$$\text{Lattice Strain} = \frac{\beta}{4\tan\theta} \tag{3}$$

$$\frac{1}{d^2} = \frac{h^2+k^2}{a^2} + \frac{l^2}{c^2} \tag{4}$$

Inter-planar spacing, crystallite size, lattice strain and lattice constants for pure TiO_2 and NTO films have been calculated and are shown in Table 1. The graph between crystallite size and lattice strain is shown in supplementary Fig. S2.

Raman spectroscopy

Raman spectra of pure and Nb-doped TiO_2 thin films between 100 and 800 cm^{-1} are shown in Fig. 2. Obtained Raman modes of TiO_2 are in good agreement with the XRD results. No other impurity phase was observed. Four main peaks of anatase TiO_2 appear at 146, 396, 518 and 639 cm^{-1}; these peaks are assigned to E_g ($v6$), B_{1g}, A_{1g} and E_g ($v1$) vibration modes of TiO_2 [15]. Trizio et al. [16] reported that separate Nb phase may possibly appear if the Nb concentration increases beyond a certain limit (>10 mol%). No such feature has been observed in the range of Nb doping in our case. A slight shift of the B_{1g}, A_{1g} and E_g ($v1$) modes to lower wavenumber is observed with increasing Nb content.

The shift in the Raman spectra with increasing Nb content is not only due to particle size but also due to varying stoichiometry of the system with increasing Nb. The Nb atoms produce some strain in TiO_2 lattice due to the size difference, which may hamper the growth of TiO_2 as a result of which the particle size decreases. Another reason could be variation in oxygen percentage and non-stoichiometry of TiO_2 with Nb doping with annealing at 550 °C [17, 18]. The doping generated defects which include O vacancies, Ti vacancies and O interstitials cause shift in the Raman modes of anatase TiO_2. The particle size of NTO films is ~15 nm and variation is also small (3 nm) on doping, which is very less to effect the E_g ($v6$) mode of Raman spectrum [19]. B_{1g} mode appears because of stretching of Ti–O bond [20], and this observed shift in B_{1g} mode proves that Nb is perfectly doped in TiO_2 lattice [21], which is consistent with XRD results. The varying intensity of E_g ($v1$) modes positioned at 639 cm^{-1} peak is explained by the formation of Nb–O bond [16]. Raman modes and Raman peak positions of pure TiO_2 and NTO films with different Nb concentration are tabulated in Table 2.

Fourier transmission infrared spectroscopy

Figure 3 shows the FTIR spectra of pure TiO_2 and NTO films for 400 to 4000 cm^{-1}. It can be seen from the spectrum that a band in the 600–660 cm^{-1} range is assigned to characteristic modes of TiO_2 [22]. FTIR mode centered at 1363 cm^{-1} is due to CH_3 bending [23]. The mode appearing at 2922 cm^{-1} indicates C–H vibration mode of CH_2 groups, which is designated as antisymmetric mode [24]. The broad range band centered at 3360–3600 cm^{-1} indicates the existence of

Table 2 Raman modes and Raman peak positions of pure TiO_2 and NTO films with different Nb concentration

S. no.	Raman mode	Raman peak position (cm^{-1})						
		Pure TiO_2	0.3 Nb/TiO_2	0.5 Nb/TiO_2	0.8 Nb/TiO_2	1.0 Nb/TiO_2	1.5 Nb/TiO_2	2.0 Nb/TiO_2
1	E_g ($v6$)	146	145.8	145.6	145.5	145.6	145.4	145.3
2	B_{1g}	396	385	382	380	376	370	365
3	A_{1g}	518	512	508	506	504	495	485
4	E_g ($v1$)	639	630	627	625	619	607	603

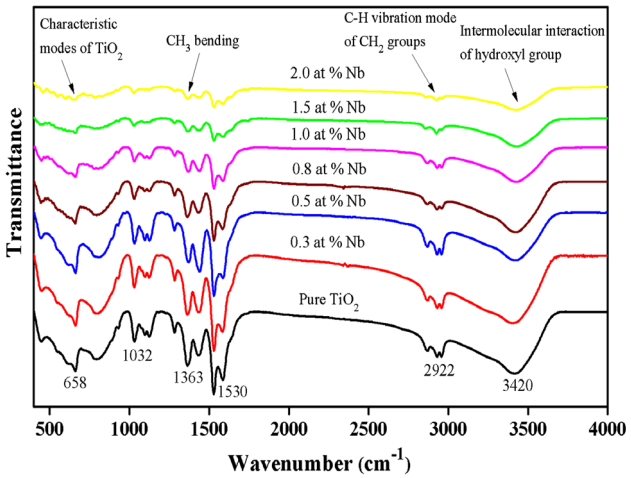

Figure 3 FTIR spectra of pure TiO_2 and NTO films.

hydroxyl groups, which is possibly due to read-sorption of water from the environment [25].

Transmission electron microscope analysis

The microstructure of pure TiO_2 and NTO (2 at.%) films was further analyzed by TEM. TEM results along with selected area electron diffraction (SAED) pattern provide better understanding about the crystalline nature of TiO_2. Figure 4a, c exhibits TEM images of pure TiO_2 and NTO (2 at.%) films. Figure 4b, d shows the high-resolution micrographs obtained from TEM and further investigated by digital micrograph to measure the inter-planar distance. The *d*-spacing for pure TiO_2 and NTO samples was 3.51 ± 0.05 and 3.56 ± 0.05 Å, respectively, which is nearly equal to the *d*-spacing values obtained XRD results. The inset of Fig. 4b, d shows the SAED pattern, which confirms the existence of anatase TiO_2 (101) and (200) diffraction planes. Figure 4e–h shows the elemental mapping confirming the presence of Ti, O and Nb in the NTO film [26].

Surface characterization

The surface morphology of NTO thin films was studied by FE-SEM for various Nb concentrations. Figure 5 shows the SEM images of TiO_2 thin films with 0, 0.5, 1.5 and 2 at.% Nb at 100 k× magnification. SEM micrographs show homogeneous and uniform surface morphology of NTO films. It is seen from SEM micrographs that films consist of spherical

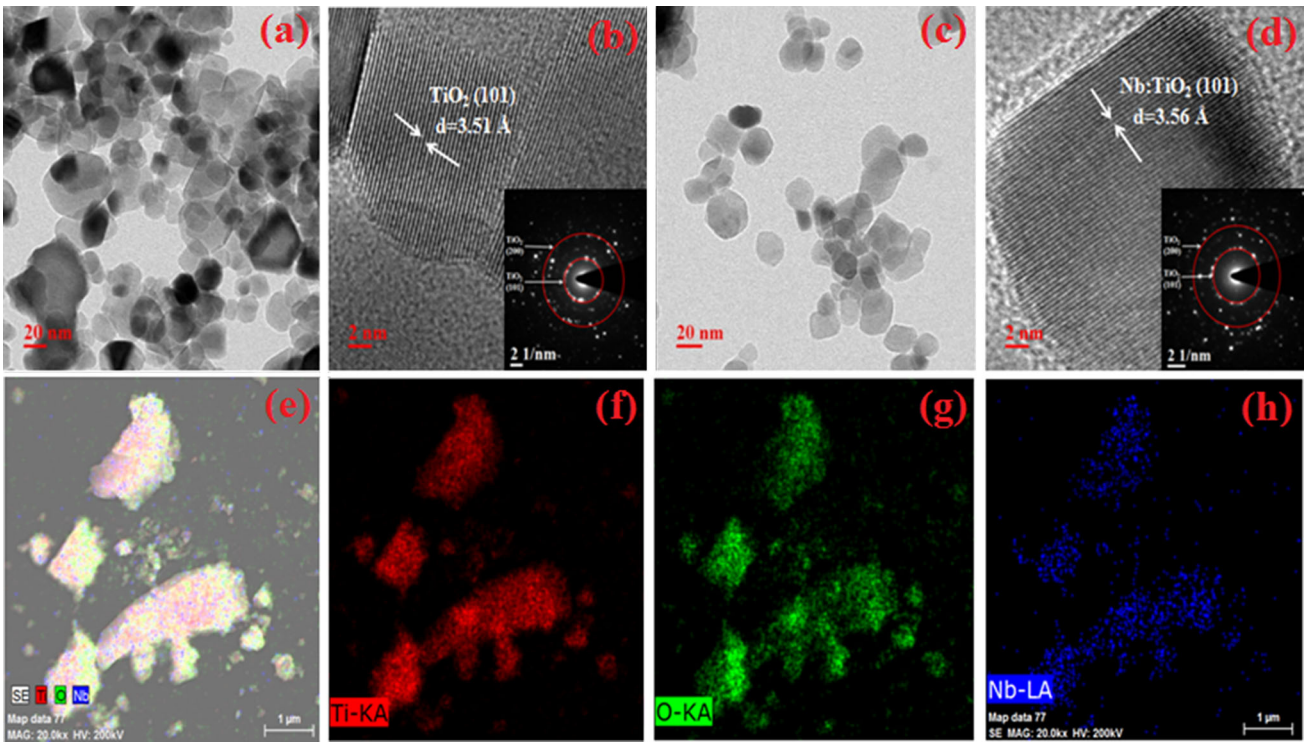

Figure 4 TEM images of pure TiO_2 and NTO (2 at.% Nb) thin films **a** pure TiO_2 TEM image, **b** HRTEM image of pure TiO_2 with SAED pattern, **c** NTO TEM image, **d** HRTEM image of NTO with SAED pattern and **e**–**h** elemental mapping of NTO film for Ti, O and Nb.

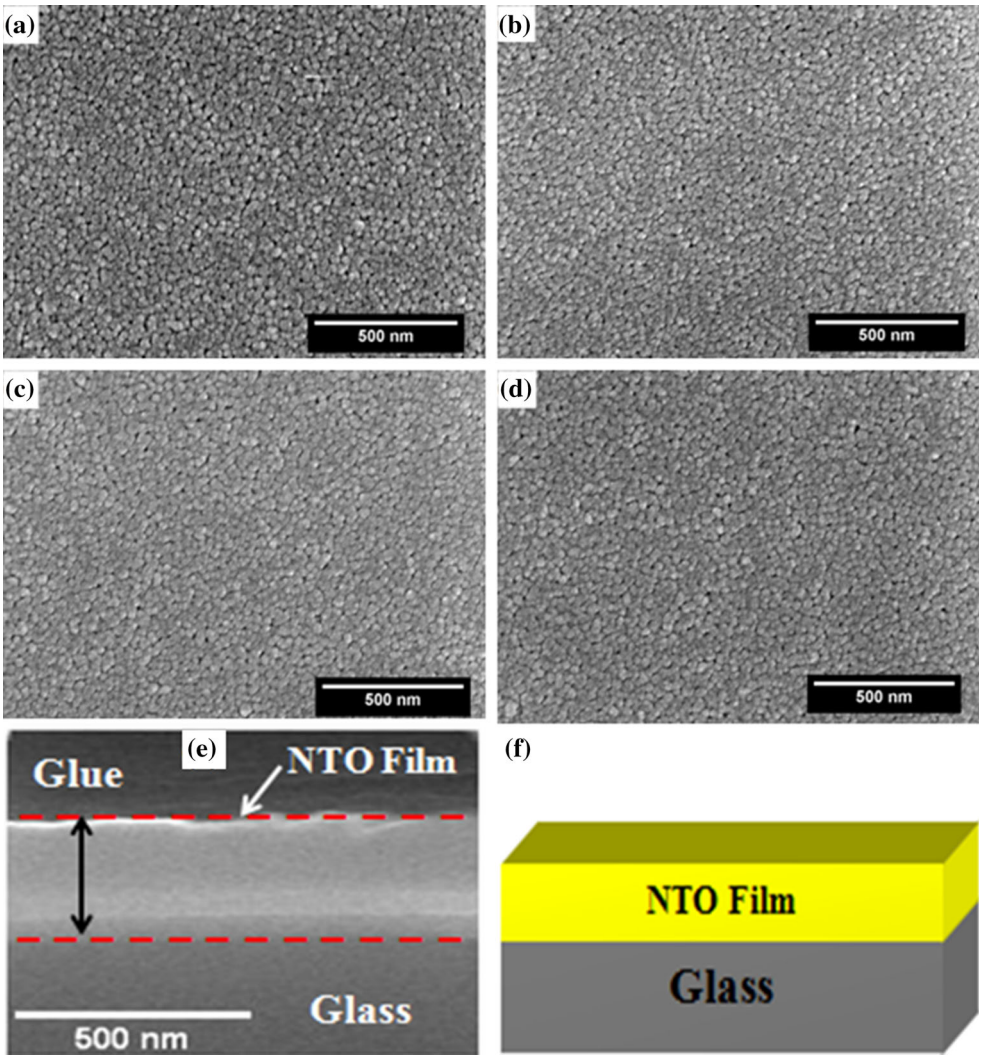

Figure 5 SEM images **a** pure TiO_2, **b** 0.5 at.% Nb/TiO_2, **c** 1 at.% Nb/TiO_2, **d** 2 at.% Nb/TiO_2, **e** cross-sectional FESEM image of 2 at% NTO film and **f** schematic diagram of NTO film.

grains and niobium particles are not visible separately in the thin films, showing complete miscibility of Nb in TiO_2. The similar kind of surface morphology of Nb-doped TiO_2 was observed in other reports [27, 28]. Figure 5e shows the FE-SEM cross-sectional image of 2 at% NTO film, which indicates the smooth and uniform deposition of film on corning glass substrate. The estimated thickness of the NTO film is about 400 nm. Figure 5f shows the schematic diagram of NTO film prepared on glass substrate. Figure 6a shows energy-dispersive X-ray (EDS) spectrum of 2 at.% NTO film annealed at 550 °C for 1 h obtained from SEM. EDS spectra confirms the presence of titanium, oxygen and niobium contents in the deposited film. The silicon peak appears due to substrate. The obtained results from EDS spectrum of NTO films show the existence of 1.75% niobium in the film that is close to the amount of 2% Nb used for NTO film preparation, further assuring presence of no other impurity in the film. Figure 6b shows the EDS spectrum of 2 at.% NTO film obtained from the TEM.

The topography of NTO films was observed by atomic force microscopy (AFM) with scan area of $1 \times 1\ \mu m^2$. Figure 7 shows the AFM images for the samples that were annealed at 550 °C. The surfaces of the thin films were very smooth and exhibited low values of root mean square roughness. The undoped film had the highest root mean square (RMS) surface roughness as 0.72 nm and the RMS value decreases with the rising of niobium concentration with a minimum value of 0.28 nm for 2 at.% Nb concentration. The decrease in particle size with Nb content may result in reduction of the surface roughness

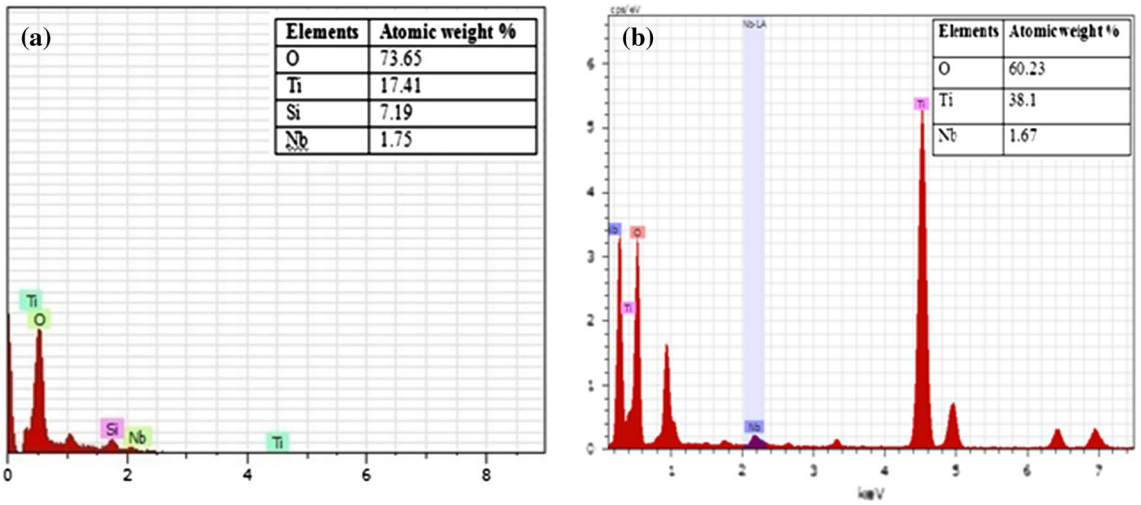

Figure 6 **a** SEM EDS, **b** TEM EDS spectra of NTO film (2 at.% Nb).

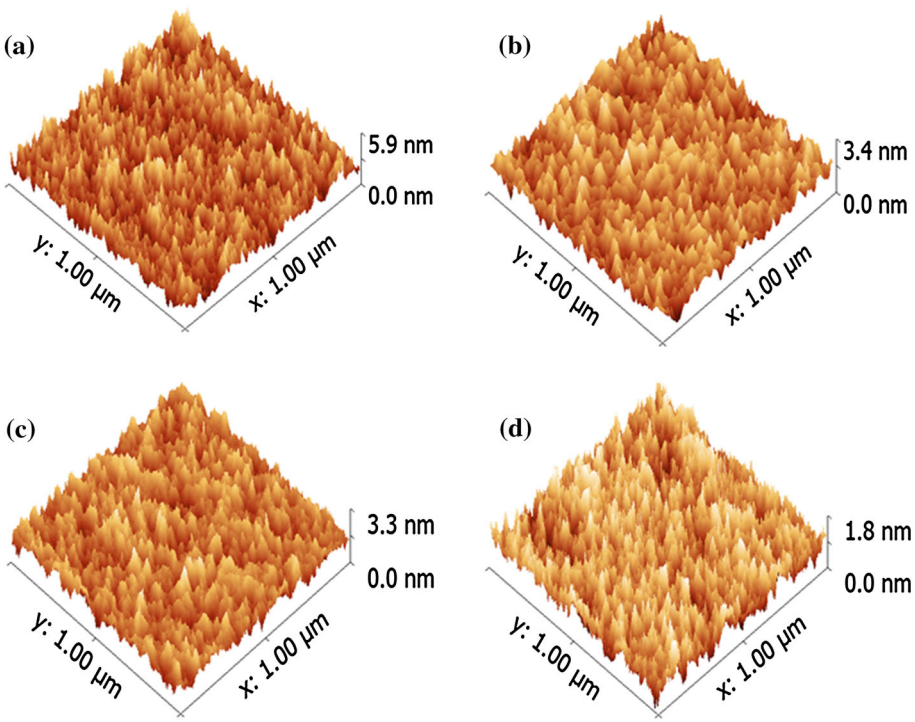

Figure 7 3-D AFM images **a** pure TiO_2, **b** 0.5 at.% Nb/TiO_2, **c** 1 at.% Nb/TiO_2 and **d** 2 at.% Nb/TiO_2.

giving smoother films [29]. Software Gwyddion was used to process and analyze the AFM images.

Thermogravimetric analysis

Figure 8 shows the thermogravimetric analysis (TGA) (in the temperature range of 30–850 °C) of pure TiO_2 and NTO samples. It can be observed from the graph that all samples show three steps of weight loss. The first loss observed at ~100 °C occurs because of expulsion of adsorbed water [30]. The second weight loss between 150 and 300 °C is due to removal of organics present in the sample. The third weight loss (in the range of 380–420 °C) occurs because of expulsion of hydroxyls which exist inside the sol–gel prepared films [31]. TGA results exhibit that the organic impurities are eliminated approximately below the annealing temperature. The TGA (in the temperature range of 850–30 °C) has been also

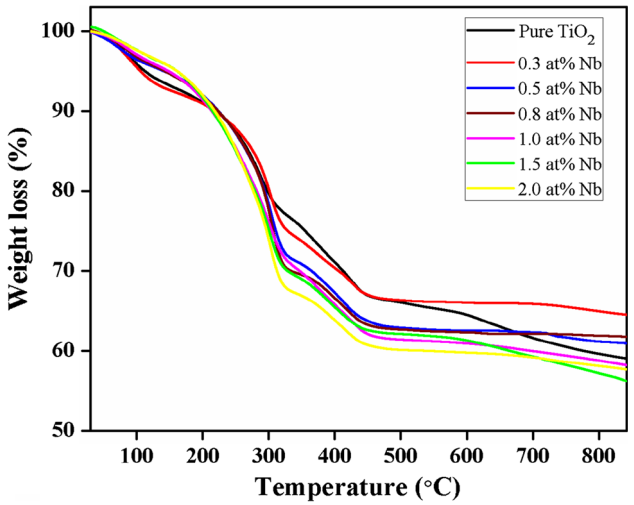

Figure 8 TGA (30–850 °C) spectra of pure and Nb-doped TiO_2 thin films.

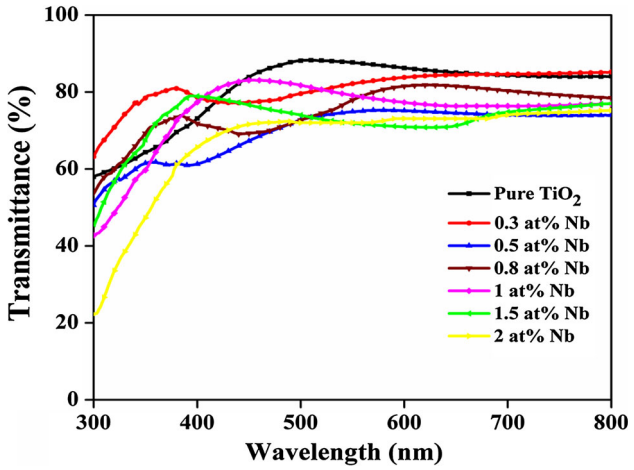

Figure 9 Optical transmittance spectra of pure TiO_2 and NTO films.

done for all samples and is shown in supplementary Fig. S3.

Optical analysis

The UV–Vis optical transmittance spectra for $Nb_xTi_{1-x}O_2$ ($x = 0$, 0.003, 0.005, 0.008, 0.01, 0.015, 0.02) films annealed at 550 °C are shown in Fig. 9. The average transmittance for pure TiO_2 film was ~85% in the visible region (400 nm < λ < 800 nm). Pure TiO_2 film shows higher transmittance than Nb-doped TiO_2 thin films. The average transmittance decreases from 85 to 70% with increase in Nb concentration from 0 to 2 at.%. Moreover, the average transmittance of these sol–gel spin-coated films is lower than that of the NTO film prepared by sputtering or PLD technique [32, 33]. This may be because of oxygen deficiency produced during annealing in the films and low crystalline quality of the sol–gel deposited films as compared to that produced by sputtering or PLD. Tauc plot [34] between $(\alpha h\nu)^{1/2}$ and photon energy ($h\nu$) has been plotted to calculate the band gap of NTO films and shown in supplementary Fig. S4. The band gap was obtained as 3.5 eV for pristine TiO_2 film from the intersection of fitted line with abscissa and exhibited a decrease to 3.43 and 3.22 eV for 1.0 at.% Nb and 2.0 at.% Nb-doped TiO_2 films, respectively. Decrease in transmittance of the NTO films with increasing metal doping is primarily due to creation of the scattering centers by Nb atoms [35]. The decreasing surface roughness with Nb content may lead to increase in reflection, resulting in degradation of transmittance properties.

Electrical analysis

Figure 10 shows room temperature electrical properties of the NTO thin films annealed at 550 °C. The resistivity of thin films was measured by the Van der Pauw method [36] using semiconductor device analyzer (Agilent B1500A) applied to 10 × 10 mm^2 samples. A plot of resistivity at room temperature versus Nb concentration shows decrease in resistivity with increasing Nb content. Nb doping led to a decrease in resistivity from 171.2 Ω cm for 0.2 at.% to 3.6 Ω cm for 2 at.% Nb. The minimum resistivity was approximately 3.6 Ω cm, which is comparable to the

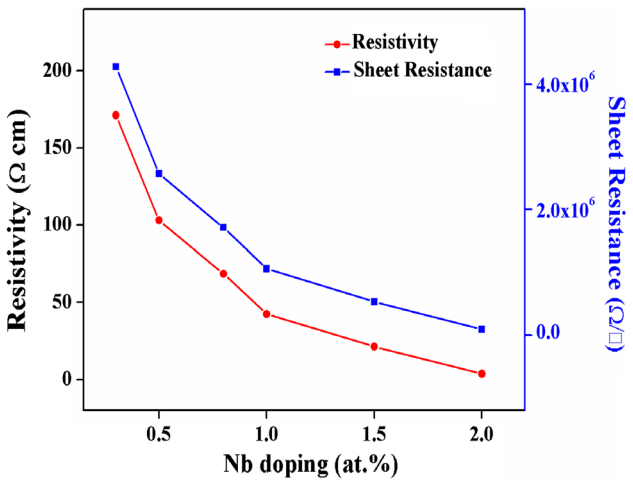

Figure 10 Electrical resistivity and sheet resistance of NTO thin films annealed at 550 °C.

Table 3 Optical transmittance, band gap, resistivity and sheet resistance of pure TiO_2 and NTO films with different Nb concentration

S. no.	Nb concentration (at.%)	Transmittance (%)	Band gap (eV)	Resistivity (Ω cm)	Sheet resistance (MΩ/□)
1	0	85	3.5	–	–
2	0.3	82	3.49	171.168	8.558
3	0.5	75	3.47	102.928	5.164
4	0.8	78	3.45	68.589	3.429
5	1.0	77	3.43	42.465	2.123
6	1.5	74	3.36	21.376	1.068
7	2.0	72	3.22	3.652	0.182

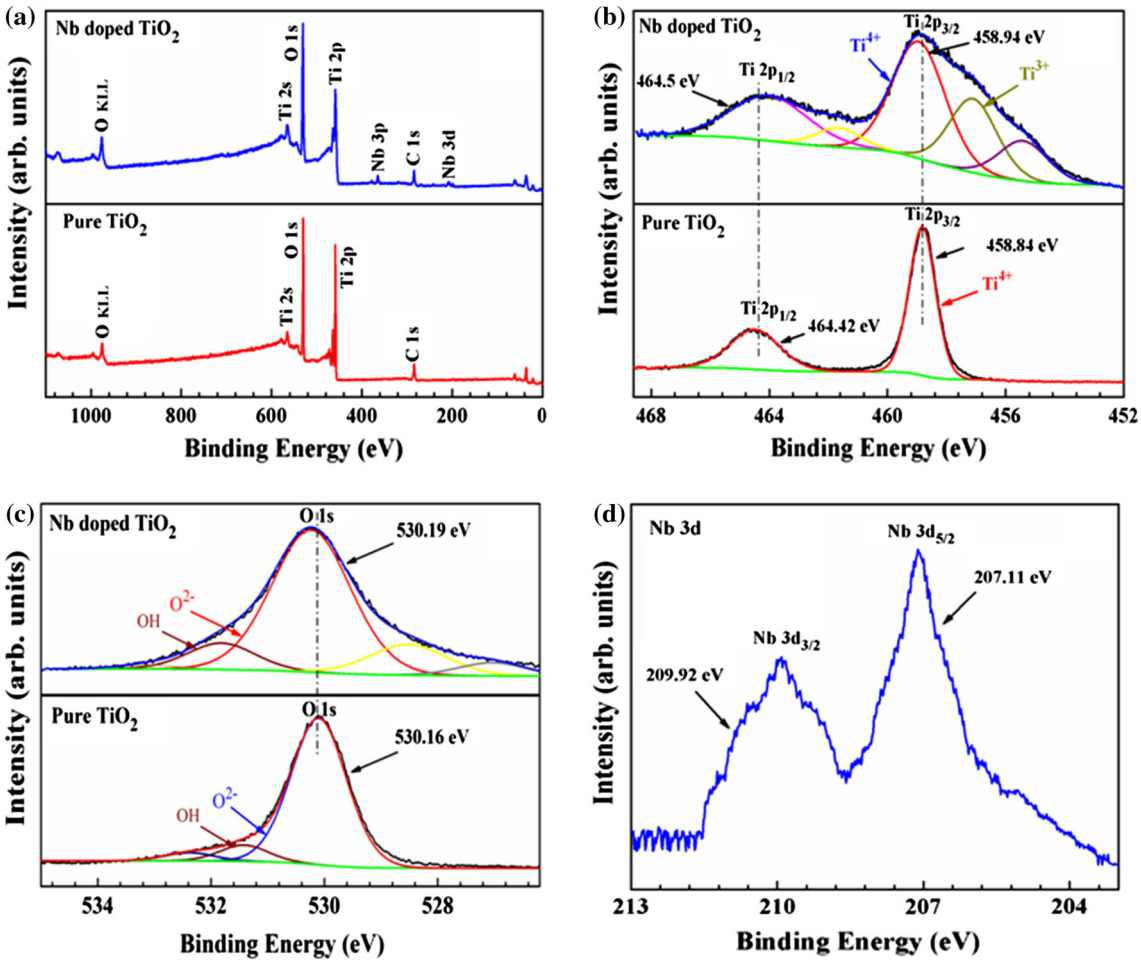

Figure 11 XPS spectra of pure TiO_2 and NTO (2 at.% Nb) films **a** survey scan, **b** Ti 2*p*, **c** O 1s and **d** Nb 3*d*.

results reported by Liu et al. [37] for sol–gel method and lower than the reported by Zhao et al. [38] for films prepared by same method. Annealing of films reduces resistivity which might be because of the oxygen vacancies introduced during annealing and helpful for Nb ions to contribute electrons to the conduction band of the TiO_2 thin films. Obtained optical transmittance, band gap, resistivity and sheet resistance of pure TiO_2 and NTO films are shown in Table 3.

X-ray photoelectron spectroscopy

The chemical composition of the pristine and doped TiO_2 films was determined using XPS. The typical survey spectra of TiO_2 and NTO (2 at.% Nb) films are

shown in Fig. 11a. The survey spectrum contains the dominant signals of Ti 2*p* and O 1*s* and weak signals of the C 1*s* and niobium (Nb 3*d* and 3*p*). The core-level spectra of Ti 2*p* for pristine and doped films are shown in Fig. 11b. The spectra exhibit binding energy as 458.84 and 464.42 eV for Ti $2p_{3/2}$ and Ti $2p_{1/2}$, respectively. The binding energy difference of Ti $2p_{1/2}$ and Ti $2p_{3/2}$ peaks is 5.6 eV, which is consistent with energy splitting reported for Ti 2*p* [39, 40]. Meanwhile, for NTO these peaks are shifted to 458.94 and 464.5 eV positions, which is because of substitution by Nb^{5+} in TiO_2 lattice and the existence of Nb–O–Ti bond formation [14]. The intensity of Ti $2p_{3/2}$ peak in doped film decreased slightly, and doping causes a low-energy shoulder on Ti $2p_{3/2}$ peak, which can be interpreted as due to Ti^{3+} peak at 457 eV [41]. Defects were created due to Nb doping in form of oxygen vacancies confirmed by the presence of Ti^{3+} state in XPS spectra. The existence of Ti^{3+} state causes band gap reduction validated by Tauc plot shown in supplementary Fig. S4, which results decrement in electrical resistivity.

The core-level spectra of O 1*s* for both films are shown in Fig. 11c. The high intensity peak at 530.16 eV is characteristic of metallic oxide, which is in good agreement with binding energy of O 1*s* for TiO_2 [42]. Another peak at 531.4 eV may be assigned to oxidized hydrocarbon [43], and peak positioned at 532.6 eV is assigned to hydroxyl group (Ti–OH) present on the TiO_2 film surface. The OH group belongs to hydroxyl group formed during sol–gel preparation of films [14]. Figure 11d shows the core-level spectra of Nb 3*d* for the doped film. The binding energies of 207.11 and 209.92 eV are assigned to $3d_{5/2}$ and $3d_{3/2}$ of Nb^{5+}, respectively, which contain a spin–orbit splitting of 2.8 eV. The result indicates that the oxidation state of Nb in NTO film is mainly 5+ [13]. The Nb concentration (~1.8 at.%) in doped film determined through XPS is nearly equal to our experimental value and is also in agreement with the EDS result.

Conclusion

NTO thin films were fabricated on corning glass substrates with varying Nb content (0–2 at.%) using sol–gel spin coating method. Annealing of as-deposited amorphous films at 550 °C in air led to good crystallinity and increase in electrical conduction. The average particle size calculated using Debye-Scherrer formula came out to be 15 nm. The resistivity decreased with increase in Nb, and minimum resistivity of 3.56 Ω cm was observed at 2 at.% Nb. The films exhibited good transparency, 70–85% in the visible range. The films were smooth having very small value of roughness and became smoother greater Nb content. XPS analysis showed appearance of Ti^{3+} peak at 457 eV in doped films, leading to band gap narrowing and decrement in electrical resistivity. HRTEM investigations confirmed the high crystallinity of TiO_2 and elemental mapping exhibit the presence of Nb in NTO films. It can be concluded that such low-cost sol–gel deposited NTO thin films have a good scope to be used for TCO applications.

Acknowledgements

This work was supported by the Department of Physics, MNIT Jaipur. The authors are grateful to Materials Research Centre, MNIT Jaipur, for various fabrication and characterization facilities.

Electronic supplementary material: The online version of this article (doi:10.1007/s10853-017-1328-7) contains supplementary material, which is available to authorized users.

References

[1] Chopra KL, Major S, Pandya DK (1983) Transparent conductors—a status review. Thin Solid Films 102:1–46. doi:10.1016/0040-6090(83)90256-0

[2] Minami T (2008) Present status of transparent conducting oxide thin-film development for indium–tin-oxide (ITO) substitutes. Thin Solid Films 516:5822–5828. doi:10.1016/j.tsf.2007.10.063

[3] Ellmer K (2012) Past achievements and future challenges in the development of optically transparent electrodes. Nat Photonics 6:808–816. doi:10.1038/nphoton.2012.282

[4] Exarhos GJ, Zhou X-D (2007) Discovery-based design of transparent conducting oxide films. Thin Solid Films 515:7025–7052. doi:10.1016/j.tsf.2007.03.014

[5] Guillén C, Herrero J (2011) TCO/metal/TCO structures for energy and flexible electronics. Thin Solid Films 520:1–17. doi:10.1016/j.tsf.2011.06.091

[6] Sharma V, Vyas R, Bazylewski P et al (2016) Probing the highly transparent and conducting SnO_x/Au/SnO_x structure for futuristic TCO applications. RSC Adv 6:29135–29141. doi:10.1039/C5RA24422F

[7] Sharma V, Singh S, Asokan K, Sachdev K (2016) A study on 100 MeV O^{7+} irradiated SnO_2/Ag/SnO_2 multilayer as transparent electrode for flat panel display application. Nuclear Inst Methods Phys Res B. doi:10.1016/j.nimb.2016.04.059

[8] Duta M, Simeonov S, Teodorescu V et al (2016) Structural and electrical properties of Nb doped TiO_2 films prepared by the sol–gel layer-by-layer technique. Mater Res Bull 74:15–20. doi:10.1016/j.materresbull.2015.10.009

[9] Kasai J, Hitosugi T, Moriyama M et al (2010) Properties of TiO_2-based transparent conducting oxide thin films on GaN(0001) surfaces. J Appl Phys. doi:10.1063/1.3326943

[10] Hung KH, Lee PW, Hsu WC et al (2011) Transparent conducting oxide films of heavily Nb-doped titania by reactive co-sputtering. J Alloys Compd 509:10190–10194. doi:10.1016/j.jallcom.2011.08.020

[11] Fallah M, Zamani-Meymian M-R, Rahimi R, Rabbani M (2014) Effect of annealing treatment on electrical and optical properties of Nb doped TiO_2 thin films as a TCO prepared by sol–gel spin coating method. Appl Surf Sci 316:456–462. doi:10.1016/j.apsusc.2014.08.029

[12] Lee JK, Jung HS, Valdez JA et al (2006) Room temperature ferromagnetism of Co doped TiO_2 using ion implantation and defect engineering. Nucl Instrum Methods Phys Res Sect B 250:279–282. doi:10.1016/j.nimb.2006.04.171

[13] Su H, Huang YT, Chang YH et al (2015) The synthesis of Nb-doped TiO_2 nanoparticles for improved-performance dye sensitized solar cells. Electrochim Acta 182:230–237. doi:10.1016/j.electacta.2015.09.072

[14] Uyanga E, Gibaud A, Daniel P et al (2014) Structural and vibrational investigations of Nb-doped TiO_2 thin films. Mater Res Bull 60:222–231. doi:10.1016/j.materresbull.2014.08.035

[15] Zhang WF, He YL, Zhang MS et al (2000) Raman scattering study on anatase TiO_2 nanocrystals. J Phys D Appl Phys 33:912–916. doi:10.1088/0022-3727/33/8/305

[16] De Trizio L, Buonsanti R, Schimpf AM et al (2013) Nb-doped colloidal TiO_2 nanocrystals with tunable infrared absorption. Chem Mater 25:3383–3390. doi:10.1021/cm402396c

[17] Parker JC, Siegel RW (1990) Raman microprobe study of nanophase TiO_2 and oxidation-induced spectral changes. J Mater Res 5:1246–1252. doi:10.1557/JMR.1990.1246

[18] Parker JC, Siegel RW (1990) Calibration of the Raman spectrum to the oxygen stoichiometry of nanophase TiO_2. Appl Phys Lett 57:943–945. doi:10.1063/1.104274

[19] Mazzolini P, Russo V, Casari CS et al (2016) Vibrational–electrical properties relationship in donor-doped TiO_2 by Raman spectroscopy. J Phys Chem C 120:18878–18886. doi:10.1021/acs.jpcc.6b05282

[20] Yang J, Zhang X, Wang C et al (2012) Solar photocatalytic activities of porous Nb-doped TiO_2 microspheres prepared by ultrasonic spray pyrolysis. Solid State Sci 14:139–144. doi:10.1016/j.solidstatesciences.2011.11.010

[21] Yang M, Hume C, Lee S et al (2010) Correlation between photocatalytic efficacy and electronic band structure in hydrothermally grown TiO_2 nanoparticles. J Phys Chem C 114:15292–15297. doi:10.1021/jp103764n

[22] Perumal S, Sambandam GC, Prabu MK, Ananthakumar S (2014) Synthesis and characterization studies of nano TiO_2 prepared via sol–gel method. Int J Res Eng Technol 3:651–657

[23] Battiston G, Gerbasi R, Porchia M (1994) Influence of substrate on structural properties of TiO_2 thin films obtained via MOCVD. Thin Solid Films 239:186–191

[24] Sambandam CG, Mohamed AP (2014) Synthesis and characterization studies of solvothermally synthesized undoped and ag-doped TiO_2 nanoparticles using toluene as a solvent. J Eng Res Appl 4:184–187

[25] Al-taweel SS, Saud HR (2016) New route for synthesis of pure anatase TiO_2 nanoparticles via utrasound-assisted sol–gel method $D = \beta \cos \theta$. J Chem Pharm Res 8(2):620–626

[26] Nikolay T, Larina L, Shevaleevskiy O, Ahn BT (2011) Electronic structure study of lightly Nb-doped TiO_2 electrode for dye-sensitized solar cells. Energy Environ Sci 4:1480. doi:10.1039/c0ee00678e

[27] Gan L, Wu C, Tan Y et al (2014) Oxygen sensing performance of Nb-doped TiO_2 thin film with porous structure. J Alloys Compd 585:729–733. doi:10.1016/j.jallcom.2013.09.161

[28] Singh S, Sharma V, Sachdev K (2016) Investigation of post annealing effects on Nb:TiO_2 transparent conducting thin films. Adv Sci Lett 22:3773–3776

[29] Wang M, Gao Y, Chen Z et al (2013) Transparent and conductive W-doped SnO_2 thin films fabricated by an aqueous solution process. Thin Solid Films 544:419–426. doi:10.1016/j.tsf.2013.02.088

[30] Wang Y, Smarsly BM, Djerdj I (2010) Niobium doped TiO_2 with mesoporosity and its application for lithium insertion. Chem Mater 22:6624–6631. doi:10.1021/cm1020977

[31] Sibu CP, Kumar SR, Mukundan P, Warrier KGK (2002) Structural modifications and associated properties of lanthanum oxide doped sol–gel nanosized titanium oxide. Chem Mater 14:2876–2881. doi:10.1021/cm010966p

[32] Potlog T, Dumitriu P, Dobromir M et al (2015) Nb-doped TiO_2 thin films for photovoltaic applications. Mater Des 85:558–563. doi:10.1016/j.matdes.2015.07.034

[33] Wang C, Li J, Dho J (2014) Post-deposition annealing effects on the transparent conducting properties of anatase Nb:TiO_2 films on glass substrates. Mater Sci Eng B Solid-State Mater Adv Technol 182:1–5. doi:10.1016/j.mseb.2013.11.021

[34] Tauc J (1974) Optical properties of amorphous semiconductors. Amorph Liq Semicond. doi:10.1007/978-1-4615-8705-7_4

[35] Chen M, Pei ZL, Wang X et al (2000) Intrinsic limit of electrical properties. J Phys D Appl Phys 33:2538–2548

[36] van der Pauw LJ (1958) A method of measuring the resistivity and Hall coefficient on lamellae of arbitrary shape. Philips Tech Rev 20:220–224

[37] Liu J, Zhao X, Duan L et al (2011) Influence of annealing process on conductive properties of Nb-doped TiO_2 polycrystalline films prepared by sol–gel method. Appl Surf Sci 257:10156–10160. doi:10.1016/j.apsusc.2011.07.009

[38] Zhao L, Zhao X, Liu J et al (2010) Fabrications of Nb-doped TiO_2 (TNO) transparent conductive oxide polycrystalline films on glass substrates by sol–gel method. J Sol–Gel Sci Technol 53:475–479. doi:10.1007/s10971-009-2102-3

[39] Rao CNR, Sarma DD, Vasudevan S, Hegde MS (1979) Study of transition metal oxides by photoelectron spectroscopy. Proc R Soc A Math Phys Eng Sci 367:239–252. doi:10.1098/rspa.1979.0085

[40] Sanjinés R, Tang H, Berger H et al (1994) Electronic structure of anatase TiO_2 oxide. J Appl Phys 75:2945–2951. doi:10.1063/1.356190

[41] Berko A, Ulrych I, Prince KC (1998) Encapsulation of Rh nanoparticles supported on TiO_2(110)-(1x1) surface: XPS and STM studies. J Phys Chem B 102:3379–3386. doi:10.1021/jp973255g

[42] Song Z, Hrbek J, Osgood R (2005) Formation of TiO_2 nanoparticles by reactive-layer-assisted deposition and characterization by XPS and STM. Nano Lett 5:1327–1332. doi:10.1021/nl0505703

[43] Atashbar MZ, Sun HT, Gong B et al (1998) XPS study of Nb-doped oxygen sensing TiO_2 thin films prepared by sol–gel method. Thin Solid Films 326:238–244

Materials Science in Semiconductor Processing 75 (2018) 18–25

Contents lists available at ScienceDirect

Materials Science in Semiconductor Processing

journal homepage: www.elsevier.com/locate/mssp

Influence of 100 keV Ar^+ implantation on electrical and optical properties of $TiO_2/Ag/TiO_2$ multilayer films

Satyavir Singh[a], Vikas Sharma[a,*], Dinesh Saini[a], Surbhi Shekhawat[a], K. Asokan[c], Kanupriya Sachdev[a,b]

[a] Department of Physics, Malaviya National Institute of Technology, Jaipur 302017, India
[b] Materials Research Centre, Malaviya National Institute of Technology, Jaipur 302017, India
[c] Inter-University Accelerator Centre, Aruna Asaf Ali Road, New Delhi 110067, India

ARTICLE INFO

Keywords:
Transparent conducting oxide
Implantation
Multilayer films
Hall measurement
Transmittance

ABSTRACT

The objective of this study was to investigate the effect of 100 keV Ar^+ ion implantation with fluence ranging from 1×10^{14} to 1×10^{16} ions/cm^2 on structural, electrical and optical properties of $TiO_2/Ag/TiO_2$ films. The $TiO_2/Ag/TiO_2$ multilayer films with a total thickness of 100 nm were prepared by sputtering at room temperature on glass and silicon substrates. The structural properties studied via X-ray diffraction showed amorphous nature of TiO_2 and a peak centred at 38.15° assigned to Ag (111) diffraction plane. Morphological analysis carried by field emission scanning electron microscopy and atomic force microscopy exhibit uniform deposition of films. A decrease in surface roughness was observed from 1.71 to 0.87 nm with increase in ion fluence from 0 to 1×10^{16} ions/cm^2. Measured resistivity of the pristine film was 2.04×10^{-4} Ω cm, which minimized to 9.14×10^{-5} Ω cm at the highest fluence of 1×10^{16} ions/cm^2. The transmittance decreases from 80% to 73% for higher fluences. Changes in electrical resistivity and transmittance can be attributed to the structural changes in the samples due to amorphization, defect creation and doping on ion implantation. Carrier concentration, mobility of charge carriers and sheet resistance for pristine and implanted films have been calculated as a function of ion fluence. X-ray photoelectron spectroscopy data revealed creation of Ti ions (Ti^{3+}) after Ar^+ ion implantation. The core level spectrum of O 1s was also studied and presence of some OH species is found on the surface. Optical and transport properties of implanted TAT films are comparable to that of indium tin oxide (ITO) and make them a good choice for the current and future transparent conducting electrode (TCE) applications.

1. Introduction

A need for the development of efficient transparent conducting oxides (TCOs) comes from a large variety of applications in the field of optoelectronics including newly emerging devices like dye-sensitized solar cells and organic light-emitting diodes [1,2]. In literature, the terms transparent conducting oxide (TCO) and transparent conducting electrode (TCE) are used interchangeably. In general, the TCO refers the materials and their films in devices are known as TCE. TCO is electrically conductive and optically transparent material to be used in solar cell, light emitting diode, flat panel display application etc. [3,4]. Popular metal doped TCOs are tin-doped indium oxide (ITO), Nb doped TiO_2 [5], fluorine doped tin oxide [6] and Al doped ZnO [7]. ITO is most widely used due to its excellent combination of electrical conductivity and optical transmittance, but scarcity of this material reflects in its high and fluctuating cost. Recently, oxide/metal/oxide sandwich structure has emerged as an alternative to ITO showing low resistivity and high transmittance. Multilayers of ZnO/Ag/ZnO [8], $SnO_2/Ag/SnO_2$ [9], $SnO_x/Au/SnO_x$ [10] and $TiO_2/Ag/TiO_2$ (TAT) [11] have been actively investigated in recent years. Ag (< 20 nm thick) [12] is chosen as inter layer because it exhibits low resistance and high transmittance in the visible region. TiO_2 is a technologically important material due to its wide band gap (~ 3.5 eV), high transmittance, high refractive index combined with good mechanical and thermal stability. Jia et al. [13] investigated the effect of oxide and Ag layer thickness variation on the performance of the $TiO_2/Ag/TiO_2$ multilayer films and concluded that the optimum thickness of Ag layer is ~ 8 nm and gave lowest sheet resistance 30 Ω/□. Kim et al. [14] studied the effect of oxide layer thickness variation on the electrical and optical properties and it was seen that the optimized $TiO_2/Ag/TiO_2$ (40 nm/18.8 nm/40 nm) structure gave best results. The carrier concentration decreased from 2.2×10^{22} to 6.1×10^{21} cm^{-3} with increasing TiO_2 thickness and all samples showed sheet resistances of 3.9–4.4 Ω/□.

In ion implantation process, one can implant specific ions in host

* Corresponding author.
E-mail addresses: phyvikas@gmail.com, ksachdev.phy@mnit.ac.in (V. Sharma).

https://doi.org/10.1016/j.mssp.2017.11.016
Received 1 September 2017; Received in revised form 9 November 2017; Accepted 11 November 2017

material at desired depth by selecting suitable energy. The range of ions depends on the ion species, mass and energy and the target material composition. Depending upon these parameters, the mechanism of modification of the physical and chemical properties of solids differs. Generally, the interest of implantation is to engineer the structural and electrical properties of the materials by choosing the proper ions [15]. Out of the many techniques used for modifying the basic properties of the materials; ion implantation has been found to effective and useful for defect production and impurity doping in materials to tune their properties for desired application [15,16]. Ion implantation or irradiation method influences the lattice structure of metal oxides and also affects the optical properties and electronic structures. Ion beam induced defects in the solids entirely depends on the electronic energy loss (inelastic process) and nuclear energy loss (elastic process), occurred after passing of ions via host material [17]. When ion passes through the material, it losses energy by two distinct processes: elastic collision with the nuclei, also called as nuclear energy loss, (S_n) and inelastic collisions of ions with electrons, also referred as electronic energy loss (S_e). While elastic collisions produces cascade collisions with nuclei before ion gets implanted and comes to rest, inelastic collisions results in interaction of ion with electrons and inducing excitation of target atoms and energy of electrons transmitted to lattice via electron-phonon interaction. These S_n and S_e vary from few eV/nm to some keV/nm and depend on energy, species and mass of ion. It is observed that S_n dominates at low energies and S_e at high energies. In our experiment the energy of implanted ion is 100 keV which is low energy; hence nuclear energy loss is higher than electronic energy loss.

Ar is the inert gas and it does not make bonds with host material. However, Ar ions are most suitable for creating or annealing the defects mainly in form of oxygen vacancies that are responsible for modifying the electrical and optical properties. A few reports are available on ion implantation in TCE, but our group has been investigating the ion implantation and irradiation effects on the multilayer TCE [9,18,19]. It has been reported that the Ar^+ ion implantation leads to large increase in electrical conductivity [20]. In the present study, sputter deposited TiO_2/Ag/TiO_2 (45 ± 5 nm/9 ± 2 nm/45 ± 5 nm) multilayer structure was implanted by 100 keV Ar^+ ions. The middle layer of Ag (~9 nm thick) forms a continuous layer, required for good electrical conductivity. The pristine and implanted samples were then characterized using X-ray diffraction (XRD), X-ray photoelectron spectroscopy (XPS), field emission scanning electron microscopy (FESEM), atomic force microscopy (AFM), UV–Vis and Hall measurement technique.

2. Experimental details

2.1. Sample preparation

Anatase TiO_2 powder (99.99% purity) from Alfa-Aesar was used to prepare the 2-in. target. Powder was pressed as pallet and then sintered at 1100 °C for 10 h. Commercial target was used to deposit the Ag film. Prior to film deposition TiO_2 and Ag targets were pre-sputtered for 10 min to remove impurities. RF source (100 W) and DC source (16 W) of magnetron sputtering were used for oxide and metal layers respectively. Ar flow of 15 sccm was maintained while deposition. The TiO_2/Ag/TiO_2 (45 ± 5 nm/9 ± 2 nm/45 ± 5 nm) structure was deposited sequentially on pre-cleaned glass substrates at room temperature. The chamber was evacuated to ~ 5×10^{-6} mbar before starting the deposition process. The working pressure for TiO_2 deposition was kept constant at ~ 6×10^{-3} mbar and ~ 1.6×10^{-2} mbar for silver layer. The as-prepared TAT films were implanted with 100 keV Ar^+ ions with fluence range (1×10^{14}–1×10^{16} ions/cm^2) at room temperature using the low energy ion beam facility at Inter-University Accelerator Centre (IUAC), New Delhi, India. The Ar^+ implanted TAT multilayer films at 1×10^{16} ions/cm^2 fluence will be referred hereafter as A-TAT films. The stopping range of Ar^+ ions was ~ 60 nm measured by the SRIM-2010 software, which is less than the total film thickness (100 nm). The nuclear energy loss (S_n) and electronic energy loss (S_e) as a function of penetration depth have been calculated and shown in supplementary Fig. S1.

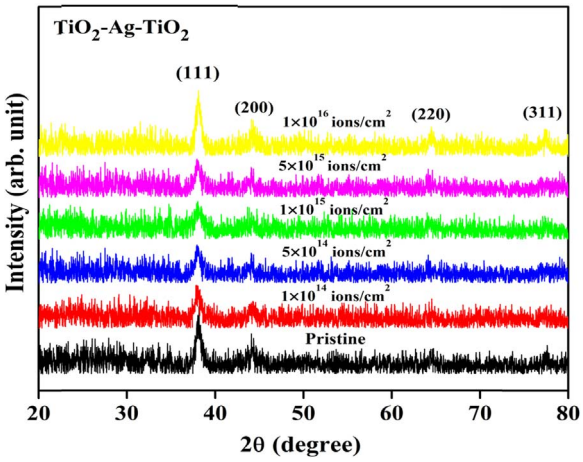

Fig. 1. XRD pattern of pristine and Ar implanted TiO_2/Ag/TiO_2 multilayer films with fluence.

Table 1
FWHM, crystallite size, lattice constants and residual stress of pristine and Ar implanted TAT multilayer films.

Fluence (ion cm^{-2})	FWHM (deg.) with error	Crystallite size (nm) with error	Lattice constant c (Å)	Residual stress (GPa)
0	0.6605 ± 0.03	13.3 ± 0.6	4.093 ± 0.003	− 0.401
1×10^{14}	0.8132 ± 0.07	10.9 ± 0.9	4.096 ± 0.004	− 0.571
5×10^{14}	0.7815 ± 0.05	11.2 ± 0.6	4.098 ± 0.005	− 0.684
1×10^{15}	0.9106 ± 0.04	09.6 ± 0.3	4.088 ± 0.004	− 0.114
5×10^{15}	0.7962 ± 0.06	11.1 ± 0.8	4.090 ± 0.001	− 0.228
1×10^{16}	0.6785 ± 0.03	12.9 ± 0.5	4.091 ± 0.002	− 0.285

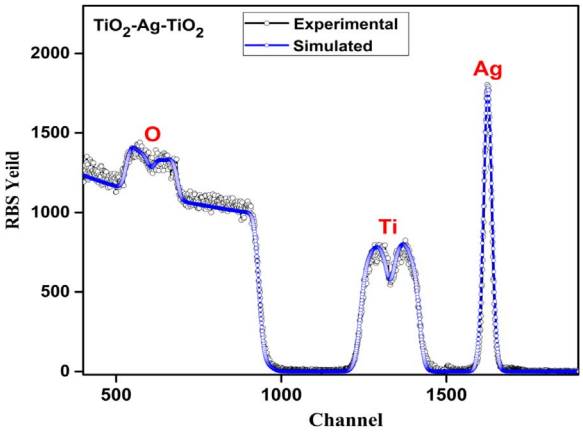

Fig. 2. RBS spectrum of pristine TiO_2/Ag/TiO_2 multilayer film with fitted profile.

2.2. Characterization

X-Ray Diffractometer (Panalytical X-Pert Pro) was used to investigate the constituent phases and the crystal structure. The topography and morphology were measured by Atomic Force Microscopy (Bruker) and Nova Nano FE-SEM) 450 (FEI). Optical transmittance was obtained using LAMBDA 750 (Perkin Elmer) UV–Vis–NIR Spectrophotometer. The electrical parameters were measured by using HMS3000, Ecopia with magnetic field of 0.57 T. Chemical composition was determined from X-ray photoelectron spectroscopy (XPS, Omicron

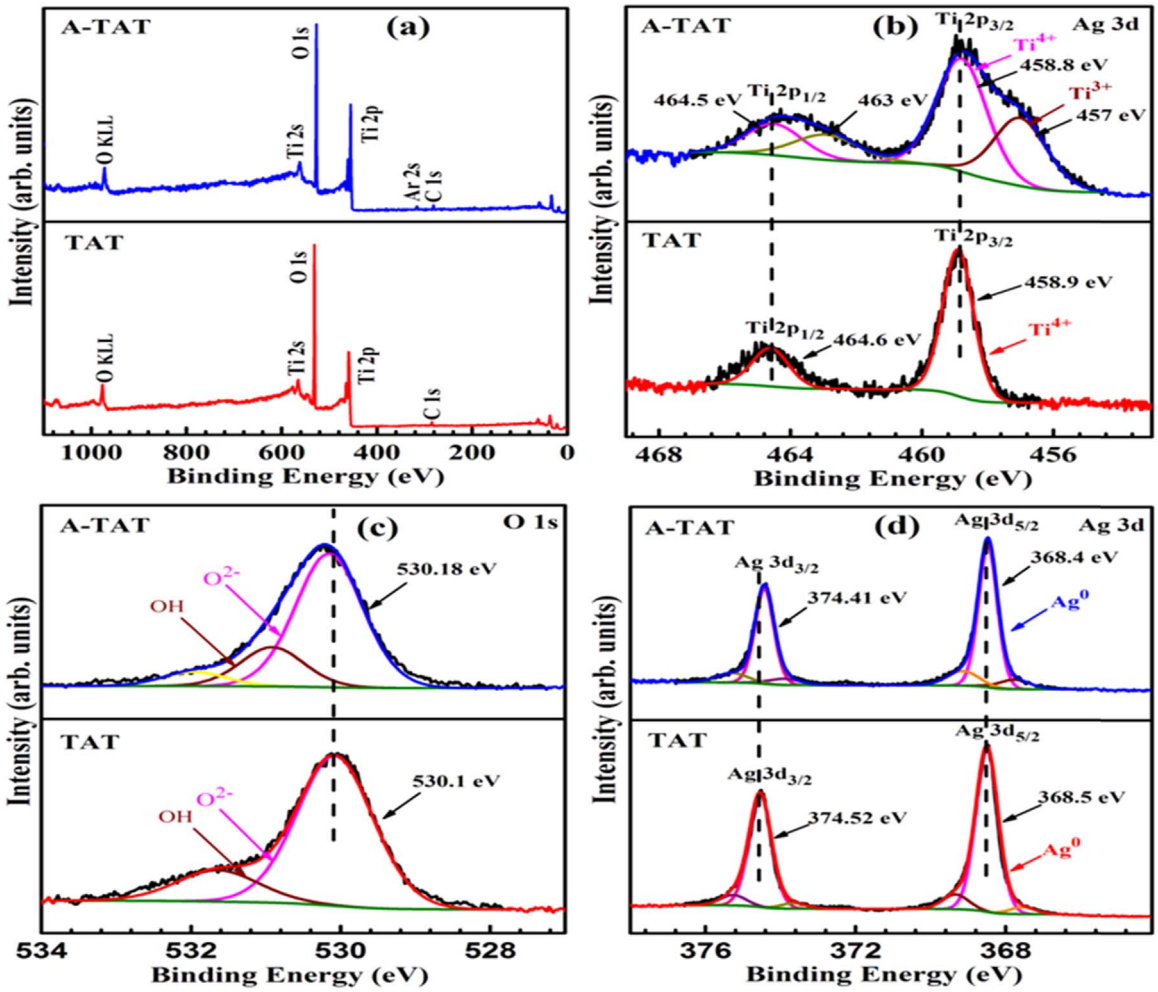

Fig. 3. XPS spectra of pristine and Ar implanted (1×10^{16} ions/cm^2) TiO_2/Ag/TiO_2 multilayer films (a) survey scan, (b) Ti 2p, (c) O 1s and (d) Ag 3d.

ESCA) with monochromatic *Al* K_α (1486.7 eV) source.

3. Results and discussion

3.1. Structural properties

Fig. 1 shows the X-ray diffraction pattern of pristine and implanted TAT films. Peaks in the XRD pattern of pristine and implanted films match well with the JCPDS data (card no. 04-0783). The intensity of Ag (111), (200) and (220) positioned at $2\theta = 38.15^\circ$, 44.3° and 64.6° slightly varies with the fluence. No peak related to anatase TiO_2 was observed as TiO_2 is amorphous due to room temperature deposition. The amorphous structure of metal oxides film makes them suitable for deposition of these films on a flexible plastic substrate [21]. The intensity of the Ag (111) peak for the film implanted with the highest fluence of 1×10^{16} ions/cm^2 exhibits slight increment. The full width at half maximum FWHM (β) of this peak increases to 0.9106° at 1×10^{15} ions/cm^2 as fluence and then decreases to 0.6785° as the fluence increases. The crystallite size calculated using Debye–Scherrer formula decreases from 13.3 to 12.9 nm with increasing fluence. The lattice constant (c) and residual stress were calculated and are shown in Table 1. The negative sign of obtained residual stress represent that stress for the TAT films is compressive. The stress induced by implantation process hinders the growth of crystallites and it can be observed that as the stress increasing the crystallite size is decreasing and vice versa. Reports [22,23] indicate that Ar^+ ions can be used to control stress in the specimen. In our specimen, initial implantation of Ar^+ ions has generated stress which increases with increasing fluence up to 5×10^{14} ions/cm^2. On further increase of fluence, stress decreases. The decrement of stress in the TAT multilayer structure may be assigned to changes in microstructures induced by higher dose of Ar^+ ion implantation. Pieńkos et al. [24] reported that structure changes, reduction of grain boundary voids and amorphization may influence the stress of the film. In present study, stress may also be reduce by reduction of grain boundary voids [25].

3.2. Rutherford Back Scattering

The thickness and stoichiometry of TiO_2/Ag/TiO_2 multilayer structure were measured using Rutherford Back Scattering (RBS). RBS spectrum with SIMNRA-fitted graph of TAT multilayer structure is shown in Fig. 2. The elemental peaks of Ag, Ti and O ions can be seen in the RBS spectra. The thickness of individual layer was calculated using fitted data and found to be TiO_2 (45 ± 5 nm)/Ag (9 ± 1 nm)/TiO_2 (45 ± 5 nm). RBS data confirm the formation of TiO_2 with Ag middle layer, which is consistent with XPS results given in next section. RBS provides the thickness of the film of different layers including Ag the middle layer. Numerous reports [19,26] including our previous study [18] indicates the formation of continuous Ag layer at ~ 9 nm. The FESEM image (supplementary Fig. S2) confirms the formation of continuous Ag middle layer, which indicates that the sputtering deposited Ag layer is smooth and continuous. The electrical measurements of 9 nm thick Ag layer are also supporting the formation of continuous Ag layer.

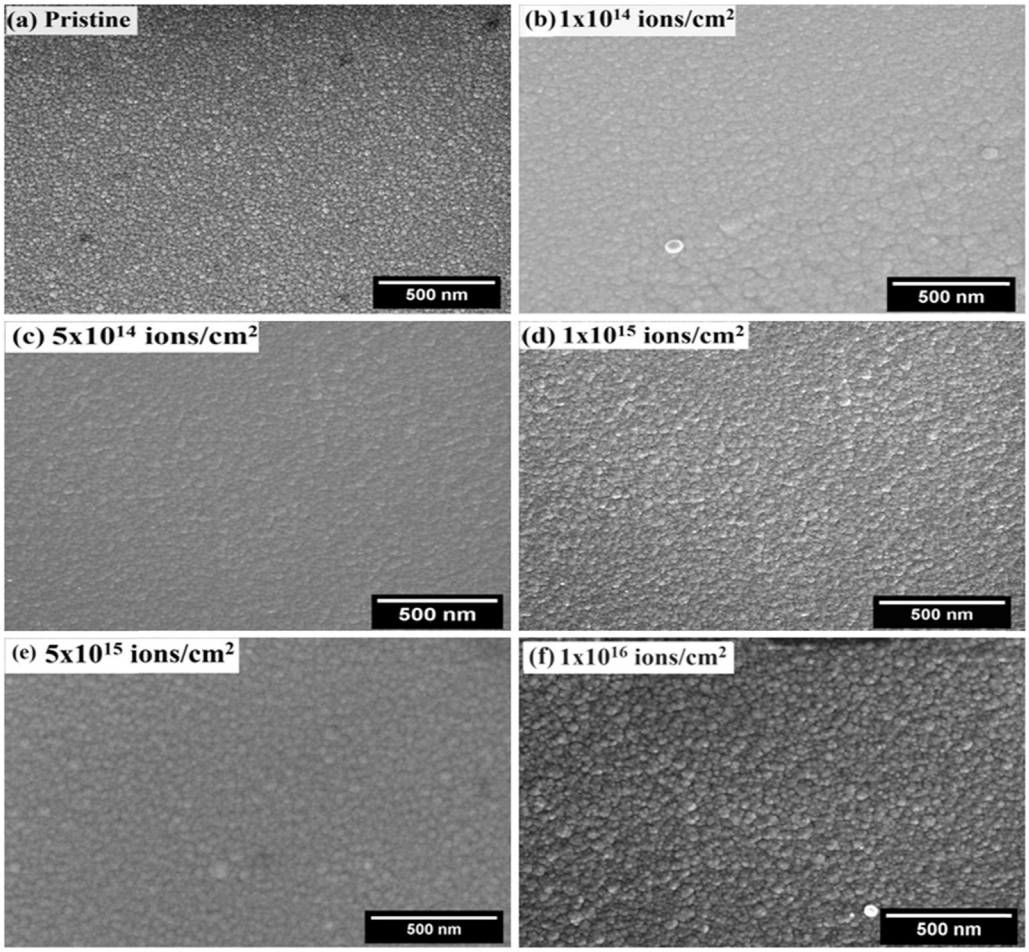

Fig. 4. SEM images of pristine and Ar implanted $TiO_2/Ag/TiO_2$ multilayer films.

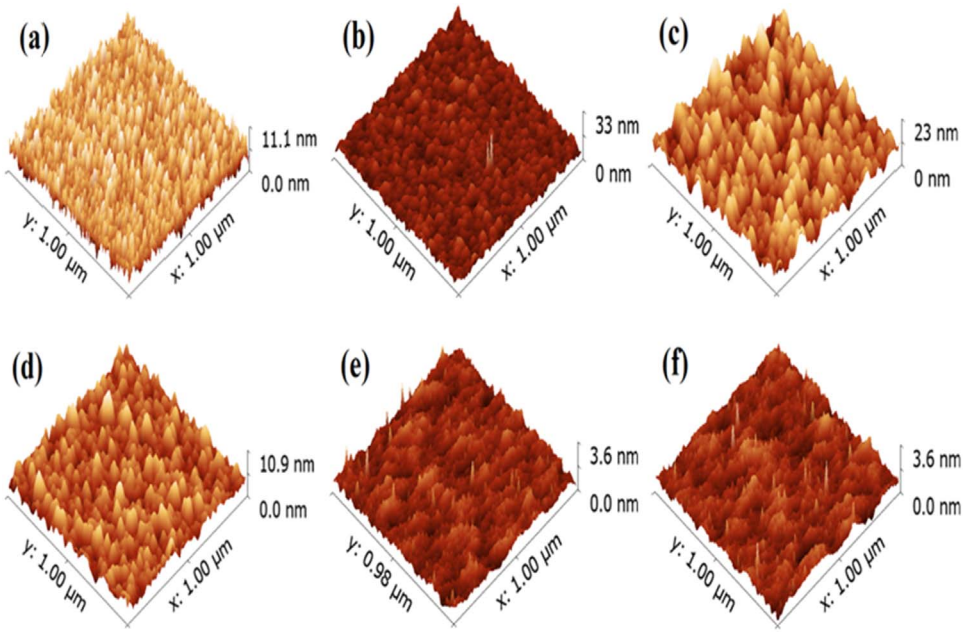

Fig. 5. Three-dimensional AFM images of pristine and Ar implanted $TiO_2/Ag/TiO_2$ multilayer films (a) pristine, (b) 1×10^{14}, (c) 5×10^{14}, (d) 1×10^{15}, (e) 5×10^{15} and 1×10^{16} ions/cm^2.

3.3. X-ray photoelectron spectroscopy

X-ray photoelectron spectroscopy is performed to analyze the chemical compositions of the $TiO_2/Ag/TiO_2$ pristine and Ar^+ implanted (fluence of 1×10^{16} ions/cm^2) (A−TAT) films. Fig. 3 shows the XPS spectra of TAT films. Fig. 3(a) shows that survey scan of TAT and A−TAT films containing dominant signals from Ti and O and weak signals from Ar and C. The low intensity C signal arises because of ex-situ transfer of samples to UHV chamber. Fig. 3(b) shows the Ti 2p core level spectra of top surface of TAT and A−TAT films. The Ti-$2p_{3/2}$ and

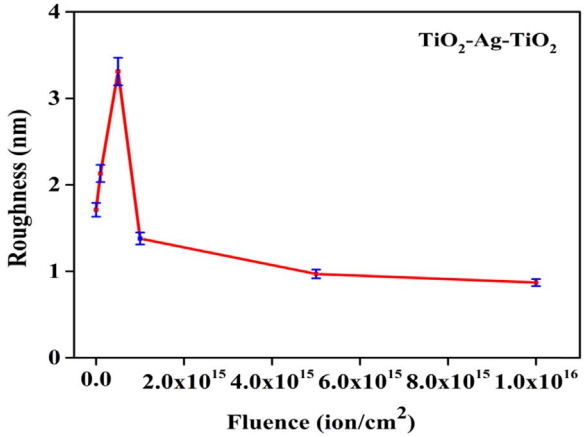

Fig. 6. Average surface roughness of TiO_2/Ag/TiO_2 multilayer films with fluence.

Ti-2$p_{1/2}$ peaks of pristine films appearing at 458.9 and 464.6 eV are assigned to Ti^{4+} oxidation state of TiO_2 and match well with reported data [27]. The binding energy difference between Ti-2$p_{1/2}$ and Ti-2$p_{3/2}$ peak is 5.7 eV which is consistent with +4 oxidation state [28]. Meanwhile, peaks of Ti-2$p_{3/2}$ and Ti-2$p_{1/2}$ for A−TAT sample are positioned at 458.8 and 464.5 eV respectively and a peak corresponding to reduced specie of Ti ion (Ti^{3+}) is created at binding energy of 457 eV on Ar^+ implantation. The appearance of Ti^{3+} has been reported by other researchers also on Ar^+ bombardment [29]. This appearance of Ti^{3+} state leads to band gap decrement that is validated by Tauc plot shown in Fig. 7(b), producing reduced electrical resistivity, giving the highest figure of merit for the A−TAT sample. Hashimoto et al. [30] studied Ar bombardment on the TiO_2 single crystal and reported the Ti^{4+} component appeared for as-received TiO_2. Two additional peaks at 456.6 and 454.4 eV appeared after 30 s and 2 min of sputtering, respectively. The observed peaks at 456.6 and 454.4 eV are assigned to Ti^{3+} and Ti^{2+}, respectively. The reduced species of TiO_2 may be appeared due to recombination of the O and Ti atoms. The recoiled atoms from Ar bombardment process are not able to recombine in accurate coordination of TiO_2.

Fig. 3(c) shows the core level spectra of O 1s for TAT and A-TAT samples. The O 1 s signal of pristine samples appears at 530.1 eV, and after deconvolution, another peak is seen at 531.6 eV which indicates the presence of OH groups on the surface. The O 1s spectrum of A-TAT sample is positioned at 530.18 eV, and the other peak is at 531.1 eV assigned to OH species, present on the surface of sample. The O 1s peak of both TAT and A-TAT samples is at the same position suggesting the nature of oxygen to be similar. Nitrogen doped TiO_2 [31] studies also suggest the similar nature of oxygen 1s, which was also positioned around 530 eV. Liu et al. [32] reported the three components of O 1s of TiO_2 films: first component at 530.6 eV assigned to titanium dioxide; second component at 531.5 ± 0.5 eV may be due to defective oxides or hydroxyl groups and other component at 533 ± 1 eV appeared because of adsorbed water. Fig. 3(d) shows the core spectra of Ag 3d for both samples. Ag signals from the sandwich layer were obtained using the depth profile mode XPS. Ag 3$d_{5/2}$ and Ag 3$d_{3/2}$ peaks appear at binding energies of 368.5 and 374.52 eV showing the presence of metallic Ag^0 as middle layer. After Ar^+ implantation peaks of Ag 3$d_{3/2}$ and Ag 3$d_{5/2}$ appear at 368.4 and 374.41 eV, respectively. A small shift towards lower binding energy is observed which could be due to interaction of Ti and O ions with Ag at the interface [33]. Harifi et al. [34] studied Ag/TiO_2 and found the Ag 3$d_{5/2}$ and Ag 3$d_{3/2}$ peaks at 368.8 eV and 374.8 eV, respectively. There was no peak correspond to Ag_2O (367.8 eV) or AgO (367.4 eV), indicating the presence of metallic silver.

3.4. Surface characterization

TAT pristine and implanted multilayer films were characterized by FESEM for surface morphology and images are shown in Fig. 4. All films were observed at the 100k × magnification. SEM images show growth of spherical shape particles on the top surface. It can be seen that there is no major morphological change on implantation. The particle size has been calculated using surface morphology and found to vary in the range of 20–30 nm. Similar SEM micrographs of TiO_2 surface have been reported by other studies [35]. The RMS surface roughness and average particle size calculated using SEM images are shown in supplementary Table S1.

Surface topography of the TAT pristine and implanted multilayer films as observed by AFM is shown in Fig. 5(a)–(e). The scan area of measurement was taken 1 × 1 μm^2. The average surface roughness of films as a function of fluence is shown in Fig. 6. The pristine film exhibits roughness of 1.71 nm and it becomes 3.31 nm for fluence of 5 × 10^{14} ions/cm^2 and then decreases to 0.87 nm for the highest fluence (1 × 10^{16} ions/cm^2). Surface roughness increment on initial ion implantation is caused by sputtering of surface by energetic Ar^+ ions incident on the sample [36]. High energy ions etch the surface and roughen the surface. Further increasing the fluence leads to the lower roughness which is due to ion implantation induced emission of atoms

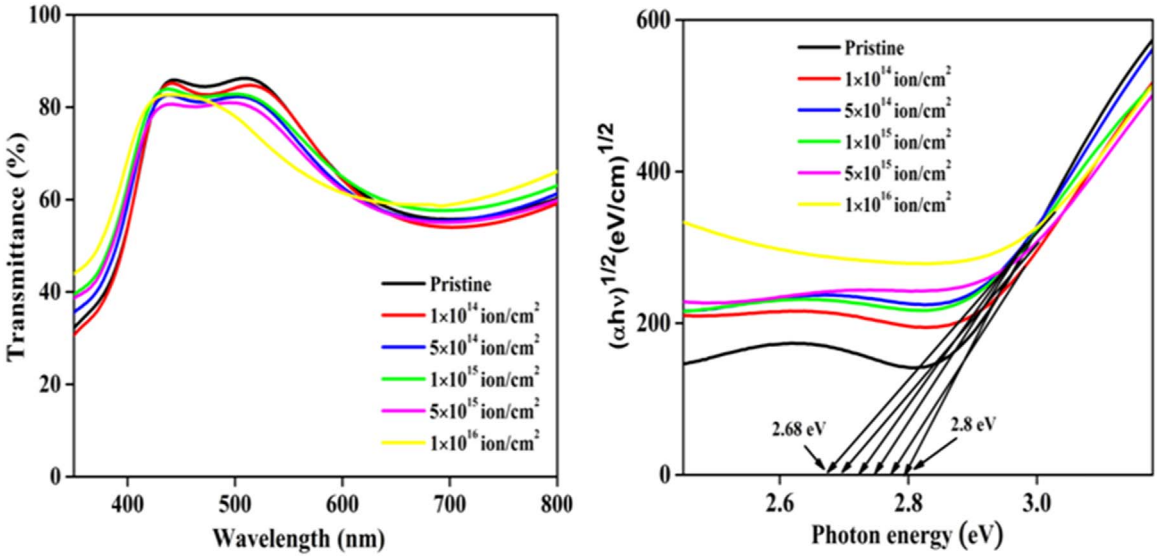

Fig. 7. (a) Transmittance and (b) Tauc plot of pristine and Ar implanted TiO_2/Ag/TiO_2 multilayer films with fluence.

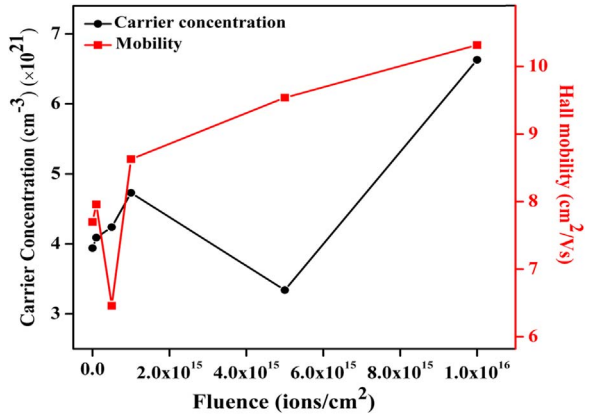

Fig. 8. Carrier concentration and Hall mobility of pristine and Ar ion implanted TiO_2/Ag/TiO_2 multilayer films with fluence.

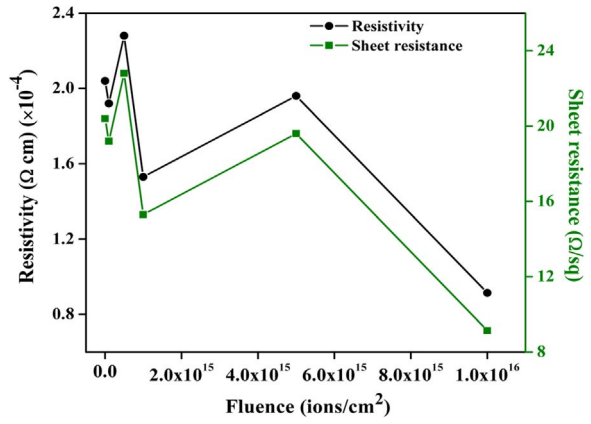

Fig. 9. Resistivity and sheet resistance of pristine and Ar ion implanted TiO_2/Ag/TiO_2 multilayer films with fluence.

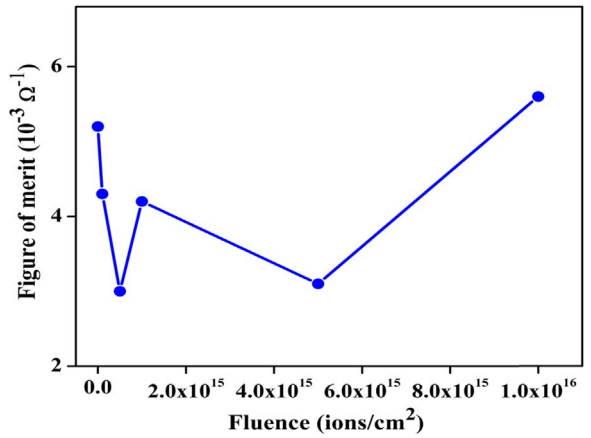

Fig. 10. Haacke FOM (Ψ_{TC}) of pristine and Ar ion implanted TiO_2/Ag/TiO_2 multilayer films with fluence.

from the top surface [19]. The morphology of films exhibits similar shaped grains at different fluences. The peak height of the grains of the top surface as seen through AFM image varies with implantation fluence with no observation of cluster formation. Smooth TAT films with surface roughness of ~ 2 nm which is nearly equal to ITO films (~ 2 to 3 nm) is a good choice as TCEs and makes them suitable for optoelectronic devices.

3.5. Optical analysis

The optical transmittance spectra of TAT multilayer films in the visible region (400 nm < λ < 800 nm) for different ion fluence are shown in Fig. 7(a). Average transmittance of pristine film is observed ~ 80% which reduces to ~ 73% for the highest fluence (1 × 10^{16} ions/cm^2). Transmittance for all samples shows a similar trend. An initial increase in transmittance is seen with increase in wavelength, attaining a maximum at a particular wavelength and then a decrease with further increase in wavelength. Increasing fluence leads to degradation in optical transmittance suggesting creation of defects in the system and removal of oxygen, on Ar^+ implantation. Higher surface roughness of 3.31 nm at 5 × 10^{14} ions/cm^2 fluence, causes more scattering of light and as a result transmittance decreases. Now, further increasing fluence results in lower roughness and scattering of light decreases but reflection increases due to smooth top surface and it may degrade the transmittance. The film becomes oxygen deficient, which is also confirmed by XPS analysis seen by appearance of Ti^{3+} state (reduced species of Ti ions). The absorbance and reflectance spectra of pristine and Ar implanted TAT films are shown in supplementary Figs. S3 and S4 respectively. The absorption of visible light depends upon the oxygen vacancies and could increase by the presence of oxygen vacancies in the system. The optical transition in visible region (400 nm < λ < 800 nm) is because of electronic transition from valence band to localized mid-gap states and then to conduction band edge. The removal of oxygen from the system leads to increase the Ti/O ratio or more metallic content in the metal oxide layer which would absorb more light and consequently transmittance decreases. The XPS study also supports the reduction of band gap (i.e more absorption) by showing the reduced species of Ti (Ti^{3+}).

The optical band gap of samples was estimated using the standard formula [37].

$$\alpha h\nu = B(h\nu - E_g)^n \quad (1)$$

where α is absorption coefficient, $h\nu$ the photon energy, B is a constant and E_g is optical band gap. Here the value of n is 2, because TiO_2 is indirect band gap material.

Absorption coefficient (α) was estimated using the Beer–Lambert's expression [38].

$$\alpha = \frac{2.303}{d}A \quad (2)$$

where d is total thickness of the multilayer film and A is absorbance of TAT films. Optical band gap of TAT films was calculated using Tauc plot between $(\alpha h\nu)^{1/2}$ and photon energy ($h\nu$) and shown in Fig. 7(b). Pristine film exhibits band gap of 2.8 ± 0.01 eV and it decreases to 2.68 ± 0.01 eV for the 1 × 10^{16} ions/cm^2 fluence. Band gap reduction for the highest fluence sample is supported by XPS results by showing creation of Ti^{3+} state at lower binding energy [39]. The average surface roughness, transmittance, band gap extinction coefficient and refractive index have been calculated for pristine and implanted TAT films and are shown in supplementary Table S2.

3.6. Electrical analysis

Fig. 8 shows the variation of Hall mobility and carrier concentration of TAT multilayer films with varying ion fluences. The carrier concentration of pristine TAT film is 3.94 × 10^{21} cm^{-3}, which increases to 6.63 × 10^{21} cm^{-3} with ion fluence. Simultaneously, Hall mobility increases from 7.8 to 10.32 cm^2/V-s with increasing fluence. Fig. 9 shows the variation of electrical resistivity and sheet resistance of the TAT films with fluence. Pristine film exhibits electrical resistivity of 2.04 × 10^{-4} Ω cm and it decreases to 9.14 × 10^{-5} Ω cm for the highest fluence (1 × 10^{16} ions/cm^2). Meanwhile, sheet resistance varied from 20.4 Ω/□ to 9.14 Ω/□ with increase in fluence. The reduction in electrical resistivity is mainly due to enhancement in carrier mobility

Table 2
Carrier concentration, mobility, resistivity, sheet resistance, transmittance and Haacke figure of merit (FOM) of pristine and implanted TAT multilayer films as a function of fluence.

Ion fluence (cm^{-2})	Carrier concentration (cm^{-3})	Mobility (cm^2/V-s)	Resistivity (Ω cm)	Sheet resistance (Ω/□)	Transmittance (%) at 530 nm	Haacke FOM ($10^{-3}\,\Omega^{-1}$)
0	3.94×10^{21}	7.77	2.04×10^{-4}	20.4	83	5.2
1×10^{14}	4.09×10^{21}	7.96	1.92×10^{-4}	19.2	81	4.3
5×10^{14}	4.24×10^{21}	6.46	2.28×10^{-4}	22.8	79	3.0
1×10^{15}	4.73×10^{21}	8.63	1.53×10^{-4}	15.3	80	4.2
5×10^{15}	3.34×10^{21}	9.54	1.96×10^{-4}	19.6	77	3.1
1×10^{16}	6.63×10^{21}	10.32	9.14×10^{-5}	9.14	74	5.6

from 7.8 to 10.32 cm^2/V-s, caused by decreasing grain boundary effects which were acting as scattering centres [40,41]. It has been reported that oxygen vacancies generated through implantation increase the electrical conductivity of TiO_2 by many fold [20,42]. Moreover, defects created by noble gas implantation results in enhancement of the electrical conductivity. The band gap is narrowing with increasing ion fluence which is responsible for the better conductivity of the specimens. The variation in electrical resistivity can be explained by the following expression:

$$\rho = \frac{1}{n_e \mu e} \tag{3}$$

where ρ is resistivity, n_e is carrier concentration, μ is the mobility, and e is charge on the carrier.

The slight variation in resistivity at lower fluence is due to small variation in carrier concentartion and mobilty values but significant change in resistivity at highest fluence is mainly dominated by considerable increase in carrier concentartion and mobilty values. A continuous film of silver is essential for good electrical conduction [43]. The electrical resistivity and sheet resistance of this study suggest the formation of continuous Ag inter layer. The figure of merit (FOM) is a important parameter to define the performance of any TCE. Haacke [44] figure of merit (Ψ_{TC}) has been calculated using following formula:

$$\Psi_{TC} = \frac{{T_{av}}^{10}}{R_s} \tag{4}$$

where R_s is the sheet resistance and T_{av} is average transmittance.

Fig. 10 shows the FOM (Ψ_{TC}) for the TAT pristine and implanted films. Figure of merit measured for the pristine film is $5.2 \times 10^{-3}\,\Omega^{-1}$. This changes with fluence due to variation in the charge carriers and mobility and shows a maximum value of $5.6 \times 10^{-3}\,\Omega^{-1}$ at fluence of 1×10^{16} ions/cm^2. This change was observed because of variation in sheet resistance and transmittance with the fluence. The present figure of merit indicates acceptability of TAT films to be used as a transparent conductive electrode. The electronic and nuclear energy losses produced after Ar implantation in TAT films, measured by SRIM-2010 software and shown in supplementary Fig. S1. It can be observed that nuclear energy loss is higher than electronic energy loss. The carrier concentration, mobility, resistivity, sheet resistance, transmittance and Haacke figure of merit (FOM) have been calculated for TAT pristine and implanted films are shown in Table 2.

Our recent investigation on the effect of N ion implantation in TAT multilayer films [18] demonstrated that N ions replace the O sites in TiO_2 lattice and add new electronic states just above the valence band and narrowing the band gap. This consequently increases the electrical conductivity but decreases the optical transmittance. In the present study, it is observed that Ar^+ ion implantation increases the electrical conductivity significantly with reduction in transmittance. The Ar^+ ion implantation causes enhancement of mobility due to reduction in the grain boundary effects and the electrical conductivity increases due to this and annealing of oxygen vacancies on implantation. While, the N^+ ion implantation in TiO_2 gives the maximum carrier mobility of 9.2 cm^2/V-s, in the case of Ar^+ implantation it is 10.32 cm^2/V-s. The optical transmittance at 1×10^{16} ions/cm^2 fluence, increases from 70% (for N^+ ion) to 73% for Ar^+ implantation. Based on the XPS studies, it is also evident that implanting N results in occupation of O site and modifies the electronic structure [39]. On the other hand implanting Ar ions affect the Ti sites and reduces Ti^{4+} to Ti^{3+} which also causes modification in the electronic structure.

4. Conclusion

The as prepared TAT films were implanted with 100 keV Ar^+ ions to modify optical and electrical properties for their use as transparent conducting electrode with enhanced figure of merit. While XRD shows the amorphous nature of TiO_2, the XPS analysis implies the presence of peak due to Ti^{3+} ions on implantation indicating lower binding energy of Ti state and consequent band gap reduction confirmed by optical measurement result. Lower band gap leads to decrease in the electrical resistivity which was the main objective of this study. The FESEM and AFM show homogeneous deposition of films with small roughness values. The optical transmittance was found to decrease from ~ 80% to ~ 73% after ion implantation. The electrical resistivity of pristine film was $2.04 \times 10^{-4}\,\Omega$ cm, which decreased to $9.14 \times 10^{-5}\,\Omega$ cm at the highest fluence of 1×10^{16} ions/cm^2. The sheet resistance shows a significant decrease from 20.4 Ω/□ to 9.14 Ω/□. The Haacke figure of merit have been calculated for all samples and highest FOM (Ψ_{TC}) was found to $5.6 \times 10^{-3}\,\Omega^{-1}$ for the highest fluence of 1×10^{16} ions/cm^2. Our results demonstrate that Ar implantation is a suitable method to develop TAT multilayer based transparent conducting electrode with enhanced FOM.

Acknowledgement

The authors acknowledge Materials Research Centre, MNITJ, India for the characterization facilities and Inter University Accelerator Center (IUAC), New Delhi, India for providing the low energy ion beam facility.

Appendix A. Supplementary material

Supplementary data associated with this article can be found in the online version at http://dx.doi.org/10.1016/j.mssp.2017.11.016.

References

[1] T. Hitosugi, N. Yamada, S. Nakao, Y. Hirose, T. Hasegawa, Properties of TiO_2-based transparent conducting oxides, Phys. Status Solidi A 207 (2010) 1529–1537, http://dx.doi.org/10.1002/pssa.200983774.
[2] K. Ellmer, Past achievements and future challenges in the development of optically transparent electrodes, Nat. Photonics 6 (2012) 808–816, http://dx.doi.org/10.1038/nphoton.2012.282.
[3] A. Stadler, Transparent conducting oxides—an up-to-date overview, Materials 5 (2012) 661–683, http://dx.doi.org/10.3390/ma5040661.
[4] K.L. Chopra, S. Major, D.K. Pandya, Transparent conductors-a status review, Thin Solid Films 102 (1983) 1–46, http://dx.doi.org/10.1016/0040-6090(83)90256-0.
[5] N. Yamada, T. Hitosugi, J. Kasai, N.L.H. Hoang, S. Nakao, Y. Hirose, T. Shimada, T. Hasegawa, Direct growth of transparent conducting Nb-doped anatase TiO_2 polycrystalline films on glass, J. Appl. Phys. 105 (2009), http://dx.doi.org/10.1063/1.3148267.
[6] S.M. Kong, Y. Xiao, K.H. Kim, W.I. Lee, C.W. Chung, Performance improvement of

dye-sensitized solar cells by surface patterning of fluorine-doped tin oxide transparent electrodes, Thin Solid Films 519 (2011) 3173–3176, http://dx.doi.org/10.1016/j.tsf.2011.01.251.
[7] R.K. Shukla, A. Srivastava, A. Srivastava, K.C. Dubey, Growth of transparent conducting nanocrystalline Al doped ZnO thin films by pulsed laser deposition, J. Cryst. Growth 294 (2006) 427–431, http://dx.doi.org/10.1016/j.jcrysgro.2006.06.035.
[8] J. Ho Kim, J. Hwan Lee, S.W. Kim, Y.Z. Yoo, T.Y. Seong, Highly flexible ZnO/Ag/ZnO conducting electrode for organic photonic devices, Ceram. Int. 41 (2015) 7146–7150, http://dx.doi.org/10.1016/j.ceramint.2015.02.031.
[9] V. Sharma, S. Singh, K. Asokan, K. Sachdev, A study on 100 MeV O^{7+} irradiated SnO_2/Ag/SnO_2 multilayer as transparent electrode for flat panel display application, Nucl. Instrum. Methods Phys. Res. B 379 (2016) 141–145, http://dx.doi.org/10.1016/j.nimb.2016.04.059.
[10] V. Sharma, R. Vyas, P. Bazylewski, G.S. Chang, K. Asokan, K. Sachdev, Probing the highly transparent and conducting SnO_x/Au/SnO_x structure for futuristic TCO, RSC Adv. 6 (2016) 29135–29141, http://dx.doi.org/10.1039/C5RA24422F.
[11] M.-Q. Zhu, H.-D. Jin, P.-Q. Bi, F.-J. Zong, J. Ma, X.-T. Hao, Performance improvement of TiO_2/Ag/TiO_2 multilayer transparent conducting electrode films for application on photodetectors, J. Phys. D: Appl. Phys. 49 (2016) 115108, http://dx.doi.org/10.1088/0022-3727/49/11/115108.
[12] J.H. Kim, H. Lee, J. Na, S. Kim, Y. Yoo, T.-Y. Seong, Dependence of optical and electrical properties on Ag thickness in TiO_2/Ag/TiO_2 multilayer films for photovoltaic devices, Ceram. Int. 41 (2015) 8059–8063, http://dx.doi.org/10.1016/j.ceramint.2015.03.002.
[13] J.H. Jia, P. Zhou, H. Xie, H.Y. You, J. Li, L.Y. Chen, Study of Optical and Electrical Properties of TiO_2/Ag/TiO_2 Multilayers, vol. 44, 2004, pp. 717–721.
[14] J.H. Kim, D.H. Kim, T.Y. Seong, Realization of highly transparent and low resistance TiO_2/Ag/TiO_2 conducting electrode for optoelectronic devices, Ceram. Int. 41 (2015) 3064–3068, http://dx.doi.org/10.1016/j.ceramint.2014.10.148.
[15] D.K. Avasthi, G.K. Mehta, Swift heavy ions for materials engineering and nanostructuring, Springer. Ser. Mater. Sci. (2011).
[16] S. Keshri, A. Kumar, D. Kabiraj, Tailoring of optical and gas sensitivity behaviors of WO_3 films by low energy Ar^+ ion implantation, Thin Solid Films 526 (2012) 50–58, http://dx.doi.org/10.1016/j.tsf.2012.10.101.
[17] H. Thakur, S. Gautam, P. Thakur, K.K. Sharma, A.P. Singh, Y. Kumar, R. Kumar, K. H. Chae, On the optical properties of Ag^{+15} ion-beam irradiated TiO_2 and SnO_2 thin films, 2011. ⟨http://doi.org/10.3938/jkps.61.1609⟩.
[18] S. Singh, V. Sharma, Surbhi, D. Saini, K. Asokan, K. Sachdev, Fabrication of highly efficient TiO_2/Ag/TiO_2 multilayer transparent conducting electrode with N ion implantation for optoelectronic applications, Ceram. Int. 43 (2017) 9759–9768, http://dx.doi.org/10.1016/j.ceramint.2017.04.152.
[19] V. Sharma, P. Kumar, A. Kumar, Surbhi, K. Asokan, K. Sachdev, High-performance radiation stable ZnO/Ag/ZnO multilayer transparent conductive electrode, Sol. Energy Mater. Sol. Cells 169 (2017) 122–131, http://dx.doi.org/10.1016/j.solmat.2017.05.009.
[20] R. Fromknecht, R. Auer, I. Khubeis, Lattice location and electrical conductivity in ion implanted TiO, single crystals, Energy 120 (1996) 252–256.
[21] N. Zhou, D.B. Buchholz, G. Zhu, X. Yu, H. Lin, A. Facchetti, T.J. Marks, R.P.H. Chang, Ultraflexible polymer solar cells using amorphous zinc-indium-tin oxide transparent electrodes, Adv. Mater. 26 (2014) 1098–1104, http://dx.doi.org/10.1002/adma.201302303.
[22] H.-G. Boyen, P. Widmayer, D. Schwertberger, N. Deyneka, P. Ziemann, Sequential ion-induced stress relaxation and growth: a way to prepare stress-relieved thick films of cubic boron nitride, Appl. Phys. Lett. 76 (2000) 709, http://dx.doi.org/10.1063/1.125869.
[23] S. Mohapatra, N. Bhardwaj, A. Pandey, MeV ion irradiation induced evolution of morphological, structural and optical properties of nanostructured SnO2 thin films, Mater. Res. Express 2 (2015) 45013, http://dx.doi.org/10.1088/2053-1591/2/4/045013.
[24] T. Pieńkos, L. Gładyszewski, A. Prószyński, D. Chocyk, G. Gładyszewski, F. Martin, C. Jaouen, M. Drouet, B. Lamongie, Stress development during thin film growth and its modification under ion irradiation, Use. Model. Use.-Adapt. Interact. 70 (2003) 243–248, http://dx.doi.org/10.1016/S0042-207X(02)00650-4.
[25] S. Chandramohan, R. Sathyamoorthy, P. Sudhagar, D. Kanjilal, D. Kabiraj, K. Asokan, V. Ganesan, Influence of SHI irradiation on the structure and surface topography of CdTe thin films on flexible substrate, J. Mater. Sci.: Mater. Electron. 18 (2007) 1093–1098, http://dx.doi.org/10.1007/s10854-007-9137-4.
[26] A. Dhar, T.L. Alford, High quality transparent TiO_2/Ag/TiO_2 composite electrode films deposited on flexible substrate at room temperature by sputtering, APL Mater. 1 (2013) 012102, http://dx.doi.org/10.1063/1.4808438.
[27] Z. Song, J. Hrbek, R. Osgood, Formation of TiO_2 nanoparticles by reactive-layer-assisted deposition and characterization by XPS and STM, Nano Lett. 5 (2005) 1327–1332, http://dx.doi.org/10.1021/nl0505703.
[28] R. Sanjines, H. Tang, H. Berger, F. Gozzo, G. Margaritondo, F. Levy, Electronic structure of anatase TiO_2 oxide, J. Appl. Phys. 75 (1994) 2945–2951, http://dx.doi.org/10.1063/1.356190.
[29] A. Berko, I. Ulrych, K.C. Prince, Encapsulation of Rh nanoparticles supported on TiO_2(110)-(1 × 1) surface: XPS and STM studies, J. Phys. Chem. B. 102 (1998) 3379–3386, http://dx.doi.org/10.1021/jp973255g.
[30] S. Hashimoto, A. Tanaka, Alteration of Ti 2p XPS spectrum for titanium oxide by low-energy Ar ion bombardment, Surf. Interface Anal. 34 (2002) 262–265, http://dx.doi.org/10.1002/sia.1296.
[31] M. Sathish, B. Viswanathan, R.P. Viswanath, C.S. Gopinath, Synthesis, characterization, electronic structure, and photocatalytic activity of nitrogen-doped TiO_2 nanocatalyst, Chem. Mater. 17 (2005) 6349–6353, http://dx.doi.org/10.1021/cm052047v.
[32] G. Liu, W. Jaegermann, J. He, V. Sundstro, L. Sun, XPS and UPS Characterization of the TiO_2/ZnPcGly Heterointerface: alignment of Energy Levels, J. Phys. Chem. B 106 (2002) 5814–5819.
[33] H. Chen, G. Liu, L. Wang, Switched photocurrent direction in Au/TiO_2 bilayer thin films, Sci. Rep. 5 (2015) 10852, http://dx.doi.org/10.1038/srep10852.
[34] T. Harifi, M. Montazer, Fe^{3+}:Ag/TiO_2 nanocomposite: synthesis, characterization and photocatalytic activity under UV and visible light irradiation, Appl. Catal. A: Gen. 473 (2014) 104–115, http://dx.doi.org/10.1016/j.apcata.2014.01.005.
[35] L. Gan, C. Wu, Y. Tan, B. Chi, J. Pu, L. Jian, Oxygen sensing performance of Nb-doped TiO_2 thin film with porous structure, J. Alloy. Compd. 585 (2014) 729–733, http://dx.doi.org/10.1016/j.jallcom.2013.09.161.
[36] H. Liu, L. Li, T. Yao, W. Ding, D. Ju, W. Chai, The effect of ion source working power on the composition and optical properties of TiO2 films bombarded by N ion beam, Surf. Coat. Technol. 219 (2013) 88–93, http://dx.doi.org/10.1016/j.surfcoat.2013.01.009.
[37] J. Tauc, Optical properties of amorphous semiconductors, amorphous and liquid, Semiconductors (1974) 159–220, http://dx.doi.org/10.1007/978-1-4615-8705-7_4.
[38] B. Joseph, P.K. Manoj, V.K. Vaidyan, Studies on the structural, electrical and optical properties of Al-doped ZnO thin films prepared by chemical spray deposition, Ceram. Int. 32 (2006) 487–493, http://dx.doi.org/10.1016/j.ceramint.2005.03.029.
[39] M. Shirkhanzadeh, XRD and XPS characterization of superplastic TiO_2 coatings prepared on Ti6Al4V surgical alloy by an electrochemical method, J. Mater. Sci.: Mater. Med. 6 (1995) 206–210, http://dx.doi.org/10.1007/BF00146857.
[40] M. Miyakawa, K. Ueda, H. Hosono, Carrier generation in highly oriented WO_3 films by proton or helium implantation, J. Appl. Phys. 92 (2002) 2017–2022, http://dx.doi.org/10.1063/1.1496120.
[41] M. Miyakawa, K. Kawamura, H. Hosono, H. Kawazoe, Large electrical conductivity enhancement of WO_3 thin films produced by ion implantation, J. Appl. Phys. 84 (1998) 5610–5613, http://dx.doi.org/10.1063/1.368608.
[42] R. Fromknecht, I. Khubeis, S. Massing, O. Meyer, Ion implantation in TiO_2: damage production and recovery, lattice site location and electrical conductivity, Nucl. Instrum. Methods Phys. Res. Sect. B: Beam Interact. Mater. At. 147 (1999) 191–201, http://dx.doi.org/10.1016/S0168-583X(98)00551-5.
[43] K. Seal, M.A. Nelson, Z.C. Ying, D.A. Genov, A.K. Sarychev, V.M. Shalaev, Growth, morphology, and optical and electrical properties of semicontinuous metallic films, Phys. Rev. B. 67 (2003) 35318, http://dx.doi.org/10.1103/PhysRevB.67.035318.
[44] G. Haacke, New figure of merit for transparent conductors*, J. Appl. Phys. 47 (1976) 4086–4089, http://dx.doi.org/10.1063/1.323240.

Investigation of Post Annealing Effects on Nb:TiO_2 Transparent Conducting Thin Films

Authors: Singh, Satyavir; Sharma, Vikas; Sachdev, K
Source: Advanced Science Letters, Volume 22, Number 11, November 2016, pp. 3773-3776(4)
Publisher: American Scientific Publishers
DOI: https://doi.org/10.1166/asl.2016.8069

Nb doped TiO_2 (TNO) has been identified as an alternative transparent conductor to ITO. Three percent Nb doped TiO_2 ($Ti_{0.97}Nb_{0.03}O_2$) films were deposited by rf magnetron sputtering on glass and silicon substrates at room temperature. The as deposited films were annealed at temperature ranging from 350 °C to 550 °C in air. The XRD data suggest that as deposited amorphous films led to the (101) oriented anatase phase after annealing. The surface morphology investigated by FESEM and AFM show formation of very smooth and homogeneous films. A minimum electrical resistivity of $3.2 \times 10^{-2}\Omega \cdot$ cm and maximum carrier density of 9.1×10^{19} cm^{-3} was obtained at 450 °C annealing temperature for the anatase TNO films. The as prepared and annealed films were transparent with an average transparency above 75%. The root mean square roughness measured by AFM for pristine sample was 1.97 nm which increases to 4.46 nm with an increase in annealing temperature to 550 °C. These results indicate that post annealing method has considerable potential for enhancing the properties of transparent conducting oxides.

Keywords: Annealing; Niobium Doping; Titanium Dioxide; Transparent Conducting Oxides

Document Type: Research Article

Affiliations: Department of Physics, Malaviya National Institute of Technology Jaipur 302017, India

Publication date: 01 November 2016

Solar Energy 173 (2018) 651–664

Contents lists available at ScienceDirect

Solar Energy

journal homepage: www.elsevier.com/locate/solener

NTO/Ag/NTO multilayer transparent conducting electrodes for photovoltaic applications tuned by low energy ion implantation

Satyavir Singh[a], Vikas Sharma[a,b,*], K. Asokan[c], Kanupriya Sachdev[a,d,*]

[a] Department of Physics, Malaviya National Institute of Technology, Jaipur 302017, India
[b] Department of Physics, Indian Institute of Technology Delhi, New Delhi 110016, India
[c] Inter-University Accelerator Centre, Aruna Asaf Ali Marg, New Delhi 110067, India
[d] Materials Research Centre, Malaviya National Institute of Technology, Jaipur 302017, India

ARTICLE INFO

Keywords:
Transparent conducting films
Photovoltaic
Ion implantation
Hall measurement
X-ray photoelectron spectroscopy (XPS)

ABSTRACT

Multilayer structures with optimized Nb (3.7 at.%) doped TiO_2 (NTO) having the layers as NTO/Ag/NTO (NAN) were fabricated to obtain high optical transmittance and low electrical resistivity which could be a suitable replacement of the conventional transparent conducting electrodes used in the energy conversion and optoelectronics devices. These optimized pristine films of NAN layers were deposited by sputtering and implanted with 40 keV N^+ ions with fluences ranging from 1×10^{14} to 1×10^{16} ions/cm^2. The N^+ ion implantation leads to the improvement in the electrical conductivity of NAN films, confirmed by the Hall measurement. The resistivity of pristine film is $9.6 \times 10^{-5}\,\Omega$ cm which decreases to $5.5 \times 10^{-5}\,\Omega$ cm after ion implantation for the N^+ ion fluence of 1×10^{16} ions/cm^2. Electrical transport properties were studied in the temperature range of 80–340 K, and the results show stable behavior of films. This substitutional doping causes narrowing of band gap and improvement in the electrical conductivity. The optimized NAN multilayer films show a low sheet resistance of 6.9 Ω/□ and a high transmittance of ~81% for the 1×10^{16} ions/cm^2 fluence. The Haacke figure of merit (FOM) of $18 \times 10^{-3}\,\Omega^{-1}$ was obtained for the highest fluence (1×10^{16} ions/cm^2). The X-ray photoemission spectroscopy study of the implanted samples revealed substitution of Ti by Nb in NTO film and appearance of Ti^{3+} state. The work function of pristine NAN films, measured using ultravoilet photoemission spectroscopy (UPS) was found to 4.63 eV, which matches with the work function of active layer of photovoltaic cell. On implantation, the O ions are replaced by N^+ ions. These results indicate that the NAN films with N^+ ion implantation are suitable for potential transparent conducting electrode (TCE) applications in photovoltaics due to their high transmittance, low electrical resistivity and compatibility for growth of further layers.

1. Introduction

Transparent conducting electrodes (TCE) having high transmittance and low electrical resistance are an important component in light conversion applications such as photovoltaic cell, smart windows and light emitting diodes (LEDs) and they are used in touch-panel screen and flat-panel displays as well, and hence have a huge market (Kim et al., 2013; Sharma et al., 2016a; Sibin et al., 2017). TCE an essential component in solar cell technologies acts as a front electrode in both inorganic solar cells (CdTe) (Green, 2007) and organic solar cells (Günes et al., 2007). Having large use and crucial role in optoelectronic devices; the TCE should posses the low electrical resistivity and high optical transmittance over a wide optical range. Since the photovoltaic is a large area application therefore a durable and cost effective TCE is required. As transparent conductors (TCs) are a significant component in all electrical and optically activated devices so there is need of high quality and low cost TC. Moreover, the TCs need a low electrical resistivity to produce a low voltage drop through the conductor surface. TCs are widely used in smart windows (Sun et al., 2017) and solar thermal collectors (Colangelo et al., 2016). In smart windows, the purpose of TC is to transmit maximum light and to control the solar heat gain. Meanwhile, in solar thermal collectors it allows solar radiation to collector and stops the heat loss. Although, Indium doped Tin oxide (ITO) is the most widely used TCE in optoelectronic devices, it shows some feasibility problems such as, scarcity of In, high deposition temperature, and low mechanical stability etc (Kumar and Zhou, 2010). This has led to researchers investigating several alternatives – doped metal oxides viz. Nb:TiO_2 (Singh et al., 2017a), Al:ZnO (Ayadi et al., 2014), carbon nanostructures viz. carbon nanotubes (Hecht et al., 2011), graphene (Bae et al., 2009), and their components, conducting

* Corresponding authors at: Department of Physics, Malaviya National Institute of Technology, Jaipur 302017, India.
E-mail addresses: phyvikas@gmail.com (V. Sharma), ksachdev.phy@mnit.ac.in (K. Sachdev).

https://doi.org/10.1016/j.solener.2018.08.001
Received 7 February 2018; Received in revised form 9 June 2018; Accepted 1 August 2018
Available online 08 August 2018
0038-092X/

polymers (Ha et al., 2004), metallic mesh and nanowires (Park et al., 2014). Although substantial investigations have been carried out on above mentioned transparent electrodes, but each category has problems of its own like high resistivity for conductive polymers and low contact surface area and low transmittance for 3D structure. Of the mostly used metals oxides, viz. TiO_2, ZnO, SnO_2 and WO_3 for the transparent electrode application, TiO_2 is considered as the prime candidate due to its several advantageous characteristics like wide band gap (~3.2 eV), high refractive index (2.7), high transmittance (~95%) in the visible region and good mechanical stability (Hashimoto et al., 2007; Heo et al., 2005). TiO_2 exhibits very good chemical stability, which can be exploited for its use in TCE development (Ellmer, 2012). A very thin layer of Ag (< 10 nm) provides excellent electrical conductivity with low absorbance and sufficient transmittance. The transmittance of this layer can be increased by inserting the metal layer between two oxide layers that reduces the reflection from the Ag surface (Guillén and Herrero, 2011).

Based on the above concept, oxide/metal/oxide (OMO) multilayer structures have emerged as a potential inspiring alternative due to the coexistence of their extraordinary electrical and optical properties. OMO structures not only give improved electrical properties but also exhibit other useful characteristics such as low roughness, good corrosion resistance and high work function. In OMO structure, the researchers have used the metals of Ag, Au and Cu as middle layer (Girtan, 2012; Guillén and Herrero, 2008), and which is primarily responsible for the charge transport activity. The primary goal of inserting metal layer between the two oxides layer is to minimize the reflection effect and increase the transmittance in the visible region and by varying oxide layer thickness the desired maximum transmittance position can also be adjusted. Recently, performance of OMO based structure like ZnO/Ag/ZnO (Sharma et al., 2017), ITO/Ag/ITO (Sibin et al., 2017), SnO_2/Ag/SnO_2 (Liu et al., 2015), TiO_2/Ag/TiO_2 (Singh et al., 2017b), AZO/Ag/AZO (Qi et al., 2013) and ZnO/MWCNT-Ag/ZnO/PET (ZCAZ) (Surbhi et al., 2018) have been reported. Zhu et al. (Zhu et al., 2016) have reported the sputtering current variation effect on the optical and electrical properties of TiO_2/Ag/TiO_2 multilayer TCE sputtered on glass. They have obtained the optimized TAT electrode with sheet resistance of 7.2 Ω/□ and ~91% transmittance with a sputtering current of 0.48 A. Zhao et al. (Zhao and Alford, 2016) studied the effect of TiO_2, Ag layer thickness and deposition rate on the performance of TCE and have observed that thickness of TiO_2 and Ag as 42 nm and 10 nm, respectively gives better results. Kim et al. (Kim et al., 2015) investigated the TiO_2 layer thickness effect on the TiO_2/Ag/TiO_2 multilayer films and reported that TiO_2 (40 nm)/Ag (18.8 nm)/TiO_2 (40 nm) multilayer provides the sheet resistances of 3.9–4.4 Ω/□ and ~95% transmittance at 550 nm wavelength. Dhar and Alford (2013) have reported the critical thickness of Ag layer as ~9 nm to form a continuous film in TiO_2/Ag/TiO_2 multilayer structure for good transport properties. The sputtering method has been extensively used for uniform, stoichiometric and large area deposition and also employed for roll-to-roll deposition of TCO films on glass and plastic substrates, which satisfy industry requirements. The TCE is one of the key components of solar cells and widely used in various type of organic solar cell devices. These TCE have been used in ZnO/Cu_2O based solar cells (Zang, 2018; Zang et al., 2013) and $CH_3NH_3PbI_{3-x}Cl_x$ perovskite solar cells (Zeng et al., 2017).

Researchers have proposed different methods viz. doping and tracing of impurities in TiO_2, chemical mixing, sol-gel, ion assisted sputtering, ion implantation etc to improve properties of TiO_2. Nb doped TiO_2 has shown enhanced performance as TCE (Hitosugi et al., 2010). A single layer Nb doped TiO_2 (NTO) used as TCE in optoelectronic applications, have shown less working efficiency in terms of electrical conductivity and the films are thicker than the multilayer structure (Tucker et al., 2012). The multilayer structure with Nb doped TiO_2 embedded with metal layer gives higher electrical conductivity with nearly same transmittance while having lower thickness (~80 nm). Ion implantation has been reported as one of the most promising technologies for modification of TiO_2, due to its good process control and restoring of vacant oxygen sites in a TiO_2 lattice (Asahi et al., 2001; Stepanov, 2012). The present work reports the fabrication and characterization of NTO/Ag/NTO multilayer films with varying NTO thickness (25–65 nm) and Ag thickness kept constant at ~9 nm. An optimized thickness for NTO layer was obtained and the structure with NTO/Ag/NTO (35 nm/9 nm/35 nm) shows highest figure of merit (FOM) of $12 \times 10^{-3}\,\Omega^{-1}$. These multilayer films were further implanted with 40 keV N^+ ions to improve the properties with the fluence ranging from 1×10^{14} to 1×10^{16} ions/cm^2. It is seen that doping Nb in TiO_2 and the N^+ ion implantation both contribute in enhancement of electrical conductivity. There is decrement in optical transmittance but the overall FOM has significantly increased to $18 \times 10^{-3}\,\Omega^{-1}$. We have also measured the work function of pristine NAN films using ultravoilet photoemission spectroscopy (UPS). The work function of the TCE is a key factor and have significant impact on the performance of the solar cell because it affects the band alignment of TCE and the next active layer (Po et al., 2011). H.M. Lee et al. (2016) have reported improved power conversion efficiency (3.6%) with MoO_3 graded ITO anodes. Lei et al. (2015) increased the work function of ITO using CuS to gain higher power conversion efficiency (7.4%).

2. Experimental details

Nb powder (Strem Chemicals, 99.9% purity) and TiO_2 powder (Alfa-Aesar, 99.98% purity) were used to fabricate the Nb doped TiO_2 (NTO) sputtering target. These powders were mixed by solid state method and pressed into a 2-in. diameter pellet and then sintered at 1200 °C for 12 h. The first NTO layer of multilayer structure was deposited on corning glass substrate by RF sputtering (120 W) at room temperature. Middle layer of Ag was deposited by DC sputtering (16 W) using silver target (99.98% purity) and the top NTO layer was deposited over the middle Ag layer. Initially vacuum chamber was evacuated to 5×10^{-6} mbar and chamber pressure during deposition was 5×10^{-3} mbar for NTO layer and 1.5×10^{-2} mbar for Ag layer with constant Ar flow at 15 sccm. The distance of target to substrates was 100 mm and deposition rate for NTO and Ag layers were obtained as 1 Å/s and 6 Å/s, respectively. The optimized NTO/Ag/NTO (35 ± 4 nm/9 ± 1 nm/35 ± 4 nm) multilayer structure was consecutively deposited on cleaned glass substrates without a vacuum break. The as-prepared multilayer films were then implanted with 40 keV N^+ ions of fluence ranging from 1×10^{14} ions/cm^2 to 1×10^{16} ions/cm^2 using low energy ion beam facility (LEIBF) at the Inter-University Accelerator Centre (IUAC), New Delhi, India. The thickness of top and bottom NTO layers were varied from 25 nm to 65 nm keeping the same sputtering conditions to find optimized thickness, in terms of maximum FOM.

The electrical properties of pristine and implanted films were measured using ECOPIA-5000 low-temperature Hall Measurement unit using a magnetic field of 0.57 T for temperature range of 80–340 K. The optical transmittance and absorbance were obtained from LAMBDA 750 (Perkin Elmer) UV–Vis-NIR Spectrophotometer with bare glass as a reference in the visible range (300–800 nm) of light. The crystalline properties of pristine and implanted films of NAN structure were probed by X-Ray Diffractometer (Panalytical X-Pert Pro) with CuKα radiation. The morphology of the films was examined by Nova Nano FE-SEM 450 (FEI) and topography was observed by using atomic force microscopy Multimode Scanning Probe Microscope (Bruker). Detailed study of chemical states of elements and the interfacial stability of NAN films were carried out by X-ray photoelectron spectroscopy (XPS, Omicron ESCA). Monochromatic source Al Kα (1486.7 eV) of 124 mm mean radius and X-ray resolution of 0.6 eV and 3×10^{-10} mbar chamber pressure has been used for XPS measurement. The thickness and elemental composition of the films were studied by Rutherford Backscattering (RBS) Spectrometry. These measurements were carried

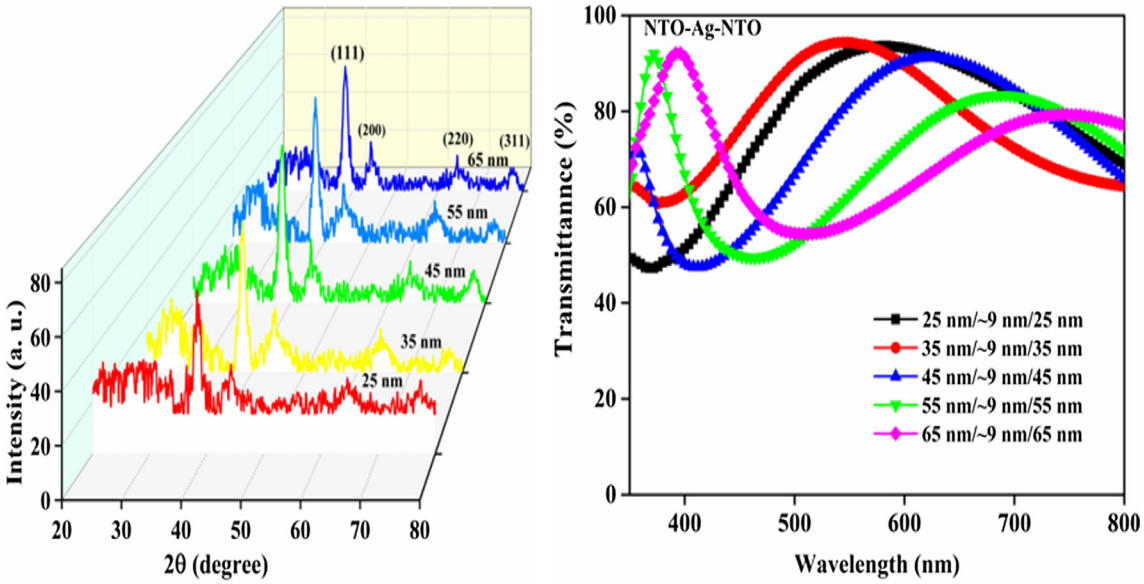

Fig. 1. (a) XRD pattern and (b) Transmittance spectra of NAN multilayer films with different NTO thickness.

out using 2 MeV He^+ ions at back scattering angle of 165° with 1.7 MV tandem accelerator facility at IUAC, New Delhi. The electronic and nuclear energy loss values for this implantation were found to be 12.1 and 25.6 eV/Å, respectively, showing that nuclear energy loss dominates over electronic energy loss. The stopping range as calculated by the SRIM-2010 software was obtained as 58 nm which is less than 80 nm, total thickness of the film meaning there by that the ions have been implanted in the film.

3. Results and discussion

3.1. Optimization of NTO thickness

Nb (3.7 at.%) doped TiO_2 (NTO) based multilayer structure were deposited at room temperature and were optimized for thickness of oxide layer. Fig. 1(a) shows the XRD pattern of NAN multilayer films with varying NTO thickness. The thickness of NTO film was varied from 25 to 65 nm. It can be observed from the figure that there is a dominant peak at 38.18°, which is assigned to Ag (1 1 1) diffraction plane (JCPDS No. 04-0783). Other peaks at 44.28°, 64.62° and 77.51° are attributed to Ag (2 0 0), (2 2 0) and (3 1 1), respectively. No peak is observed for TiO_2 as room temperature deposition results in an amorphous Nb doped TiO_2 layer. The XRD graph exhibits a similar pattern for all NAN multilayer structures. The crystallite size, lattice constant and residual stress, have been calculated and shown in supplementary table ST1. Fig. 1(b) demonstrates optical transmittance of NAN films for different NTO thickness for the visible region (350 nm $< \lambda <$ 800 nm). The average transmittance in the visible region for NTO thickness of 25, 35, 45, 55 and 65 nm were observed as 84%, 83%, 82%, 80% and 81%, respectively. The maximum transmittance peak is shifting towards higher wavelength as the NTO thickness is increasing. The highest transmittance of ~94% was obtained for the 35 nm NTO thickness at 550 nm wavelength, which is most preferred operating wavelength for the optoelectronic devices so the NAN structure with (~35 nm/~9 nm/~35 nm) exhibits the desirable optical results. The absorbance spectra of NAN multilayer films as a function of NTO thickness is given in supplementary Fig. S1. The transmittance of these specimens initially increases with wavelength and attains a maximum and then decreases with further increasing wavelength. It can be also seen that; transmittance peaks of NAN structures are red-shifted with increasing NTO thickness. Transmission window broadens and is shifted to lower energies with the NTO thickness. However, the increasing thickness of NTO layers in NTO/Ag/NTO multilayer structure leads to more absorbance of light intensity and consequently the transparency reduces. Large difference in the refractive indices of oxide layer and Ag may produce a plasmon coupling to give higher transmittance (> 80%) (Cattin et al., 2010). Therefore, good transmittance (~84%) of our specimen may be attributed to surface plasmon resonance in Ag layer with optimized NTO thickness of 35 nm.

Supplementary data associated with this article can be found, in the online version, at https://doi.org/10.1016/j.solener.2018.08.001.

The top layer added on the metal layer serves as an antireflective coating. The optical properties of such a stacked layer depends on the film thickness and the peak of transmittance curve representing minimum reflectance is obtained by adjusting the thickness of the film (Guillén and Herrero, 2011, 2009). As the film thickness increases, the peak shifts towards the longer wavelengths (Guillén and Herrero, 2010; Koike and Fukuda, 2008; Zhao and Alford, 2016). Material of high refractive index coated on the metal layer enhances its antireflective properties. Initial decrease in refractive index of NTO with wavelength shown in supplementary Fig. S4 could be a reason for initial increase of transmittance with wacvelength. Further, the transmittance enhances due to the screening effect of the bound electrons with an increase in energy. At higher wavelengths or for low energy region, the free charge carrier absorption is dominant and causes decrease in transmittance (Ehrenreich and Philipp, 1962; Sivaramakrishnan et al., 2009). Similar transmittance behavior for transparent conducting electrodes has been reported in previous studies (Kim et al., 2015; Mohamed, 2008; Zhao and Alford, 2016).

The role of NTO layers in NAN multilayer system is to increase the transmittance by reducing the reflection of light from the Ag surface. The transmittance value is limited by the Ag layer mainly due to reflection losses, which can be boosted by adding two NTO layers and behave as antireflective coatings. The intention is to tune the interference phenomena that happen between multiple reflections from the interfaces and to obtain the minimum reflectance or maximum transmittance. To fulfill this condition, the thickness of NTO layers is varied and finely tuned to get maximum transmittance at a particular wavelength say 550 nm (Bender et al., 1998; Koike and Fukuda, 2008). It is reported that the shape of the transmittance curve depends upon the amount of oxygen in metal oxide film and its thickness. Therefore, an improvement in transmittance for particular wavelength region can be obtained by adjusting the film thickness of metal oxide (Bender et al., 1998; Guillén and Herrero, 2009; Koike and Fukuda, 2008).

Fig. 2(a) shows the electrical resistivity, carrier mobility and carrier concentration of NAN multilayer films for different NTO thickness. Resistivity for 25 nm NTO thickness was obtained $9.9 \times 10^{-5}\,\Omega$ cm, which reduces to $9.7 \times 10^{-5}\,\Omega$ cm for 35 nm and increases to $2.1 \times 10^{-4}\,\Omega$ cm as the NTO thickness increases. Fig. 2(b) illustrates the sheet resistance and the Haacke FOM for NAN films. The sheet resistance varied from 16.5 Ω/□ to 15 Ω/□ with NTO thickness and a minimum value of 12.12 Ω/□ was obtained for 35 nm. The decrease in resistivity can be explained in terms of change carrier concentration and their mobility values. NAN multilayer system consists of a continuous Ag layer between two doped dielectric layers so interfacial scattering and ionized-impurity scattering would be dominant here. NAN multilayer structure was prepared by using two different materials (NTO and Ag) having different refractive indices and electronic structures. The refractive indices of NTO (~35 nm) and Ag (~9 nm) layers in the NAN multilayer system are ~2.1 and ~1.3 respectively. Therefore, the interfaces between NTO and Ag in the NAN structure are responsible for interfacial scattering (Han et al., 2008; Indluru and Alford, 2009). The schematic diagram of the Fermi energy level (E_f) alignment in the electronic structure of the interfaces in NAN multilayer structure is shown in Fig. 14. The NAN multilayer structure was fabricated using sputtering method. During the stacked multilayer deposition, the Ag atoms are expected to diffuse into NTO matrix and this is evident in the RBS spectra. These diffused Ag ions are present in the top and bottom of the NTO matrix and causes ionized impurity scattering (Han et al., 2008; Indluru and Alford, 2009). The schematic diagram of diffused ions of Ag, Ti and O in NTO and Ag layers of NAN structure is shown in supplementary Fig. S2.

The Haacke FOM (Haacke and Haacke, 1976) has been calculated using the following formula.

$$\Psi_{TC} = \frac{T_{av}{}^{10}}{R_s} \quad (1)$$

As observed from Fig. 2(b) giving variation of FOM with NTO film thickness, highest FOM of $12.7 \times 10^{-3}\,\Omega^{-1}$ is obtained for 35 nm thickness. Hence the multilayer structure with this thickness of NTO layers was chosen for N ion implantation to modify the properties. The optimized NAN structure with 35 nm NTO layers and 9 nm thick Ag layer implanted using 40 keV nitrogen ions with different ion fluences and investigated for change in the structural, optical and electrical behavior. The ion implantation parameters viz. range and energy loss were measured by SRIM calculations.

3.2. Structural properties

Fig. 3 shows the XRD patterns of the pristine NAN and N^+ ion implanted NAN (referred as N-NAN) multilayer structures for the fluence range of 1×10^{14} ions/cm^2 to 1×10^{16} ions/cm^2. It can be observed from the graph, the diffraction planes of Ag (1 1 1), (2 0 0), (2 2 0) and (3 1 1) at 38.18°, 44.28°, 64.62° and 77.51° positions respectively and matching well with JCPDS No. 04-0783. The crystallite size of the Ag particles was calculated using Debye–Scherrer formula ($0.9\lambda/\beta\cos\theta$) and found to be 8.1 nm for pristine film which decreases to 7.1 nm with increase in fluence to 1×10^{16} ions/cm^2. The variation in crystallite size of Ag is due to the annealing effect produced by ion implantation and may be explained by the thermal spike model (Kumar et al., 2013). The calculated lattice parameters were found to be identical with standard value (4.086 Å). The implantation process generates the residual stress in the system and it changes from −0.108 to −0.570 GPa with increase in fluence. The negative sign of residual stress shows that the stress in the system is compressive. The increased intensity of Ag peaks indicates that implantation causes improvement in the crystallinity and it may contribute to get lower resistivity in the specimen. The crystallite size, lattice constant and residual stress of pristine and N-NAN multilayer films is given in Table 1.

The XRD results show the amorphous behavior of oxide layer which generally appears in the films deposited at room temperature and it is advantageous for flexible electrode when deposited on plastic substrates (Sharma et al., 2016b). The crystalline peak of metal layer confirms the good quality continuous metal layer, which enhances the overall electrical behavior of NAN structure in pristine and implanted samples. A small variation in the XRD of NAN structure also confirms the structural stability of the films in low energetic ion environment.

3.3. Rutherford back scattering spectrometry

The RBS measurements were carried out for pristine NAN and N-NAN multilayer films deposited on Si substrates to evaluate the thickness of each layer. Fig. 4 shows the RBS spectra of pristine NAN and N-NAN multilayer structures. SIMNRA software has been used for the simulation of these two samples. The primary purpose of this measurement was to determine the stoichiometry and thickness of the multilayer films. Both fitted spectra exhibit distinct elemental peaks corresponding to Ti, O, Nb and Ag ions. The Nb concentration of ~3.7 at.% in TiO_2 matrix was estimated from RBS results. The thickness of first, second and third layers have been calculated from the fitted curves and found to be NTO (35 ± 4 nm)/Ag (9 ± 1 nm)/NTO

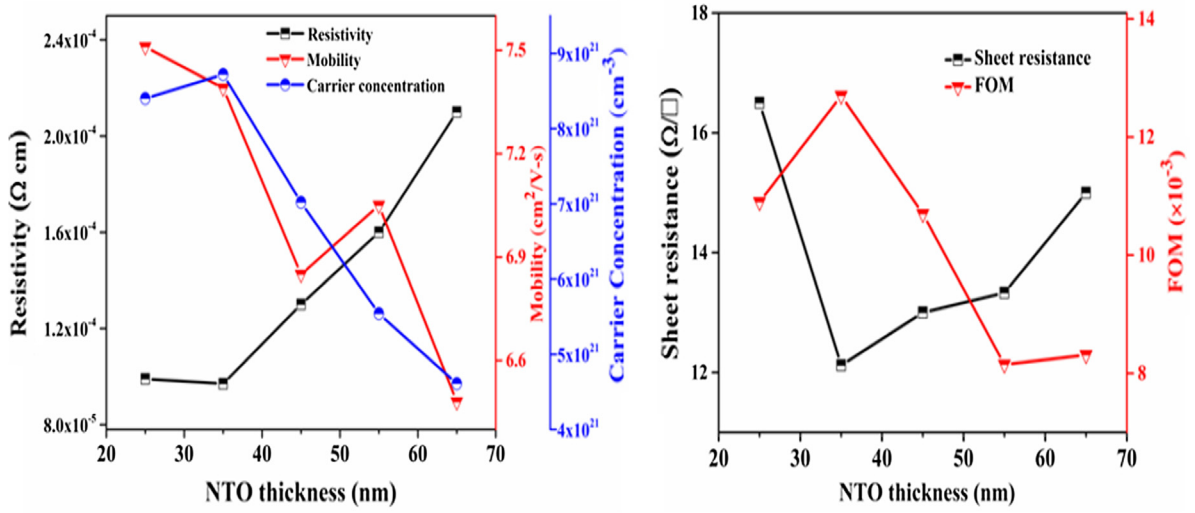

Fig. 2. (a) Resistivity, mobility and carrier concentration and (b) Sheet resistance and the Haacke figure of NAN multilayer films with different NTO thickness.

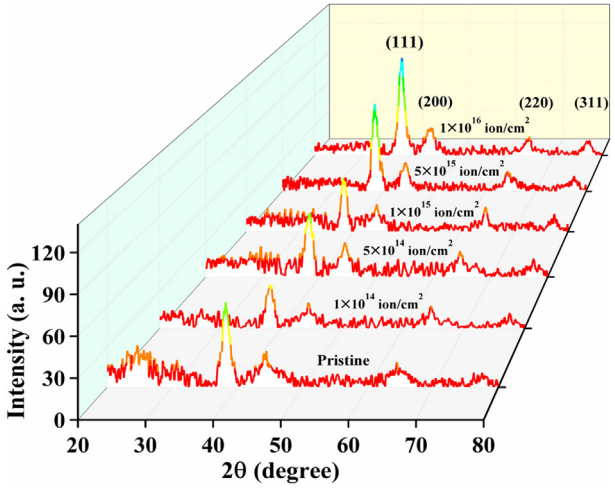

Fig. 3. XRD pattern of NAN multilayer films with different ion fluences.

Table 1
FWHM, crystallite size, lattice constant and residual stress of Ag (1 1 1) plane of pristine NAN and N-NAN multilayer films with different ion fluences.

Samples details	FWHM (deg.)	Crystallite size (nm)	Lattice constant c (Å)	Residual stress (GPa)
0	1.084 ± 0.06	8.1 ± 0.5	4.088 ± 0.007	−0.108
1×10^{14}	1.098 ± 0.05	8.0 ± 0.4	4.089 ± 0.004	−0.172
5×10^{14}	1.141 ± 0.09	7.7 ± 0.6	4.091 ± 0.003	−0.284
1×10^{15}	1.156 ± 0.07	7.6 ± 0.5	4.095 ± 0.007	−0.513
5×10^{15}	1.203 ± 0.12	7.3 ± 0.7	4.094 ± 0.005	−0.456
1×10^{16}	1.237 ± 0.11	7.1 ± 0.6	4.096 ± 0.006	−0.570

(35 ± 4 nm). These RBS results indicate the formation of Nb doped TiO_2 lower and upper layers with pure Ag middle layer. Some of the energetic Ag ions diffused in to TiO_2 layers during the film deposition process. The implantation leads to slight increase in the diffusion length due to transfer of ion energy to the host multilayer films, which is confirmed by RBS measurements (Han et al., 2008).

3.4. Surface characterization

A smooth and homogeneous deposition of top surface of the multilayer films was observed by FESEM, which is essential for the device formation on the electrode. Fig. 5 illustrates the FESEM micrographs of NAN multilayer structures for pristine and N ion implanted films with 1×10^{14}, 5×10^{14}, 1×10^{15}, 5×10^{15} and 1×10^{16} ions/cm^2. All images were recorded at 100 k× magnification. It can be noticed from the images that films composed of spherical shape nanoparticles with 15–30 nm size. The top surface of the pristine film shows regularly arranged particles with smooth surface. On ion implantation, the surface roughens with reduction in particle size. This phenomenon can be understood by existing studies that suggest sputtering of atoms during implantation process. The sputtering causes the removal of atoms from the upper surface and resulting in decrease in particle size and consequently the surface is also becoming rougher. Similar morphology has been observed for the Nb doped TiO_2 films (Singh et al., 2016).

Fig. 6 exhibits a three dimensional AFM images of the pristine NAN and N-NAN multilayer films. The scanning area for these measurements was taken as 2 × 2 μm^2. The top surface depicts continuous formation of the multilayer films. The surface roughness are 1.6 nm, 1.6 nm, 1.7 nm, 1.4 nm, 1.1 nm and 0.7 nm for the pristine, 1×10^{14}, 5×10^{14}, 1×10^{15}, 5×10^{15} and 1×10^{16} ions/cm^2 respectively. The root mean square (rms) roughness of the pristine sample was observed as 1.6 nm, which first increases to 1.7 nm for 1×10^{15} ions/cm^2 fluence and then decreases to 0.7 nm at 1×10^{16} ions/cm^2 fluence. Initially, when the energetic N^+ ions are incident on the top surface of NAN multilayer structure they sputter the atoms from the NTO layer, which causes slight increase in rms roughness. As the energy of N^+ ions further increases, they behave as a cutting tool for the irregularities and microstructures which exist on the surface and consequently the surface roughness decreases. Ion beam interaction, both irradiation and implantation, modifies the surface roughness of film. It results in the smoothening of the surface of specimen and this has been reported by many research groups (Sharma et al., 2017; Thomas et al., 2012, 2009). Thomas et al. (Thomas et al., 2012) observed the smoothening of surface after irradiation and explained that the roughness can be reduced due to irradiation induced surface diffusion or volume diffusion. The material transport in ion beam interactions leads to the surface diffusion and hence the reduction in roughness. Hence, the development of NAN electrodes with use of ion implantation leads to smoother surface, which promotes their applicability in radiation environment (H.J. Lee et al., 2016). NAN films show an average surface roughness of approximately 1.5 nm which is lower than commercial ITO film (≈2.5 nm) and hence is more suitable for TCE applications in optoelectronic devices because higher roughness leads to more scattering of light from the top surface and may reduce flow of current between anode and cathode (Tak et al., 2002).

The surface roughness measured from AFM and particle size calculated from SEM micrographs of NAN multilayer structures at various ion fluences are shown in Fig. 7(a) and (b) respectively. It is clear from the roughness curve and particle size distribution that higher particle size of specimen correspond to higher roughness and lower particle size correspond to lower roughness. A small shift was observed in the flat region of transmittance of NAN films and is mainly attributed to variation in surface morphology. Initially, the optical transmittance reduced by the increased optical scattering of light is due to higher surface roughness (Lee and Park, 2003) and for higher fluences it dominated by the decreasing band gap.

3.5. Optical analysis

The optical transmittance is an important parameter for the transparent electrode and it should as much as high to transmit visible light. Fig. 8(a) shows the transmittance spectra of pristine and N ion implanted NAN multilayer structures in the visible range (350 nm < λ < 800 nm) of light with varying fluence. The transmittance of pristine film is ~83% and it decreases to ~81% as the fluence increases to 1×10^{16} ions/cm^2. A standard ITO film (Sigma-Aldrich, Product Number: 703192, CAS Number: 50926-11-9 with sheet resistance of 8–12 Ω/□) shows an optical transmittance of ~81%. Therefore, the results of NAN films with implantation are comparable with commercial available ITO and ITO/Ag/ITO (Sibin et al., 2017) and AZO/Ag/AZO (Zhou et al., 2012).

The optical band gap of the NAN multilayer structure is determined by using the following standard relation (Tauc, 1974).

$$\alpha h\nu = B(h\nu - E_g)^n \quad (2)$$

where α is absorption coefficient, hν photon energy, B is a constant and Eg is the optical band gap. The value of n is chosen as 2, because TiO_2 is an indirect band gap semiconductor.

Absorption coefficient (α) was measured by the Beer–Lambert's relation (Joseph et al., 2006).

$$\alpha = \frac{1}{d}\ln\frac{1}{T} = \frac{2.303}{d}A \quad (3)$$

where A is absorbance of NAN multilayer film, T is transmittance and d is thickness of the film.

Using the absorption coefficient the band gap of NAN films has been calculated. Fig. 8(b) depict the Tauc plot between $(\alpha h\nu)^{1/2}$ and incident photon energy (hν) for NAN films. The band gap of the pristine film is 2.71 eV and decreases to 2.57 eV at 1×10^{16} ions/cm^2. Generally, the

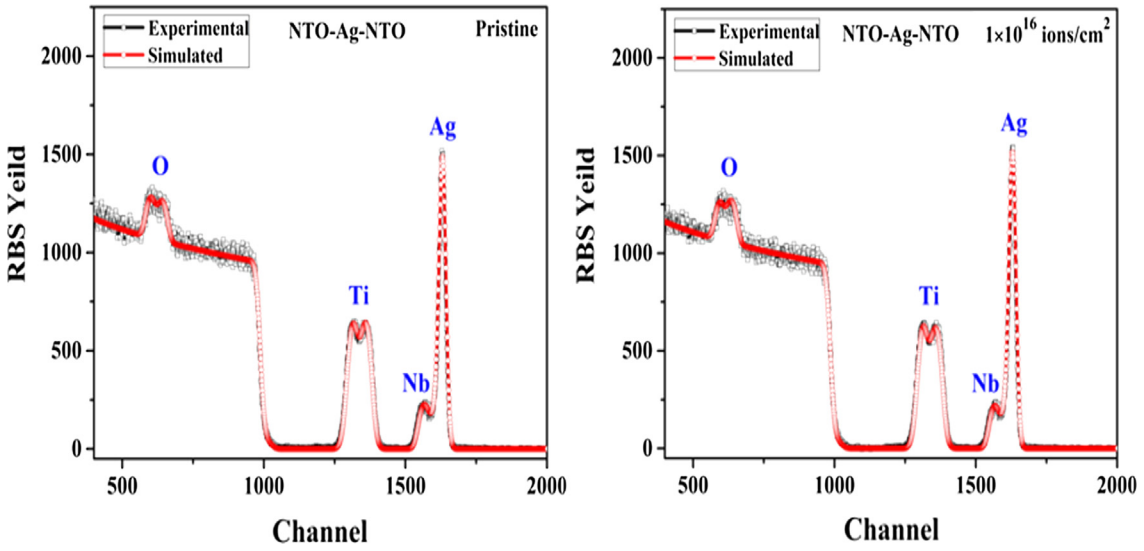

Fig. 4. RBS spectra of pristine NAN and N-NAN multilayer films, with fitted profile.

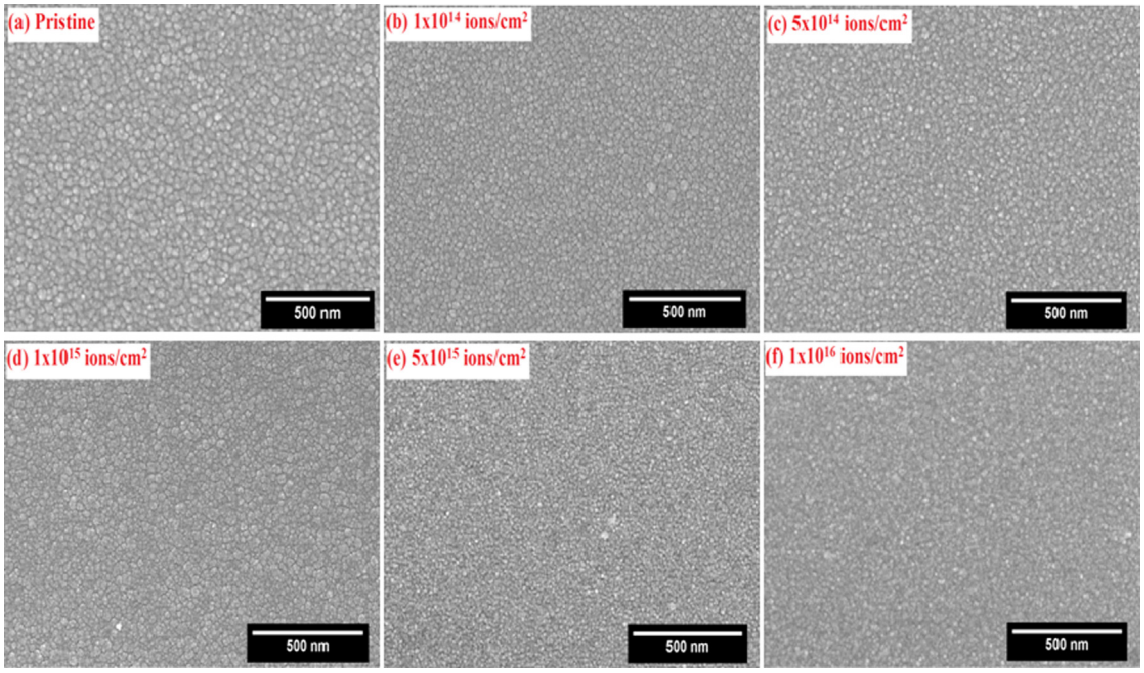

Fig. 5. SEM images of the pristine NAN and N-NAN multilayer films with different ion fluences.

band gap decreases on ion implantation which leads to improve the electrical conductivity. Appearance of Ti^{3+} state of TiO_2 in NTO on substitutional doping of N and increased grain size on implantation are responsible for band gap narrowing for N-NAN system. Morikawa et al. (2001), Wu et al. (2005) and Asahi et al. (2001) have investigated N doping in TiO_2 and found that band gap is narrowing with increasing N concentration and it was suggested that band gap is decreasing due to merging of N 2p states with 2p states of O. Normally, ion implantation causes sputtering of Ag ions from the surface to the oxide layers which generates scattering centres for the incident light and implantation also creates defects resulting in more absorption and decreased transparency. The refractive index plays an important role for tuning the transmittance and antireflective effect in optical materials and can be calculated by following relation (Giulio et al., 1993).

$$n = \sqrt{\frac{4R}{(1-R^2)} - k^2} + \left(\frac{1+R}{1-R}\right) \tag{4}$$

where k is the extinction coefficient and R is reflectivity of multilayer structure. Extinction coefficient is given by:

$$k = \frac{\alpha\lambda}{4\pi} \tag{5}$$

where λ is wavelength and α is absorption coefficient of NAN films. The extinction coefficient of NAN films vary from 0.27 to 0.32 as shown in Table 2. The refractive index of pristine specimen is 2.11 and it increases to 2.21 for 5×10^{15} ions/cm^2 and then decreases to 2.18 for 1×10^{16} ions/cm^2 fluence. The RMS surface roughness, transmittance at wavelength of 550 nm, extinction coefficient, refractive index and band gap of pristine and implanted NAN films are give in Table 2. Extinction coefficient and refractive index curves are presented in the supplementary Figs. S3 and S4 respectively.

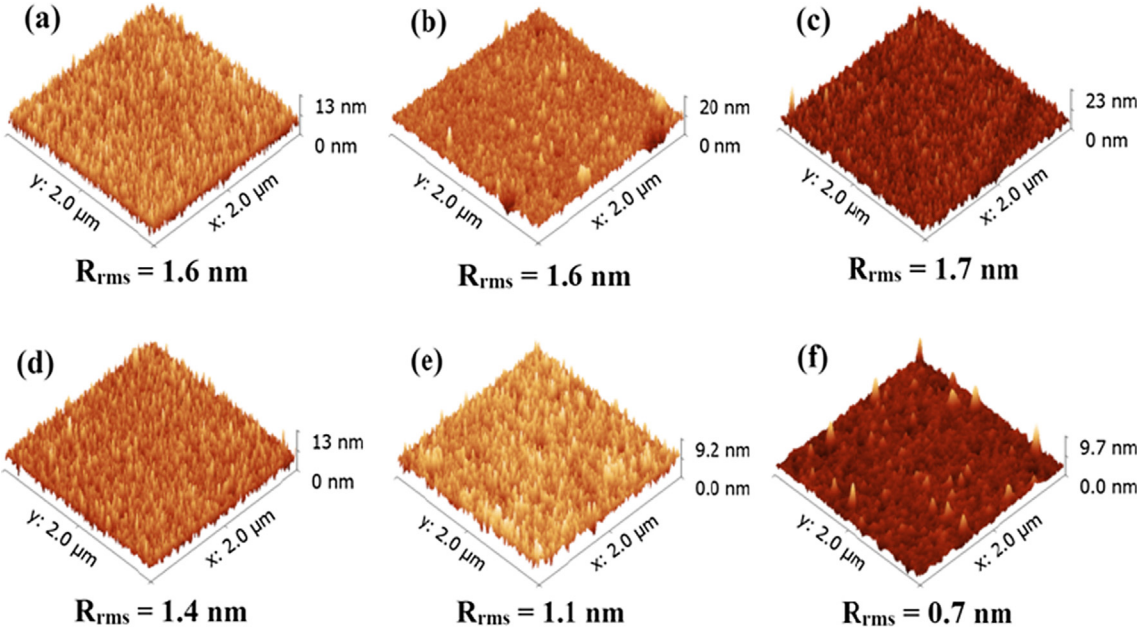

Fig. 6. Three dimensional AFM images of the NAN multilayer films: (a) pristine, and N ion implanted with fluence of (b) 1×10^{14}, (c) 5×10^{14}, (d) 1×10^{15}, (e) 5×10^{15} and (f) 1×10^{16} ions/cm^2.

3.6. Electrical analysis

Electrical resistivity is the other important parameter for TCEs requiring large number of charge carrier concentration with high mobility. Electrical performance of the proposed alternative TCE are compared with that of standard ITO film and is found to be stable in a broad temperature range. The transport properties of as prepared films were investigated by using the Hall measurement with Vander Pauw method (Lamellae and Arbitrary, 1958). The pristine NAN film exhibits resistivity of $9.7 \times 10^{-5}\,\Omega$ cm and sheet resistance of 12.12 Ω/□ at room temperature, and these results are better than commercial ITO film (Product Number: 576360, CAS Number: 50926-11-9). The resistivity of a conductor is given by: $\rho = 1/n_e \mu e$, where n_e is carrier concentration density, μ is mobility; e is charge on the electron. The resistivity of specimen decreases with increase in charge carrier density and the mobility. For the OMO structure, the lower resistivity of the order of $\sim 10^{-4}$ or $\sim 10^{-5}\,\Omega$ cm is mainly obtained because of inter metal layer (Ag). This metal layer needs to be thick enough to provide structural continuity and it should be thin as possible to reduce absorption of light. This thickness is 8–9 nm, as discussed in the introduction part. The oxide layer thickness should be chosen as to minimize the surface plasmon coupling absorption (Kim and Lee, 2012). Hence, the selection of thickness for both layers oxide and metal is crucial to obtain low resistivity and high transparency. Therefore, in the present case, the multilayer was adopted as 35 nm/9 nm/35 nm to address both issues and tuning of thickness of both metal and metal oxide layers, which help us to achieve higher FOM for the prepared TCE. The total resistance for the multilayer structure is obtained by using parallel connection method of three resistances and is given as below:

$$\frac{1}{R_{total}} = \frac{1}{R_{metal}} + \frac{1}{R_{oxide}} + \frac{1}{R_{oxide}}$$

As the two oxide layers are deposited using same parameters, so their resistance can be taken as equal. Hence, above equation can be written as;

$$\frac{1}{R_{total}} = \frac{1}{R_{metal}} + \frac{2}{R_{oxide}}$$

Since $R_{oxide} \geq 1000 R_{metal}$ so $R_{total} \approx R_{metal}$ (Guillén and Herrero, 2011).

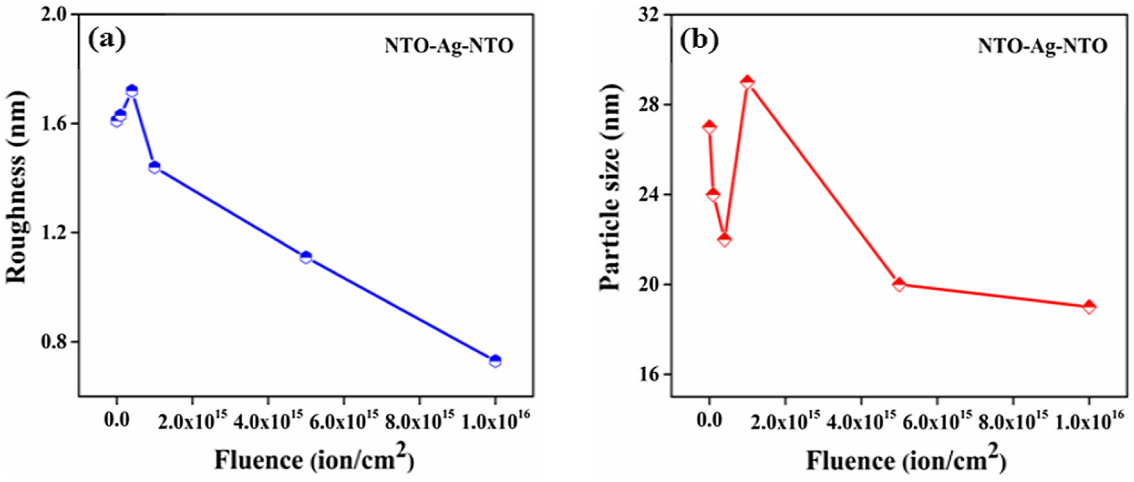

Fig. 7. Morphology of NAN multilayer structure with N^+ ion implantations: (a) Ion fluence vs Surface roughness and (b) ion fluence vs particle size.

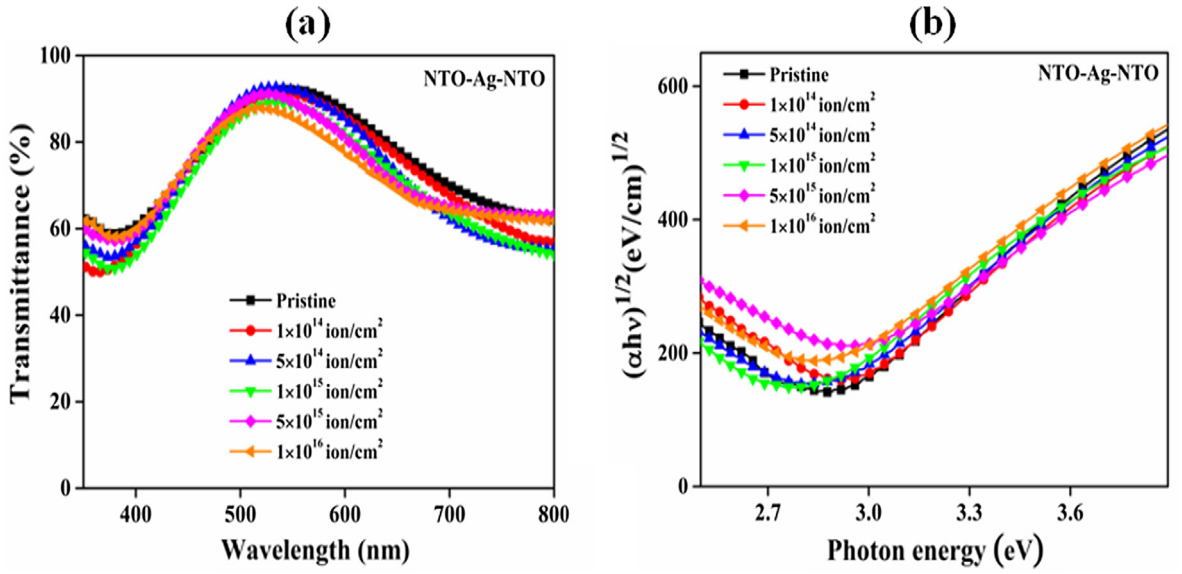

Fig. 8. (a) Transmittance and (b) Tauc plots of pristine NAN and N-NAN multilayer films with different ion fluences.

The resistance of the oxide layer is much higher than the Ag layer, thus the total resistance of embedded multilayer would be equal to middle Ag layer. Hence, the high conductivity of the NAN multilayer films comes entirely from the middle metal layer. The results of resistivity and sheet resistance confirm the continuous formation of Ag layer.

Charge carrier concentration, mobility and sheet resistance have been measured for the specimens in temperature ranging from 80 K to 340 K at an interval of 20 K and shown in Fig. 9. Resistivity and sheet resistance were found to increase with temperature which is a characteristic of degenerate semiconductors. Since, the upper and lower layers in NAN structure is Nb doped TiO_2 (NTO), this gives the system a degenerate semiconductor behavior. Many studies have reported the n-type degenerate semiconductor behavior in Nb doped TiO_2 (Sahasrabudhe et al., 2016), B-doped ZnO films (Myong et al., 2007) and SnO_2/Ag (Yu et al., 2013) systems. In this study, Nb doping in TiO_2 and diffusion of Ag atoms into NTO, both are responsible for variation in resistivity and sheet resistance. A slight variation in carrier concentration and mobility was observed with temperature. The mobility in NAN system is a combined effect of mobility in NTO and Ag layer thickness. The variation in mobility occurs due to grain boundary effect; interface and ionized impurity scattering (Han et al., 2008). Charge carrier density and mobility in degenerate semiconductors do not change with temperature but changes occur due to scattering from interface and ionized impurities. For our films, small variation in n_e and μ is observed at low temperatures, indicating small grain boundary scattering and less thermally activated conductance (Gaspar et al., 2017) but at high temperatures n_e and μ change irregularly (Sharma et al., 2017).

Fig. 10 shows resistivity, carrier concentration and mobility of pristine and N^+ ion implanted NAN mutilayer films for 1×10^{14}, 5×10^{14}, 1×10^{15}, 5×10^{15} and 1×10^{16} ions/cm^2 flence at room temperature. The resistivity changes from $9.7 \times 10^{-5}\,\Omega$ cm to $5.52 \times 10^{-5}\,\Omega$ cm as the fluence increase from 0 to 1×10^{16} ions/cm^2. Simeltaneously, carrier concentration increases from 7.48×10^{21} cm^{-3} to 9.72×10^{21} cm^{-3} and mobility values improve from 8.6 cm^2/V-s to 11.67 cm^2/V-s. Fig. 11 illustrates the sheet resistance and Haacke's FOM variation as a function of ion fluence. It can be seen from the curves that sheet resistance for the pristine specimen is 12.12 Ω/□ and it is reducing to 6.9 Ω/□ at the maximum fluence of 1×10^{16} ions/cm^2. Meanwhile, FOM for as deposited sample was found to $12.7 \times 10^{-3}\,\Omega^{-1}$ and it is increasing with the fluence and reaches to a maximum of $18 \times 10^{-3}\,\Omega^{-1}$ for highest fluence of 1×10^{16} ions/cm^2. For these specimen the Fraser and Cook FOM was also calculated and is given as supplementary data Fig. S5. In our previous work (Singh et al., 2018, 2017b), we have implanted the N^+ and Ar^+ ions in optimized TiO_2/Ag/TiO_2 (45 nm/9 nm/45 nm) multilayer structure and found improved electrical conductivity with FOM of $5.7 \times 10^{-3}\,\Omega^{-1}$ and $5.6 \times 10^{-3}\,\Omega^{-1}$ respectively.

In addition, there are many factors which are responsible to get such superior electrical properties like resistivity of $5.52 \times 10^{-5}\,\Omega$ cm and sheet resistance of 6.9 Ω/□ with > 81% optical transmittance for N-NAN films. Nb doping in TiO_2 causes appearance of Ti^{3+} chemical state of Ti in NTO upper and lower layers of NAN structure and as a result the band gap is reduced. Then, these specimens were exposed to N^+ ion implantation to further enhance the electrical conductivity. The main

Table 2
Surface roughness (RMS), transmittance (at 550 nm), extinction coefficient, refractive index and band gap of pristine NAN and N-NAN multilayer films with different ion fluences.

Samples details	RMS (nm)	Transmittance (%) at 550 nm	Extinction coefficient (k)	Refractive index (n)	Band gap (eV)
0	1.61 ± 0.08	92	0.27	2.11	2.71 ± 0.01
1×10^{14}	1.63 ± 0.08	91	0.29	2.12	2.68 ± 0.01
5×10^{14}	1.72 ± 0.09	90	0.32	2.15	2.65 ± 0.01
1×10^{15}	1.44 ± 0.07	88	0.32	2.16	2.63 ± 0.01
5×10^{15}	1.11 ± 0.05	89	0.30	2.21	2.59 ± 0.01
1×10^{16}	0.73 ± 0.03	86	0.31	2.18	2.57 ± 0.01

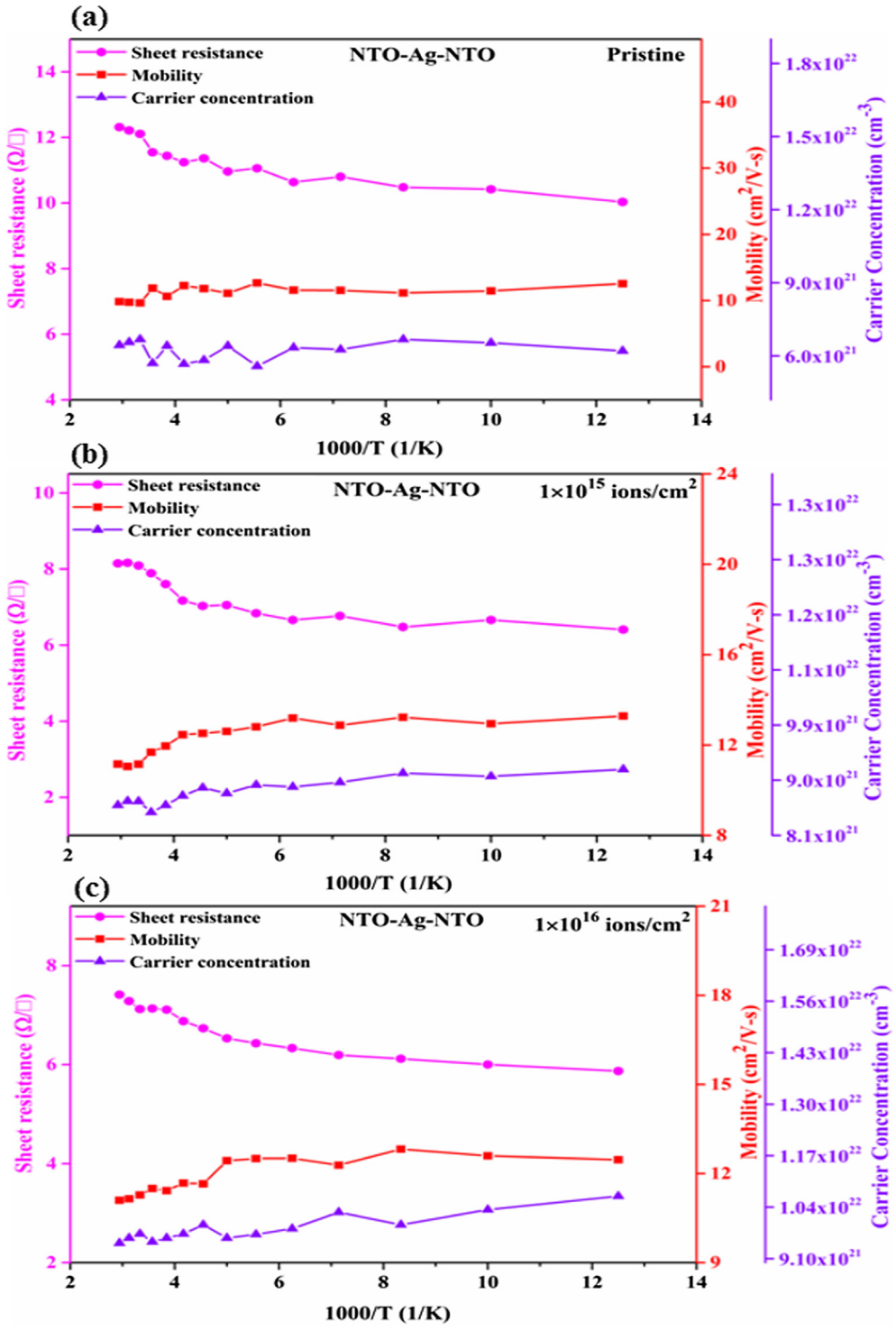

Fig. 9. Resistivity, carrier concentration and Hall mobility of pristine NAN and N-NAN multilayer films for different fluence with temperature variation (a) pristine, (b) 1×10^{15} and (c) 1×10^{16} ions/cm^2.

effect of this implantation was; N^+ ions substituted the oxygen ions into the TiO_2 lattice inserting new electronic states above the valance band. Appearance of Ti^{3+} states of TiO_2 on Nb doping and arising of new electronic states just the valance band after N^+ implantation, both are responsible for band gap narrowing which is confirmed by Tauc's plot shown in Fig. 8(b). The lower band gap leads to lower resistivity and sheet resistance of NAN films. XPS measurements studies confirm that the N^+ ions replaces the O sites by showing the N peak at ~396 eV, reported by many researchers (Asahi et al., 2001; Yoshida et al., 2014) and existence of Ti^{3+} state, positioned at 457 eV binding energy. Besides the substitutional impurity or capturing of electrical active lattice sites, ion implantation generates or anneals the defects and hence causing changes in carrier density and mobility (Fromknecht et al., 1999, 1996). The structural, optical and electrical properties of metal

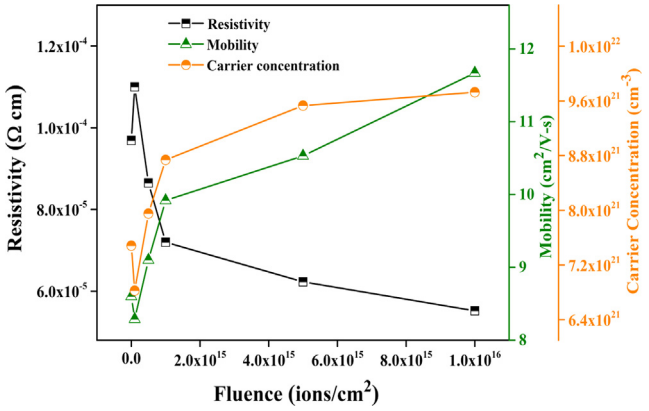

Fig. 10. Resistivity, carrier concentration and Hall mobility of pristine NAN and N-NAN multilayer films with different ion fluences.

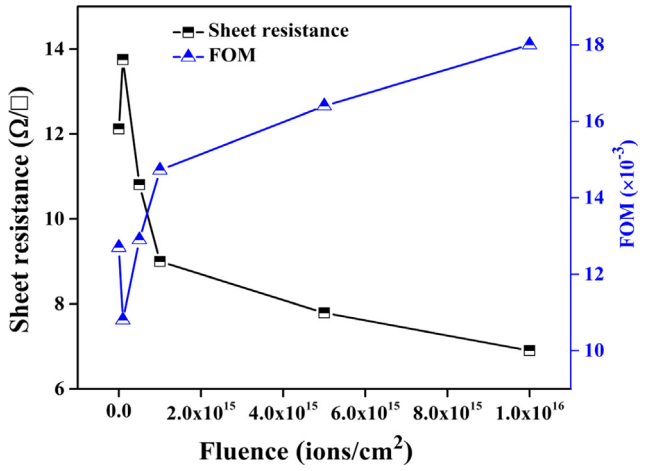

Fig. 11. Sheet resistance and Haacke FOM of pristine NAN and N-NAN multilayer films with different ion fluences.

oxides can be altered by implantation (Fromknecht et al., 1999, 1996; Yang et al., 2006). It has been suggested that, besides N implantation, creation and annealing of charged oxygen vacancies may also help to get lower resistivity. Apart from this, the change in microstructure and decreasing surface roughness on ion implantation may also contribute to improve electrical conductivity. The absorption of oxide donors (Yang et al., 2006) decreases due to reduced grain boundaries and resulting in higher carrier concentration and mobility. Table 3 gives the mobility, carrier concentration, resistivity, sheet resistance and Haacke FOM measured at room temperature for pristine and implanted NAN films.

3.7. X-ray photoelectron spectroscopy

XPS measurements have been performed on pristine NAN and N-NAN multilayer structures to study the chemical states and stoichiometry using surface scan and depth profiling mode. The specific elemental signals were taken from all three layers by etching of previous layer and existence of Ti, Nb, O, Ag and N elements were confirmed in the respective layers. Fig. 12(a) illustrates the survey scan of NAN pristine and N-NAN films, which exhibit high intensity signals of Ti, O and Ag and low intensity signals of Nb, N and C. The C peak arises due to ex-situ transfer of sample to XPS chamber. Fig. 12(b) represents the high resolution scan of Ti 2p for first layer (top) of pristine NAN and N-NAN films. The peak of Ti-$2p_{3/2}$ of pristine film appeared at 458.92 eV (Rao et al., 1979; Sanjinés et al., 1994). The peak positions of Ti-$2p_{3/2}$ and Ti-$2p_{1/2}$ for first NTO layer of pristine sample agreed with the fact of substitution of Ti atom by Nb^{5+} in TiO_2 lattice (Singh et al., 2017a). On implantation Ti $2p_{3/2}$ peak shows peak asymmetry and is deconvoluted in two peaks; one at 459.2 eV (Ti^{4+}) and another at 457 eV is a low energy shoulder assigned to Ti^{3+} peak (Berko et al., 1998). The binding energy of Ti-$2p_{3/2}$ peak is shifted by 0.3 eV on implantation due to change in nature of interaction of Ti with anions in case of pristine NAN and N-NAN structures. The N ion implantation produces considerable modifications in NTO due to dopant-induced strain. The observed binding energy shifts in N implanted NTO is assigned to enhancement of covalent behavior of bond between N and Ti (Jagadale et al., 2008). Fig. 12(c) represents the high resolution scan of O 1s of pristine NAN and N-NAN films. The peak fitting of O 1s of pristine film results in two consecutive peaks, one positioned at 530.05 eV, assigned to O^{2-}, bulk oxygen in TiO_2 (Södergren et al., 1997) and another peak positioned at 531.5 eV, corresponds to OH groups existing on the surface. The peaks of O 1s of N-NAN positioned at 530.12 eV and 531.6 eV correspond to O^{2-} and OH groups respectively. No significant change was observed in O 1s peaks, which indicates that the behavior of the oxygen is not changing on implantation.

Fig. 12(d) represents the core level spectra of Ag 3d of pristine NAN and N-NAN multilayer films. The XPS signals of Ag were taken from middle layer of NAN multilayer structure after etching of first layer by Ar sputtering. The peaks observed at 368.5 eV and 374.5 eV in the Ag spectra are assigned to pristine Ag $3d_{5/2}$ and Ag $3d_{3/2}$ respectively. These peaks were slightly shifted towards lower binding energy for N-NAN films and appear at 368.46 eV (Ag $3d_{5/2}$) and 374.46 eV (Ag $3d_{3/2}$). This shift may occur because of interaction of Ag atoms with Ti, Nb and O ions at the interface (Chen et al., 2011). The XPS spectra of Ag confirms the metallic nature of the middle metal layer ensuring the stability of silver layer against the oxidation. This stability of Ag layer will contribute to electrical behavior of both pristine and implanted samples. Fig. 12(e) illustrates the high resolution scans of the XPS spectra of Nb 3d for the both samples. Pristine film exhibits two peaks at 207.12 eV and 209.85 eV, attributed to Nb $3d_{5/2}$ and Nb $3d_{3/2}$, respectively. The spin-orbit splitting between these two peaks is 2.73 eV. The Nb in NTO of the upper and lower films are found to be in Nb^{5+} state (Su et al., 2015). Fig. 12(f) exhibits the high resolution scan of N

Table 3
Room temperature mobility, Carrier concentration, resistivity, sheet resistance and Haacke FOM of pristine NAN and N-NAN multilayer films with different ion fluences.

Samples details	Mobility (cm^2/V-s)	Carrier concentration (cm^{-3})	Resistivity (Ω·cm)	Sheet resistance (Ω/□)	Haacke FOM ($10^{-3}\,\Omega^{-1}$)
0	8.61	7.48×10^{21}	9.69×10^{-5}	12.12	12.7
1×10^{14}	8.29	6.82×10^{21}	1.10×10^{-4}	13.75	10.8
5×10^{14}	9.11	7.95×10^{21}	8.65×10^{-5}	10.81	12.9
1×10^{15}	9.92	8.73×10^{21}	7.22×10^{-5}	9.01	14.7
5×10^{15}	10.53	9.53×10^{21}	6.23×10^{-5}	7.79	16.4
1×10^{16}	11.67	9.72×10^{21}	5.52×10^{-5}	6.92	18.0

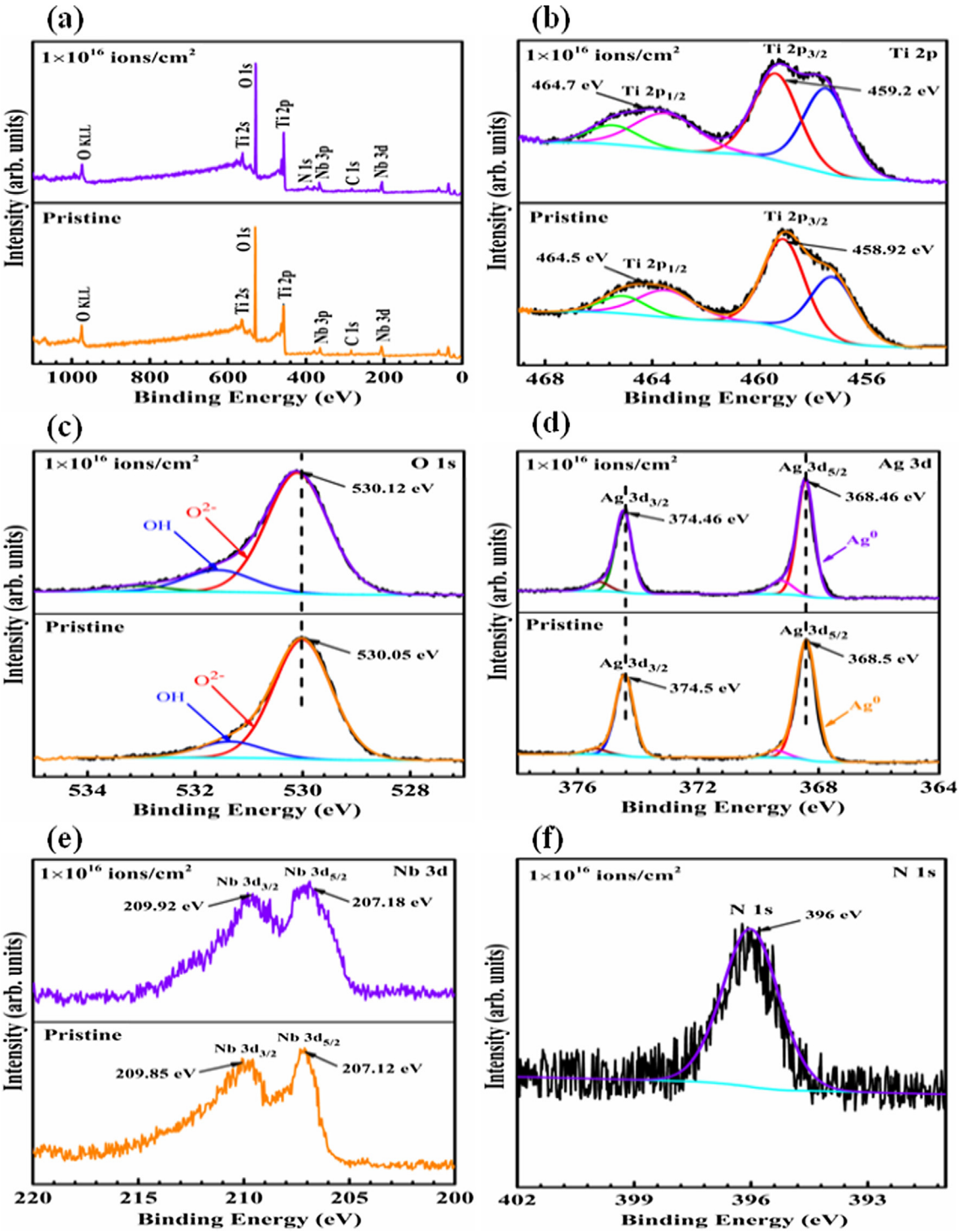

Fig. 12. XPS spectra of pristine NAN and N^+ implanted NAN multilayer films with the fluence of 1×10^{16} ions/cm^2 (a) survey scan, (b) Ti 2p, (c) O 1s, (d) Ag 3d, (e) Nb 3d and (f) N 1s.

1s that was obtained from N implanted NAN films at the highest fluence 1×10^{16} ions/cm^2. For this specimen the N peak appeared at ~396 eV suggesting replacement of O sites in the TiO_2 lattice by N (Yoshida et al., 2014). This XPS study of NAN pristine and implanted films confirmed the presence of Ti, O, Nb, Ag and N in multilayer structure. The Nb core level spectra revealed the substitution of Ti atoms by Nb atoms and formation of Nb-O bond. The N core level spectra explain the substitution of O ions by N ions, resulting in the decrease in the band gap and improving the electrical conductivity giving higher FOM.

Fig. 13 exhibits the UPS spectrum for the pristine NTO/Ag/NTO films. The binding energy of the electrons right at secondary cutoff is calculated using the secondary edge. The work function of the films has been determined directly from the graph by taking the difference of the energy of the UV photons (21.2 eV in this case) and the binding energy of secondary cutoff (16.57 eV in the case of NAN films), i.e. $\Phi_{NAN} = 21.2\,eV - 16.57\,eV = 4.63\,eV$.

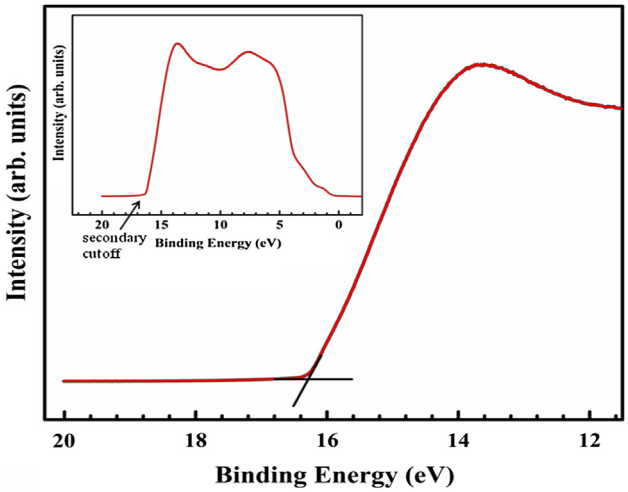

Fig. 13. UPS measurements of pristine NAN multilayer films.

The work function of NAN films to be used as transparent electrode in photovoltaics can be tuned according to work function of active layer and hence the efficiency of device can be improved. It has been reported that high work function of TCO leads to higher efficiency; higher open circuit voltage and larger photo generated current (Chen et al., 2016).

The conducting mechanism of NAN multilayer structure can be understood by the energy level diagram of NTO and Ag. Fig. 14 shows the E_f alignment at the interface in multilayer structure. NAN films are prepared using two materials with different work functions NTO (4.8 eV) and Ag (4.4 eV). Before contact the E_f of both materials are not aligned but when two materials come into contact at interface the electrons are transferred from Ag to NTO due to band bending as alignment of E_f occurs. This explains the conduction in the multilayer through the middle Ag layer.

4. Conclusion

In this work, the effect of N^+ ion implantation on the electrical and optical properties of NTO/Ag/NTO multilayer films has been explored. Incorporation of N^+ ions in the NTO matrix leads to the oxygen replacement by N^+ ions and this influences the physical properties of the system. The XRD confirms the amorphous nature of TiO_2 and crystalline Ag with dominant peak at 38.2°. The optimization of the NTO thickness has been reported and NTO/Ag/NTO (~35 nm/~9 nm/~35 nm) with highest FOM ($12.7 \times 10^{-3}\,\Omega^{-1}$) is chosen for N^+ ion implantation. The chemical states of N ions measured using XPS exhibit that the N^+ replaces O sites by showing the peak postion at 396 eV. The UPS results suggest that the work function of NAN films matches well with that of the active layer of the photovoltaic and TCE with proper work function can be used to fabricate a photovoltaic cell with better performance. The smooth morphology and low surface roughness (< 2 nm) make them suitable for TCE applications. The optical transmittance varies from ~83% to ~81% as the ion fluence increases from 0 to 1×10^{16} ions/cm^2, and the band gap of the NAN films decreases from 2.71 to 2.57 eV with fluence. The main motivation of N^+ ion implantation in this study was to reduce the band gap and lower the resistivity keeping optimum transparency. The electrical resistivity is found to decrease from $9.69 \times 10^{-5}\,\Omega$ cm to $5.52 \times 10^{-5}\,\Omega$ cm and sheet resistance also varies from 12.12 Ω/□ to 6.9 Ω/□ with increasing fluence. The maximum FOM of $18 \times 10^{-3}\,\Omega^{-1}$ is obtained for the fluence of 1×10^{16} ions/cm^2. The N^+ ion implanted NAN multilayer films with low sheet resistance and high transmittance provide an alternative to ITO and can be used as futuristic TCE giving enhanced performance.

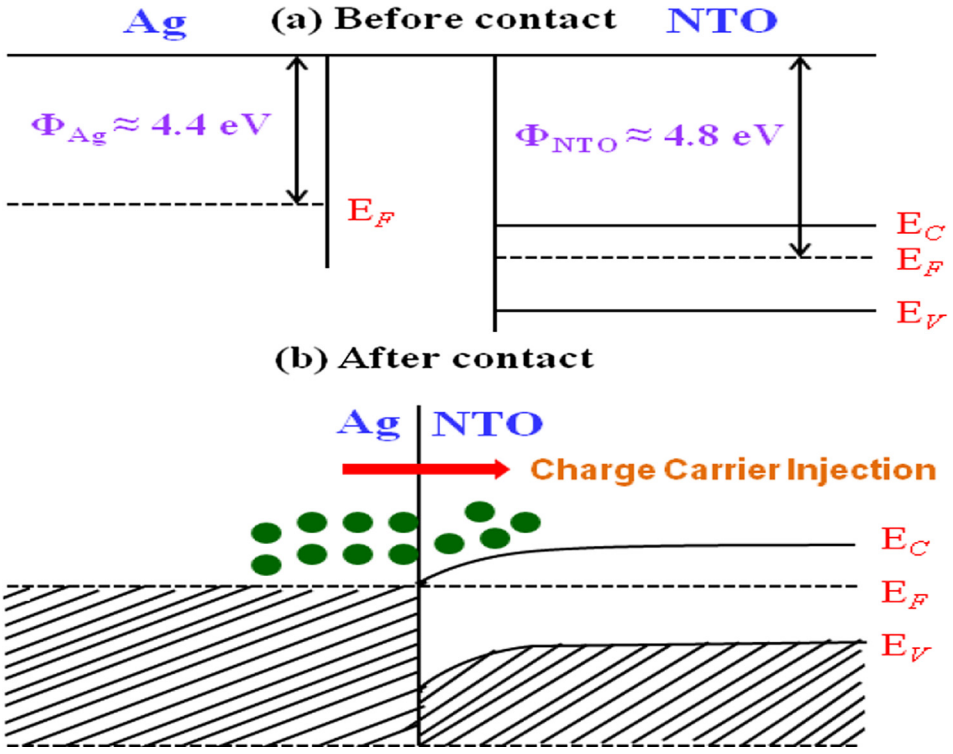

Fig. 14. The energy level diagrams of NTO and Ag before and after contact and show the E_f alignment at the interface.

Acknowledgement

Authors are grateful to Materials Research Centre, MNIT Jaipur, India for providing the deposition and characterization facilities and Inter University Accelerator Center (IUAC), New Delhi, India for the low energy ion implantation facility. Authors are also thankful to Mr. Sunil Ojha and Dr. Parmod Kumar at IUAC, New Delhi for RBS measurements and ion implantation studies respectively.

References

Asahi, R., Mikawa, T., Ohwaki, T., Aoki, K., Taga, Y., 2001. Visible light photocatalysis in nitrogen-doped titanium oxides. Science 293, 269–271. https://doi.org/10.1126/science.1061051.

Ayadi, Z. Ben, Mahdhi, H., Djessas, K., Gauf, J.L., Mir, L. El, Alaya, S., 2014. Sputtered Al-doped ZnO transparent conducting thin films suitable for silicon solar cells. Thin Solid Films 553, 123–126.

Bae, S., Kim, H.K., Lee, Y., Xu, X., Park, J.-S., Zheng, Y., Balakrishnan, J., Im, D., Lei, T., Song, Y. Il, Kim, Y.J., Kim, K.S., Özyilmaz, B., Ahn, J.-H., Hong, B.H., Iijima, S., 2009. 30 inch roll-based production of high-quality graphene films for flexible transparent electrodes. Nature Nanotech. 5, 1–5. https://doi.org/10.1038/nnano.2010.132.

Bender, M., Seelig, W., Daube, C., Frankenberger, H., Ocker, B., Stollenwerk, J., 1998. Dependence of film composition and thicknesses on optical and electrical properties of ITO–metal–ITO multilayers. Thin Solid Films 326, 67–71. https://doi.org/10.1016/S0040-6090(98)00520-3.

Berko, A., Ulrych, I., Prince, K.C., 1998. Encapsulation of Rh nanoparticles supported on TiO_9(110)-(1x1) surface: XPS and STM studies. J. Phys. Chem. B 102, 3379–3386. https://doi.org/10.1021/jp973255g.

Cattin, L., Morsli, M., Dahou, F., Abe, S.Y., Khelil, A., Bernède, J.C., 2010. Investigation of low resistance transparent MoO_3/Ag/MoO_3 multilayer and application as anode in organic solar cells. Thin Solid Films 518, 4560–4563. https://doi.org/10.1016/j.tsf.2009.12.031.

Chen, A., Zhu, K., Shao, Q., Ji, Z., 2016. Understanding the effects of TCO work function on the performance of organic solar cells by numerical simulation. Semicond. Sci. Technol. 31, 1–6. https://doi.org/10.1088/0268-1242/31/6/065025.

Chen, R., Zou, C., Bian, J., Sandhu, A., Gao, W., 2011. Microstructure and optical properties of Ag-doped ZnO nanostructures prepared by a wet oxidation doping process. Nanotechnology 22, 105706. https://doi.org/10.1088/0957-4484/22/10/105706.

Colangelo, G., Favale, E., Miglietta, P., De Risi, A., 2016. Innovation in flat solar thermal collectors: a review of the last ten years experimental results. Renew. Sustain. Energy Rev. 57, 1141–1159. https://doi.org/10.1016/j.rser.2015.12.142.

Dhar, A., Alford, T.L., 2013. High quality transparent TiO_2/Ag/TiO_2 composite electrode films deposited on flexible substrate at room temperature by sputtering. APL Mater. 1, 10–17. https://doi.org/10.1063/1.4808438.

Ehrenreich, H., Philipp, H.R., 1962. Optical properties of Ag and Cu. Phys. Rev. 128, 1622–1629. https://doi.org/10.1103/PhysRev. 128.1622.

Ellmer, K., 2012. Past achievements and future challenges in the development of optically transparent electrodes. Nat. Photo. 6, 808–816. https://doi.org/10.1038/nphoton.2012.282.

Fromknecht, R., Auer, R., Khubeis, I., Meyer, O., 1996. Lattice location and electrical conductivity in ion implanted TiO_2 single crystals. Nucl. Instrum. Methods Phys. Res. Sect. B 120, 252–256. https://doi.org/10.1016/s0168-583x(96)00520-4.

Fromknecht, R., Khubeis, I., Massing, S., Meyer, O., 1999. Ion implantation in TiO_2: damage production and recovery, lattice site location and electrical conductivity. Nucl. Instrum. Methods Phys. Res., Sect. B 147, 191–201. https://doi.org/10.1016/S0168-583X(98)00551-5.

Gaspar, D., Pereira, L., Gehrke, K., Galler, B., Fortunato, E., Martins, R., 2017. High mobility hydrogenated zinc oxide thin films. Sol. Energy Mater. Sol. Cells 163, 255–262. https://doi.org/10.1016/j.solmat.2017.01.030.

Girtan, M., 2012. Comparison of ITO/metal/ITO and ZnO/metal/ZnO characteristics as transparent electrodes for third generation solar cells. Sol. Energy Mater. Sol. Cells 100, 153–161. https://doi.org/10.1016/j.solmat.2012.01.007.

Giulio, M. Di, Micocci, G., Rella, R., Siciliano, P., Tepore, A., 1993. Optical Absorption of Tellurium Suboxide Thin Films. Phys. Stat. Sol. (a) 136, K101–K104. https://doi.org/10.1002/pssa.2211360236.

Green, M.A., 2007. Thin-film solar cells: review of materials, technologies and commercial status. J. Mater. Sci.: Mater. Electron. 18, 15–19. https://doi.org/10.1007/s10854-007-9177-9.

Guillén, C., Herrero, J., 2011. TCO/metal/TCO structures for energy and flexible electronics. Thin Solid Films 520, 1–17. https://doi.org/10.1016/j.tsf.2011.06.091.

Guillén, C., Herrero, J., 2010. Transparent electrodes based on metal and metal oxide stacked layers grown at room temperature on polymer substrate. Phys. Stat. Sol. (A) Appl. Mater. Sci. 207, 1563–1567. https://doi.org/10.1002/pssa.200983707.

Guillén, C., Herrero, J., 2009. Transparent conductive ITO/Ag/ITO multilayer electrodes deposited by sputtering at room temperature. Opt. Commun. 282, 574–578. https://doi.org/10.1016/j.optcom.2008.10.075.

Guillén, C., Herrero, J., 2008. ITO/metal/ITO multilayer structures based on Ag and Cu metal films for high-performance transparent electrodes. Sol. Energy Mater. Sol. Cells 92, 938–941. https://doi.org/10.1016/j.solmat.2008.02.038.

Günes, S., Neugebauer, H., Sariciftci, N.S., 2007. Conjugated polymer-based organic solar cells. Chem. Rev. (Washington, DC, U.S.) 107, 1324–1338. https://doi.org/10.1021/cr050149z.

Ha, Y.H., Nikolov, N., Pollack, S.K., Mastrangelo, J., Martin, B.D., Shashidhar, R., 2004. Towards a transparent, highly conductive poly (3,4-ethylenedioxythiophene). Adv. Funct. Mater. 14, 615–622. https://doi.org/10.1002/adfm.200305059.

Haacke, G., Haacke, G., 1976. New figure of merit for transparent conductors. J. Appl. Phys. 4086, 1. https://doi.org/10.1063/1.323240.

Han, H., Theodore, N.D., Alford, T.L., 2008. Improved conductivity and mechanism of carrier transport in zinc oxide with embedded silver layer. J. Appl. Phys. 103. https://doi.org/10.1063/1.2829788.

Hashimoto, K., Irie, H., Fujishima, A., 2007. A historical overview and future prospects. AAPPS Bull. 17, 12–28. https://doi.org/10.1007/BF00290457.

Hecht, D.S., Hu, L., Irvin, G., 2011. Emerging transparent electrodes based on thin films of carbon nanotubes, graphene, and metallic nanostructures. Adv. Mater. 23, 1482–1513. https://doi.org/10.1002/adma.201003188.

Heo, C.H., Lee, S.-B., Boo, J.-H., 2005. Deposition of TiO_2 thin films using RF magnetron sputtering method and study of their surface characteristics. Thin Solid Films 475, 183–188. https://doi.org/10.1016/j.tsf.2004.08.033.

Hitosugi, T., Yamada, N., Nakao, S., Hirose, Y., Hasegawa, T., 2010. Properties of TiO_2-based transparent conducting oxides. Phys. Stat. Sol. (a) 207, 1529–1537. https://doi.org/10.1002/pssa.200983774.

Indluru, A., Alford, T.L., 2009. Effect of Ag thickness on electrical transport and optical properties of indium tin oxide-Ag-indium tin oxide multilayers. J. Appl. Phys. 105. https://doi.org/10.1063/1.3153977.

Jagadale, T.C., Takale, S.P., Sonawane, R.S., Joshi, H.M., Patil, S.I., Kale, B.B., Ogale, S.B., 2008. N-doped TiO_2 nanoparticle based visible light photocatalyst by modified peroxide sol-gel method. J. Phys. Chem. C 112, 14595–14602. https://doi.org/10.1021/jp803567f.

Joseph, B., Manoj, P.K., Vaidyan, V.K., 2006. Studies on the structural, electrical and optical properties of Al-doped ZnO thin films prepared by chemical spray deposition. Ceram. Int. 32, 487–493. https://doi.org/10.1016/j.ceramint.2005.03.029.

Kim, A., Won, Y., Woo, K., Kim, C.H., Moon, J., 2013. Highly transparent low resistance ZnO/Ag nanowire/ZnO composite electrode for thin film solar cells. ACS Nano 7, 1081–1091. https://doi.org/10.1021/nn305491x.

Kim, J.H., Kim, D.H., Seong, T.Y., 2015. Realization of highly transparent and low resistance TiO_2/Ag/TiO_2 conducting electrode for optoelectronic devices. Ceram. Int. 41, 3064–3068. https://doi.org/10.1016/j.ceramint.2014.10.148.

Kim, S., Lee, J.-L., 2012. Design of dielectric/metal/dielectric transparent electrodes for flexible electronics. J. Photo. Energy 2, 21215. https://doi.org/10.1117/1.JPE.2.021215.

Koike, K., Fukuda, S., 2008. Multilayer transparent electrode consisting of silver alloy layer and metal oxide layers for organic luminescent electronic display device. J. Vacu. Sci. Technol. A: Vacu. Surf. Films 26, 444–454. https://doi.org/10.1116/1.2897315.

Kumar, A., Zhou, C., 2010. The race to replace tin-doped indium oxide: which material will win? ACS Nano 4, 11–14. https://doi.org/10.1021/nn901903b.

Kumar, V., Singh, F., Ntwaeaborwa, O.M., Swart, H.C., 2013. Effect of Br + 6 ions on the structural, morphological and luminescent properties of ZnO/Si thin films. Appl. Surf. Sci. 279, 472–478. https://doi.org/10.1016/j.apsusc.2013.04.145.

Lamellae, O.N., Arbitrary, O.F., 1958. a M,Ethod of measuring the resistivity and hall' coefficient on lamellae of arbitrary shape. Phillps Tech. Rev 1958, 220–224.

Lee, H.J., Kang, J.W., Hong, S.H., Song, S.H., Park, S.J., 2016a. $Mg_xZn_{1x}O$/Ag/$Mg_xZn_{1-x}O$ multilayers as high-performance transparent conductive electrodes. ACS Appl. Mater. Interfaces 8, 1565–1570. https://doi.org/10.1021/acsami.5b09974.

Lee, H.M., Kim, S.S., Kim, H.K., 2016b. Artificially MoO_3graded ITO anodes for acidic buffer layer free organic photovoltaics. Appl. Surf. Sci. 364, 340–348. https://doi.org/10.1016/j.apsusc.2015.12.171.

Lee, J.H., Park, B.O., 2003. Transparent conducting ZnO:Al, In and Sn thin films deposited by the sol-gel method. Thin Solid Films 426, 94–99. https://doi.org/10.1016/S0040-6090(03)00014-2.

Lei, H., Qin, P., Ke, W., Guo, Y., Dai, X., Chen, Z., Wang, H., Li, B., Zheng, Q., Fang, G., 2015. Performance enhancement of polymer solar cells with high work function CuS modified ITO as anodes. Organ. Electron. Phys. Mater. Appl. 22, 173–179. https://doi.org/10.1016/j.orgel.2015.03.051.

Liu, L., Ma, S., Wu, H., Zhu, B., Yang, H., Tang, J., Zhao, X., 2015. Effect of the annealing process on electrical and optical properties of SnO_2/Ag/SnO_2 nanometric multilayer film. Mater. Lett. 149, 43–46. https://doi.org/10.1016/j.matlet.2015.02.093.

Mohamed, S.H., 2008. Effects of Ag layer and ZnO top layer thicknesses on the physical properties of ZnO/Ag/Zno multilayer system. J. Phys. Chem. Solids 69, 2378–2384. https://doi.org/10.1016/j.jpcs.2008.03.019.

Morikawa, T., Asahi, R., Ohwaki, T., Aoki, K., Taga, Y., 2001. Band-gap narrowing of titanium dioxide by nitrogen doping. Jpn. J. Appl. Phys. 40, L561–L563. https://doi.org/10.1143/JJAP.40.L561.

Myong, S.Y., Steinhauser, J., Schlüchter, R., Faÿ, S., Vallat-Sauvain, E., Shah, A., Ballif, C., Rüfenacht, A., 2007. Temperature dependence of the conductivity in large-grained boron-doped ZnO films. Sol. Energy Mater. Sol. Cells 91, 1269–1274. https://doi.org/10.1016/j.solmat.2007.04.022.

Park, J.H., Lee, D.Y., Kim, Y.H., Kim, J.K., Lee, J.H., Park, J.H., Lee, T.W., Cho, J.H., 2014. Flexible and transparent metallic grid electrodes prepared by evaporative assembly. ACS Appl. Mater. Interfaces 6, 12380–12387. https://doi.org/10.1021/am502233y.

Po, R., Carbonera, C., Bernardi, A., Camaioni, N., 2011. The role of buffer layers in polymer solar cells. Energy Environ. Sci. 4, 285–310. https://doi.org/10.1039/C0EE00273A.

Qi, J.-H., Li, Y., Duong, T.-T., Choi, H.-J., Yoon, S.-G., 2013. Dye-sensitized solar cell based on AZO/Ag/AZO multilayer transparent conductive oxide film. J. Alloy. Compd. 556, 121–126. https://doi.org/10.1016/j.jallcom.2012.12.127.

Rao, C.N.R., Sarma, D.D., Vasudevan, S., Hegde, M.S., 1979. Study of transition metal oxides by photoelectron spectroscopy. Proc. the Roy. Soc. A: Math. Phys. Eng. Sci.

367, 239–252. https://doi.org/10.1098/rspa.1979.0085.
Sahasrabudhe, G., Krizan, J., Bergman, S.L., Cava, R.J., Schwartz, J., 2016. Million-fold increase of the conductivity in TiO_2 rutile through 3% niobium incorporation. Chem. Mater. 28, 3630–3633. https://doi.org/10.1021/acs.chemmater.6b02031.
Sanjinés, R., Tang, H., Berger, H., Gozzo, F., Margaritondo, G., Lévy, F., 1994. Electronic structure of anatase TiO_2 oxide. J. Appl. Phys. 75, 2945–2951. https://doi.org/10.1063/1.356190.
Sharma, V., Kumar, P., Kumar, A., Surbhi, Asokan, K., Sachdev, K., 2017. High-performance radiation stable ZnO/Ag/ZnO multilayer transparent conductive electrode. Sol. Energy Mater. Sol. Cells 169, 122–131. https://doi.org/10.1016/j.solmat.2017.05.009.
Sharma, V., Vyas, R., Bazylewski, P., Chang, G.S., Asokan, K., Sachdev, K., 2016a. Probing the highly transparent and conducting SnO_x/Au/SnO_x structure for futuristic TCO. RSC Adv. 29135–29141. https://doi.org/10.1039/C5RA24422F.
Sharma, V., Singh, S., Asokan, K., Sachdev, K., 2016b. A study on 100 MeV O 7 + irradiated SnO_2/Ag/SnO_2 multilayer as transparent electrode for flat panel display application. Nucl. Inst. Methods Phys. Res. B 2–6. https://doi.org/10.1016/j.nimb.2016.04.059.
Sibin, K.P., Srinivas, G., Shashikala, H.D., Dey, A., Sridhara, N., Kumar Sharma, A., Barshilia, H.C., 2017. Highly transparent and conducting ITO/Ag/ITO multilayer thin films on FEP substrates for flexible electronics applications. Sol. Energy Mater. Sol. Cells 172, 277–284. https://doi.org/10.1016/j.solmat.2017.08.001.
Singh, S., Sharma, V., Sachdev, K., 2017a. Investigation of effect of doping concentration in Nb-doped TiO_2 thin films for TCO applications. J. Mater. Sci. 52, 11580–11591. https://doi.org/10.1007/s10853-017-1328-7.
Singh, S., Sharma, V., Sachdev, K., 2016. Investigation of post annealing effects on Nb:TiO_2 transparent conducting thin films. Adv. Sci. Lett. 22.
Singh, S., Sharma, V., Saini, D., Shekhawat, S., Asokan, K., Sachdev, K., 2018. Influence of 100 keV Ar^+ implantation on electrical and optical properties of TiO_2/Ag/TiO_2 multilayer films. Mater. Sci. Semicond. Process. 75, 18–25. https://doi.org/10.1016/j.mssp.2017.11.016.
Singh, S., Sharma, V., Surbhi, Saini, D., Asokan, K., Sachdev, K., 2017b. Fabrication of highly efficient TiO_2/Ag/TiO_2 multilayer transparent conducting electrode with N ion implantation for optoelectronic applications. Ceram. Int. 43, 9759–9768. https://doi.org/10.1016/j.ceramint.2017.04.152.
Sivaramakrishnan, K., Theodore, N.D., Moulder, J.F., Alford, T.L., 2009. The role of copper in ZnO/Cu/ZnO thin films for flexible electronics. J. Appl. Phys. 106. https://doi.org/10.1063/1.3213385.
Södergren, S., Siegbahn, H., Rensmo, H., Lindström, H., Hagfeldt, A., Lindquist, S.-E., 1997. Lithium intercalation in nanoporous anatase TiO_2 studied with XPS. J. Phys. Chem. B 101, 3087–3090. https://doi.org/10.1021/jp9639399.
Stepanov, A.L., 2012. Applications of ion implantation for modification of TiO_2: a review. Rev. Adv. Mater. Sci. 30, 150–165.
Su, H., Huang, Y.T., Chang, Y.H., Zhai, P., Hau, N.Y., Cheung, P.C.H., Yeh, W.T., Wei, T.C., Feng, S.P., 2015. The synthesis of Nb-doped TiO_2 nanoparticles for improved-performance dye sensitized solar cells. Electrochim. Acta 182, 230–237. https://doi.org/10.1016/j.electacta.2015.09.072.
Sun, G.Y., Cao, X., Zhou, H., Bao, S., Jin, P., 2017. A novel multifunctional thermochromic structure with skin comfort design for smart window application. Sol. Energy Mater. Sol. Cells 159, 553–559. https://doi.org/10.1016/j.solmat.2016.09.045.
Surbhi, Sharma, V., Singh, S., Garg, P., Asokan, K., Sachdev, K., 2018. Enhanced electrical conductivity in Xe ion irradiated CNT based transparent conducting electrode on PET substrate. Mater. Res. Express 5, 025037. https://doi.org/10.1088/2053-1591/aaaele.
Tak, Y.H., Kim, K.B., Park, H.G., Lee, K.H., Lee, J.R., 2002. Criteria for ITO (indium-tin-oxide) thin film as the bottom electrode of an organic light emitting diode. Thin Solid Films 411, 12–16. https://doi.org/10.1016/S0040-6090(02)00165-7.
Tauc, J., 1974. Optical properties of amorphous semiconductors. Amorph. Liq. Semicond. 159–220. https://doi.org/10.1007/978-1-4615-8705-7_4.
Thomas, H., Thomas, S., Ramanujan, R.V., Avasthi, D.K., Al- Omari, I.A., Al-Harthi, S., Anantharaman, M.R., 2012. Swift heavy ion induced surface and microstructural evolution in metallic glass thin films. Nucl. Instrum. Methods Phys. Res., Sect. B Beam Interact. Mater. Atoms 287, 85–90. https://doi.org/10.1016/j.nimb.2012.05.039.
Thomas, S., Thomas, H., Avasthi, D.K., Tripathi, A., Ramanujan, R.V., Anantharaman, M.R., 2009. Swift heavy ion induced surface modification for tailoring coercivity in Fe-Ni based amorphous thin films. J. Appl. Phys. 105. https://doi.org/10.1063/1.3075581.
Tucker, R.T., Beckers, N.A., Fleischauer, M.D., Brett, M.J., 2012. Electron beam deposited Nb-doped TiO_2 toward nanostructured transparent conductive thin films. Thin Solid Films 525, 28–34. https://doi.org/10.1016/j.tsf.2012.10.075.
Wu, P., Ma, C., Shang, J., 2005. Effects of nitrogen doping on optical properties of TiO_2 thin films. Appl. Phys. A: Mater. Sci. Process. 81, 1411–1417. https://doi.org/10.1007/s00339-004-3101-4.
Yang, C.-H., Lee, S.-C., Chen, S.-C., Lin, T.-C., 2006. The effect of annealing treatment on microstructure and properties of indium tin oxides films. Mater. Sci. Eng. B 129, 154–160. https://doi.org/10.1016/j.mseb.2006.01.012.
Yoshida, T., Niimi, S., Yamamoto, M., Nomoto, T., Yagi, S., 2014. Effective nitrogen doping into TiO_2 (N-TiO_2) for visible light response photocatalysis. J. Colloid Interface Sci. 447, 278–281. https://doi.org/10.1016/j.jcis.2014.12.097.
Yu, S., Zhang, W., Li, L., Xu, D., Dong, H., Jin, Y., 2013. Transparent conductive Sb-doped SnO_2/Ag multilayer films fabricated by magnetron sputtering for flexible electronics. Acta Mater. 61, 5429–5436. https://doi.org/10.1016/j.actamat.2013.05.031.
Zang, Z., 2018. Efficiency enhancement of ZnO/Cu_2O solar cells with well oriented and micrometer grain sized Cu_2O films. Appl. Phys. Lett. 112, 42106. https://doi.org/10.1063/1.5017002.
Zang, Z., Nakamura, A., Temmyo, J., 2013. Single cuprous oxide films synthesized by radical oxidation at low temperature for PV application. Opt. Express 21, 11448. https://doi.org/10.1364/OE.21.011448.
Zeng, X., Zhou, T., Leng, C., Zang, Z., Wang, M., Hu, W., Tang, X., Lu, S., Fang, L., Zhou, M., 2017. Performance improvement of perovskite solar cells by employing a CdSe quantum dot/PCBM composite as an electron transport layer. J. Mater. Chem. A. https://doi.org/10.1039/C7TA00203C.
Zhao, Z., Alford, T.L., 2016. The optimal TiO_2/Ag/TiO_2 electrode for organic solar cell application with high device-specific Haacke figure of merit. Sol. Energy Mater. Sol. Cells 157, 599–603. https://doi.org/10.1016/j.solmat.2016.07.044.
Zhou, L., Chen, X., Zhu, F., Sun, X., Sun, Z., 2012. Improving temperature-stable AZO–Ag–AZO multilayer transparent electrodes using thin Al layer modification. J. Phys. D Appl. Phys. 45, 505103. https://doi.org/10.1088/0022-3727/45/50/505103.
Zhu, M.-Q., Jin, H.-D., Bi, P.-Q., Zong, F.-J., Ma, J., Hao, X.-T., 2016. Performance improvement of TiO_2/Ag/TiO_2 multilayer transparent conducting electrode films for application on photodetectors. J. Phys. D Appl. Phys. 49, 115108. https://doi.org/10.1088/0022-3727/49/11/115108.